

UNIVERSITY OF OKLAHOMA

GRADUATE COLLEGE

A PRACTICING ENGINEER'S PERSPECTIVE

ON

NONLINEAR FINITE ELEMENT ANALYSIS TECHNIQUES

FOR

REINFORCED CONCRETE STRUCTURES

A Dissertation

SUBMITTED TO THE GRADUATE FACULTY

in partial fulfillment of the requirements for the

degree of

Doctor of Philosophy

By

Gene Alan Paulsgrove, P.E.

Norman, Oklahoma

2004

UMI Number: 3148884



UMI Microform 3148884

Copyright 2005 by ProQuest Information and Learning Company.
All rights reserved. This microform edition is protected against
unauthorized copying under Title 17, United States Code.

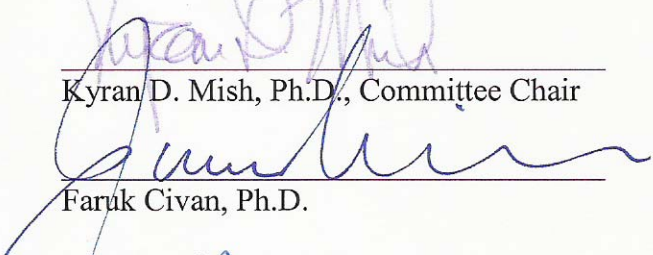
ProQuest Information and Learning Company
300 North Zeeb Road
P.O. Box 1346
Ann Arbor, MI 48106-1346

**A PRACTICING ENGINEER'S PERSPECTIVE
ON
NONLINEAR FINITE ELEMENT ANALYSIS TECHNIQUES
FOR
REINFORCED CONCRETE STRUCTURES**

**A DISSERTATION APPROVED FOR THE
SCHOOL OF CIVIL ENGINEERING
AND ENVIRONMENTAL SCIENCE**

BY

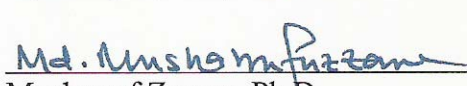


Kyran D. Mish, Ph.D., Committee Chair

Faruk Civan, Ph.D.

Kanthasamy K. Muraleetharan, Ph.D.

Jin-Song Pei, Ph.D.

Luther W. White, Ph.D.

Musharraf Zaman, Ph.D.

ACKNOWLEDGEMENTS

The research described in this dissertation was performed for the benefit of other researchers who share a desire to increase their knowledge of the behavior of reinforced concrete structures through the use of the finite element analysis technique. The contents of this report reflect the view of the author, who is responsible for the facts and accuracy of the data presented herein. The contents do not necessarily reflect the official views or policies of any of the individuals and organizations that may have provided assistance. This dissertation does not constitute a standard, specification or regulation.

The author wishes to express his appreciation to dissertation committee chairman Dr. Kyran D. Mish for his unending advice and untiring guidance on this topic. A sincere appreciation is also extended to committee members Dr. Faruk Civan, Dr. Kanthasamy K. Muraleetharan, Dr. Jin-Song Pei, Dr. Luther W. White and Dr. Musharraf Zaman for their assistance.

The author also wishes to extend his deep appreciation to Dr. Lee Taylor and TeraScale, LLC for the use of their TeraDyn explicit dynamics computing software for this engineering mechanics application, and also to Mr. Robert L. Clay and Mr. Colin Potter for their assistance. Appreciation is also extended to Mr. Y. R. Rashid, Mr. Robert S. Dunham and ANATECH Corp. for the use of their constitutive models for concrete and reinforcing steel.

DEDICATION

This work is dedicated to my family. Without their encouragement the effort would have been diminished. Special thanks go to my wife Carol for her continuous and unquestioning support. Also thanks to my children Jay, James, Sara and Jana from whom I obtain both humor and motivation.

TABLE OF CONTENTS

	Page
LIST OF TABLES	XI
LIST OF FIGURES	XII
ABSTRACT	XVI
CHAPTER 1 INTRODUCTION	1
1.1 INTRODUCTION	1
1.2 IMPORTANCE OF FINITE ELEMENT METHOD.....	2
1.3 RESEARCH OBJECTIVE	4
1.4 RESEARCH PROGRAM	5
CHAPTER 2 LITERATURE REVIEW	9
2.1 INTRODUCTION	9
2.2 GENERAL THEORY	10
2.3 STIFFNESS METHOD	11
2.4 NONLINEARITY	12
2.5 MATERIAL NONLINEARITY	13
2.6 CONSTITUTIVE MODEL.....	15
2.6.1 FAILURE THEORY	17
2.6.2 PRESSURE SENSITIVE MODEL.....	18
2.6.3 TENSILE VS COMPRESSIVE STRENGTH	18
2.6.4 WORK HARDENING	19
2.6.5 FLOW RULE	20
2.6.5.1 ASSOCIATED FLOW RULE	23
2.6.5.2 NONASSOCIATED FLOW RULE	24
2.6.6 STRAIN SOFTENING	24
2.6.7 CONCRETE	25
2.6.8 MILD STEEL AND PRESTRESSING STRAND.....	31
2.6.9 CRACK MODEL	32
2.6.10 BOND MODEL	33
2.7 NUMERICAL ANALYSIS	33

2.7.1	CONSISTENT TANGENT STIFFNESS	35
2.7.2	SOLUTION METHODS	36
2.7.2.1	h-METHOD	36
2.7.2.2	p-METHOD	37
2.8	APPLICATIONS OF FINITE ELEMENT ANALYSES	37
2.8.1	STATIC ANALYSIS	37
2.8.2	MODAL ANALYSIS	38
2.8.3	HARMONIC RESPONSE ANALYSIS	38
2.8.4	TRANSIENT DYNAMIC ANALYSIS	39
2.8.5	SPECTRUM ANALYSIS	40
2.8.6	BUCKLING ANALYSIS	40
2.8.7	EXPLICIT DYNAMIC ANALYSES	41
2.9	LITERATURE REVIEW	42
2.9.1	RECENT FEM USE BY DESIGN PRACTICIONERS, SPILLWAY STRUCTURE	42
2.9.2	RECENT FEM USE BY RESEARCHERS	44
2.9.2.1	ANALYSIS OF REINFORCED CONCRETE BEAM	44
2.9.2.2	ANALYSIS OF REINFORCED AND POST-TENSIONED CONCRETE BEAMS	49
2.9.2.3	ANALYSIS OF COLUMN ELEMENTS	52
2.9.2.4	ANALYSIS OF COLUMN – BEAM CONNECTION	57
2.9.2.5	DYNAMIC ANALYSIS OF SIX STORY Laterally Loaded STRUCTURE	59
2.9.2.6	ANACAP MODEL OF PASSIVELY CONFINED CONCRETE COLUMNS	60
2.9.3	ANATECH's ANAMAT CONCRETE MATERIAL MODEL	65
CHAPTER 3 PRESTRESSED CONCRETE BEAM ANALYSIS		68
3.1	INTRODUCTION	68
3.2	PRESTRESSED CONCRETE BEAM BEHAVIOR	68
3.3	MODELING TECHNIQUE	69
3.3.1	MODELING SEQUENCE	72
3.4	CONSTITUTIVE MODELS	72
3.4.1	CONCRETE CONSTITUTIVE MODEL	72
3.4.2	REINFORCING STEEL CONSTITUTIVE MODEL	74
3.5	ELEMENT TYPES	74
3.5.1	CONCRETE ELEMENT TYPE	74
3.5.2	REINFORCING STEEL ELEMENT TYPE	76
3.6	MODELING ALTERNATIVES	76
3.6.1	LONGITUDINAL REINFORCING STEEL	76
3.6.2	TRANSVERSE REINFORCING STEEL	77
3.6.3	CONCRETE CONSTITUTIVE MODEL	77
3.6.4	EXPERIMENTAL TESTING PROGRAM	78

3.7	COMPARISON OF RESULTS	80
3.7.1	INTRODUCTION	80
3.7.2	TYPICAL ANSYS ANALYSIS RESULTS	80
3.8	RESEARCH VARIABLES	82
3.8.1	MESH REFINEMENT	82
3.8.2	MATERIAL MODEL	84
3.9	DISCUSSION OF NUMERICAL RESULTS	85
3.9.1	INTRODUCTION	85
3.9.2	FLEXURAL TEST RESULTS	85
3.9.3	MESH REFINEMENT	86
3.9.4	EXPLANATION OF RESULTS	87
3.10	SUMMARY OF CONCLUSIONS	87
3.10.1	INTRODUCTION	87
3.10.2	CONCLUSIONS	87
3.11	ANSYS PLAIN CONCRETE SPECIMEN ANALYSIS	88
CHAPTER 4 REINFORCED CONCRETE TORNADO SHELTER		90
4.1	INTRODUCTION	90
4.2	TORNADO CHARACTERIZATION	91
4.3	TORNADO SHELTER DESIGN	96
4.3.1	TORNADO RISK ASSESSMENT	97
4.3.2	TORNADO SHELTER DESIGN WIND PRESSURE	99
4.3.3	TORNADO SHELTER DESIGN PROJECTILE IMPACT LOAD	100
4.3.4	STRUCTURAL REQUIREMENTS FOR FEMA STANDARD DESIGN	101
4.4	TORNADO SHELTER FEM ANALYSIS	102
4.4.1	GEOMETRY OF TORNADO SHELTER	103
4.4.2	MATERIAL PROPERTIES OF TORNADO SHELTER	105
4.4.3	LOADING CONDITION OF TORNADO SHELTER	107
4.5	TORNADO SHELTER FEM RESULTS	109
4.6	TORNADO SHELTER FEM DISCUSSION	115
4.7	TORNADO SHELTER FEM CONCLUSIONS	115
CHAPTER 5 REINFORCED CONCRETE SLAB ANALYSIS		116
5.1	INTRODUCTION	116
5.2	BLAST WAVES AND BLAST LOADING	117
5.3	OKLAHOMA CITY BOMBING	119
5.3.1	MURRAH BUILDING COMPLEX DESIGN	123

5.3.2	BLAST WAVE FRONT PARAMETERS	129
5.3.3	BLAST EFFECTS TO STRUCTURE	133
5.4	MURRAH BUILDING FIFTH FLOOR SLAB FEM ANALYSIS	139
5.4.1	GEOMETRY OF FIFTH FLOOR SLAB	139
5.4.2	MESH CONFIGURATIONS	140
5.4.3	MATERIAL PROPERTIES OF MURRAH SLAB	143
5.4.4	LOADING CONDITION OF MURRAH SLAB	144
5.5	MURRAH SLAB FEM RESULTS.....	147
5.6	MURRAH SLAB FEM DISCUSSION OF RESULTS.....	161
5.7	MURRAH SLAB FEM CONCLUSIONS.....	162
5.8	VALIDATION OF MURRAH SLAB FEM ANALYSIS	162
5.8.1	PREDICTED SLAB STRIP LOAD-DEFLECTION RESPONSE	163
5.8.2	FINITE ELEMENT MODEL OF SLAB STRIP	168
5.8.3	LOADING CONDITIONS IN VALIDATION MODELS.....	171
5.8.4	RESULTS OF FINITE ELEMENT ANALYSIS OF SLAB STRIP	172
5.8.4.1	RESULTS OF IMPULSE LOADING FINITE ELEMENT ANALYSIS.....	172
5.8.4.2	RESULTS OF QUASI-STATIC LOADING FINITE ELEMENT ANALYSIS.....	177
5.8.5	COMPARISON OF PREDICTED AND FEA RESULTS OF SLAB STRIP	181
5.8.5.1	IMPULSIVE LOADING COMPARISON OF RESULTS	181
5.8.5.2	QUASI-STATIC LOADING COMPARISON OF RESULTS	185
5.8.6	CONCLUSIONS OF FINITE ELEMENT ANALYSIS OF SLAB STRIP	188
	CHAPTER 6 SUMMARY OF CONCLUSIONS	189
6.1	INTRODUCTION	189
6.2	SUMMARY	190
6.2.1	SUMMARY OF PRESTRESSED CONCRETE BEAM ANALYSIS	192
6.2.2	SUMMARY OF TORNADO SHELTER ANALYSIS.....	194
6.2.3	SUMMARY OF MURRAH BUILDING FLOOR SLAB ANALYSIS.....	198
6.2.4	SUMMARY OF VALIDATION OF FLOOR SLAB ANALYSIS	202
6.3	CONCLUSIONS	205
6.3.1	CONCLUSIONS FROM PRESTRESSED CONCRETE BEAM ANALYSIS..	206
6.3.2	CONCLUSIONS FROM TORNADO SHELTER ANALYSIS	207
6.3.3	CONCLUSIONS FROM MURRAH BUILDING FLOOR SLAB ANALYSIS	207
6.3.4	CONCLUSIONS FROM VALIDATION OF FLOOR SLAB ANALYSIS	207
6.4	RECOMMENDATIONS.....	208
	REFERENCES.....	209
	LIST OF APPENDICES	212

APPENDIX A RECTANGULAR BEAM CA3-S TEST DATA.....	213
APPENDIX B RECTANGULAR BEAM ANSYS TEST DATA	222
APPENDIX C PLAIN CONCRETE RECTANGULAR BEAM	237
APPENDIX D FUJITA TORNADO DAMAGE SCALE	239
APPENDIX E USING TERASCALE’S MESHER PROGRAM.....	241
APPENDIX F USING TERASCALE’S TERADYN PROGRAM.....	256
APPENDIX G TORNADO SHELTER IMPACT LOAD PROPERTIES	259
APPENDIX H TORNADO SHELTER HYDROSTATIC PRESSURE.....	262
APPENDIX I MURRAH FLOOR SLAB MEMBER PROPERTIES	268
APPENDIX J MURRAH SLAB MOVING PRESSURE LOADING.....	271
APPENDIX K MURRAH SLAB LOAD-DEFLECTION RESPONSE	283
APPENDIX L MURRAH SLAB FLEXURAL STRESS	303
APPENDIX M FOOT SLAB QUASI-STATIC LOAD-DEFLECTION	309
APPENDIX N LITERATURE REVIEW	312

LIST OF TABLES

	Page
Table 1: ANSYS Concrete Material Model (Barbosa & Ribeiro 1998).....	46
Table 2: Rectangular Beam Mesh Refinement	83
Table 3: Fujita Tornado Damage Scale (FEMA 2004).....	92
Table 4: Murrah Slab Impulsive Load Negative Moment Results	148
Table 5: Murrah Slab Impulsive Load Positive Moment Results.....	149
Table 6: Slab Strip Load-Deflection Predicted Response.....	166
Table 7: Slab Strip Impulsive Load Negative Moment Results	182
Table 8: Slab Strip Impulsive Load Positive Moment Results	184

LIST OF FIGURES

	Page
Figure 1: Concrete Biaxial Failure Surface (Jirasek 2002).....	26
Figure 2: Concrete Uniaxial Hardening & Softening (Jirasek 2002)	27
Figure 3: Concrete Biaxial Failure Surface (Jirasek 2002).....	28
Figure 4: Concrete Models in 3D Space (Chen 1995).....	29
Figure 5: Concrete Yield Surface (Jirasek 2002).....	30
Figure 6: Mild Steel Material Model (Boresi 1987)	31
Figure 7: Prestressing Steel Model (Nawy 1996).....	32
Figure 8: Solution Methods (Bittnar 1996).....	35
Figure 9: ANSYS Reinforcement Model (Barbosa & Ribeiro 1998).....	45
Figure 10: Discrete Reinforcement (Barbosa & Ribeiro 1998)	47
Figure 11: Smeared Reinforcement (Barbosa & Ribeiro 1998)	47
Figure 12: ANSYS Nonlinear Concrete Model, (Barbosa & Ribeiro 1998)	48
Figure 13: Rectangular Beam Response (Fanning 2001)	50
Figure 14: T Beam Response (Fanning 2001)	50
Figure 15: Material Model Sensitivity in Rectangular Beams (Fanning 2001)...	51
Figure 16: Concrete Column (Balan, Spacone and Kwon 2001).....	53
Figure 17: Concrete Model (Balan, Spacone and Kwon 2001)	54
Figure 18: Column R1 (Balan, Spacone and Kwon 2001)	55
Figure 19: Column R3 (Balan, Spacone and Kwon 2001)	56
Figure 20: Column R5 (Balan, Spacone and Kwon 2001)	56
Figure 21: Effect of Confinement on Strength (Dunham and Dowell 2000)	63
Figure 22: Confined Column Model (Dunham and Dowell 2000).....	64
Figure 23: Confined Column Response (Dunham and Dowell 2000).....	65
Figure 24: Rectangular Beam Concrete Solid Element Mesh	70
Figure 25: Rectangular Beam Longitudinal Reinforcing Steel.....	71
Figure 26: Concrete Failure Surface (ANSYS 2003)	73
Figure 27: Solid 65 Element Geometry (ANSYS 2003)	75
Figure 28: Link 180 Element Geometry (ANSYS 2003)	76
Figure 29: Rectangular Beam Deflected Shape	81
Figure 30: Prestressed Rectangular Beam Response	81
Figure 31: Rectangular Beam Mesh Refinement.....	84
Figure 32: Unreinforced Beam Response	89
Figure 33: May 3, 1999 Midwest Tornadoes (The Oklahoman 1999)	91
Figure 34: Tornado Intensity Distribution (FEMA 2003)	93
Figure 35: Tornado Geographic Activity (FEMA 2004).....	94
Figure 36: Tornado Annual Distribution (FEMA 2003).....	95
Figure 37: Tornado Daily Distribution (FEMA 2003)	95
Figure 38: Above Ground Tornado Shelters (FEMA 2004).....	96
Figure 39: Above Ground Tornado Shelter (FEMA 2004)	97

Figure 40: Tornado Design Wind Speed (FEMA 2004).....	98
Figure 41: Tornado Risk Assessment (FEMA 2004)	98
Figure 42: Tornado Design Wind Pressure (FEMA 2004).....	100
Figure 43: Damage Caused By Wood Projectile (FEMA 2004)	101
Figure 44: Tornado Shelter Mesh	104
Figure 45: Tornado Shelter Rebar Mesh.....	105
Figure 46: Concrete Compressive Stress–Strain Relation	106
Figure 47: Pressure-Time Curve For Shelter Load (psi, sec)	108
Figure 48: Pressure Distance Curve For Shelter Load (psi, inch)	108
Figure 49: Data Input Screen For Shelter Load (psi, inch).....	109
Figure 50: Shelter Cracking at 4 msec	110
Figure 51: Shelter Cracking at 6 msec	111
Figure 52: Shelter Cracking at 8 msec	111
Figure 53: Shelter Cracking at 10 msec	112
Figure 54: Shelter Cracking at 12 msec	112
Figure 55: Shelter Cracking at 14 msec	113
Figure 56: Shelter Cracking at 16 msec	113
Figure 57: Shelter Cracking at 18 msec	114
Figure 58: Shelter Cracking at 20 msec	114
Figure 59: North Elevation of Murrah Building (FEMA 1996)	117
Figure 60: Blast Wave Pressure-Time Profile (Smith and Hetherington 1994)	118
Figure 61: Damage to North Elevation of Murrah Building (FEMA 1996).....	120
Figure 62: Aerial View Of Damaged Structures (FEMA 1996).....	121
Figure 63: Damaged Structures In Vicinity (FEMA 1996)	122
Figure 64: Murrah Building Prior To Blast (FEMA 1996).....	124
Figure 65: Murrah Building Complex Site Plan	125
Figure 66: North Elevation Of Murrah Building (FEMA 1996)	126
Figure 67: West Elevation Of Murrah Building (FEMA 1996)	127
Figure 68: First Floor Plan Of Murrah Building (FEMA 1996).....	128
Figure 69: Fourth Thru Ninth Floor Plan Of Murrah Building (FEMA 1996)..	129
Figure 70: Location of Truck & Extent of Crater (FEMA 1996)	130
Figure 71: Bomb Crater Covered By Tarp (FEMA 1996).....	130
Figure 72: Peak Overpressures At North Elevation (FEMA 1996).....	131
Figure 73: Positive Phase Duration At North Elevation (FEMA 1996)	132
Figure 74: Peak Overpressures In Blast Vicinity (FEMA 1996).....	132
Figure 75: Failure Extent In Murrah Building (FEMA 1996)	133
Figure 76: Damage At Column Line G (FEMA 1996).....	134
Figure 77: Blast Load Fifth Floor Slab Between Grid 20 & 22 (FEMA 1996)..	135
Figure 78: Model Of Floor Slab Used By BPAT Engineers (FEMA 1996).....	135
Figure 79: Fifth Floor Slab Response Predicted By BPAT (FEMA 1996)	136
Figure 80: Floor Slab Reinforcement (FEMA 1996).....	137
Figure 81: Slab Damage Predicted By BPAT North Elevation (FEMA 1996) ..	138
Figure 82: Extent Of Slab Damage Predicted By BPAT (FEMA 1996)	138
Figure 83: Murrah Fifth Floor Slab Mesh, 3 elements thick	141

Figure 84: Murrah Slab Positive Moment Steel Mesh.....	142
Figure 85: Murrah Slab Near Edge Negative Moment Steel Mesh.....	142
Figure 86: Murrah Slab Temperature Steel Mesh.....	143
Figure 87: Pressure-Time Curve For Blast Wave Front (psi, sec).....	145
Figure 88: Pressure Distance Curve For Blast Wave Front (psi, inch).....	146
Figure 89: Murrah Slab Deflected Shape At 5 msec	151
Figure 90: Murrah Slab Deflected Shape At 10 msec	151
Figure 91: Murrah Slab Deflected Shape At 15 msec	152
Figure 92: Murrah Slab Deflected Shape At 20 msec	152
Figure 93: Murrah Slab Deflected Shape At 25 msec	153
Figure 94: Murrah Slab Deflected Shape At 30 msec	153
Figure 95: Murrah Slab Deflected Shape At 35 msec	154
Figure 96: Murrah Slab Deflected Shape At 40 msec	154
Figure 97: Murrah Slab Deflected Shape At 45 msec	155
Figure 98: Murrah Slab Deflected Shape At 50 msec	155
Figure 99: Murrah Slab Cracking On Deflected Shape At 5 msec.....	156
Figure 100: Murrah Slab Cracking On Deflected Shape At 10 msec.....	157
Figure 101: Murrah Slab Cracking On Deflected Shape At 15 msec.....	157
Figure 102: Murrah Slab Cracking On Deflected Shape At 20 msec.....	158
Figure 103: Murrah Slab Cracking On Deflected Shape At 25 msec.....	158
Figure 104: Murrah Slab Cracking On Deflected Shape At 30 msec.....	159
Figure 105: Murrah Slab Cracking On Deflected Shape At 35 msec.....	159
Figure 106: Murrah Slab Cracking On Deflected Shape At 40 msec.....	160
Figure 107: Murrah Slab Cracking On Deflected Shape At 45 msec.....	160
Figure 108: Murrah Slab Cracking On Deflected Shape At 50 msec.....	161
Figure 109: Slab Strip Static Load-Deflection Predicted Response	164
Figure 110: Slab Strip Impulse Load-Deflection Predicted Response	165
Figure 111: Slab Strip Reinforcement Pattern.....	169
Figure 112: Slab Strip Mesh; 3 elements Through Slab Depth	169
Figure 113: Slab Strip Mesh; 6 elements Through Slab Depth	170
Figure 114: Slab Strip Mesh; 12 elements Through Slab Depth	170
Figure 115: Slab Strip 3 Element Mesh; First Cracking At Fixed Ends.....	173
Figure 116: Slab Strip 3 Element Mesh; First Cracking At Midspan.....	173
Figure 117: Slab Strip 3 Element Mesh; Flexural Strength At Midspan.....	174
Figure 118: Slab Strip 6 Element Mesh; First Cracking At Fixed Ends.....	174
Figure 119: Slab Strip 6 Element Mesh; First Cracking At Midspan.....	175
Figure 120: Slab Strip 6 Element Mesh; Flexural Strength At Midspan.....	175
Figure 121: Slab Strip 12 Element Mesh; First Cracking At Fixed Ends.....	176
Figure 122: Slab Strip 12 Element Mesh; First Cracking At Midspan.....	176
Figure 123: Slab Strip 12 Element Mesh; Flexural Strength At Midspan.....	177
Figure 124: Slab Strip Cracking At 20 msec	178
Figure 125: Slab Strip Cracking At 24 msec	178
Figure 126: Slab Strip Cracking At 28 msec	179
Figure 127: Slab Strip Cracking At 32 msec	179

Figure 128: Slab Strip Cracking At 36 msec	180
Figure 129: Slab Strip Cracking At 40 msec	180
Figure 130: Slab Strip Impulsive Load Negative Moment Results	182
Figure 131: Slab Strip Impulsive Load Positive Moment Results.....	184
Figure 132: Simply Supported Slab Quasi-Static Loading Response	186
Figure 133: Fixed Ends Slab Quasi-Static Loading Response	186

ABSTRACT

A PRACTICING ENGINEER'S PERSPECTIVE ON NONLINEAR FINITE ELEMENT ANALYSIS TECHNIQUES FOR REINFORCED CONCRETE STRUCTURES

Present design practice of reinforced concrete structures is principally based on linear elastic material properties. Deflections are generally taken as simple multiples of the elastic analysis. However, structural engineers are becoming increasingly proficient with the finite element method since it is a useful technique in solving nonlinear problems in continuum mechanics. Simplified linear analysis techniques are not suitable in quantifying the behavior of a reinforced concrete structure, especially approaching its failure load. The structure's response is load path dependent due to the presence of nonlinearities.

In this research, commercially available software with nonlinear concrete and steel material models, was used to model reinforced concrete structures near their failure loads. Analysis validation consisted of comparison with either experimental results or classical analyses. An implicit dynamic analysis was performed using ANSYS of a rectangular prestressed concrete beam subjected to point loads, and compared with experimental results. Explicit dynamic analyses were performed using TeraScale's TeraDyn code of a tornado shelter and a floor slab subjected to an impulsive pressure load, and compared to classical analyses.

The research demonstrates the continued progress in finite element analysis of reinforced concrete structures. Increasingly, structural engineers will use this method in their designs, and in research into materials and systems.

CHAPTER 1 INTRODUCTION

1.1 INTRODUCTION

The research described in this dissertation is provided for the benefit of other researchers who desire to increase their knowledge of the behavior of reinforced concrete structures using the finite element analysis technique. The finite element method is a useful technique in solving highly nonlinear problems in continuum mechanics.

Reinforced concrete structures exhibit highly nonlinear behavior, especially approaching failure load. Simplified linear analysis techniques are not suitable in quantifying the behavior of these structures near their ultimate strength, where the response is significantly nonlinear due to the plastic behavior of the concrete and reinforcing steel. Concrete exhibits a strain hardening and subsequent strain softening behavior, and the reinforcing steel exhibits a large plastic strain region. The displacement solution for a reinforced concrete structure is highly load path dependent, typical to materials which exhibit plastic, nonlinear stress-strain behavior.

1.2 IMPORTANCE OF FINITE ELEMENT METHOD

Present design practice of reinforced concrete structures is principally based on linear, elastic material properties. Reinforced concrete structures are assumed uncracked for analysis purposes. When cracking or time-dependent effects are considered, deflections are generally taken as simple multiples of the elastic analysis. Until the last two decades, the lack of three dimensional concrete material properties, and limited computer capabilities, have restricted the use of computational methods to model reinforced concrete systems as general three dimensional solids.

Today, nonlinear methods of analysis are often used by structural engineers to solve design problems that in the past were solved to the required degree of accuracy using simplified linear models. Problems that previously were solved using empirical relations developed from experimental methods are now solved using finite element discretization combined with nonlinear material models. The numerical results can be validated by test data, obtained either from prior experimental research from the literature, when available, or from a supporting experimental program. Thus, the finite element method is increasingly used in design of reinforced concrete structures, and also in research where the computational method can reduce the need for experimental testing over the full range of test variables.

Increasing numbers of structural engineers are becoming proficient with the finite element method. The method is one of the most powerful computational tools used today. The use of this tool, along with validation of the analysis with experimental results, will likely contribute to future productivity gains in both research and commercial enterprises. This tool, after further development, will be more broadly used by structural engineers in the design of complex structures, and for continued research in materials and structural components and systems.

Failure analysis using the finite element analysis technique requires an understanding of the potential sources of nonlinearity. Both geometry and material behavior can be a source of nonlinearity. A geometric nonlinearity can be introduced as large deformations occur in a structure, e.g. buckling of a flexible column.

Material nonlinearity and inelasticity are observed for most materials, especially near the failure load. A material behaves elastically only when the load path is reversible. The state of strain can be determined uniquely from the current state of stress and is not dependent on the load path. A linear material exhibits a linear stress strain relationship. A nonlinear elastic material model will exhibit a nonlinear but reversible stress-strain relationship, i.e. reversible dilation and distortion. For inelastic materials, knowledge of the load history is required to determine the current state of stress and strain.

A third source of nonlinearity is introduced in the computational modeling of some structures. It's called a "changing status" nonlinearity, and occurs when a structural behavior is dependent on a status or condition that can change during the loading. Contact models are part of this classification of nonlinearities. Unless either perfect bond or linear bond is assumed to transfer forces between the concrete and reinforcing steel, nonlinearity is introduced from the contact model for the bond surface between the concrete and reinforcing steel.

The bond between the reinforcing steel and concrete is essential to the performance of reinforced concrete (Paulsgrove 1996). Forces are transferred from steel to concrete through bond stresses. The application of external loads causes increases in steel stress as the cross section deforms to resist external moments. As loads increase and applied moment approaches the nominal flexural capacity, flexural cracking can occur and extend towards the ends of simply supported beams. The presence of flexural cracking is evidence of the transfer of forces between reinforcing steel and concrete through bond stress.

1.3 RESEARCH OBJECTIVE

This research emphasizes the study of nonlinearity in the finite element analysis of reinforced concrete structures. This research focuses on an evaluation of commercial software currently available to structural engineers for their use in the design of complex reinforced concrete structures, and their research into

materials and systems. This research studies the continued progress in finite element analysis of reinforced concrete structures, and the likely future contribution for research and commerce.

This research focuses on the current capability of commercially available finite element software to accurately predict the behavior of reinforced concrete structures. The accuracy depends not only on the type of nonlinear finite element analysis used, but also on the material models of both the concrete and the reinforcement. The behavior of reinforced concrete structures is highly nonlinear. Reinforced concrete behaves as an anisotropic material. The reinforcement and the concrete materials can either be meshed separately, or “smeared” reinforcement concrete elements can be used.

The goal of this research is to demonstrate the importance of the concrete material model, especially the strain softening region, in predicting the behavior of reinforced concrete structures. The reinforcement and concrete materials each exhibit nonlinear behavior. Both materials exhibit a strain hardening region, followed by strain softening.

1.4 RESEARCH PROGRAM

This research reviews, for the benefit of a practicing structural engineer, the fundamentals of the finite element analysis method. The review focuses on

identifying the sources of nonlinearity inherent in an analysis of a reinforced concrete structure, especially geometry and material model. Some past research is reviewed that involves finite element modeling of reinforced concrete members. Finally, some commercially available software will be evaluated in their capability to model the nonlinear behavior of a wide range of reinforced concrete structures and their loading conditions, with the objective of benefiting the practicing structural engineer.

More specifically, the research program will:

- Use ANSYS to computationally model the flexural behavior of a prestressed concrete beam subjected to static load, and compare the results to experimental tests performed in 1995 at the Fears Structural Engineering Laboratory.
- Use TeraScale's TeraDyn explicit dynamics code to computationally model an above ground reinforced concrete tornado shelter subjected to an impulsive pressure load.
- Use TeraScale's TeraDyn explicit dynamics code to computationally model a reinforced concrete one way floor slab subjected to an impact load, and compare the results to the Murrah Building blast damage on April 19, 1995.

In this research, commercially available software developed by ANSYS Corporation and TeraScale, LLC. are used to model the nonlinear behavior of reinforced concrete structures near their failure load. Analyses validation consists of a comparison with either experimental results or classical analyses. An implicit dynamic analysis is performed using ANSYS on a rectangular prestressed concrete beam subjected to point loads. The ANSYS results are compared with experimental results. An explicit dynamic analyses is performed using TeraScale's TeraDyn code on a one-way slab subjected to an impulsive pressure load, and the results are compared to classical analyses.

This engineering mechanics research utilizes the commercially available explicit dynamics computing software TeraDyn, developed by TeraScale, LLC. A beta version of the TeraDyn explicit dynamics code was provided as part of a cooperative research effort. This beta version of the code is a work in progress and this Ph.D. research provided a mechanism for validating and debugging many aspects of the reinforced concrete modeling details of the finite element application.

The constitutive model for concrete and reinforcing steel used with TeraScale's TeraDyn explicit dynamics finite element analysis software was developed by ANATECH Corporation. The commercially available finite

analysis software developed by ANSYS Corporation also includes a nonlinear concrete and reinforcing steel material model.

CHAPTER 2 LITERATURE REVIEW

2.1 INTRODUCTION

Some basic theory of the finite element method, and a general introduction to the constitutive modeling of concrete and reinforcing steel, are provided in the first portion of this chapter. Readers not requiring a review of this material may desire to skip ahead to section 2.8, to where the review of the previous research in analytical modeling of reinforced concrete structures begins. Appendix N provides some additional background material in constitutive modeling and basic theory of finite element analysis.

The most common application of the finite element method is in solving problems in structural mechanics. In fact, the method was invented by structural engineers to solve problems in elasticity and structural mechanics. The finite element analysis method is increasingly used as an analysis technique by structural design engineers. The current state of development of commercial software in combination with the power of personal computers, allow both

researchers and practitioners the benefit of increasing their knowledge of the behavior of concrete structures through the use of finite element analysis.

2.2 GENERAL THEORY

The finite element method obtains an approximation of the solution of a continuum problem in structural mechanics. The structure is modeled as an assemblage of elements, interconnected at their joints, or nodes. Thus, the finite element model is a discretization of the real, continuous, structure. Known are the initial geometry of the structure, the structural stiffness of the elements, and the structure's support conditions. The structure is loaded, and the displacements of the node points are determined approximately through numeric computations. A balance is obtained between the internal strain energy contained within the structure's elements as the internal nodes displace due to the loads, and the external work exerted on the structure as the external nodal loads act through their nodal displacements. The additional terms, kinetic energy and viscous dissipation energy, must also be considered in a dynamic analysis. The stresses in the structure's elements are then determined from the nodal displacements and the corresponding constitutive laws.

The finite element method can be used to solve many problems in structural mechanics. The theoretical basis for the analysis method is the principle of virtual work, and the variational principles of mechanics (Bittnar and Sejnoha, 1996). The method is based upon the first law of thermodynamics,

which states that energy is conserved. Therefore, the external work performed to deform a structural system must equal the structure's internal strain energy. The laws of thermodynamics also state that for a process to be reversible, any deformations in the process must be reversible, i.e. in an elastic deformation the external work equals the change in internal strain energy. But a real deformation is often an irreversible process that dissipates energy, i.e. in an inelastic deformation, the external work must equal the internal strain energy plus any energy losses due to the plastic deformation of the material. The additional terms, kinetic energy and viscous dissipation energy, must also be considered in a dynamic analysis.

2.3 STIFFNESS METHOD

The principle of virtual displacements leads to the Lagrange variational principle, and is the basis for the displacement, equilibrium, or stiffness, method used in structural analysis. The Lagrange variational principle states that the solution minimizes the potential energy of the system. The minimum potential energy principle leads to the Cauchy equilibrium equations and the natural, or Neumann, boundary conditions. A displacement field is approximated using the structural stiffness matrix while enforcing compatibility. The material properties, or constitutive relations, are used in the solution. Thus, as required to solve any problem in structural mechanics, equilibrium, compatibility, and constitutive laws are satisfied.

2.4 NONLINEARITY

Failure analysis using the finite element analysis technique requires an understanding of the potential sources of nonlinearity. The assumptions used to develop the computational model must reasonably address the problem's nonlinearities, in order to obtain accurate results. The load-response history of the structure must be carefully modeled, with adequate attention given to the size of the load increment. Near failure, large deformations can occur, and sources of nonlinearity can cause inaccuracies and instabilities in the analysis.

Linearity is exhibited when the load-displacement curve is linear throughout the range of loading and displacements. Thus, linearity occurs only when the structural stiffness remains constant for each increment of displacement. A constant structural stiffness requires a linear strain-displacement relation and a linear stress-strain relation. Stated more simply, linearity only occurs when geometry and material properties are linear.

However, many real problems are not linear problems, and use of linear approximations may lead to inaccurate results. Nonlinear structural behavior is characterized as a nonlinear load-deflection curve, and a varying structural stiffness. Geometry and material behavior are the predominant sources of nonlinearity.

2.5 MATERIAL NONLINEARITY

Temperature effects, and time dependent effects such as volumetric changes from creep and shrinkage, are potential sources of material nonlinearity. A material can exhibit other nonlinearities, such as a dependency on the rate of loading, cyclic loading, or the magnitude of stress.

Materials can be assumed to behave either linearly or nonlinearly, and either elastically or inelastically. A linear elastic material exhibits a constant material stiffness throughout the load path, and the current stress and strain state can be uniquely determined from the current loading condition. In contrast, the stress and strain state for a nonlinear inelastic material cannot be uniquely determined from the current loading, but rather is dependent upon the load path.

A material behaves elastically only when the load path is reversible. The external work expended by loading an elastic material is converted into internal strain energy within the material, as the material deforms under the loading. Both the deformations and the energy are fully recovered upon unloading the structure. The state of strain can be determined uniquely from the current state of stress and is not dependent on the load path. Conversely, the state of stress can be determined uniquely from the current state of strain and is not dependent on the load path. The principal stress axes coincide with the principal strain axes.

Elastic materials can behave either linearly or nonlinearly. A linear elastic material will exhibit a reversible, linear, stress-strain relation. A nonlinear elastic material model will exhibit a nonlinear but reversible stress-strain relationship, i.e. reversible dilation and distortion (Chen and Han, 1995). Although the material stiffness is nonlinear, the loading is unique, and the deformations and the internal strain energy are fully recoverable.

All real materials exhibit nonlinear inelastic behavior, although some materials exhibit nearly linear elastic behavior in a portion of the range of their stress-strain relation. Therefore, an elastic material is an idealized material, since any real deformation dissipates energy, and results in at least some permanent deformation.

All real materials deform in an irreversible process, i.e. the deformations cannot be fully reversed without expending additional energy. The second law of thermodynamics states that entropy is a monotonically increasing function. It further states that a process cannot yield a negative internal entropy increment. A process that yields constant internal entropy is a reversible process. A reversible process only occurs in theory. All real processes are irreversible, i.e. heat is generated as a result of the process.

Material nonlinearity and inelasticity are observed for most materials, especially near the failure load. A nonlinear material exhibits a changing material stiffness upon loading. The deformations and internal strain energy of an inelastic material under loading are not fully recoverable upon unloading, and some permanent deformations remain in the material. For inelastic materials, knowledge of the load history is required to determine the current state of stress and strain; i.e. the current stress state is dependent upon the load path.

2.6 CONSTITUTIVE MODEL

A constitutive model is a mathematical formulation for the material's stress strain relationship during loading, in three dimensional stress space. The model describes the relationship both before initial yielding, and after yielding. These mathematical models have been developed for both linear and nonlinear materials, exhibiting either elastic or inelastic behavior.

Constitutive relations must be derived from experimental observations. Thus material stiffness is derived from stress-strain data obtained by experimental research. Experimentalists have recorded the data after performing tension, compression, pure shear (torsion), and other tests on material specimens. For isotropic materials, Young's modulus and Poisson's ratio are obtained from uniaxial loading tests. Pure shear loading tests provide the shear modulus. The bulk modulus is obtained from a three dimensional, hydrostatic, compression test.

Additional material parameters are empirically derived for use in constitutive relations that model plastic material behavior.

Constitutive relations mathematically specify the behavior of materials, both in the material's elastic region before the stresses exceed the elastic limit, and in the material's work hardening region after the material yields. These relations specify the initial yield surface (failure theory), the subsequent yield surface as loading at the yield condition produces plastic deformation in the material (hardening rule), and the elastic and plastic strain increments for the stress increment at the yield condition (flow rule). These relations are discussed in the following paragraphs. The material behavior that occurs in the strain softening region, beyond the material's work hardening region, will also be discussed.

A three dimensional stress state can be decomposed into a hydrostatic stress and a deviatoric stress. The hydrostatic part is equivalent to a uniform pressure on the material; i.e. the shear stresses are zero, and the three normal stresses are equal. The remaining stresses are called the deviatoric stresses, and generally consist of both shear and normal stress components. The hydrostatic stresses cause either dilation, for the tensile case, or contraction, for the compression case. Since the deviatoric stresses consist of normal and shear

stresses, these stress components cause the associated distortional strains in the material.

These decomposed stress components, the hydrostatic and deviatoric stress components, can be plotted in the Haigh-Westergaard 3D principal stress space. The hydrostatic axis represents all possible hydrostatic stress conditions, and is a line through the origin and oriented equidistant from the three principal stress axes. A deviatoric plane is a plane normal to the hydrostatic axis. Thus for any stress state, the vector from the origin to the deviatoric plane represents the hydrostatic stress, and the vector in the deviatoric plane from the hydrostatic stress to the 3D principal stress point represents the deviatoric stress. A meridian plane is a plane containing the hydrostatic axes. The meridian planes are identified with a counterclockwise angle within the deviatoric plane from the vertical principal stress axis, σ_1 , to the point representing the stress state. The tensile meridian is $\Theta = 0^\circ$. The compressive meridian is $\Theta = 60^\circ$. These meridians represent a hydrostatic stress state, along with their respective tensile or compressive stress superimposed in one direction.

2.6.1 FAILURE THEORY

For elastic materials, either linear or nonlinear, the failure, or yield, surface remains constant for all loading conditions. The failure surface can expand for inelastic materials that can strain harden; i.e. materials that can

withstand an increase in stress beyond initial yielding. The initial failure surface will remain constant for an elastic, perfectly plastic, material, since the material cannot withstand an increase in stress after initial yield. Damage theory is commonly used to model the behavior of strain softening; i.e. the behavior of a material to withstand only a reduced stress, once a certain loading condition is reached. Damage models have the effect of contracting the failure surface, the opposite as occurs in the case of strain hardening, where the failure surface is expanding.

2.6.2 PRESSURE SENSITIVE MODEL

A pressure sensitive failure criterion introduces a second parameter, I_1 , into the material model. I_1 is the first invariant of the stress tensor. The first invariant of the stress tensor incorporates the dilational behavior of the material. Thus, a pressure sensitive model uses two parameters; J_{2D} , which incorporates the distortional behavior, and I_1 .

2.6.3 TENSILE VS COMPRESSIVE STRENGTH

Different tensile and compressive strengths are possible for the Mohr-Coulomb criteria. Thus, the Mohr-Coulomb model does not have symmetry in the tensile and compressive quadrants. The parameter m is the ratio of a material's compressive and tensile strengths. The Mohr-Coulomb model can thus be used for soils, rocks and concrete, which have little strength in tension. For

concrete, which has a ratio of compressive to tensile strength, m , of about 10, ϕ would be 55° .

In 1952, Drucker and Prager formulated a two-parameter, pressure dependent model. The Drucker-Prager model can be made to match the Mohr-Coulomb model only along one meridian, thus limiting its value for materials with differing tensile and compressive strengths.

2.6.4 WORK HARDENING

Many materials exhibit work hardening behavior, i.e., they can withstand an increase in stress after initial yielding. For the 2D and 3D loading conditions, a neutral loading is defined as a loading that does not result in additional plastic deformation. Plastic flow theory is used to relate the elastic and plastic strain increments to the stress increment at the yield condition. Three hardening rules are discussed, isotropic, kinematic, and mixed.

The isotropic hardening model predicts a uniform expansion of the yield surface as the material is loaded at the yield condition. The yield surface expands uniformly, without distortion, translation or rotation. Initial anisotropies in the material can be described by using nine dimensional stress space. The model is typically used for a monotonic loading condition, since work hardening of an initially isotropic material generally results in anisotropy, referred to as the

“Bauschinger effect”. The isotropic hardening model is contrary to the “Bauschinger effect”. The “Bauschinger effect” predicts a decrease in resistance to a plastic deformation after the material has been subjected to a plastic deformation in the opposite direction. Inaccuracies will result when this model is used for complex load paths with frequent stress reversals.

The kinematic hardening model predicts a translation of the yield surface as the material is loaded at the yield condition. The yield surface translates without distortion or rotation. For an exact reversal of loading, the model predicts the initial failure surface to return to the initial position. Thus, the model predicts the material behavior observed in the “Bauschinger effect”.

The mixed hardening model predicts both a translation and a uniform expansion of the yield surface, as the material is loaded at the yield condition. The yield surface does not distort, but retains its original shape. The yield surface translates, but does not rotate. Two hardening parameters are used to control the “Bauschinger effect”, and adjust the extent of the translation and expansion.

2.6.5 FLOW RULE

For an elastic material, the deformations are fully recoverable upon unloading. The strains are the gradients of the stress potential function, i.e. the gradients of the complementary energy density function. Thus, the strains can be derived directly by differentiating the elastic stress potential function, or the

complementary energy density function, with respect to the stresses. Similarly, the stresses are the gradients of the strain potential function, i.e. the gradients of the strain energy density function. A material with these properties is called a “hyperelastic” or a “Green elastic material”. A gradient of a potential function is normal to the potential function, thus the strains are oriented in a direction normal to the stress potential function.

Continued loading of an inelastic material at the yield condition will result in plastic strain, and the increment of energy used to deform the material is not fully recoverable. For a perfectly plastic material, none of the energy increment is recoverable. For a work hardening material, some of the energy increment is stored as elastic strain energy and is recoverable upon unloading, while the remaining part of the energy increment is used to plastically deform the material and is not recoverable.

The yield surface of a work hardening, inelastic, material expands as the material yields. Although a work hardening inelastic material exhibits a decreasing stiffness with increasing strain, the material can withstand an increase in stress. The strain increment at the yield condition has an elastic part, $d\epsilon_{ij}^e$, and a plastic part, $d\epsilon_{ij}^p$. An elastic, perfectly plastic, material can not withstand a stress increase, and the yield surface does not expand as the material yields inelastically, and the elastic strain increment is zero.

A flow rule must be formulated to relate the increment of plastic strain with the stress increment, when the material is loaded at the yield condition. The flow rule defines the magnitude and orientation of the components of the plastic strain increment. The plastic strain increment is a second order tensor, and has nine components in nine-dimensional strain space.

In the 1950's, Drucker developed the material stability postulate. The postulate states that positive work is done on a structure upon loading, and that the net work for a load increment is positive for a plastic deformation. Drucker developed the concepts of convexity, normality, linearity, continuity and uniqueness, which are significant for work hardening materials. Convexity requires that the initial and subsequent yield surfaces be convex. Normality requires that the plastic strain increment vector be normal to the yield surface. Linearity states that the plastic strain increment is linear in the stress increment. Continuity requires that there is no plastic strain increment for the neutral loading case, when the stress increment is tangential to the yield surface. Uniqueness requires that the increments of stress and strain be uniquely determined by the changes in external forces and displacements.

In 1928, von Mises proposed the concept of the plastic potential function as the logical extension of the elastic potential function used in elastic analysis.

The plastic potential function, $g(\sigma_{ij})$, is a function of the stresses, σ_{ij} . Then, the plastic strain increment, $d\epsilon_{ij}^p$, can be written as a scalar multiple, $d\lambda$, of the gradient of the plastic potential function. A gradient of a potential function is normal to the potential function, thus the increments of the plastic strains are oriented in a direction normal to the plastic potential function.

$$(1) \quad d\epsilon_{ij}^p = d\lambda \partial g(\sigma_{ij}) / \partial (\sigma_{ij}) \quad \text{nonassociated flow rule} \quad (2.1)$$

An original theory on plasticity dates from the 1864 to 1872 papers of Tresca, with the concept of a maximum shear stress yield condition (Chen and Han, 1995). In 1870, St. Venant formulated the constitutive relations for a rigid, perfectly plastic, material in plane stress. St. Venant suggested the flow rule that the principal axes of the strain increment coincide with the principal axes of stress. The yield condition was formulated in three dimensions by Levy, later in 1870, and again independently in 1913, by von Mises.

2.6.5.1 ASSOCIATED FLOW RULE

The simplest flow rule is developed from the assumption that the plastic potential function, $g(\sigma_{ij})$, coincides with the yield function, $f(\sigma_{ij})$. Then the plastic flow develops along the normal to the yield surface, $\partial f(\sigma_{ij}) / \partial (\sigma_{ij})$. The plastic flow is a scalar multiple of the gradient of the yield function. This is called an associated flow rule, because the plastic strain increment is associated with the yield function.

$$(2) \quad d\epsilon_{ij}^p = d\lambda \frac{\partial f(\sigma_{ij})}{\partial \sigma_{ij}} \quad \text{associated flow rule} \quad (2.2)$$

2.6.5.2 NONASSOCIATED FLOW RULE

A more general flow rule is developed from the assumption that the plastic potential function, $g(\sigma_{ij})$, does not coincide with the yield function, $f(\sigma_{ij})$. Then the plastic flow develops along the normal to the plastic potential function, $\partial g(\sigma_{ij})/\partial \sigma_{ij}$. This is called a nonassociated flow rule, because the plastic strain increment is not associated with the yield function.

2.6.6 STRAIN SOFTENING

Increased loading into the work hardening region can lead to strain softening in some materials. In the strain softening region, the material exhibits a reduction in its ability to resist the next load increment. The stress in the material decreases with the strain increment, as the material deforms plastically in combination with the occurrence of damage.

Structural changes can occur in the material as the loading condition enters the material's strain softening region. The internal, elastic strain energy of the material degrades with the damage that occurs in the loading increment. Damage in concrete can consist of a change in volume as the material fractures and crushes. The combination of the theory of plasticity with damage, or fracturing, theory allows the formulation of stress-strain relations in the strain softening region (Han and Chen, 1986).

2.6.7 CONCRETE

Concrete behavior is highly dependent upon the loading condition. Sources of nonlinearity include magnitude of loading, cyclic loading, rate of loading, temperature, and time dependent effects such as volumetric changes from creep and shrinkage. Cyclic loading will degrade the stiffness of reinforced concrete structures as the concrete progressively cracks, the reinforcement yields, and the bond of reinforcing steel to concrete is affected. Time dependent effects will produce additional deformation, and equilibrium will require the redistribution of stresses.

When confined, concrete will exhibit ductility under a compressive loading. The biaxial failure surface for concrete is shown in Figure 1. Concrete resists compressive loading well, but has a tensile strength of only about one-tenth its compressive strength. Inadequately reinforced concrete will exhibit an undesirable brittle tensile failure behavior. The tension response of unreinforced concrete is linear elastic, followed by brittle failure. Tensile loading results in cracking normal to the maximum principal stress direction (Jirasek and Bazant, 2002). Concrete can also fail in a shear mode.

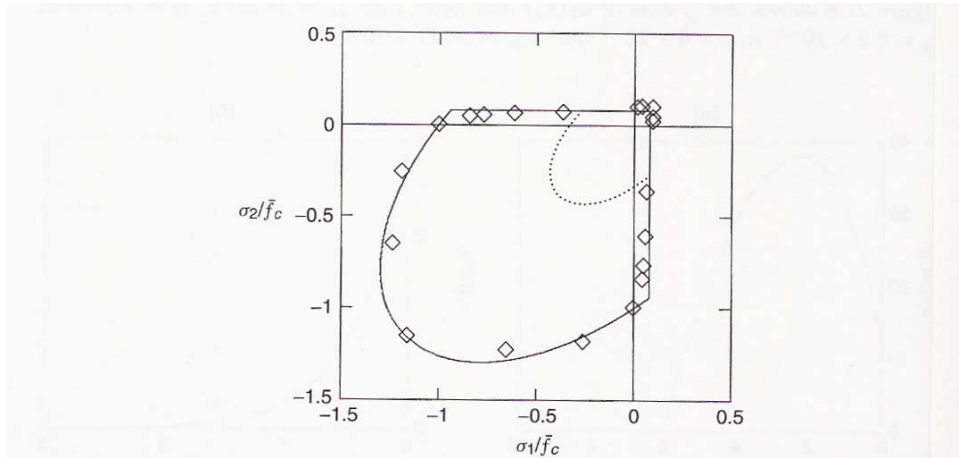


Figure 1: Concrete Biaxial Failure Surface (Jirasek 2002)

Concrete is a pressure sensitive, highly nonlinear material, and its behavior is much different in compression than in tension or pure shear. In compression, concrete can be approximated as linear elastic for only a small portion of its loading range. As shown in the left side of Figure 2, concrete has a relatively wide inelastic range, where concrete hardens after initial yield. Concrete hardening is then followed by softening, as damage in the material occurs. Concrete does not exhibit a plastic yield plateau, except in the case of large hydrostatic pressure. Instead, concrete exhibits localized effects, and softens after the peak stress as the material strains inelastically. The right side of Figure 2 shows a tension softening model for concrete.

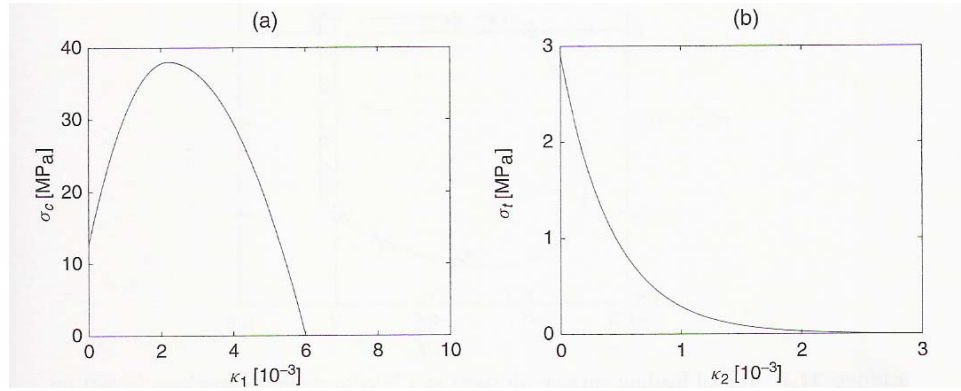


Figure 2: Concrete Uniaxial Hardening & Softening (Jirasek 2002)

Concrete is a pressure sensitive material, with a significant difference in compressive and tensile strengths. The early maximum shear stress theory failure models of Tresca and von Mises are pressure independent models. These models were modified in the Mohr-Coulomb and Drucker-Prager models, to include the effect of hydrostatic pressure. Biaxial failure surfaces of these models are shown in Figure 3. Figure 4 shows these models in 3D stress space. The Drucker-Prager model provides a continuous, smooth failure surface, advantageous in numerical modeling, but does not accurately model a material such as concrete, a material with different properties in the tensile and compressive regions. A tension cutoff, such as the Rankine model, can be superimposed onto these models.

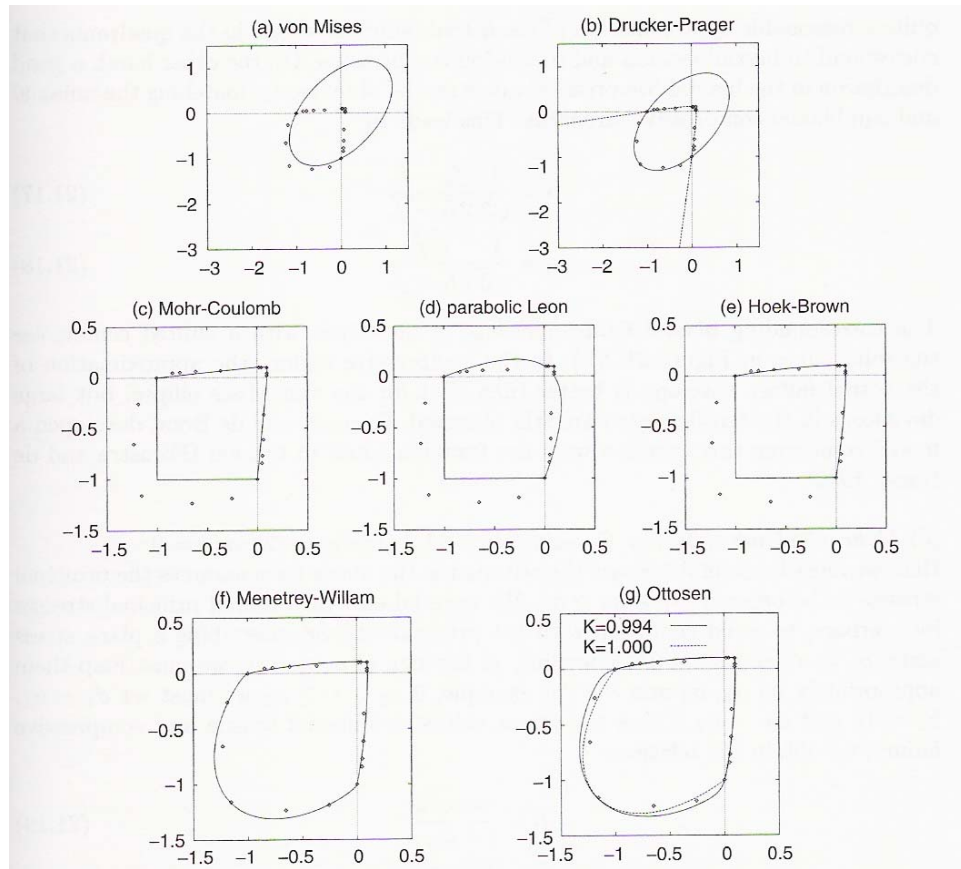


Figure 3: Concrete Biaxial Failure Surface (Jirasek 2002)

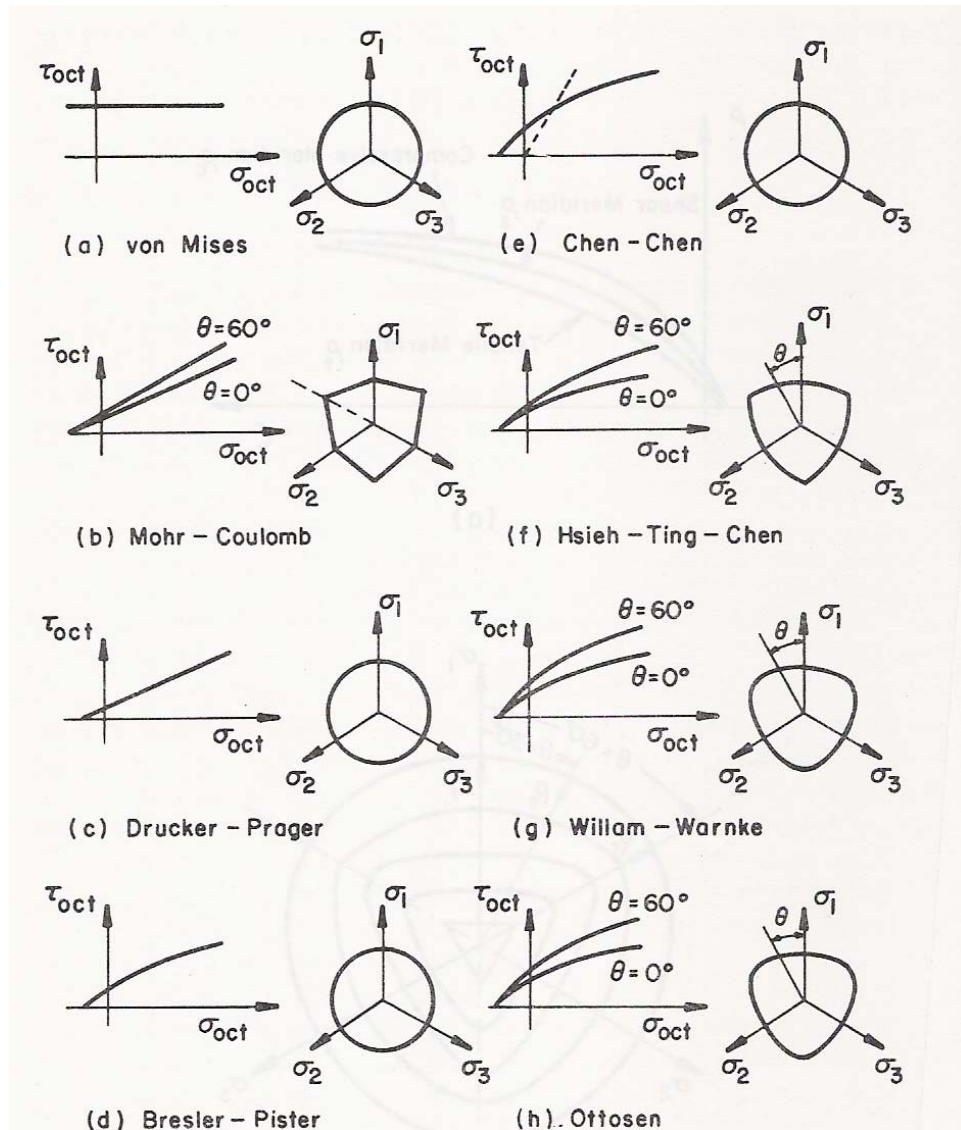


Figure 4: Concrete Models in 3D Space (Chen 1995)

Figure 5 shows a concrete's failure surface in principal stress space. The left side depicts the effect of increased hydrostatic pressure, and the successively larger failure surfaces are deviatoric sections farther out along the hydrostatic axis. The right side shows the expansion of the yield surface due to the effect of work hardening.

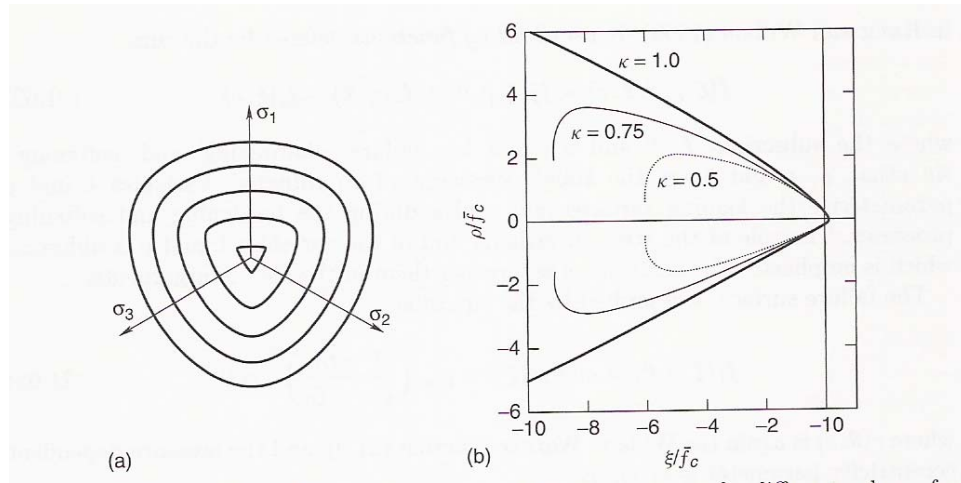


Figure 5: Concrete Yield Surface (Jirasek 2002)

In more complex models, a nonassociated flow rule with a variable dilatancy factor is used to better predict the behavior of concrete, since concrete exhibits inelastic volumetric contraction and dilation (Chen and Han, 1995). Concrete subjected to a compressive loading, exhibits inelastic volume contraction at the beginning of yielding, and volume dilation at about 75 to 90% of ultimate strength. The shape of the initial yield surface is much different than the shape of subsequent yield surfaces, and the yield surfaces are not isotropic. Therefore, nonuniform hardening rules are used which are not isotropic. Combinations of plasticity and damage theories can be used to model concrete in the softening range (Han and Chen, 1986). Experimentalists have further discovered that volumetric dilation and octahedral shear strength are influenced by concrete strength, (Chin, 2001).

2.6.8 MILD STEEL AND PRESTRESSING STRAND

Steel is a pressure independent material. Therefore, the von Mises model can be used to model the mild steel used as reinforcing steel and the tempered, high strength steel used as prestressing steel. The stress strain curve for mild steel is shown in Figure 6, and the prestressing steel in Figure 7.

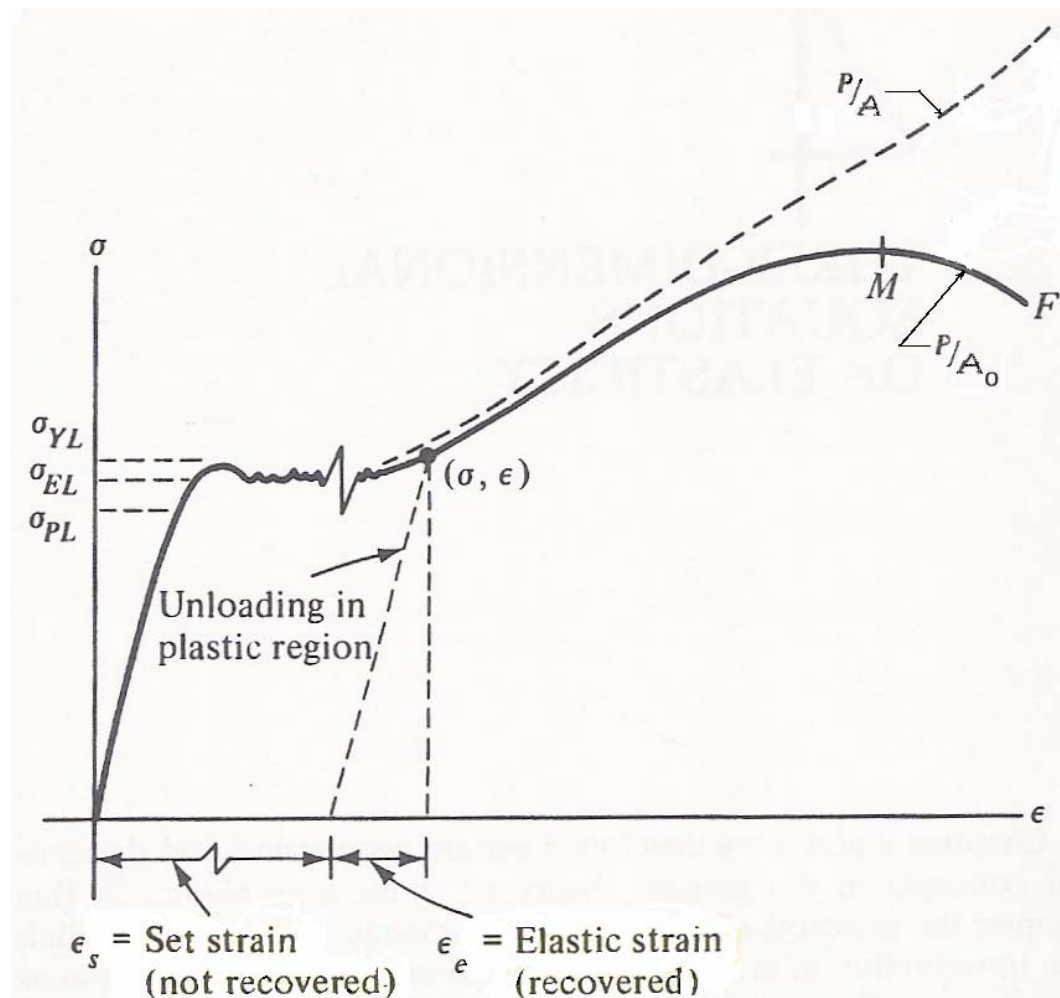


Figure 6: Mild Steel Material Model (Boresi 1987)

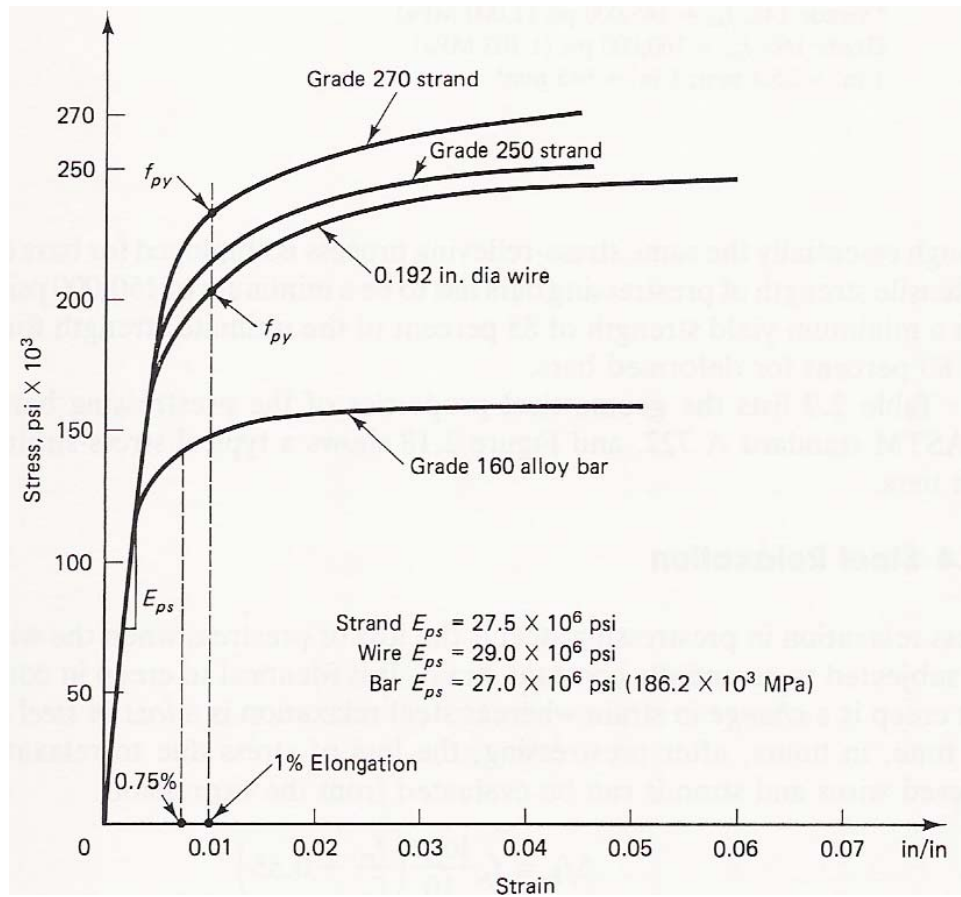


Figure 7: Prestressing Steel Model (Nawy 1996)

2.6.9 CRACK MODEL

Most present analyses use the concept of a “smeared” crack distributed either over the entire element, or at integration points within an element. The normal to the plane of the crack is oriented in the direction of the principle tensile strain. The modeling of discrete cracks is typically not performed due to the complications encountered in circumstances such as stress reversals from dynamic or cyclic loading conditions.

2.6.10 BOND MODEL

The bond model of reinforcing steel to concrete is typically simplified as either a perfect bond model, or a linear bond stress model.

2.7 NUMERICAL ANALYSIS

The following is a summary of the static, linear, finite element stiffness method. The method is derived by equating internal virtual work to external virtual work. The underscored variables are vectors, and the brackets indicate a matrix.

Before the structure can be discretized, and the structure's nodal equilibrium equations solved for the unknown displacements, the following relations must be developed for each type of structural element that will be used in the structural model.

$$(3) \quad \underline{v} = [H] \underline{u} \quad \text{the element displacement interpolation relation} \quad (2.3)$$

$$(4) \quad \underline{\epsilon} = [B] \underline{u} \quad \text{the element strain-displacement relation} \quad (2.4)$$

$$(5) \quad \underline{\sigma} = [D] \underline{\epsilon} \quad \text{the element stress-strain relation} \quad (2.5)$$

$$(6) \quad [k] = \int [B]^T [D] [B] dv \quad \text{element stiffness matrix} \quad (2.6)$$

$$(7) \quad \underline{f} = [k] \underline{u} \quad \text{element nodal equilibrium relation} \quad (2.7)$$

where,

$\underline{\epsilon}$ = element strain vector

\underline{f} = element nodal force vector

\underline{u} = element nodal point displacement vector

$[k]$ = element stiffness matrix

\underline{v} = element internal displacement vector

$[B]$ = element strain-displacement matrix

$[D]$ = element stress-strain (constitutive) matrix

$[H]$ = element displacement interpolation function

The structural global nodal equilibrium equations, Eq. (2.8), are solved to determine the unknown nodal displacements. The element strains and stresses are computed from the solution for the unknown nodal displacements. Before the global equilibrium equations can be solved, the structural global stiffness matrix is developed by assembling the stiffness of each element. Prior to the assembly, the individual element equations are transformed from local element coordinates to global structural coordinates. The stiffness matrix remains constant for all load conditions only in the case of a linear problem. Typically, nonlinearities in the problem require that the stiffness be recomputed at least as often as each load increment.

$$(8) \quad \underline{P} = [K] \underline{U} \quad \text{structural global nodal equilibrium relation} \quad (2.8)$$

where,

$[K]$ = structural stiffness matrix

\underline{P} = structural nodal force vector (knowns)

\underline{U} = structural nodal point displacement vector (unknowns)

2.7.1 CONSISTENT TANGENT STIFFNESS

Numerical analysis techniques are used to evaluate the integral in the element stiffness matrices. Newton-Raphson iterative solution is typically used to solve a structural mechanics equilibrium problem. Figure 8 shows the Euler (left in figure), Newton-Raphson (center in figure) and modified Newton-Raphson (right in figure) iterative solution schemes. Error accumulates at each increment of load for the Euler method. Equilibrium is satisfied at each load increment for the Newton-Raphson method, as shown in the center and right portions of Figure 8. Each successive trial solution for the equilibrium equations is based on the tangent stiffness matrix. The tangent stiffness matrix is computed using a variation in the stresses and strains, the variation is computed from the previous approximation to the current approximation. The basis of the modified Newton-Raphson method is to minimize computations, so the tangent stiffness matrix is not updated throughout the load increment.

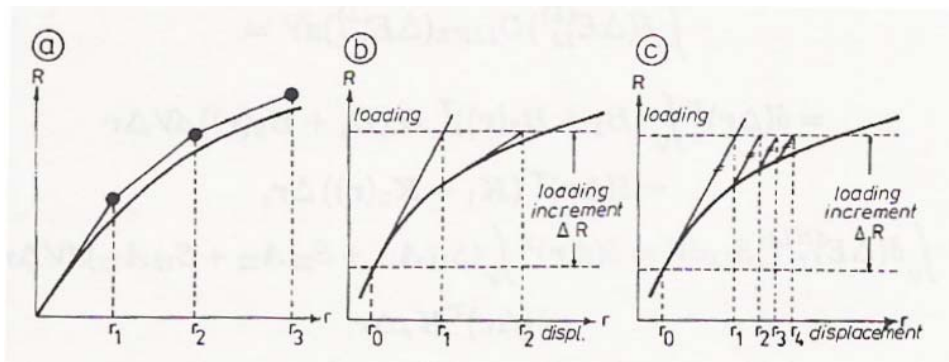


Figure 8: Solution Methods (Bittnar 1996)

The solution is iterated until convergence meets the required accuracy criteria. In nonlinear problems, the stiffness matrix can become singular, i.e. possessing non-unique solutions, resulting in convergence difficulties. For example, this can occur during a nonlinear buckling analysis where an equilibrium position is possible after an initial collapse.

A more rapid convergence rate can be obtained through the use of a “consistent tangent stiffness matrix”. The consistent tangent stiffness matrix is developed from derivatives of the stresses and strains. Since derivatives are used, the convergence rate is second order. The use of the tangent stiffness matrix provides only a first order convergence rate.

2.7.2 SOLUTION METHODS

2.7.2.1 h-METHOD

The h-method can be used for both linear and nonlinear types of analyses. Typically, the h-method requires a finer mesh than the p-method. In the h-method, the level of interpolation (e.g. linear, quadratic...) is the same in the elements. Achieving a more accurate solution generally requires refining the mesh (i.e. adding more elements). The h-method is more amenable to nonlinear analysis.

2.7.2.2 p-METHOD

The p-method can be used only for linear structural static analyses. The p-method can be used to solve a problem to a desired level of accuracy using a coarse mesh. The p-method increases the level of interpolation in the elements to achieve a required level of accuracy. Hence, the number of elements is held fixed but the interpolation may be increased to very high levels (e.g. 6, 8,... order polynomials). This method is not amenable to nonlinear analysis because it cannot handle large deformations, contact, and/or nonlinear material models well.

2.8 APPLICATIONS OF FINITE ELEMENT ANALYSES

The finite element method is a numerical technique used on a wide range of engineering problems including stress analysis, heat transfer, fluid flow and electromagnetism. Several types of structural analyses can be performed; static analysis, modal and spectrum analyses, harmonic and transient dynamic analyses, buckling analysis, and explicit dynamic analysis (ANSYS, Inc., 2002).

2.8.1 STATIC ANALYSIS

A finite element analysis determines displacements, strains, stresses, and forces in a structural system. A static analysis does not consider time varying loads, such as inertia and damping effects, but rather the structure's response reflects a steady, time independent, loading condition. The loading effects due to steady state inertia forces, such as from gravitation or rotational velocity, can be

approximated as equivalent static loads. Temperature effects, and initial strains due to prestress, can also be considered by using initial strains and stresses.

Nonlinearities can originate from various sources; from geometry such as large deformations, from material such as nonlinear elasticity and hyperelasticity and plasticity, from volume changes due to creep and shrinkage, from boundary or loading conditions, and from contact elements.

2.8.2 MODAL ANALYSIS

A modal analysis determines the free vibration characteristics of a structural system; i.e. the structure's natural frequencies and mode shapes. The structural system is typically assumed to be performing within its linear range, when determining its natural frequencies and mode shapes. Damping effects on the structure can be considered when determining its free vibration characteristics. The effects of prestress and temperature on the structure's free vibration characteristics can also be considered.

2.8.3 HARMONIC RESPONSE ANALYSIS

A harmonic, or sustained cyclic, response analysis determines the effect upon a structure due to a sustained cyclic load. This type of analysis is used to determine the effects of resonance and fatigue on a structure due to a forced vibration. The structure is subjected to harmonic loads, i.e. sinusoidal varying loads with respect to time, and the steady state response of the structure is

determined. The structure's response is determined for varying frequencies of the forced vibrations, and the structure's response is plotted versus the forcing frequency. Thus the structure's peak response is determined for the range of frequencies studied. The response values are typically deflections, but other responses such as peak reactions, strains or stresses could be studied. The response is determined for the steady state condition, and the initial, transient effects of the forced vibration are not determined by this analysis. The structural system is typically assumed to be performing within its linear range, when determining its steady state response. The effects of prestress on the structure's forced vibration characteristics can be considered, provided the effects of the prestress dominates the harmonic stresses.

2.8.4 TRANSIENT DYNAMIC ANALYSIS

When inertia or damping effects are important, i.e. they significantly influence the structure's time varying displacements, strains, stresses, and forces, a transient dynamic analysis is performed. The time history of the forced vibration is used to determine the dynamic response of the structure. All types of nonlinearities can be considered in a transient dynamic analysis. The forced vibration time history is divided into successive time points, called integration time steps, and all displacements, strains and stresses are determined for each time step.

2.8.5 SPECTRUM ANALYSIS

A spectrum analysis determines a structure's response to a known spectrum. Stresses and displacements in the structure are determined from an analysis using the structure's modal analysis results, and a response spectrum. The response spectrum used, which is a graph of some spectral value versus frequency, can capture the effect of the random or time dependent load history being studied. When used, the spectrum analysis would capture the magnitude and frequency of a transient dynamic analysis that uses a time history of the loading condition.

2.8.6 BUCKLING ANALYSIS

A buckling analysis is used to determine critical loads when a structure becomes unstable, and the structure's buckled mode shapes. A buckling analysis can be either linear or nonlinear. A linear analysis predicts the theoretical buckling strength of an ideal, linear, elastic structure. The results of a linear buckling analysis will overestimate the strength of a structure. A linear analysis ignores nonlinearities in material behavior, and imperfections in geometry such as initial straightness of axially loaded members.

In a nonlinear buckling analysis, the structure's response beyond the buckling load can be monitored, provided the nature of the structure is such that the structure buckles into a stable condition. The effect of nonlinearities can be considered, such as plastic material behavior, initial member straightness, gaps in

the structure, and large deformations. A nonlinear buckling analysis is a static analysis. In a nonlinear buckling analysis, as the structure is loaded near the buckling load, the solution begins to diverge. Therefore, for accurate results, the load increments must be small near buckling.

2.8.7 EXPLICIT DYNAMIC ANALYSES

The difference between an explicit dynamic analysis and an implicit dynamic analysis is in the method of time integration (Bittnar and Sejnoha, 1996). In an explicit dynamic analysis, the known values of the acceleration, velocity and displacement vectors are used in the equation of motion to predict the next time step. In an implicit dynamic analysis, the equation of motion is used to predict the next time step based on an average constant acceleration across the time increment. A central difference time integration method is typically used in an explicit dynamic analysis, and Newmark's "average acceleration" method is typically used in an implicit dynamic analysis.

An explicit dynamic analysis considers the inertial effects of mass and damping. The mass is typically assumed to be "lumped" at the nodes, so the mass matrix can be easily inverted. An implicit dynamic analysis is typically used for linear problems, problems with very long time durations, and problems that do not include contact. For implicit dynamic analysis, the inertia effects of mass and damping are usually not included, and the stiffness matrix is usually assumed

constant, since inversion of the stiffness matrix is required. Alternatively, an explicit dynamic analysis is typically used in a nonlinear problem, to consider the effects of nonlinearities in materials and geometry. Contact problems are particularly amenable to solution using explicit methods because no tangent stiffness matrix is required in explicit dynamics. Typically, a data table is used to describe nonlinear material properties.

2.9 LITERATURE REVIEW

Reviewed in this section are some representative examples from the literature of finite element analysis of reinforced concrete structures. This literature review is a representative sample of research articles similar to the research performed in this treatise, and is not a comprehensive literature review. The articles selected for review range from an analysis of a spillway structure performed by a practicing engineer during the design process, to several beam and column member analyses performed by research professionals. Commercially available software packages were used by these authors. At the end of the section is a review of ANATECH Corporation's ANAMAT constitutive model for concrete.

2.9.1 RECENT FEM USE BY DESIGN PRACTITIONERS, SPILLWAY STRUCTURE

Practicing structural engineers used finite element analysis as a design tool for a reinforced concrete structure. A commercially available structural engineering software package was used to model a reinforced concrete spillway

structure for a municipal water supply reservoir (Monroe and Dobmeier, 2003). The structural design package used is SAP2000, by Computers and Structures, Inc., located in Berkeley, Ca.

The authors do not describe how the model was developed. Neither the size or type of the elements used, nor the material model, were described. An indication as to whether the analysis was linear-elastic or nonlinear was not provided. The structural components are reinforced concrete walls. An illustration in the article depicts the structure divided into elements.

The spillway structure consists of a pair of 13 feet by 13 feet, vertically oriented, concrete tubes. The wall that is shared by the tubes is 12 inches in thickness. The overall plan dimension is 27 feet by 13 feet, and the height is 42 feet. Water for discharge from the reservoir enters the vertical tubes through a weir located at the top of the spillway structure. The water falls through the spillway structure and exits through openings in the wall at the bottom of the structure. The discharged water then flows under the dam through a pair of 6 feet by 6 feet reinforced concrete box culverts. The spillway structure is cantilevered from a concrete foundation.

The project owner is the Carroll County Water Authority, and is located forty miles west of Atlanta, Ga., in Carroll County, Ga. The design firm,

Schnabel Engineering, Inc., is located in Glen Allen, Va., and has an office in Alpharetta, Ga.

2.9.2 RECENT FEM USE BY RESEARCHERS

2.9.2.1 ANALYSIS OF REINFORCED CONCRETE BEAM

The researchers performed a finite element analysis on reinforced concrete rectangular shaped beams (Barbosa and Ribeiro 1998). The beams were subjected to a uniform flexural load. The computational results were compared to classical analytical methods. Although the load-deflection response was accurately predicted, only a portion of the deformation could be captured using the finite element analysis. The authors stressed the importance of the material model to accurately predict beam deflection.

ANSYS Version 5.3 was used in the analysis. Concrete was modeled using solid elements. Primary reinforcing steel was modeled using either “smeared” reinforcement within the solid elements or discrete link elements connecting solid element nodes. Figure 9 shows the ANSYS mesh for a quarter of the beam.

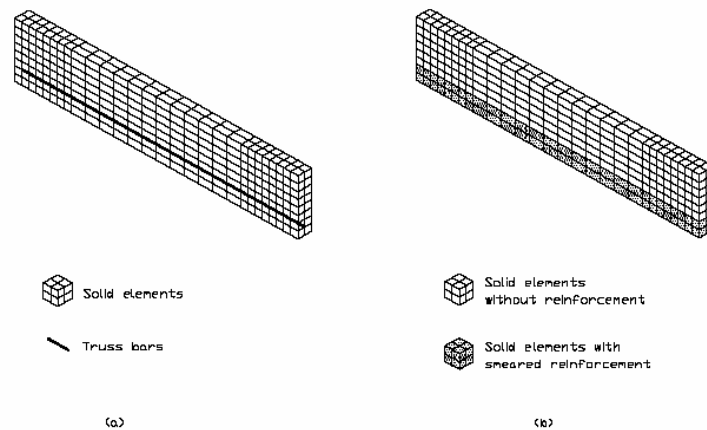


Figure 9: ANSYS Reinforcement Model (Barbosa & Ribeiro 1998)

Eight ANSYS analyses were performed as indicated in Table 1. Four concrete material models were studied, and the reinforcement was modeled as either “smeared” or discrete. The ANSYS concrete material model is capable of cracking in tension and crushing in compression. The four concrete models were linear elastic, elastic perfectly plastic, multi-linear with no concrete crushing, and multi-linear with concrete crushing. A linear elastic steel model accompanied the linear elastic concrete model. An elastic perfectly plastic steel model was used with the three nonlinear concrete models. For concrete crushing or cracking, no strain softening occurs as the failure surface is reached, but rather the stresses in that direction drop to zero. For the cases 2k and 3p, concrete crushing was turned off, and the compressive stress did not drop to zero.

Analysis	Concrete Model		Reinforcing steel model	
	Tension	Compression	Representation	Material model
Case 2f	Cracking	Linear elastic + crushing	Discrete	Linear elastic
Case 2m	Cracking	Elastic perfectly plastic (Drucker-Prager)	Discrete	Elastic perfectly plastic
Case 2k	Cracking	Multilinear work hardening (von Mises)	Discrete	Elastic perfectly plastic
Case 2L	Cracking	Multilinear work hardening + crushing	Discrete	Elastic perfectly plastic
Case 3m	Cracking	Linear elastic + crushing	Smearred	Linear elastic
Case 3n	Cracking	Elastic perfectly plastic (Drucker-Prager)	Smearred	Elastic perfectly plastic
Case 3p	Cracking	Multilinear work hardening (von Mises)	Smearred	Elastic perfectly plastic
Case 3o	Cracking	Multilinear work hardening + crushing	Smearred	Elastic perfectly plastic

Table 1: ANSYS Concrete Material Model (Barbosa & Ribeiro 1998)

The beam response to the flexural loading was similar for the four material models. Figure 10 and Figure 11 show the load deflection response. The initial stiffness was linear, followed by a sudden loss in stiffness as the beam cracked. After cracking, stiffness was again linear. The ANSYS analyses ended within this linear stiffness region for both the linear elastic and the elastic perfectly plastic models. The authors reasoned that for the elastic perfectly plastic model, the concrete “... has been able to resist to higher stresses than it would in reality as the nonlinear phase of stress-strain relation started. So, the failure of this model has been determined by crushing of compressed concrete.” The multi-linear with concrete crushing model also failed at less than the predicted strength.

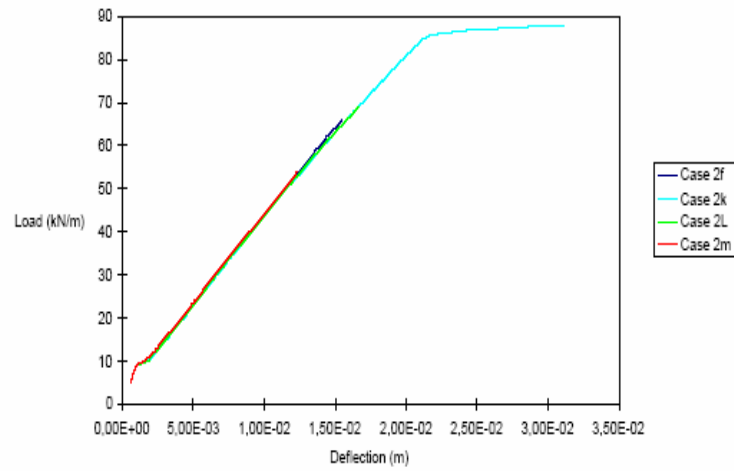


Figure 10: Discrete Reinforcement (Barbosa & Ribeiro 1998)

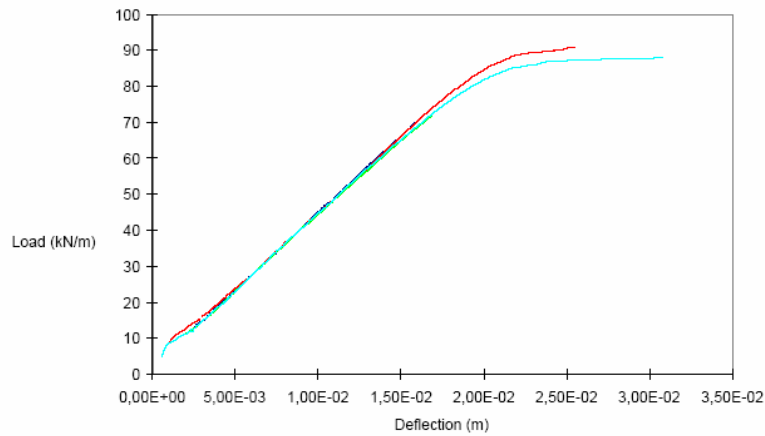


Figure 11: Smeared Reinforcement (Barbosa & Ribeiro 1998)

The authors found that the multi linear model without concrete crushing best predicted the beam's strength and deflection. This model produced the longest load deflection response history since the reinforcing steel yielded prior to concrete crushing. Figure 12 shows the results of this material model as compared to the results of a classical analysis. The classical analysis is indicated

as the “expected result” load case in the figure’s legend. The discrete versus “smeared” model for the primary reinforcing steel had little effect on the response. The discrete load case is shown as “case 2k” in the figure legend, while the “smeared” steel model is shown as “case 3p”.

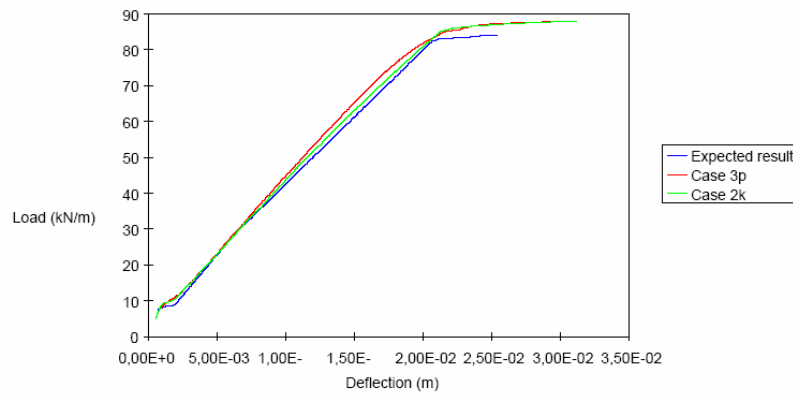


Figure 12: ANSYS Nonlinear Concrete Model, (Barbosa & Ribeiro 1998)

The ANSYS analyses, all except analyses 3n, 3p and 2k, terminate as the implicit iteration strategy fails to converge. The implicit iteration strategy, Newton’s method, does not work well in strain softening situations. The slope of the stress-strain relation tends to zero as the strain softening region is approached, and would actually be negative in the strain softening region. The slope of the stress-strain relation is used to estimate the solution for the next increment. When the researchers “turned off” the concrete’s ability to “crush” at the end of the strain hardening region, in their ANSYS analyses 3p and 2k, and used the elastic plastic concrete material model for ANSYS analyses 3n, they obtained numerical

results that produced a plateau on the load-displacement plot, i.e. more ductile flexural behavior. The concrete was able to continue to resist stress at increased strains beyond the crushing stress.

2.9.2.2 ANALYSIS OF REINFORCED AND POST-TENSIONED CONCRETE BEAMS

The researcher performed a finite element analysis on reinforced concrete rectangular shaped beams and post-tensioned T-beams using ANSYS Version 5.5 (Fanning 2001). The beams were loaded in flexure. The computational results were compared to experimental results and classical analysis methods. The ultimate strength was predicted to within one percent for the rectangular beams and 12 percent for the T-beams. Although the load-deflection response was accurately predicted, only about half of the deformation could be captured using the finite element analysis.

The rectangular beam was loaded to failure in a four-point loading configuration. The results are shown in Figure 13.

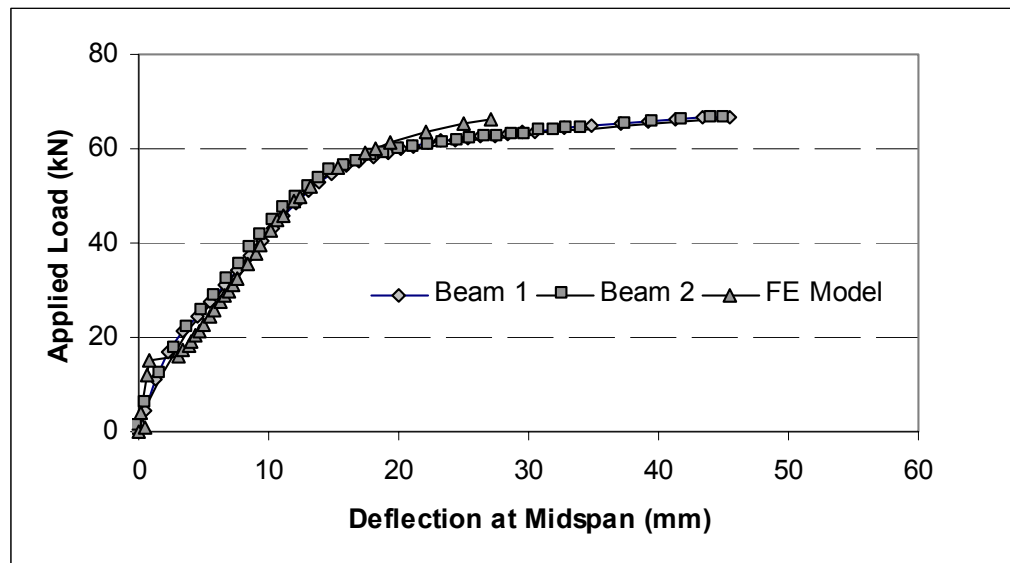


Figure 13: Rectangular Beam Response (Fanning 2001)

The T-beam primary steel was post-tensioned in an initial load step, the self weight applied as a uniform load in a second load step, and then loaded in a third load step to failure in a four-point loading configuration. The results are shown in Figure 14.

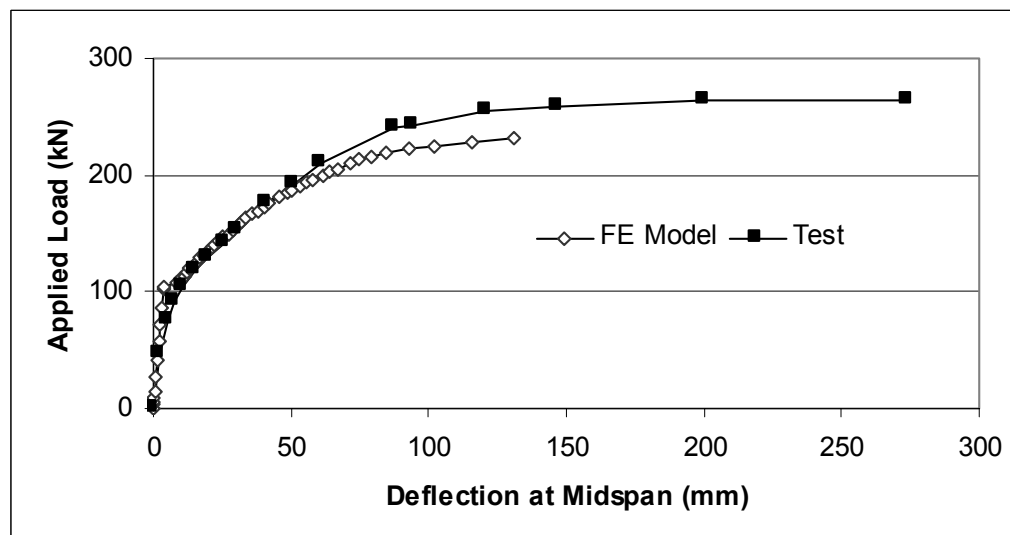


Figure 14: T Beam Response (Fanning 2001)

The author stressed the importance of the material model to achieve an accurate prediction of ultimate strength and deflection. The effect of using measured versus “specified minimum” material properties is shown in Figure 15.

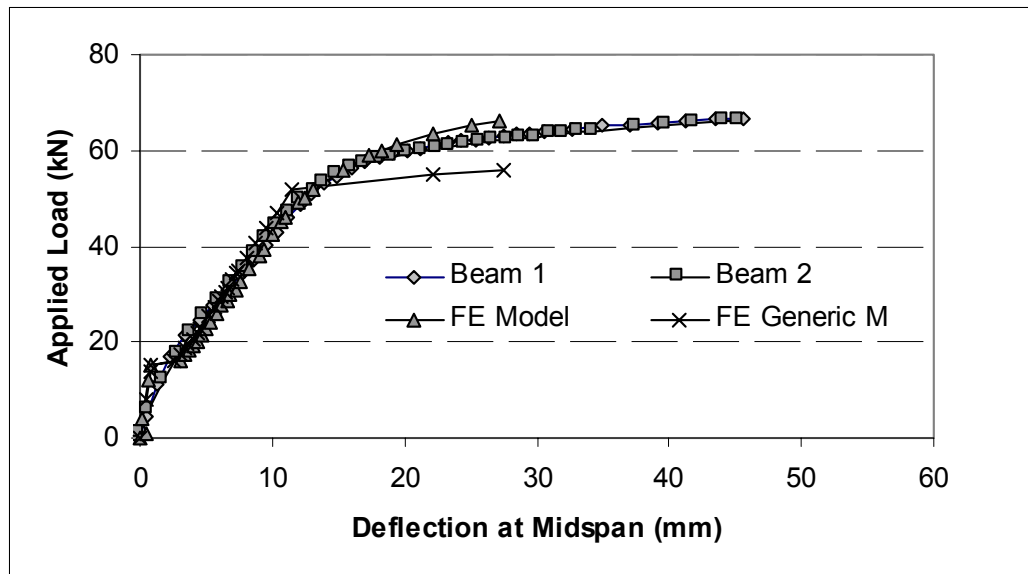


Figure 15: Material Model Sensitivity in Rectangular Beams (Fanning 2001)

Concrete was modeled using “Solid65” elements, which uses a smeared crack analogy for cracking in tension zones, and a plasticity algorithm for crushing in compression zones. The element behavior is linear elastic until either cracking or crushing occurs. Once a cracked or crushed region forms, the stresses are redistributed locally, requiring an iterative solver for the nonlinear behavior. Increased strains at constant stress occurs post crushing.

Primary reinforcement was modeled discretely using “Link8” elements. Secondary reinforcement was also modeled discretely for the rectangular beams, but “smeared” reinforcement was used to model the stiffness contribution of the secondary reinforcement for the T beams. The ANSYS “Solid65” element has the “smeared” reinforcement capability. The shear stiffness of the steel is ignored in the model. Both elastic and plastic material responses were used for the steel.

The researcher states in his article, “Increased strains at constant stress occurs post crushing.” This leads to the conclusion that the researcher “turned off” the concrete’s ability to crush at the end of the strain hardening region in their ANSYS analyses, and thus obtained numerical results that produced a plateau on the load-displacement plot, i.e. more ductile flexural behavior. The concrete was able to continue to resist stress at increased strains beyond the crushing stress. The implicit iteration strategy, Newton’s method, does not work well in strain softening situations. The slope of the stress-strain relation tends to zero as the strain softening region is approached, and would actually be negative in the strain softening region. The slope of the stress-strain relation is used to estimate the solution for the next increment.

2.9.2.3 ANALYSIS OF COLUMN ELEMENTS

The researchers performed a finite element analysis on an axially and laterally loaded reinforced concrete column with semi-fixed end restraints, and

compared the results of the analysis with experimental results (Kwon and Spacone 2002). The finite element analysis program used is from the Department of Civil and Environmental Engineering, University of California, Berkeley. The structure was modeled using eight node, three dimensional, brick elements, with a $2 \times 2 \times 2$ Gauss integration scheme. Tensile cracking was modeled using a rotating smeared crack approach. The cracks were allowed to rotate with the principal strain direction at each load step. Perfect bond was assumed between the concrete and reinforcing steel. Figure 16 depicts the column in the experimental test and in the computational model.

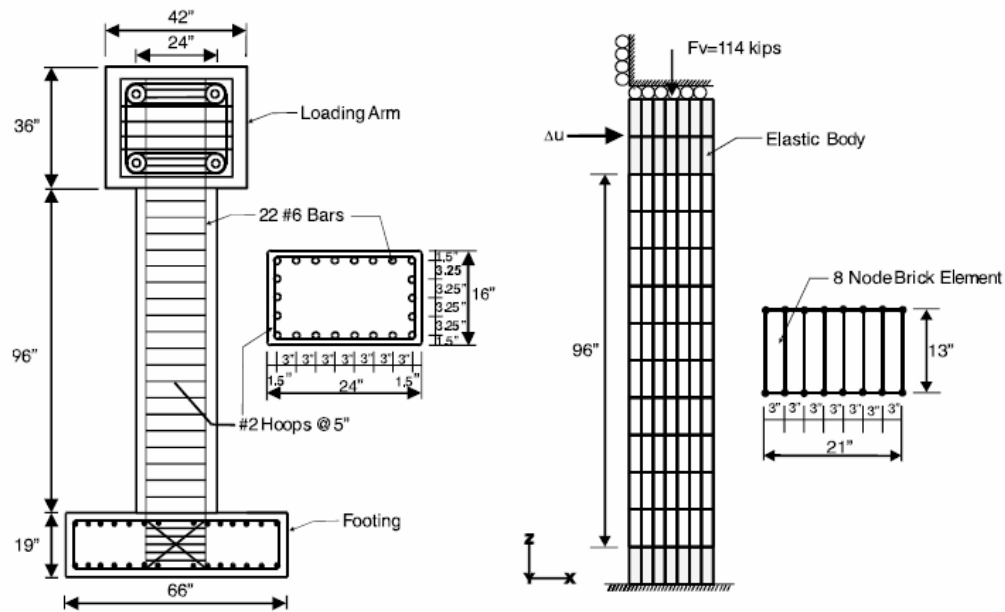


Figure 16: Concrete Column (Balan, Spacone and Kwon 2001)

The concrete material model used was a strain driven, hypo-elastic model (Balan, Spacone and Kwon 2001). See Figure 17. The material model allows for stress induced orthotropy, with the material orthotropic axes assumed parallel to the principal stress axes, which are not coaxial with the principal strain axes. Increasing lateral confinement results in an increase in strength and ductility. The deviatoric and volumetric stresses were coupled using a “coupling modulus” (Gerstle 1981). A uniaxial, bi-linear strain hardening material model was used to model the reinforcing steel.

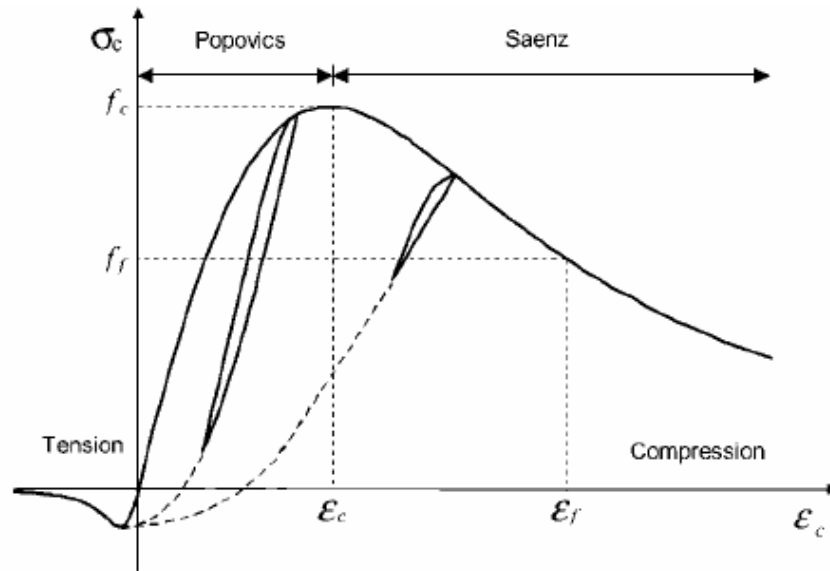


Figure 17: Concrete Model (Balan, Spacone and Kwon 2001)

Three columns were tested, Columns R1, R3 and R5. Each column was subjected to a constant axial load of 114 kips, and then to lateral displacement cycles of increasing amplitude. Column R1 was designed not to be deficient in

shear, and yielding of the longitudinal steel occurs before yielding of the shear reinforcement. Shear failure occurs in Columns R3 and R5. Figures 18, 19 and 20 show the test results for the three columns R1, R3 and R5, respectively. The yielding of the longitudinal and shear reinforcing steel correlated well between both the computational and experimental results.

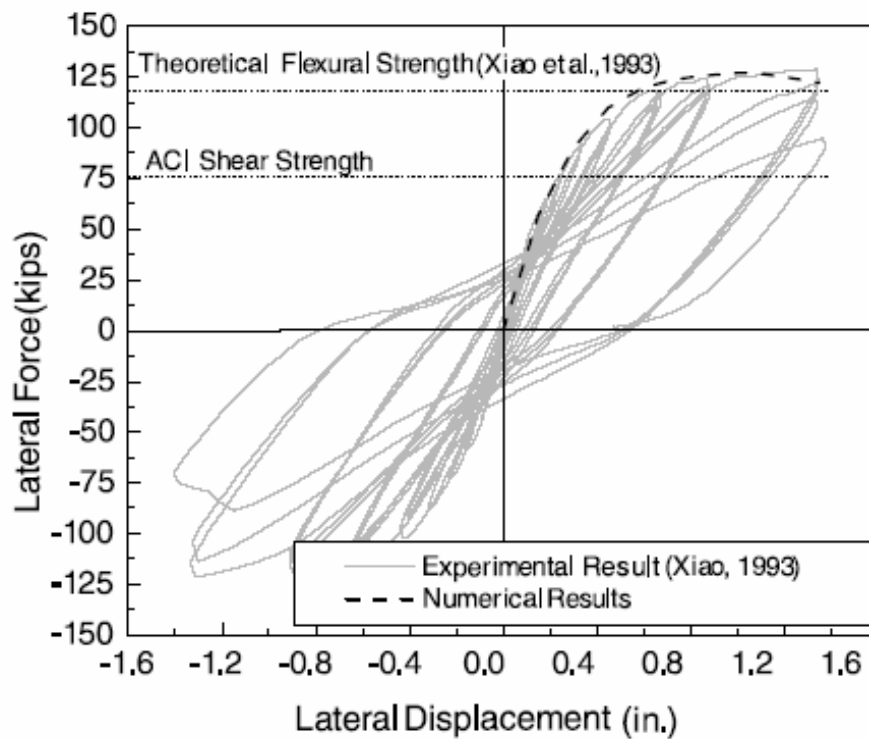


Figure 18: Column R1 (Balan, Spacone and Kwon 2001)

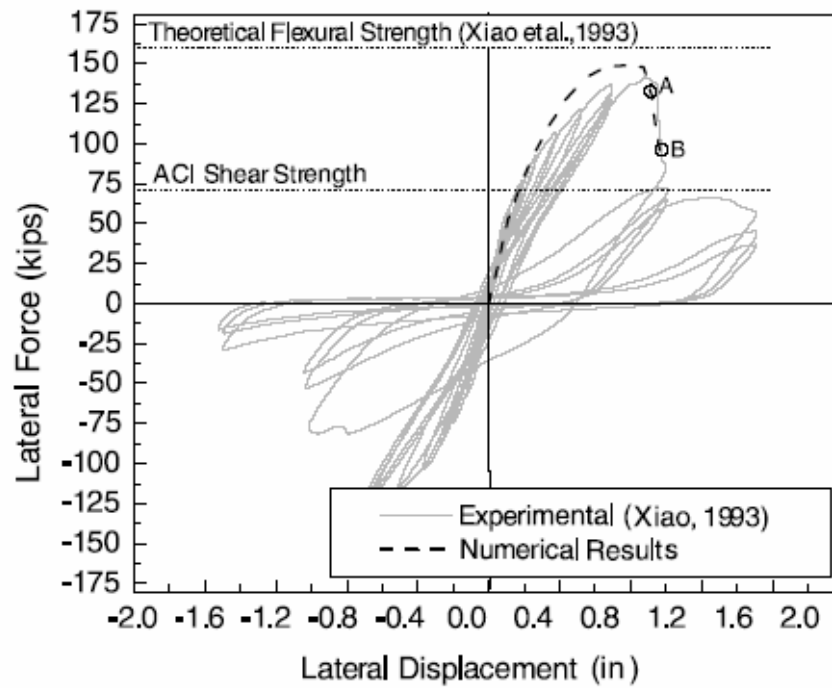


Figure 19: Column R3 (Balan, Spacone and Kwon 2001)

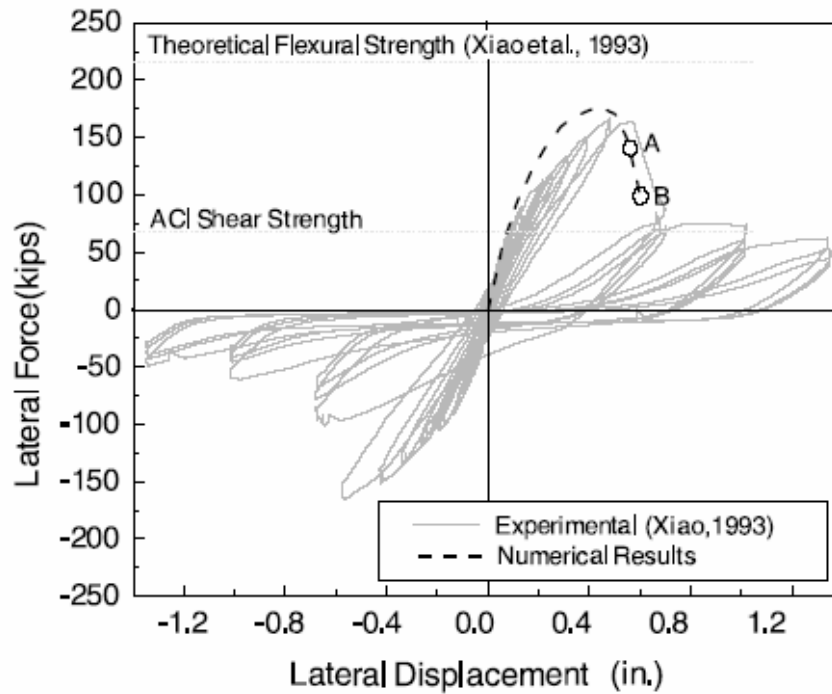


Figure 20: Column R5 (Balan, Spacone and Kwon 2001)

A three dimensional analysis more fully represents the response of the structure, and allows the use of a more sophisticated material model. A three dimensional, nonlinear, concrete material model can describe the stress-strain relationship of the material when subjected to large deformations and under cyclic loading. The material model can depict strain softening which can occur at large strains, beyond the maximum compression stress. The tri-axial model can depict the increased strength and ductility under a large lateral confining stress.

A rotating smeared crack approach can result in a quicker solution as compared to an embedded crack approach, since the latter technique requires meshing at each load increment to orient the cracks in the principal strain direction. A smeared crack approach can more accurately depict the cracking in reinforced concrete structures. The smeared crack approach can overestimate the shear stiffness of an element, but a mesh refinement can be used where this stress locking occurs.

2.9.2.4 ANALYSIS OF COLUMN – BEAM CONNECTION

The researcher cites three design examples of reinforced concrete structures using commercially available finite element analysis software (Horowitz 1997). Linear analyses were used, and the computer results were compared to the results obtained using the design codes.

The first system is a statically determinate structural system consisting of a cantilevered column and beam. A plane stress, linear finite element model of the system was analyzed using ANSYS V5.3. The author observed a stress concentration at the beam column intersection, and singularity in the strain energy norm.

A single bay frame, pinned at the base, was also analyzed using ANSYS. A plane stress, linear finite element model was performed. The singularity was observed at beam midspan for this structure.

SAP90 was used to model the third structure, which is a flat plate supported by a column at the plate's center.

The author observed that, except at the locations of high stress, the stress values compared favorably to the code prescribed analysis procedures. At the locations of singularity, refinement of the mesh decreased the amount of the structure with singular results.

Linear finite element techniques were used to obtain moments and shears required to design the structure's members. The linear analysis techniques also showed some singularities. The weakness in using linear analysis techniques is

that the structure cannot be accurately modeled beyond the design loads. Singularities, and their associated errors, decrease the accuracy of the stresses and deformations of the remaining structure.

2.9.2.5 DYNAMIC ANALYSIS OF SIX STORY LATERALLY LOADED STRUCTURE

CAMUS International Benchmark is an effort to compare experimental results with results predicted using numerical tools. The experimental tests were performed in France, and participants were invited to provide computational models for comparison. CAMUS 2000 is a follow-on program, with the test structure being subjected to a seismic event with two directions of horizontal motion.

The test specimen is a 1/3 scale model of a six story reinforced concrete structure, supported on a concrete footing, and anchored to a shaking table. The structure consists of a square floor area supported on two opposite sides by shear walls. The walls have no openings, and are designed to resist in-plane seismic forces using the French PS92 code provisions. The structure is braced for out-of-plane forces with steel braces attached to each floor.

A series of three dynamic tests was performed on the structure, with the maximum acceleration being increased for each successive test. Displacement transducers, accelerometers, and strain gages were used to obtain data on relative

floor displacement, absolute floor acceleration, and vertical reinforcing steel strain at each floor level.

ANATECH Corporation performed a nonlinear finite element analysis of the structure using their ANACAP-U material model and the ABAQUS general purpose nonlinear finite element program (Kubischta, Rashid and Dunham 2003). The results of their analysis compared favorably with the experimental measurements. The structure was modeled as a continuum using three dimensional, eight node brick elements. Modeling the structure as a continuum of solid elements more accurately reflects the yielding of the reinforcing steel, and the shear and tensile cracking and the compressive crushing of the concrete.

The authors at ANATECH are curious about the experimentalist's use of the second horizontal direction of shaking, since the structure was not designed to resist such shaking, and the experimentalist's provided steel bracing in that direction. ANATECH has the opinion that a vertical orientation to the shaking would have been more interesting for this test structure.

2.9.2.6 ANACAP MODEL OF PASSIVELY CONFINED CONCRETE COLUMNS

Confined concrete exhibits increased compressive strength and strains. Concrete confinement in the core of reinforced concrete bridge columns is provided by steel hoops or spirals for new structures, or carbon fiber composite wraps for existing structures (Dowell and Dunham 2000). The amount of

concrete confinement available in a flexural response is typically computed as that provided by yielding of the transverse reinforcement. Carbon fiber does not behave with a yield plateau as steel does, so a more advanced methodology is required to develop the moment-curvature relation required to determine the structure's response.

Plasticity theory allows for modeling of shear behavior in compression. Stresses are decomposed into volumetric and deviatoric components, and maximum shear stress plasticity theory is applied. Early forms of concrete plasticity are based on the Drucker-Prager yield function, and extensions of the Prager kinematic hardening rule to include isotropic and general hardening curves. Although these models increase the yield stress up to 10 percent in equibiaxial compression, actual behavior is underestimated. For example, experimental results show that a 5 percent biaxial confinement pressure will increase the yield stress by 15 percent.

A significant increase in compressive strength can result from a small confining pressure. And concrete behaves nearly as if unconfined, when any transverse confining pressure is zero (Mandur, Priestley and Park 1984). A hardening modulus in conventional plasticity is several orders of magnitude lower than the elastic modulus. Concrete's hardening modulus can be greater than its

elastic modulus and the slope of the yield stress to confining pressure is typically greater than one.

An elliptic interpolation function was developed (William and Warnke 1975) to express the ultimate strength surface in 3D stress space. Experimental data for biaxial and triaxial stress states match the model. The ANACAP concrete material model was modified to include Mander's stress strain curve for the confined concrete and William and Warnke's 3D ultimate strength surface. The two minor principal stresses were equated to the two confining stresses due to the transverse reinforcement. These two minor principal stresses were then used to determine the current ultimate strength from the William and Warnke strength surface. Mander's stress strain curve was used to determine the effective stress.

The influence of the confining pressure on ultimate strength was demonstrated using an eight node brick element, subjected to a confining pressure. Equal confining pressures were placed on four sides of the brick, the bottom face was restrained, and the top face loaded. Confining pressures ranging from 100 psi to 500 psi were analysed. Figure 21 shows the stress strain curve for 100 psi increments of confining pressures, and also for unconfined concrete. The ultimate strength of confined concrete is greatly increased over the unconfined concrete uniaxial compressive strength of 4,000 psi. The abrupt change in stiffness observed in the 100 psi and 200 psi confinement curves is attributed by

the authors to be due to difficulties with the algorithm at low confining pressures at the cracking load.

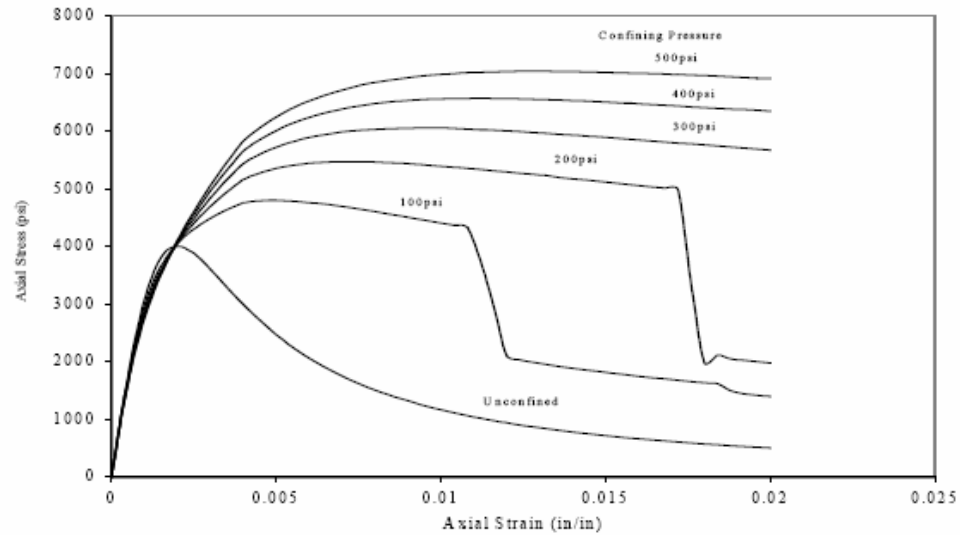


Figure 21: Effect of Confinement on Strength (Dunham and Dowell 2000)

Mandur (Mandur, Priestley and Park 1988) tested circular concrete columns with varying amounts of transverse and longitudinal steel to investigate the effects of confinement. The columns were analysed using the updated ANACAP material model. Figure 22 shows the size of the columns and the axisymmetric computational model. An active confining pressure, in an amount equivalent to that provided by the spiral as the steel yields, was placed at the location of the spiral.

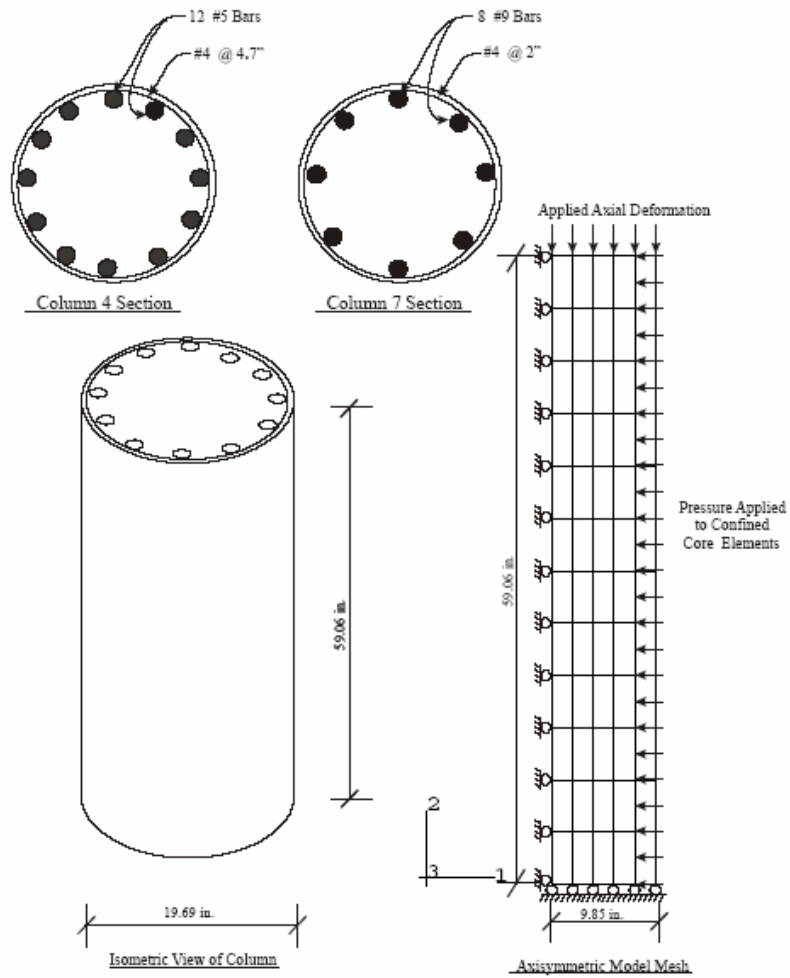


Figure 22: Confined Column Model (Dunham and Dowell 2000)

Column 4 had a transverse steel ratio of 0.60 percent, and Column 7 had 2.0 percent. This amount of steel is equivalent to a confining pressure of 123 psi and 486 psi, respectively. Figure 23 compares experimental load-displacement response with the analysis. A comparison of these results with the 100 psi and 500 psi curves from Figure 21 illustrates the significant change in concrete response due to the effects of confinement. Failure of both columns was due to

rupture of the spiral reinforcement and loss of confinement. The erratic computational response of Column 4 with 123 psi of confining pressure was attributed by the authors to be due to the algorithm at low confining pressures at concrete cracking. Concrete cracking adversely effects confinement. Active confining pressures were used in lieu of the passive transverse reinforcing due to these difficulties with the algorithm.

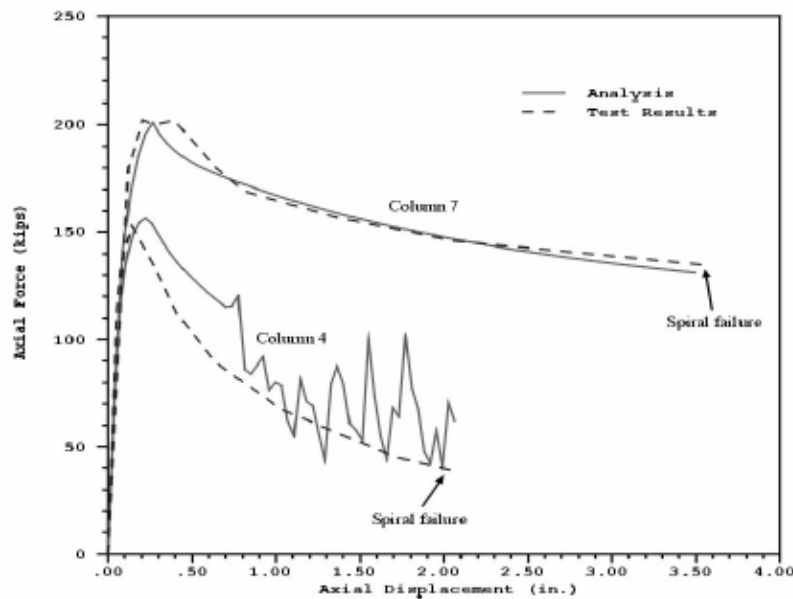


Figure 23: Confined Column Response (Dunham and Dowell 2000)

2.9.3 ANATECH's ANAMAT CONCRETE MATERIAL MODEL

This section contains a review of ANATECH Corporation's ANAMAT constitutive model for concrete. This material model is used in this research to model the tornado shelter and floor slab problems using TeraScale's TeraDyn explicit dynamics code. The use of nonlinear finite element analysis techniques is

necessary to model reinforced concrete structures. The constitutive behavior of concrete is nonlinear. Concrete “softens” in compression, and cracks in tension and shear. Stiffness degrades under cyclic loading, cracking and crushing. Stiffness is also affected by hydrostatic stress. Therefore, a three dimensional constitutive model with load history is required for accurate analyses.

ANATECH Corporation develops finite element software for the commercial market. ANAMAT is the constitutive module developed for use in the ANACAP-U nonlinear finite element program. The ANAMAT constitutive model for concrete is based on smeared cracking methodology and J_2 plasticity theory (ANATECH Corp., 1998). The material nonlinearity is treated at the finite element integration points, thus the cracking and stress/strain state can vary within an element. Cracks form perpendicular to the principal strain direction, and cracking can form in three orthogonal directions. The stress normal to the crack is reduced to zero, and the stresses around the crack are redistributed. Shear stiffness is reduced upon cracking, and decreases further as cracks open. Crack directions remain fixed.

When a crack forms (in one or more of the principal directions) the tensile strength in that direction is reduced to zero as it opens. If the loads are reversed, the crack can close and carry compressive loads. The cracks do not “heal”. That is, if the load is reversed again and the strain becomes tensile (the crack opens)

and the strength is zero. The TeraScale visualization software shows open cracks as red and closed cracks as blue.

Reinforcing steel can be modeled as either sub-elements within the concrete element, or as truss or beam elements. The constitutive model for the steel characterizes the strain hardening behavior of steel. Strain compatibility is assumed between concrete and rebar.

Y. R. Rashid developed the smeared cracking finite element methodology in the 1960's (Rashid 1968). R. A. Dameron and R. S. Dunham continued with this methodology in the analyses of nuclear containment structures in the 1980's.

CHAPTER 3 PRESTRESSED CONCRETE BEAM ANALYSIS

3.1 INTRODUCTION

The overall goal of this component of the research program is to evaluate the ability of commercially available finite element analysis software to model the flexural behavior of a prestressed concrete rectangular beam. More specifically, the program set out to compare the load versus deflection response obtained from the computational model to those obtained from experimental results and classical analysis techniques.

3.2 PRESTRESSED CONCRETE BEAM BEHAVIOR

A concrete beam is a composite member composed of steel reinforcement and concrete. Longitudinal flexural steel is located at the bottom of the member section, and provides the tension component of the internal force couple required to resist the moment produced by the application of external load. Transverse shear steel is used to resist the inclined shear cracking in the beam in areas of high shear stress.

In a prestressed beam, the longitudinal flexural steel consists of high tensile strength steel strand. In the case of a pretensioned prestressed beam, the strand is stressed prior to the placement of the concrete, and the prestress force is transferred to the beam after the concrete is cast and allowed to harden. A prestressed beam sometimes contains longitudinal compression steel consisting of mild deformed steel bars located at the top of the member section. The compression steel resists the tension at the top of the beam caused by the release of the eccentric prestressing force into the member. The compression steel is required to control the cracking at the top of the member prior to the application of the external loads. The compression steel also provides additional resistance in the compression component of the internal force couple upon application of external flexural loads, enabling an increase in the equilibrating tension force of the prestressing steel, thus allowing the beam to resist additional flexural load and deform further.

3.3 MODELING TECHNIQUE

ANSYS version 8.0 was used in the finite element analysis of the prestressed concrete beam. ANSYS is a commercially available software package. The concrete beam was modeled as a composite material comprised of concrete and reinforcing steel. The prestressing steel and the compression steel were idealized using line (1D) elements, capable of tension or compression

loading only. The concrete was modeled using 3D solid elements. Figure 24 and Figure 25 show the steel line element mesh and the concrete solid element mesh.

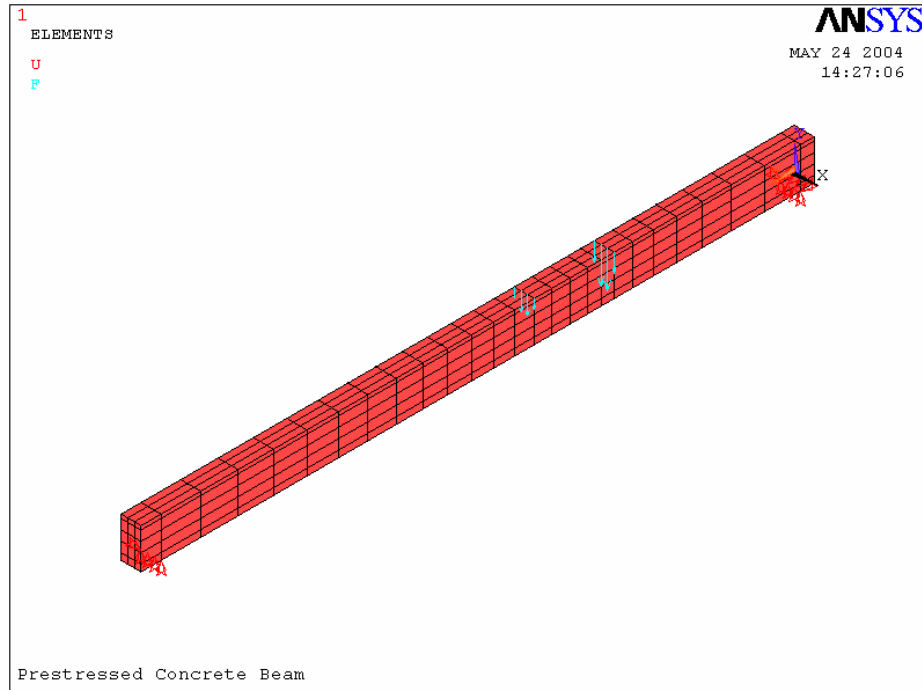


Figure 24: Rectangular Beam Concrete Solid Element Mesh

The nodes of the line elements were made to be concurrent with the nodes of the solid elements in order to provide compatibility of the displacements at these nodes. Thus perfect bond was provided between the 1D elements used to simulate the longitudinal steel and the 3D elements used to simulate the concrete and transverse shear steel. This was accomplished by assigning mesh attributes to the lines that defined the concrete volume and the longitudinal steel, prior to

meshing. Subsequent to meshing, the common nodes were “merged” into one node using the ANSYS command.

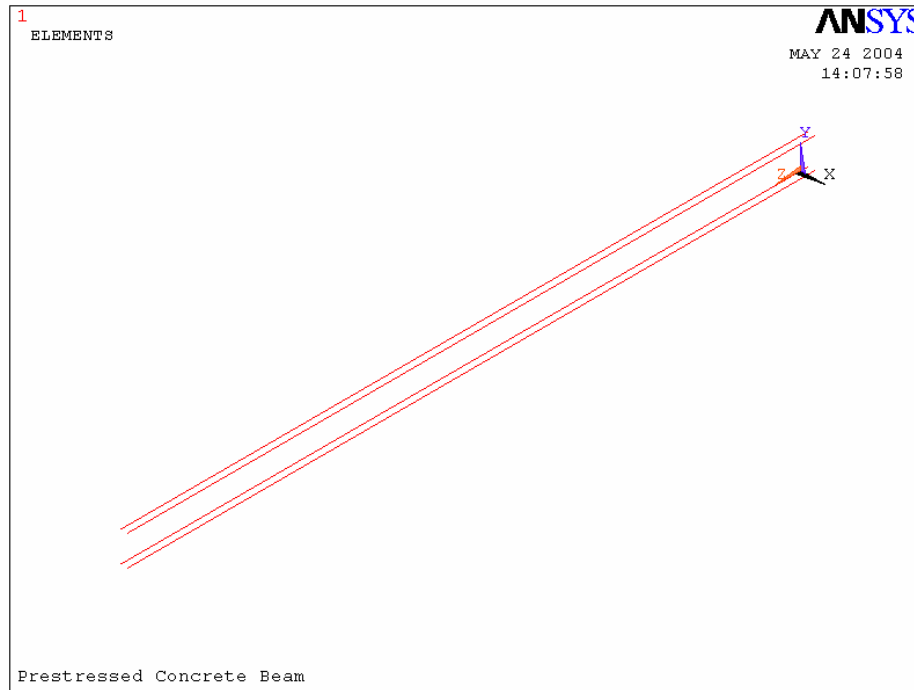


Figure 25: Rectangular Beam Longitudinal Reinforcing Steel

The transverse reinforcing steel was modeled using an ANSYS modeling feature available in the SOLID65 element. The feature allows the steel to be “smeared” throughout the 3D solid element, and oriented coincident with the vertical direction of the transverse steel. The use of shear reinforcing steel in the horizontal direction is not required since the loading conditions do not result in torsion or horizontal transverse shear.

3.3.1 MODELING SEQUENCE

A copy of the ANSYS command language, i.e. a copy of the *.lgw file, is attached in Appendix B. The file shows the commands used to create the mesh, apply loads and boundary conditions, and define the solution controls. The longitudinal steel lines and the beam volume were created from keypoints, lines and volumes. Prior to meshing, the beam volume was divided into several regions to control the element size and shape. The prestressing steel and compression steel locations were used to subdivide the member cross-section. The load points and reaction locations were used as division points along the beam. The regions were “glued” together to form a single beam volume using an ANSYS command.

After the reinforcing steel lines and the beam volume were created, meshing and material attributes were assigned to the lines. After meshing the lines and the volume, the common nodes were merged. After defining the supports and applying the loading, the prestressing steel was given an initial stress. Finally, the solution controls were defined and the solution obtained.

3.4 CONSTITUTIVE MODELS

3.4.1 CONCRETE CONSTITUTIVE MODEL

Possible concrete nonlinear material models include the ANSYS concrete model, or a user defined multi-linear model. ANSYS does not have the capability

to define a user defined material model in tension that is different in compression. Since concrete's tensile capacity is only about one-tenth that of its compressive strength, a user defined concrete model is not appropriate if both tensile and compressive stresses are anticipated for the element. Therefore, the ANSYS concrete model was used for this research. Figure 26 shows the constitutive model for the ANSYS concrete element.

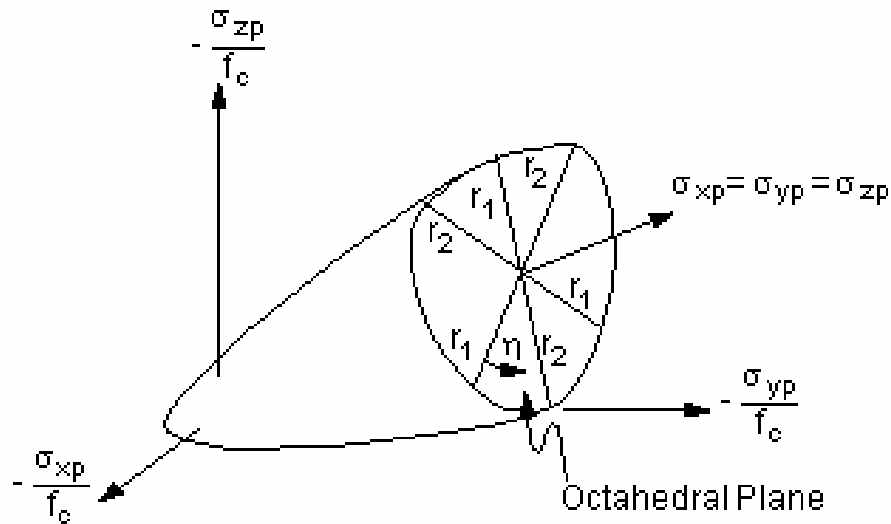


Figure 26: Concrete Failure Surface (ANSYS 2003)

The ANSYS concrete model does not contain a strain softening region to continue on after the strain hardening region. Instead, the concrete element will “crush” and will no longer be able to resist stress once the element reaches the concrete compressive strength, i.e. when all principal stresses are compressive. Some researchers “turn off” the concrete “crushing” and allow the concrete to

continue to resist stress at increased strains beyond the crushing stress. Similarly, once the tensile strength is reached, the element will crack, i.e. when any principal stress is tensile. Shear transfer across the crack face is controlled by an input variable, i.e. the percentage of shear transfer across the interface can be specified for both the “crack open” and the “crack closed” condition.

3.4.2 REINFORCING STEEL CONSTITUTIVE MODEL

Reinforcing steel nonlinear inelastic material models available in ANSYS are bilinear, multi-linear, or nonlinear models. Nonlinear models include isotropic, kinematic or combined hardening models. A bilinear material model with an isotropic hardening rule was used in this research. The isotropic hardening rule is suitable for this research since the loading condition is a monotonically increasing function. The bilinear material model was used for the compression steel and the prestressing steel. A “smeared steel” model was used for the shear steel, i.e. the shear steel is evenly distributed within the concrete element, and is oriented in the direction of the shear steel.

3.5 ELEMENT TYPES

3.5.1 CONCRETE ELEMENT TYPE

The ANSYS element Solid65 was used for the concrete. The element is a solid brick element with eight nodes, as shown in Figure 27. The element has three translational degrees of freedom per node. This concrete element has the

capability for three independent reinforcing materials. The element has the capability of cracking, and will crack in the direction of the principal stress when the stress exceeds the modulus of rupture. The material at any integration point will crush when the stress exceeds the compressive strength at that point, and the contribution to the stiffness of the element from that integration point is ignored. The shear stress transfer across a crack plane is controlled by a material input parameter. An input parameter is used for both the crack open and the crack closed conditions.

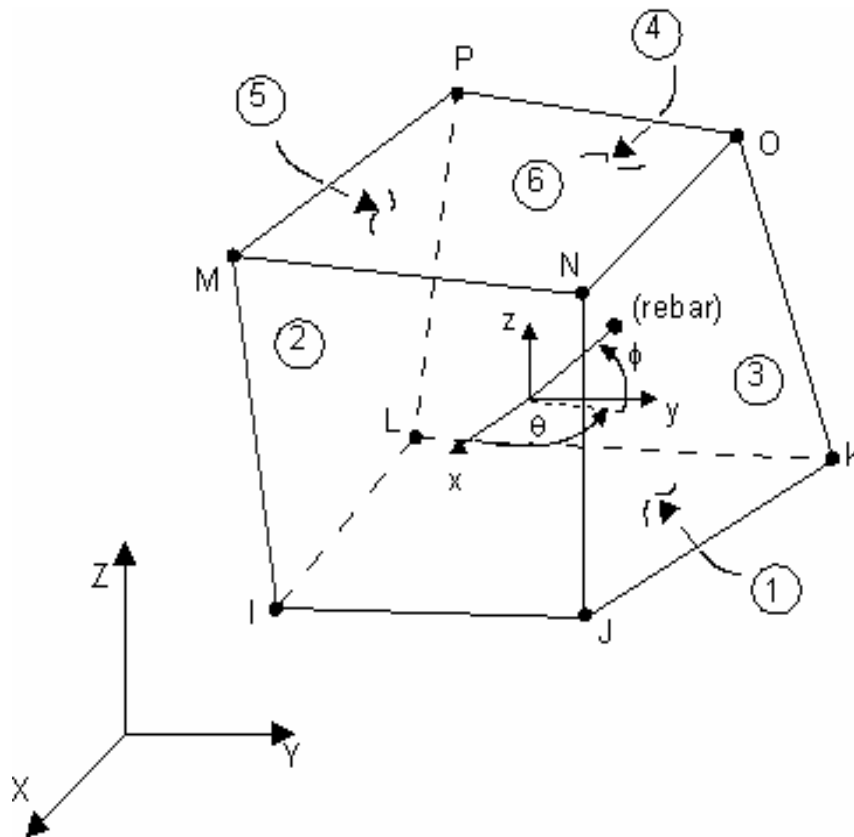


Figure 27: Solid 65 Element Geometry (ANSYS 2003)

3.5.2 REINFORCING STEEL ELEMENT TYPE

The ANSYS element Link180 was used for the compression reinforcing steel and the prestressing steel. Link180 is a uniaxial tension-compression element with two nodes, as shown in Figure 28. The element has three translational degrees of freedom per node. The link element can be prestressed.

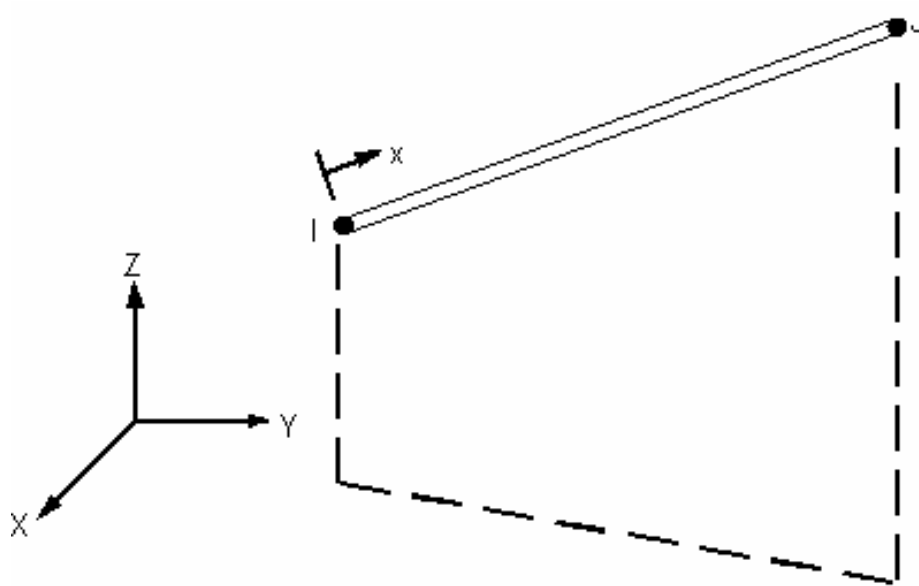


Figure 28: Link 180 Element Geometry (ANSYS 2003)

3.6 MODELING ALTERNATIVES

3.6.1 LONGITUDINAL REINFORCING STEEL

This research used a 1D element to model the longitudinal reinforcing steel. Alternatively, the longitudinal steel could have been modeled as “smeared”

reinforcing steel, using the concrete material properties available in the Solid65 3D brick element. This alternative would require precise placement of the elements containing the “smeared” reinforcing steel at the steel depth so as to simulate the tension force developed by the steel (or the compressive force in the case of compression steel). This would have complicated the modeling process. The Solid65 element has the capability for “smeared” reinforcing steel for up to three orthogonal directions.

The reinforcing steel could also have been modeled using 3D solid elements. The steel surface could have been “glued” to the concrete surface to simulate perfect bond. Alternatively, a contact surface could have been created to simulate the bond between the steel and the concrete. This alternative was not used due to the increased complexity of the model.

3.6.2 TRANSVERSE REINFORCING STEEL

In this research, the transverse reinforcing steel consists of “smeared” steel in the vertical direction. Alternatively, the transverse reinforcing steel could have been modeled using a 1D element. This alternative would have increased the complexity of the model and was not used.

3.6.3 CONCRETE CONSTITUTIVE MODEL

A multi-linear stress-strain material model can be generated using ANSYS, but only positive numbers can be input. Thus the same material

properties used in the tension loading region are used in the compression region. Since the concrete's tensile capacity is only about one-tenth that of its compressive strength, a multi-linear user defined concrete model is not appropriate for this research.

3.6.4 EXPERIMENTAL TESTING PROGRAM

The computational results using the ANSYS software are compared to experimental test results. The prestressed concrete beams were fabricated for the purpose of measuring prestressing steel strand transfer length by Rose (Rose 1995). The beams were subsequently tested in flexure by Paulsgrove (Paulsgrove 1996) to measure development length.

The experimental test results of Beam CA3-S, the subject of this research, are summarized here and described in more detail in Appendix A. The graph shows load versus deflection of both the test results and the classical analysis results. The beam's cracking patterns are sketched. A narrative description of the test events is included in the test summary. The beam reached flexural failure at an applied moment of 703 kip-inches with a deflection of 3.6 inches. The beam was designed and fabricated to achieve a flexural failure, i.e. the beam had adequate shear reinforcement for this loading condition. From a classical analysis, the beam cross-section can resist an external load of 723 kip-inches. A

graph of the moment versus curvature relationship is also provided in Appendix A.

The flexural strength and deflection are more accurately measured through the use of a two point loading condition and constant moment region. The experimental test configuration is shown in a sketch in Appendix A. The progression of cracking as loading is increased is shown in a sketch in Appendix A, for Beam BA2R-N, a similarly loaded beam. Flexural cracking initiates in the constant moment region. The cracking is vertical since the shear is zero. The cracking outside of the constant moment region is inclined due to shear effects. The depth the section cracks increases as the load is increased. Also shown in Appendix A is the crack pattern for Beam BA1R-S and Beam AA3-S, beams failing due to shear after loss of the prestress force due to loss of bond of the strand to the concrete. Beam AA3-S failed early in the loading when the test load reached that sufficient to cause the initial flexural crack. Beam BA1R-S failed after many flexural cracks had formed, and the beam had deformed significantly, at a load near the ultimate strength of the beam.

3.7 COMPARISON OF RESULTS

3.7.1 INTRODUCTION

The ANSYS results are compared to the results obtained from experimental testing and classical analysis. Also studied is the effect of the test variables, element size and concrete material model, on the computational results.

3.7.2 TYPICAL ANSYS ANALYSIS RESULTS

Figure 29 shows the deflected shape of the structure. The ANSYS results of a typical analysis are compared to the experimental results and the classical analysis results in Figure 30. The ANSYS analysis does not predict the ductility of the prestressed concrete flexural member. The ANSYS load versus deflection curve ends at about 0.5 inches of deflection, or only about 15 percent of the 3.5 inches exhibited during the experimental test.

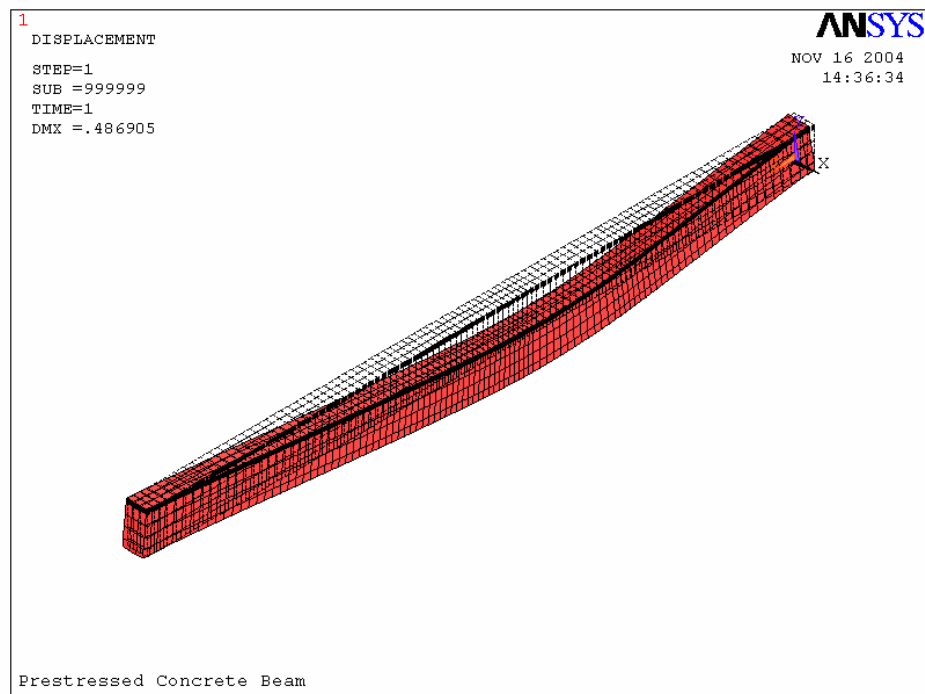


Figure 29: Rectangular Beam Deflected Shape

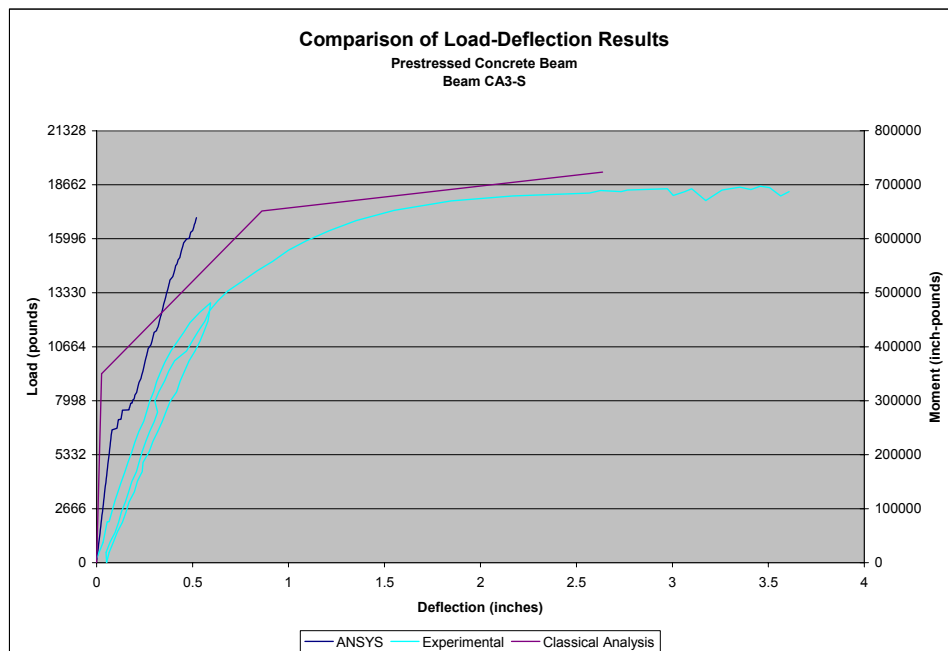


Figure 30: Prestressed Rectangular Beam Response

The ANSYS analysis terminates due to nonconvergence before reaching the ultimate flexural strength loading condition. ANSYS analysis loading reached about 640 kip-inches, or about 80 to 90 percent of the member's flexural strength as predicted by classical analysis or as determined from the experimental tests.

The ANSYS prediction indicates a flexural stiffness between the stiffer classical analysis and the less stiff experimental analysis. An explanation of why the computational results have a greater stiffness than the experimental results is that the computational prediction is an upper bound solution, and will underestimate deformation.

3.8 RESEARCH VARIABLES

Test variables were selected to compare the results obtained from the computational model with the experimental results. These variables were selected based upon an expectation of the model's sensitivity to a change in the variable. Element size and material model form the basis of the variables.

3.8.1 MESH REFINEMENT

The mesh was refined to study the effects of aspect ratio and element size. The mesh was first refined at the top of the beam above the compression steel, to reduce the size of the concrete elements with a large compressive stress. The mesh was then refined along the length of the beam to reduce the aspect ratio.

The results are shown in Table 2 and on Figure 31. The legend shows that the data is plotted for the “coarse” mesh, i.e. prior to refinement along the beam, and for the “fine” mesh, i.e. after mesh refinement along the beam.

COMPARISON OF ANALYTICAL RESULTS: ANSYS to Classical Analysis				
Classical Analysis Results		Test Set Up Dimensions		
Flexural Strength (inch pounds) 723000	deflection (inches) 2.636	span (inches) 192	shear span (inches) 56	
coarse mesh along beam				
Mesh Refinement Above Top Steel (h)	Flexural Strength (in-pounds) (ratio to classical)		Deflection (inch) (ratio to classical)	
1	635799	0.8794	0.5204	0.1974
2	608133	0.8411	0.4761	0.1806
4	596400	0.8249	0.4622	0.1754
mesh refinement along beam				
Mesh Refinement Above Top Steel (h)	Flexural Strength (in-pounds) (ratio to classical)		Deflection (inch) (ratio to classical)	
1	591179	0.8177	0.4439	0.1684
2	615693	0.8516	0.4659	0.1768
4	595553	0.8237	0.4513	0.1712

Table 2: Rectangular Beam Mesh Refinement

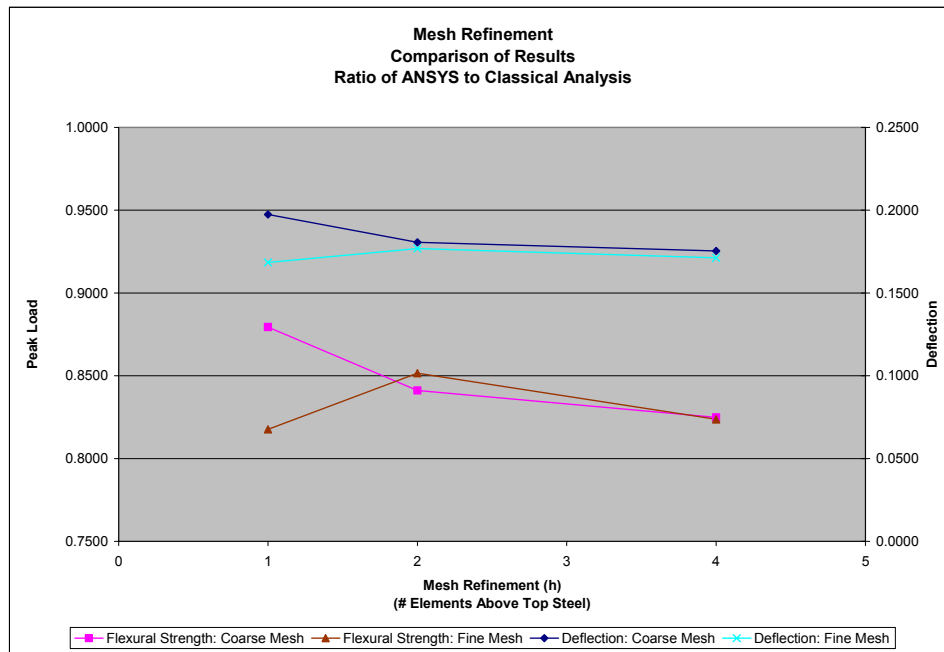


Figure 31: Rectangular Beam Mesh Refinement

Mesh refinement above the compression steel resulted in lower member strength, and decreased deformation. Flexural strength decreased from 636 to 596 kip-inches, and deflection decreased from 0.88 to 0.82 inches. Refinement along the member also resulted in a decreased flexural strength for the test cases with two and four elements above the compression steel. These values decreased from 616 to 596 kip-inches and from 0.47 to 0.45 inches.

3.8.2 MATERIAL MODEL

A user defined concrete model was attempted, but ANSYS does not allow for negative values for input of stress and strain, but instead uses the same

material properties in the tension region as the compression region. Since concrete has a tensile strength of about one-tenth of the compressive strength, the results of this material model were not realistic.

3.9 DISCUSSION OF NUMERICAL RESULTS

3.9.1 INTRODUCTION

The weakness of the ANSYS concrete material model is apparent from this test program. A representative load versus deflection plot shows that much of the nonlinear behavior of a prestressed concrete flexural member cannot be simulated using the ANSYS concrete material model. The mesh refinement results also demonstrate this weakness.

3.9.2 FLEXURAL TEST RESULTS

The load versus deflection plot of a typical flexural test, shown on Figure 30, shows the difficulty ANSYS has in predicting the strength and ductility of a prestressed concrete beam. The test results summary in Table 2 and on Figure 31 also demonstrate this deficiency. The ANSYS analysis terminates due to nonconvergence at about 80 to 90 percent of the expected flexural strength, and the ANSYS model depicts less than about 20 percent of the deformation.

The ANSYS analysis terminate as the implicit iteration strategy fails to converge. The implicit iteration strategy, Newton's method, does not work well

in strain softening situations. The slope of the stress-strain relation tends to zero as the strain softening region is approached, and would actually be negative in the strain softening region. The slope of the stress-strain relation is used to estimate the solution for the next increment. This also explains why the researchers Barbosa & Ribeiro (1998) and Fanning (2001) “turned off” the concrete “crushing” in their ANSYS models in order to get numerical results that produced a plateau on the load-displacement plot, i.e. more ductile flexural behavior. The ANSYS concrete material model does not have a softening region, but instead the material cannot resist any stress upon reaching the crushing stress.

3.9.3 MESH REFINEMENT

The mesh was refined in the region of high compressive stress, first above the compression steel, and secondly along the beam. The results are shown on Figure 31 and Table 2. The legend shows that the data is plotted for the “coarse” mesh, i.e. prior to refinement along the beam, and for the “fine” mesh, i.e. after mesh refinement along the beam.

Contrary to expectations, mesh refinement above the compression steel resulted in an earlier nonconvergence, i.e. nonconvergence occurs at a lower peak load and lower deflection. Refinement along the member also resulted in a decreased peak load for the test cases with two and four elements above the compression steel.

The mesh refinement in the region of high concrete compressive stress demonstrates the weakness of the ANSYS concrete material model. A reduction in the element size resulted in earlier nonconvergence, i.e at a lower peak load.

3.9.4 EXPLANATION OF RESULTS

Much of the ductility of a prestressed concrete beam cannot be simulated using the ANSYS concrete material model. The material model does not allow for strain softening, but instead the element “crushes” as the concrete cannot continue to resist any stress at increased strains beyond the crushing stress. The concrete “crushing” must be “turned off” in the ANSYS concrete material model, for the concrete element to continue to resist stress at increased strains beyond the crushing stress.

3.10 SUMMARY OF CONCLUSIONS

3.10.1 INTRODUCTION

This research emphasizes the importance of the concrete material model on the ability to computationally predict the nonlinear behavior of prestressed concrete flexural members. ANSYS terminates due to nonconvergence fairly close to the predicted peak load, but much earlier than the predicted deflection.

3.10.2 CONCLUSIONS

Specifically, the conclusions of this research are:

- The ANSYS analysis terminates due to nonconvergence at about 80 to 90 percent of the predicted flexural strength of a prestressed concrete flexural member. The ANSYS analysis terminates because the implicit iteration strategy fails to converge. The implicit iteration strategy, Newton's method, does not work well in strain softening situations. The slope of the stress-strain relation tends to zero as the strain softening region is approached, and would actually be negative in the strain softening region. The slope of the stress-strain relation is used to estimate the solution for the next increment. The ANSYS concrete material model does not have a softening region, but instead the material cannot resist any stress upon reaching the crushing stress.
- ANSYS cannot simulate the ductility of a prestressed concrete flexural member. The ANSYS analysis terminates due to nonconvergence at about 20 percent of the predicted deformation.
- The addition of a user-defined material with separate tension and compression behavior would benefit reinforced concrete modeling with ANSYS.

3.11 ANSYS PLAIN CONCRETE SPECIMEN ANALYSIS

An unreinforced concrete beam was modeled and compared to the results of a classical analysis. The flexural strength is limited by the modulus of rupture of concrete. Estimates of cracking moment and deflection using classical analysis

are 83.7 kip-inches, and 0.075 inches, respectively. An ANSYS model predicted failure, at 93.9 kip-inches, and deflection at 0.032 inches. The ANSYS model is a more stiff structure due to the coarse mesh, thus deflection was underestimated. The ANSYS strength prediction was 112 percent of the classical analysis estimate. Figure 32 shows a nearly linear load deflection plot, since the concrete material model is nearly linear for this loading condition. The classical analysis can be viewed in Appendix C.

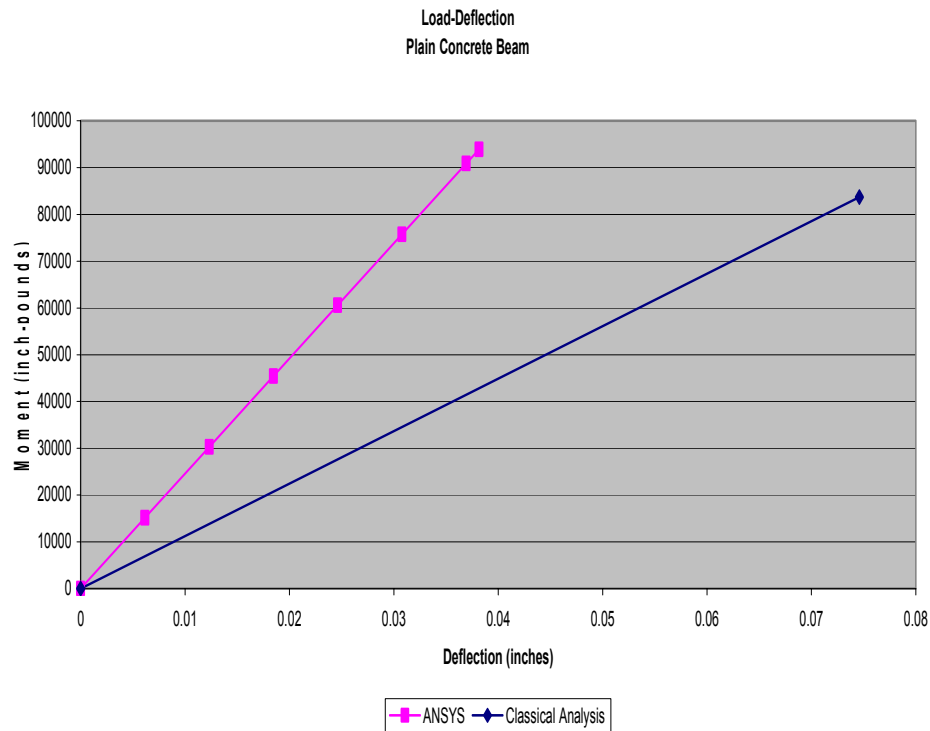


Figure 32: Unreinforced Beam Response

CHAPTER 4 REINFORCED CONCRETE TORNADO SHELTER

4.1 INTRODUCTION

The overall goal of this component of the research program is to evaluate the ability of commercially available finite element analysis software to model the nonlinear behavior of a complex reinforced concrete structure of importance to the structural engineering community. More specifically, the program set out to compare the response obtained from the computational model of a tornado shelter subjected to an impact loading to those obtained from experimental results from Texas Tech University and classical analysis techniques.

Tornadoes are the cause of significant loss of life and property damage. Each year, tornadoes are studied to improve our understanding of their formation and of their destructive force. The object of these studies from the viewpoint of a weather scientist is to improve forecasts and provide earlier warning. But from a structural engineering perspective, greater understanding will lead to improved shelters and other structures and reduced injury and property damage. The goal is to improve the design and construction standards for shelter space for building

occupants. Figure 33 shows a tornado near Newcastle, Oklahoma, during the May 3, 1999 midwest tornadoes.



Figure 33: May 3, 1999 Midwest Tornadoes (The Oklahoman 1999)

4.2 TORNADO CHARACTERIZATION

A tornado is characterized by its damaging effects as shown in Table 3. Since 1995, an average of 1,200 tornadoes has been reported nationwide each year. Tornadoes are generally short lived, and on average are less than 500 feet wide and travel less than 2,000 feet. But about 10 percent of tornadoes produce

severe damage, as shown in Figure 34. Some tornadoes have damage paths $\frac{3}{4}$ mile wide and many miles long, but these only occur a few times a year.

Category / Typical Damage	
	F0 Light: Chimneys are damaged, tree branches are broken, shallow-rooted trees are toppled.
	F1 Moderate: Roof surfaces are peeled off, windows are broken, some tree trunks are snapped, unanchored mobile homes are overturned, attached garages may be destroyed.
	F2 Considerable: Roof structures are damaged, mobile homes are destroyed, debris becomes airborne (missiles are generated), large trees are snapped or uprooted.
	F3 Severe: Roofs and some walls are torn from structures, some small buildings are destroyed, non-reinforced masonry buildings are destroyed, most trees in forest are uprooted.
	F4 Devastating: Well-constructed houses are destroyed, some structures are lifted from foundations and blown some distance, cars are blown some distance, large debris becomes airborne.
	F5 Incredible: Strong frame houses are lifted from foundations, reinforced concrete structures are damaged, automobile-sized missiles become airborne, trees are completely debarked.

Table 3: Fujita Tornado Damage Scale (FEMA 2004)

Tornadoes generally travel from southwest to northeast. Tornadoes typically travel about 25 to 40 mph, but speeds in the range of 5 to 60 mph have been recorded. In the northern hemisphere, tornadoes typically circulate counterclockwise, looking downward.

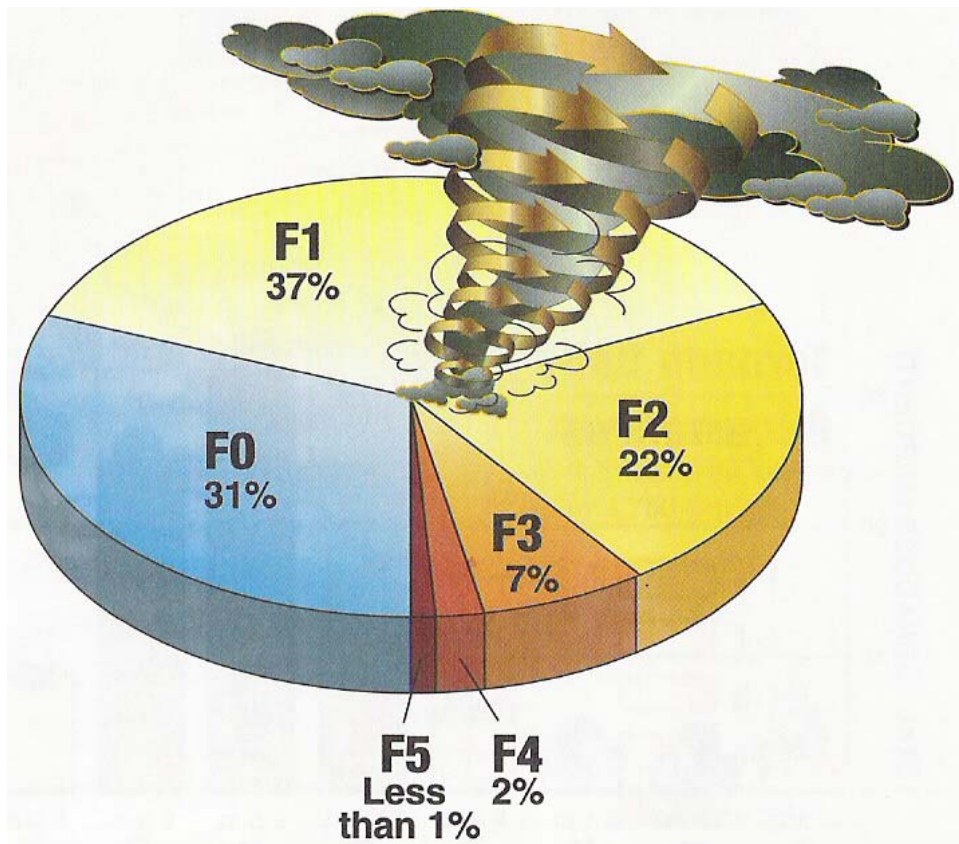


Figure 34: Tornado Intensity Distribution (FEMA 2003)

The most severe tornadoes generally occur in the midwest portion of the United States, but they can occur in most regions of the country, as shown in Figure 35.

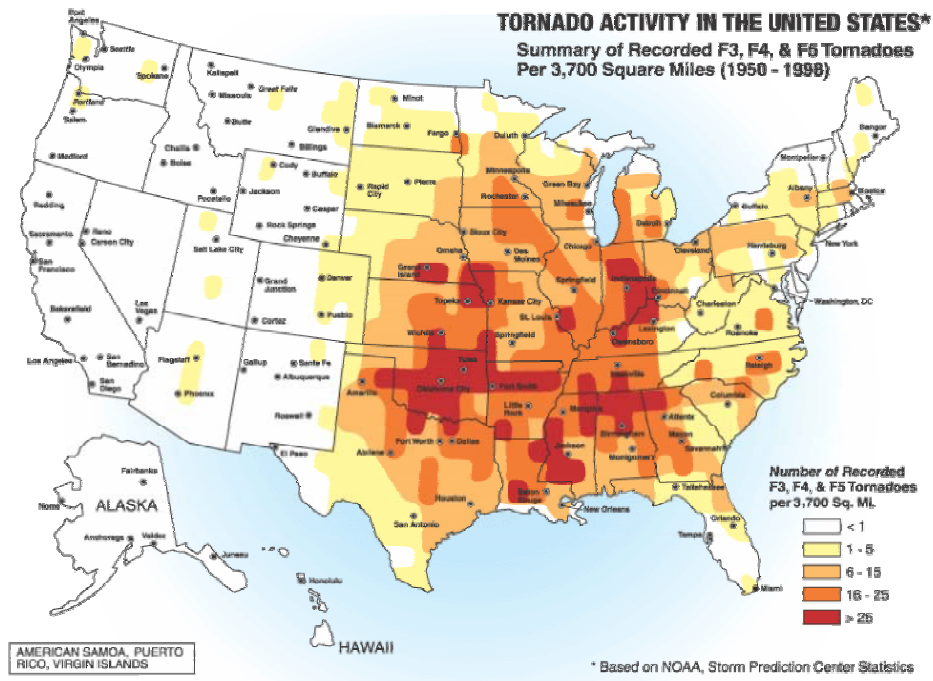


Figure 35: Tornado Geographic Activity (FEMA 2004)

Tornadoes are most likely to occur in the late spring months, during the late afternoon and early evening, but they can occur at any time of the year, as shown in Figure 36, and during any part of the day, as shown in Figure 37.

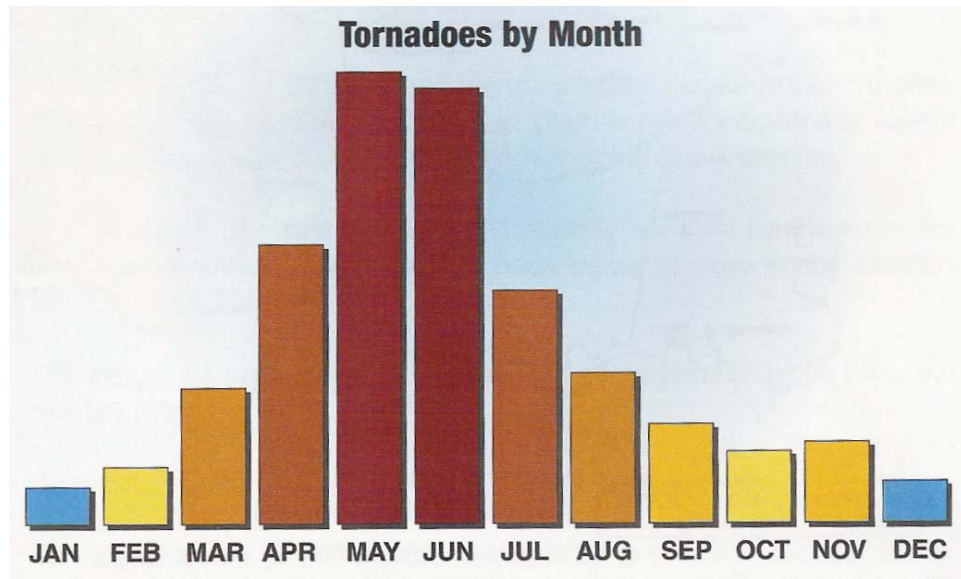


Figure 36: Tornado Annual Distribution (FEMA 2003)

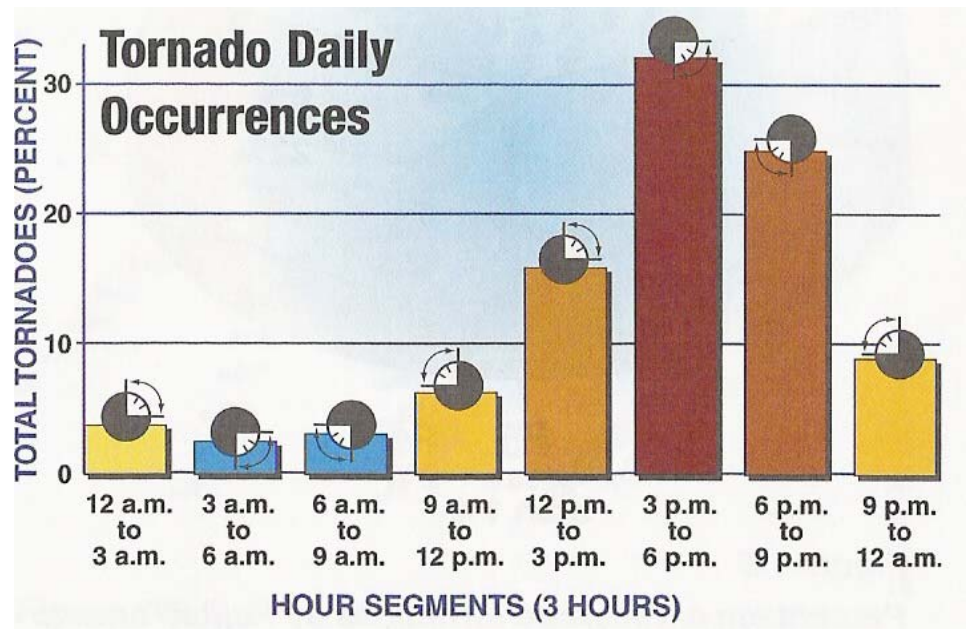


Figure 37: Tornado Daily Distribution (FEMA 2003)

4.3 TORNADO SHELTER DESIGN

The necessity for adequate design criteria for the construction of above ground tornado shelters is illustrated in Figure 38 and Figure 39. Tornado shelters must be designed to resist overturning, sliding and uplift forces due to wind pressure, and penetration by a wind borne projectile. Tornado shelter design criteria are established in FEMA publications (FEMA 1999, FEMA 2000, FEMA 2003, and FEMA 2004).



Figure 38: Above Ground Tornado Shelters (FEMA 2004)

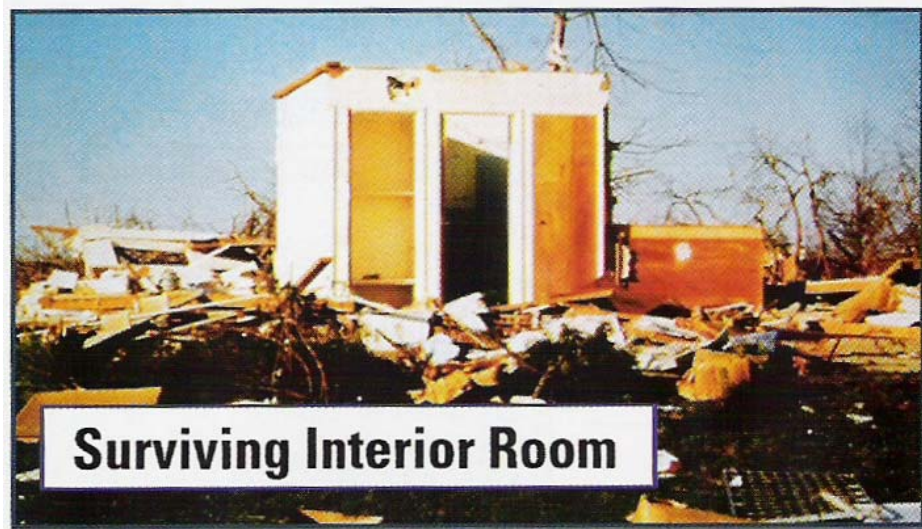


Figure 39: Above Ground Tornado Shelter (FEMA 2004)

4.3.1 TORNADO RISK ASSESSMENT

A tornado shelter mitigates the risk of injury due to a severe tornado event. Determining the risk of exposure to a tornado can be determined from FEMA Publication 320 (FEMA 2004). The risk of exposure will determine the need for a tornado shelter. The country is divided into wind zones, based upon 40 years of tornado history. Figure 40 shows the wind zone for Oklahoma City to be Zone IV, with a design wind speed of 250 mph, which is the highest risk zone. From Figure 35, the number of recorded severe tornadoes in the Oklahoma City area is shown to be greater than 25. From these two data, Figure 41 is used to determine that Oklahoma City residents have a “high risk” of exposure to high winds, and a shelter is the preferred method of protection.

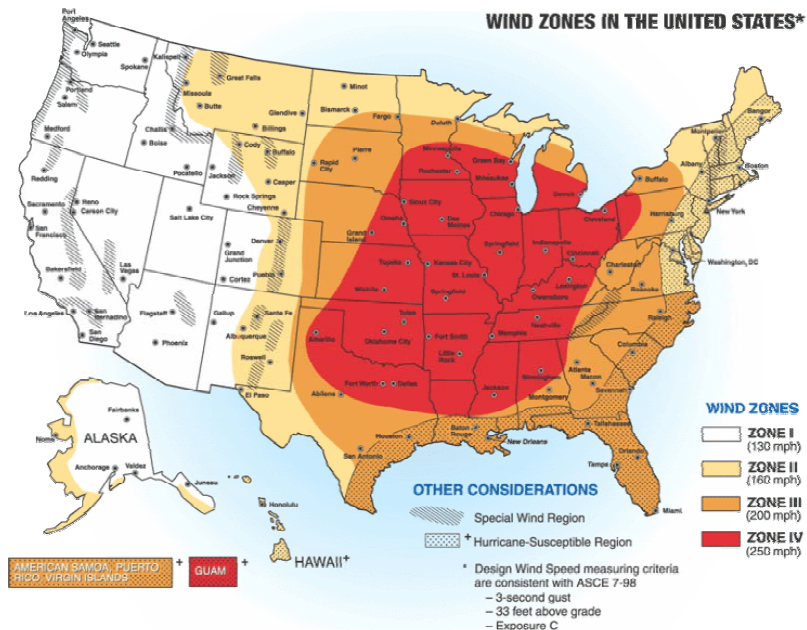


Figure 40: Tornado Design Wind Speed (FEMA 2004)

		WIND ZONE (See Figure I.2)			
		I	II	III	IV
NUMBER OF TORNADOES PER 3,700 SQUARE MILES (See Figure I.1)	<1	LOW RISK	LOW RISK ★	LOW RISK ★	MODERATE RISK
	1 - 5	LOW RISK	MODERATE RISK ★	HIGH RISK	HIGH RISK
	6 - 10	LOW RISK	MODERATE RISK ★	HIGH RISK	HIGH RISK
	11 - 15	HIGH RISK	HIGH RISK	HIGH RISK	HIGH RISK
	>15	HIGH RISK	HIGH RISK	HIGH RISK	HIGH RISK

LOW RISK

Need for high-wind shelter is a matter of homeowner preference.

MODERATE RISK

Shelter should be considered for protection from high winds.

HIGH RISK

Shelter is the preferred method of protection from high winds.

★ Shelter is the preferred method of protection from high winds if the house is in a hurricane-susceptible region.

Figure 41: Tornado Risk Assessment (FEMA 2004)

4.3.2 TORNADO SHELTER DESIGN WIND PRESSURE

The design wind speeds are estimated from the damage to structures. The design wind speed from Figure 40 is used in the design of tornado shelters. Wind speeds associated with tornado categories are also offered in Appendix D (Fujita 1971). Wind speeds greater than the design wind speeds are frequently reported following tornado events, but these measured wind speed data are often contested by engineers and scientists, and the design wind speed is accepted for the design of tornado shelters rather than any reported maximum wind speed data.

Design wind pressures, other loads and load combinations are determined using the applicable building codes including ASCE 7 Minimum Design Loads for Buildings and Other Structures, the International Building Code, and the International Residential Code (FEMA 1999 and FEMA 2000). Figure 42 indicates how openings in the building envelope will allow wind to enter the building and cause internal pressures in addition to the wind-induced aerodynamic external pressures.

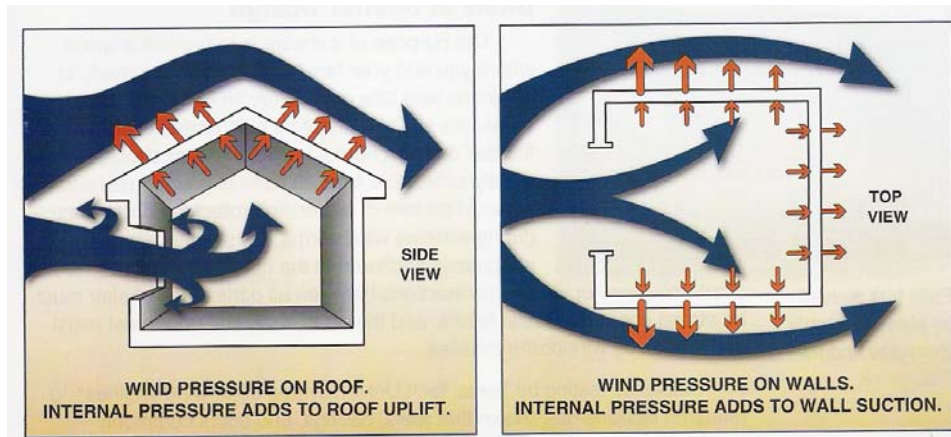


Figure 42: Tornado Design Wind Pressure (FEMA 2004)

4.3.3 TORNADO SHELTER DESIGN PROJECTILE IMPACT LOAD

Projectile impact is an important shelter design consideration. Figure 43 shows a 2" x 6" wood projectile penetrating a refrigerator, which occurred during the May 3, 1999 midwest tornadoes. The design impact load for a tornado shelter is a 2" x 4" wood stud weighing about 15 pounds, carried by a 250 mph wind (FEMA 1999). This is equivalent to 10 feet to 12 feet length of 2" x 4" lumber impacting horizontally onto a vertical wall at about 100 mph, or dropping vertically onto a horizontal roof at about 67 mph. Pitch or yaw effects are not considered, i.e. the projectile impacts the structure in a perpendicular direction and with no rotation. Clemson University and Texas Tech University have conducted projectile impact tests on building materials, and the results are available to the design professional (FEMA 2000).



Figure 43: Damage Caused By Wood Projectile (FEMA 2004)

4.3.4 STRUCTURAL REQUIREMENTS FOR FEMA STANDARD DESIGN

Strength required to resist projectile impact loading, strength required to resist strong winds from tornadoes as shown in Figure 40, strength required to resist wind and gravity loading conditions as prescribed in national building codes, together with ACI 318 detailing requirements, led to FEMA's recommended minimum standards for the design and construction of a residential tornado shelter (FEMA 2000 and FEMA 2004). Projectile impact load testing led to FEMA's recommendation for a minimum 4 inch thick concrete section reinforced with #4 deformed steel bars at 12 inches on center each way.

The minimum standard for a reinforced concrete above ground residential tornado shelter with wall height less than 10 feet and roof span less than 8 feet, is 6 inch thick walls with 4 inch thick roof slab, reinforced with #4 deformed steel bars in each direction at middepth spaced at 12 inches on center each way. Strength required to resist flexure and shear stresses led to the recommended maximum member lengths for these section thicknesses. For wall heights less than 8 feet, a minimum 4 inch thick wall section is recommended.

4.4 TORNADO SHELTER FEM ANALYSIS

TeraScale's TeraDyn explicit dynamics finite element analysis computer software was used to analyze the reinforced concrete tornado shelter. The geometry, material properties and loading condition are discussed in this section. Information on the use of TeraScale's TeraDyn explicit dynamics finite element analysis program is provided in Appendix F.

A beta version of the TeraDyn explicit dynamics code was provided as part of a cooperative research effort. This beta version of the code is a work in progress and this Ph.D. research provided a mechanism for validating and debugging many aspects of the reinforced concrete modeling details of the finite element application.

4.4.1 GEOMETRY OF TORNADO SHELTER

The reinforced concrete above ground residential tornado shelter modeled in this research is based on FEMA's minimum standard. The outside dimensions of the shelter are 8 feet, 4 inches tall by 9 feet, 0 inches wide by 6 feet, 0 inches deep. The wall thickness is 6 inches and the roof slab thickness is 4 inches, which results in a ceiling height of 8 feet, 0 inches and a roof clear span of 5 feet, 0 inches. The walls were fixed along the bottom edges by imposing zero translations for all three degrees of freedom at the nodes along these four edges.

The reinforcing steel is as recommended in FEMA's standard design. The walls and ceiling were reinforced with #4 deformed steel bars in each direction at middepth spaced at 12 inches on center each way. Grade 60 steel was used.

A 3D solid element mesh was used for the concrete walls and roof slab. TeraScale's steel reinforcement element was used to mesh the reinforcing steel. Reinforcing steel is modeled as a sub-element within the 3D solid concrete element. Strain compatibility is assumed between concrete and rebar, and no provision is made for bond slip between the reinforcing steel and concrete.

TeraScale provides a rebar generation capability that allows the analyst to place discrete rebar in the exact location that they are detailed in the physical structure. The rebar generator automatically computes the penetration by the

rebar into the solid concrete 3D 8 node brick elements. A solid concrete element may have any number of rebar penetrating through it. This capability allows the user much more flexibility in designing the mesh. There is no need for the rebar to follow mesh lines as in the ANSYS model.

The mesh for the tornado shelter is shown in Figures 44 and 45. The mesh consists of a roof slab and four walls. The reinforcing steel consists of “hoop ties”, which are the horizontal bars that extend at middepth inside the four perimeter walls, and “U” shaped bars that extend at middepth thru the opposite walls and roof slab. An example of how to generate a mesh using TeraScale’s Mesher mesh generation program is shown in Appendix E.

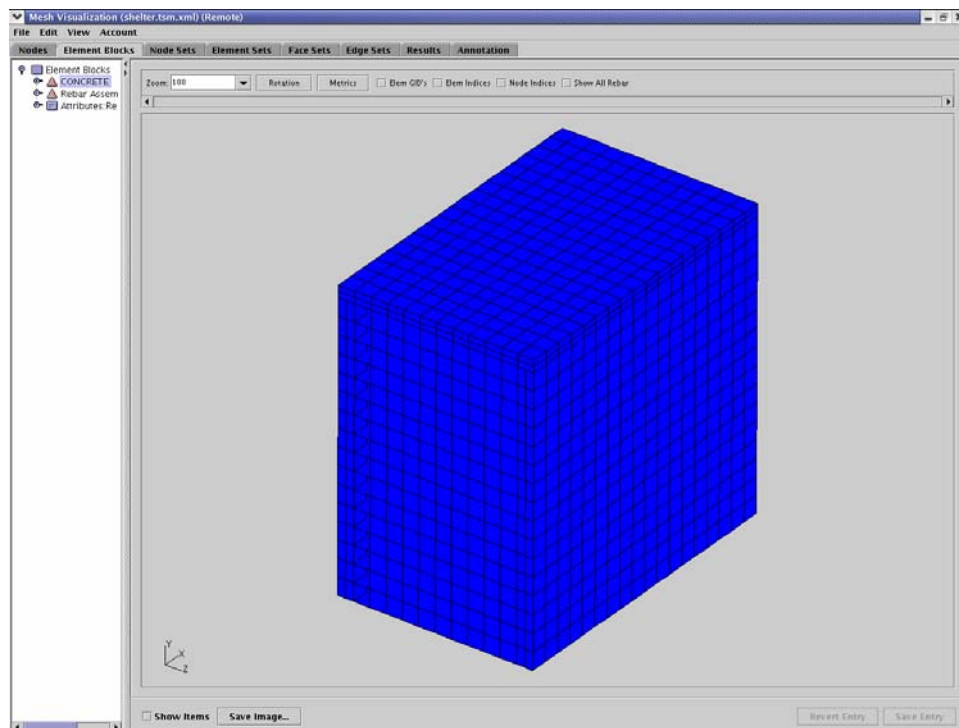


Figure 44: Tornado Shelter Mesh

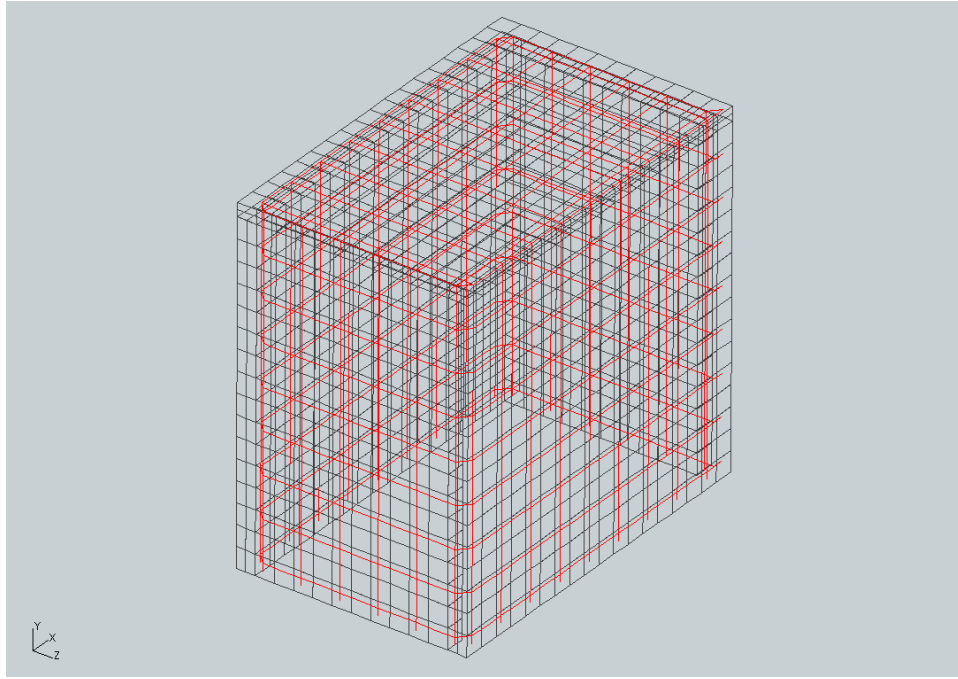


Figure 45: Tornado Shelter Rebar Mesh

4.4.2 MATERIAL PROPERTIES OF TORNADO SHELTER

A highly nonlinear constitutive model which includes the strain softening region was used for the concrete material, as shown in Figure 46. The strain hardening ANATECH Corporation's ANAMAT constitutive model for concrete was used in TeraScale's TeraDyn FEM software for the 3D solid concrete elements. As mentioned previously in section 2.7.3, the ANAMAT constitutive model for concrete is based on smeared cracking methodology and J_2 plasticity theory (ANATECH Corp., 1998). The material nonlinearity is treated at the finite element integration points, thus the cracking and stress/strain state can vary within an element. Cracks form perpendicular to the principal strain direction, and cracking can form in three orthogonal directions. The tensile stress normal to the

crack is reduced to zero, and the stresses around the crack are redistributed. Shear stiffness is reduced upon cracking, and decreases further as cracks open. Crack directions remain fixed. Cracks do not “heal”. They can open, then close and carry compressive load. Upon opening again they have zero strength.

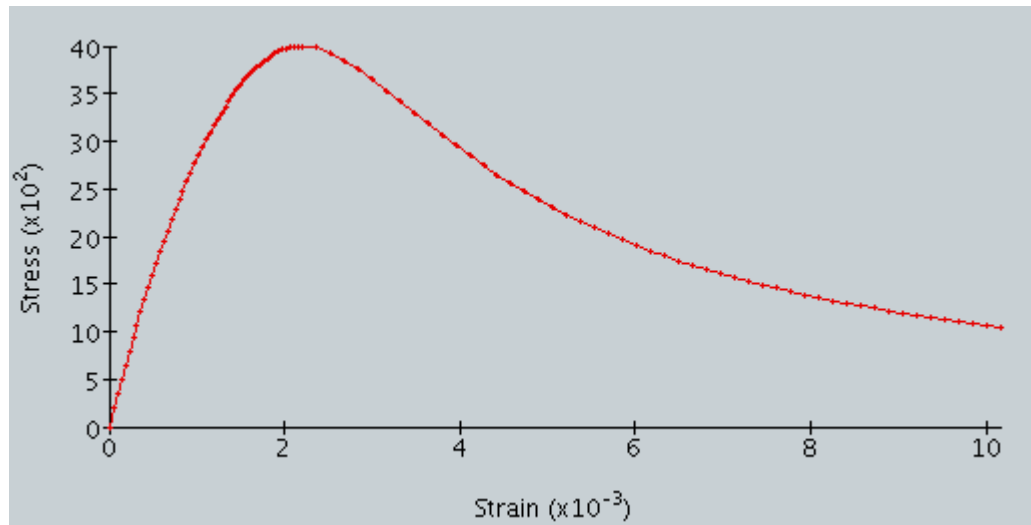


Figure 46: Concrete Compressive Stress–Strain Relation

Concrete material properties used are a concrete compressive strength of 4.0 ksi, an elastic modulus of 3,545 ksi, a Poisson’s constant of 0.18, a concrete strain at maximum compressive stress of 0.0022, and a tensile cracking strain of 0.000050.

The constitutive model for the steel characterizes the strain hardening behavior of mild steel. A bilinear stress-strain curve was used for the conventional reinforcing steel. The linear elastic portion of the curve extends to a

yield strength (σ_y) of 60.0 ksi, with a modulus of elasticity (E_s) of 30,000 ksi. The linear strain hardening portion extends to 120 ksi at an equivalent plastic strain of 1.0. A Poisson's ratio of 0.30 was used.

4.4.3 LOADING CONDITION OF TORNADO SHELTER

A moving pressure impulse load was applied to the center of the back face of the tornado shelter. The loading is similar to the blast effect of 10 pounds of TNT detonated at a distance of 22 feet (see Appendix G for classical analysis and Section 5.2 for an explanation of the blast wave front parameters). The equivalent impulse loading caused by the impact of a 15 pound length of 2 x 4 wood stud striking the shelter at 100 mph is also shown in Appendix G. This projectile, neglecting energy losses due to deformations in the wood and concrete, would be equivalent to this 10 psi pressure applied on about a quarter of the exposed tornado shelter wall. If applied over just the footprint of the stud, the pressure would be over 3,000 psi.

The impulse load used in this analysis is as shown in Figures 47 and 48. In Figure 47, the pressure is shown as a function of time that would be measured at various distances from the epicenter of the applied pressure. In Figure 48, the spatial distribution of pressure as a function of distance from the epicenter of the applied pressure is shown at various snapshots of time.

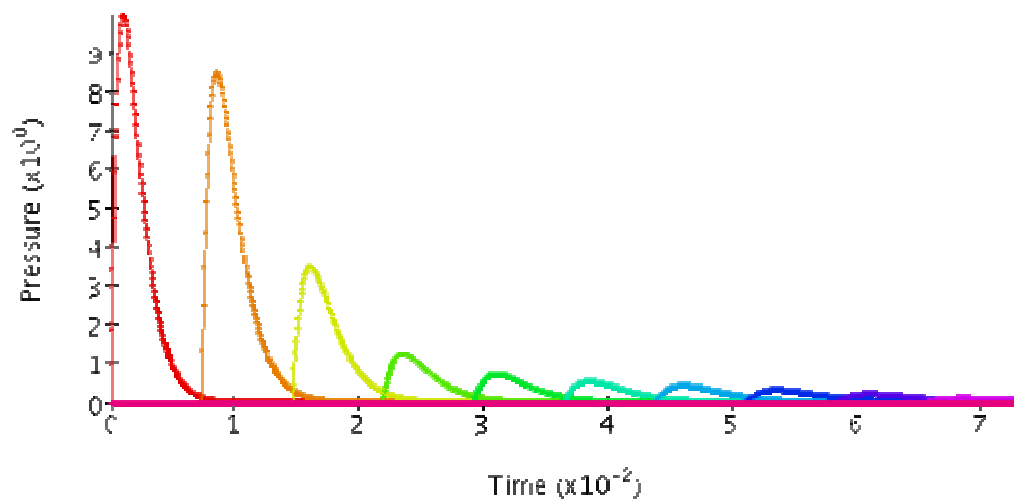


Figure 47: Pressure-Time Curve For Shelter Load (psi, sec)

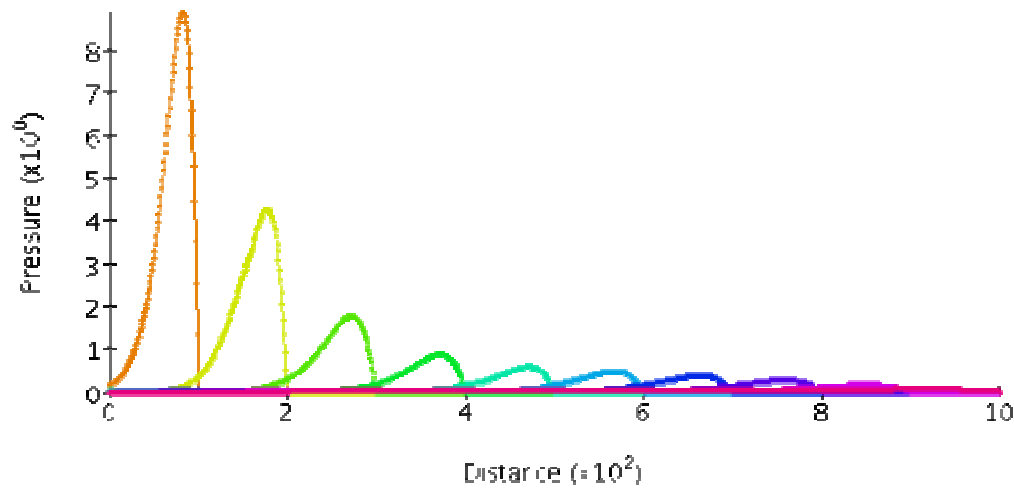


Figure 48: Pressure Distance Curve For Shelter Load (psi, inch)

A magnitude of 10 psi was used for the peak static overpressure at time zero and distance zero. The impulse load has a duration of about 5 msec. The wave front will still have a magnitude of about 85 percent of its initial peak value

after about 15 msec and traveling about 100 inches, a distance greater than the distance the wave front must travel to reach the edge of the shelter. Figure 49 shows the numeric input values used to generate the load.

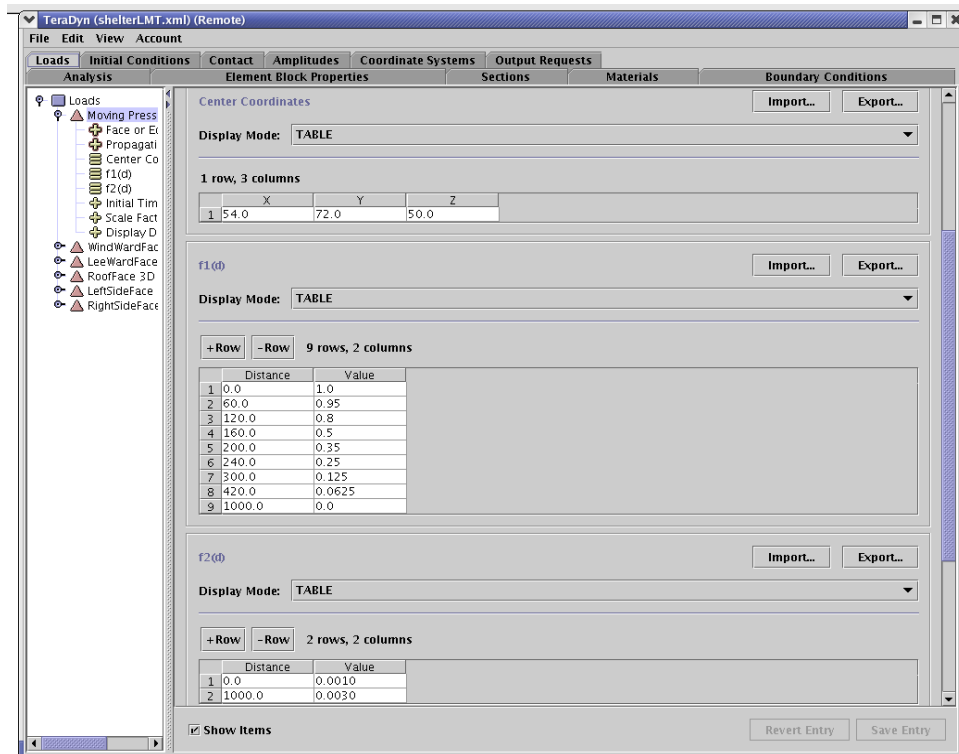


Figure 49: Data Input Screen For Shelter Load (psi, inch)

4.5 TORNADO SHELTER FEM RESULTS

Figures 50 through 58 show the crack progression through time for the tornado shelter. The analysis has a duration of 20 msec, with ten 2 msec substeps for data recording. The cracking initiates at the fixed ends of the wall receiving the loading, and then near the wall's center. Cracking later occurs at the fixed

base opposite the loaded wall. The red cracks are open cracks, and the blue cracks have closed.

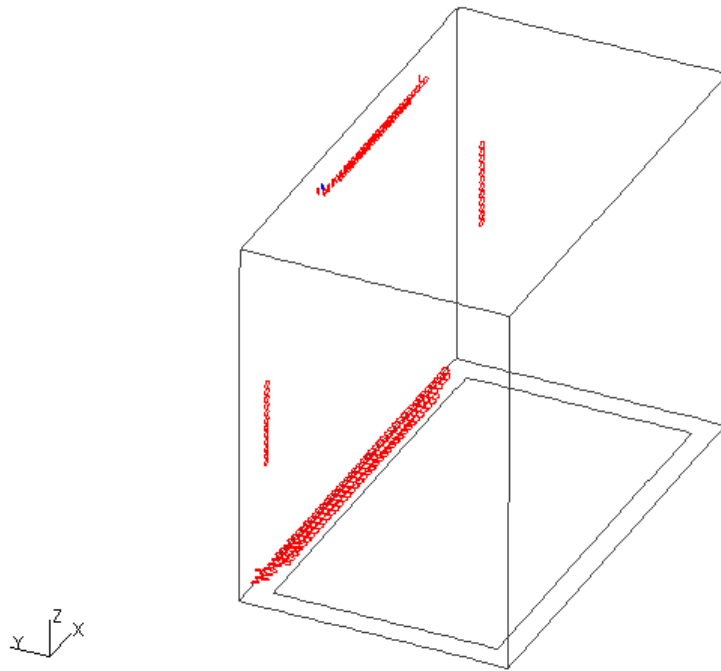


Figure 50: Shelter Cracking at 4 msec

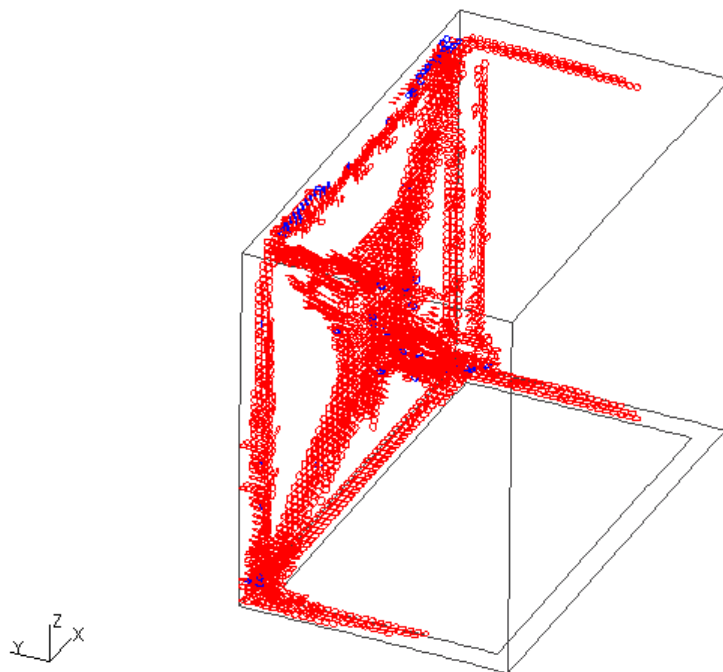


Figure 51: Shelter Cracking at 6 msec

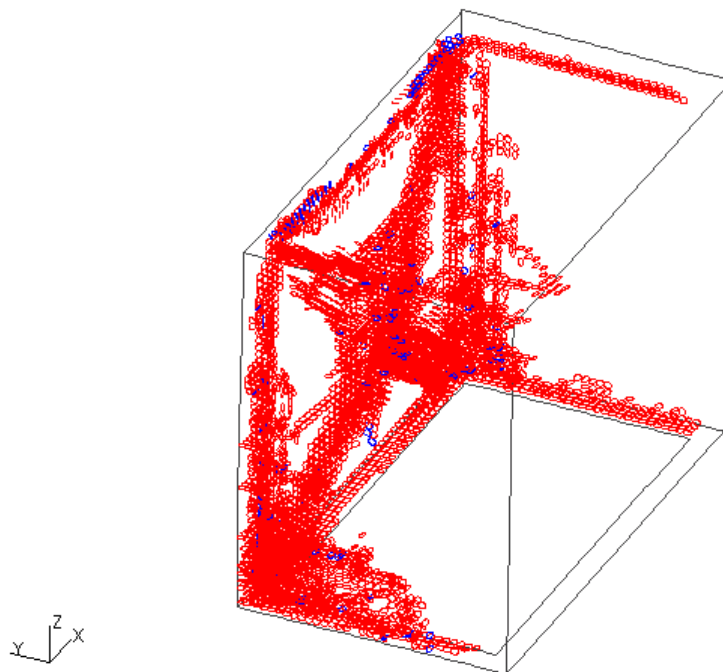


Figure 52: Shelter Cracking at 8 msec

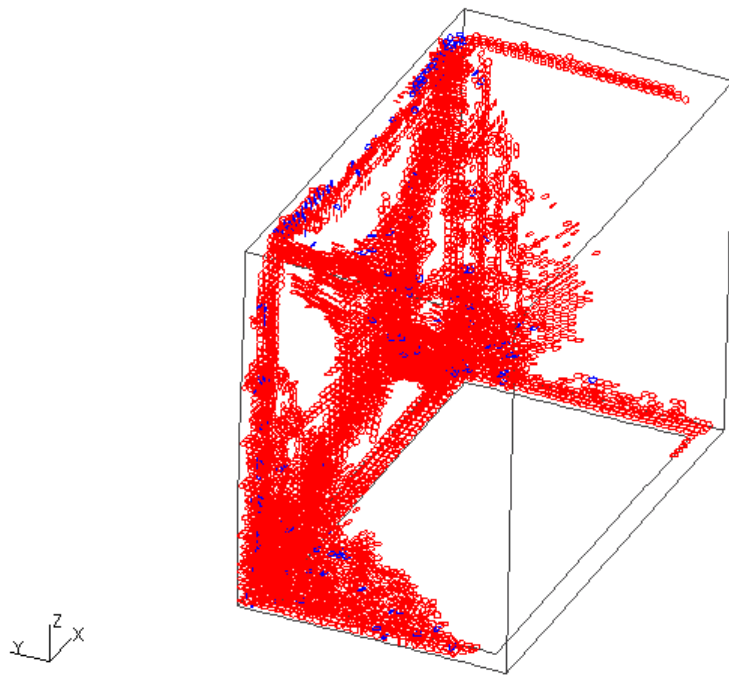


Figure 53: Shelter Cracking at 10 msec

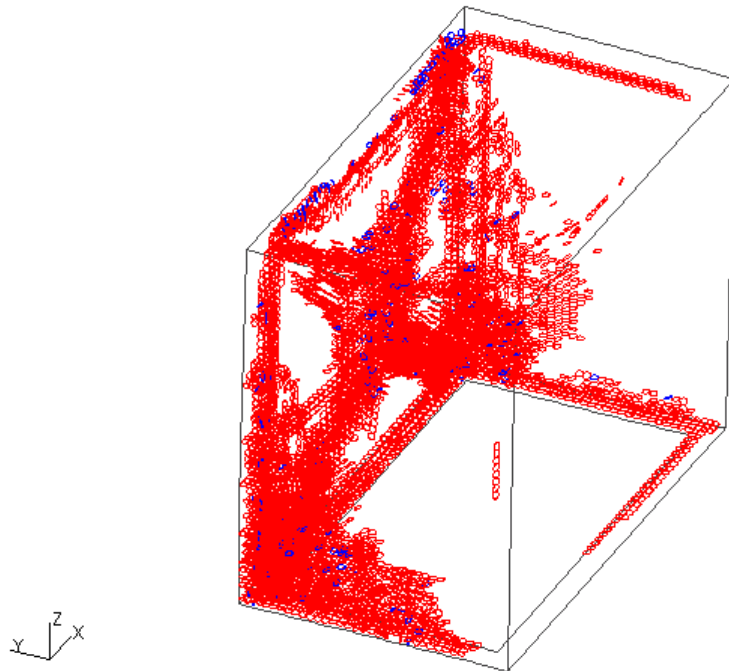


Figure 54: Shelter Cracking at 12 msec

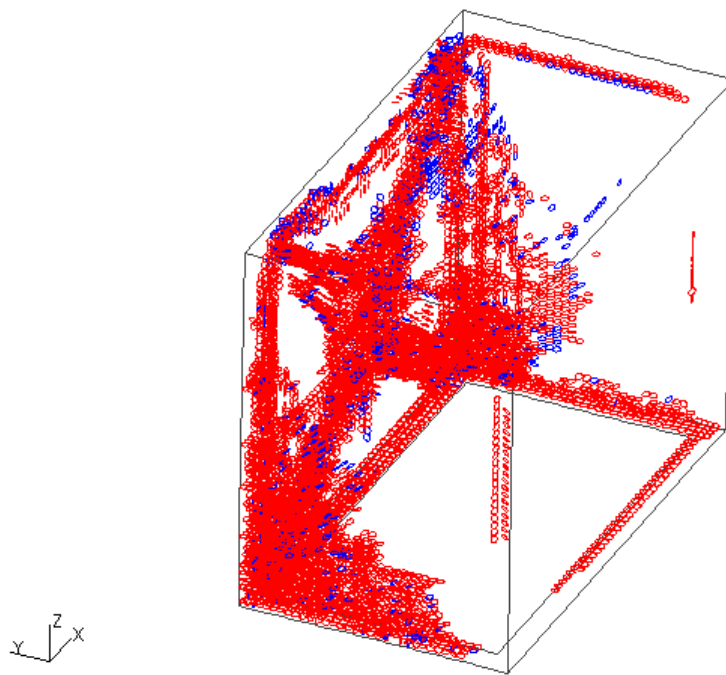


Figure 55: Shelter Cracking at 14 msec

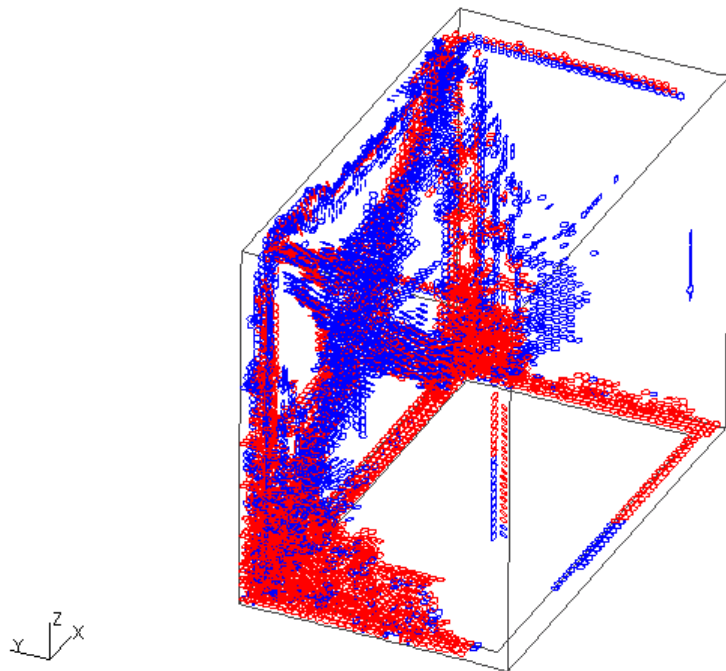


Figure 56: Shelter Cracking at 16 msec

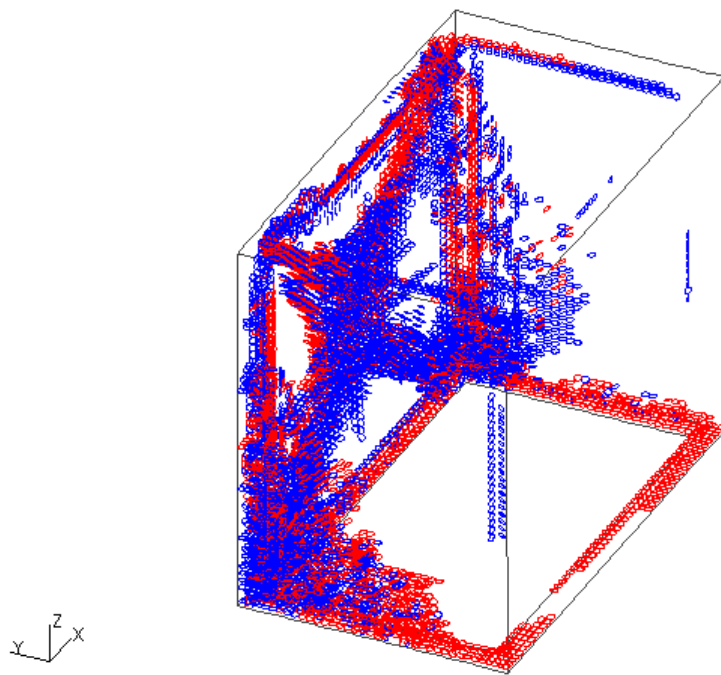


Figure 57: Shelter Cracking at 18 msec

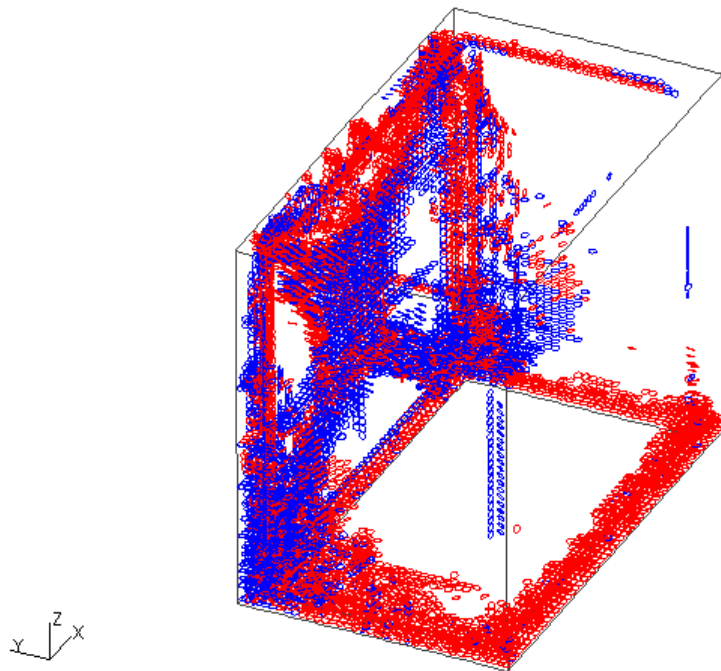


Figure 58: Shelter Cracking at 20 msec

Figures showing the hydrostatic pressure contours plotted on the deflected shape of the structure are provided in Appendix H. These figures, as well as the crack progression and crack color, will help the reader to visualize the initial inward deformation of the rear wall, and its subsequent rebounding outward movement beginning at the 16 msec time step. The shelter can also be seen to deflect due to the impulse load, and then rebound. The shear resistance of the side walls can be seen in the pressure contours. The figures in the appendix show the shelter rotated from the views that depict the cracking, i.e. the shelter wall that receives the impulse load faces the reader in the appendix, but is on the far side of the structure when looking at the figures illustrating the cracking. Deflection is magnified by 400.

4.6 TORNADO SHELTER FEM DISCUSSION

The analysis results depicting the structure's cracking behavior compares well with that expected for the type of load and geometry of the structure.

4.7 TORNADO SHELTER FEM CONCLUSIONS

The TeraDyn program and the ANAMAT constitutive model for concrete can model the nonlinear behavior expected for the impulsive loading of a reinforced concrete tornado shelter structure.

CHAPTER 5 REINFORCED CONCRETE SLAB ANALYSIS

5.1 INTRODUCTION

A post mortem analysis of a blast load to the Murrah building, another problem of interest to the structural engineering community, was selected for this portion of the research. The goal is to evaluate the ability of commercially available finite element analysis software to model the nonlinear behavior of a floor slab subjected to an impact loading, and compare the results to those obtained from classical analysis techniques.

Evaluation of disasters such as the malevolent bombing that occurred in Oklahoma City on April 19, 1995, leads to recommendations regarding design, construction and code issues. The goal of such studies is the reduction of future loss of life, injury and destruction caused by similar events.



Figure 59: North Elevation of Murrah Building (FEMA 1996)

Exposure of structures to blast damage can be mitigated by prevention, reduced exposure and increased resistance. The prevention of these types of occurrences rests with our national defense, intelligence and law enforcement agencies. The exposure and resistance of structures to the effects of blast loading are influenced by the decisions made by owners, designers and builders. Therefore, structural engineers should be aware of blast loadings on structures.

5.2 BLAST WAVES AND BLAST LOADING

When a condensed high explosive material such as trinitrotoluene (TNT) detonates, almost all of the energy liberated is converted into blast energy. The chemical reaction from the TNT explosive blast liberates large amounts of energy.

This energy heats the surrounding air, in the case of an air blast, thus producing very high local pressures. This pressure disturbance develops into a blast wave (Smith and Hetherington, 1994).

A pressure versus time plot of a typical blast is shown in Figure 60. As the blast wave moves outward, the pressure eventually drops to atmospheric pressure (P_o). The pressure at the blast wave front decreases with distance from the source. The hot gasses cool as the expansion continues, and the pressure falls a little below atmospheric pressure. This effect produces an underpressure (ΔP_{min}) that follows the initial overpressure. Finally, equilibrium is reached.

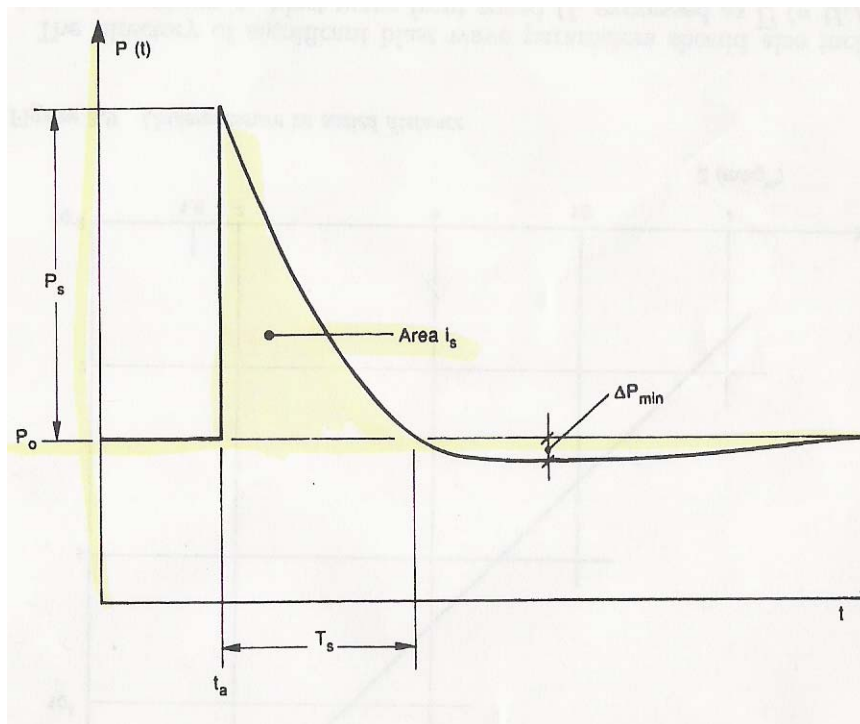


Figure 60: Blast Wave Pressure-Time Profile (Smith and Hetherington 1994)

Research in the effects of explosives has resulted in an understanding of the blast wave front parameters used to determine the effects of an explosive on a structure (Army, TM 5-855-1, 1988). These parameters are the peak static overpressure (P_s), time of arrival (t_a), duration of the positive pressure phase (T_s), specific impulse of the positive pressure wave (i_s), and scaled distance (Z). The specific impulse of the positive pressure wave (i_s) is the area under the overpressure-time curve during the positive pressure phase (T_s). The scaled distance parameter (Z), as defined in equation (9), and is used to relate blast effects at varying distances (R) resulting from varying weights of explosives (W). How these parameters are used in practice will be more fully explained in later sections.

$$(9) \quad Z = R/W^{1/3} \quad \text{scaled distance} \quad (5.1)$$

5.3 OKLAHOMA CITY BOMBING

AT 9:02AM, April 19, 1995, a blast occurred, resulting in loss of life, injury, and partial collapse of the Murrah building. Nearby buildings in the line-of-sight of the blast were also damaged. Most of the north half of the Murrah building collapsed, causing most of the fatalities. Damage extended to exterior wall and roof systems of adjacent buildings, as shown in Figures 62 and 63.

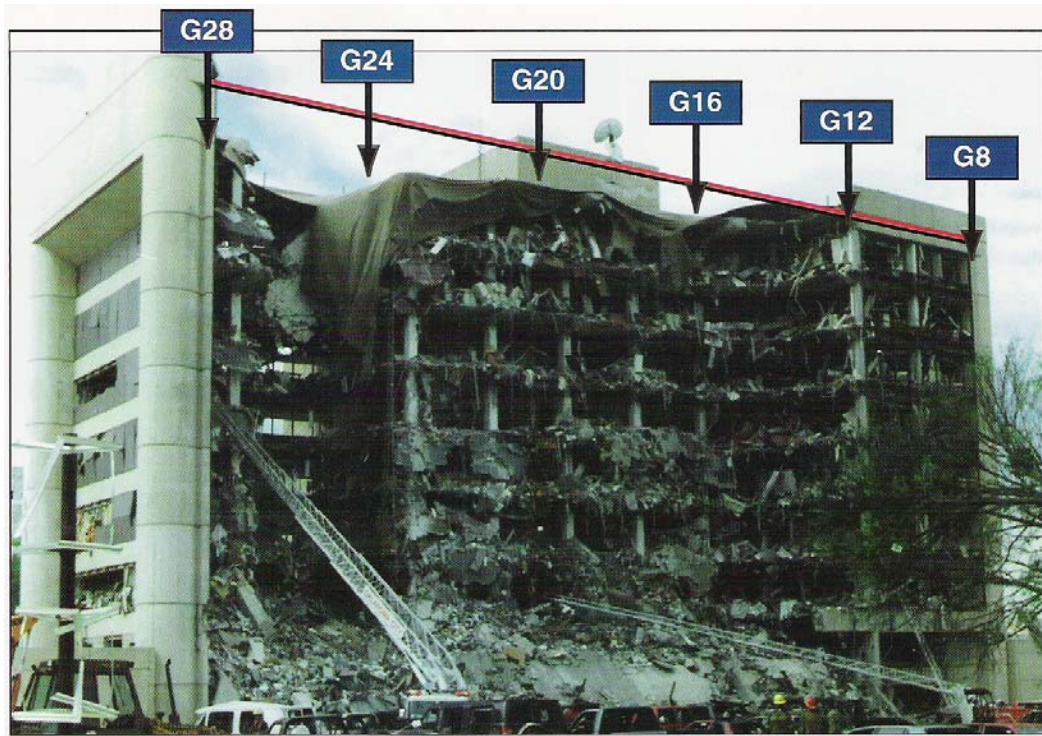


Figure 61: Damage to North Elevation of Murrah Building (FEMA 1996)

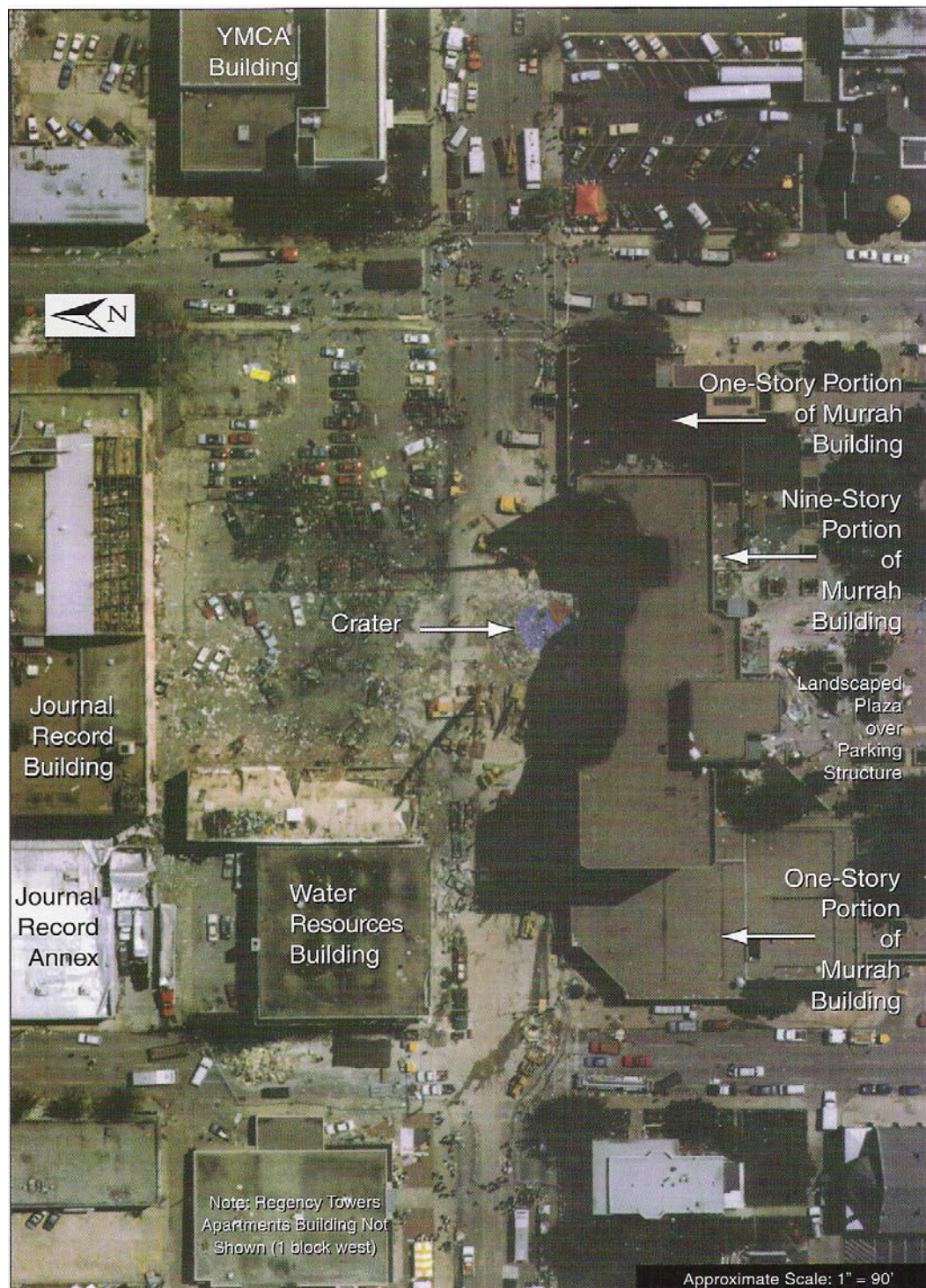


Figure 62: Aerial View Of Damaged Structures (FEMA 1996)



Figure 63: Damaged Structures In Vicinity (FEMA 1996)

The Federal Emergency Management Agency (FEMA) sent a Building Performance Assessment Team (BPAT) composed of American Society of Civil Engineers (ASCE) and federal government engineers to investigate the damage. The team concluded that some of the damage to the Murrah building was due to progressive collapse of the structure. The performance of the Murrah building indicated no needed increase in lateral load resistance, but rather special detailing would have been helpful such as recommended for earthquake resistance (FEMA, 1996).

5.3.1 MURRAH BUILDING COMPLEX DESIGN

The Murrah building complex was located in a city block bounded by Fifth Street, Fourth Street, Robinson Avenue and Harvey Avenue. The complex included a nine story office building along the north, a parking garage to the south, and one story structures to the east and west, as shown on Figure 65.



Figure 64: Murrah Building Prior To Blast (FEMA 1996)

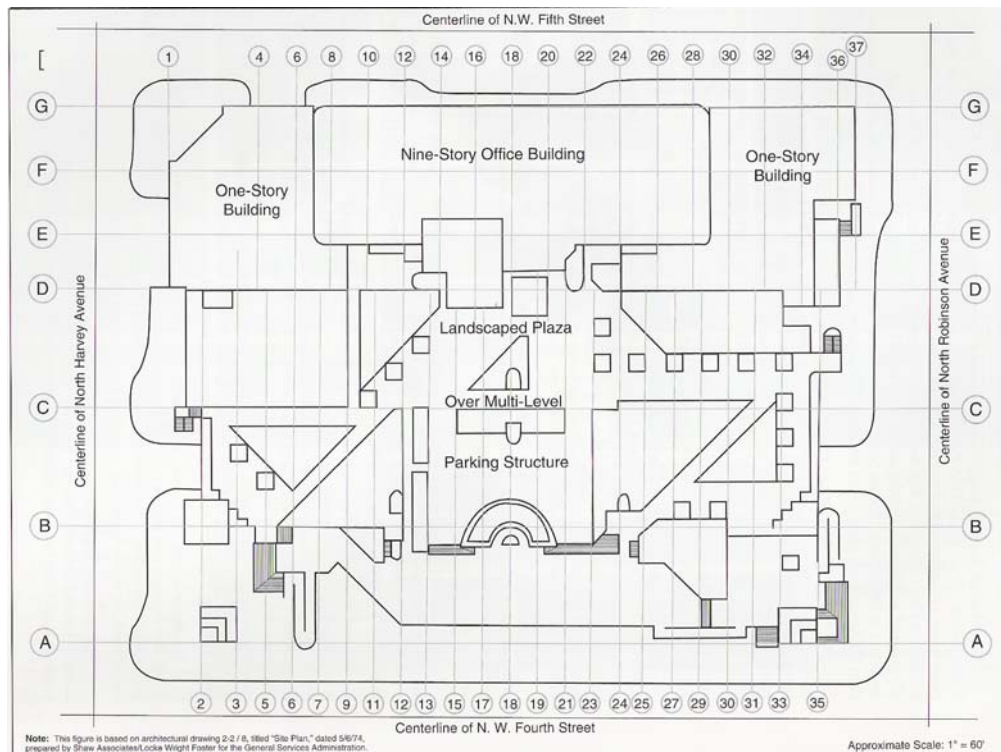


Figure 65: Murrah Building Complex Site Plan

The Murrah building was a nine-story office building designed as a conventionally reinforced cast-in-place concrete building. Along the north face, columns were not placed at grid coordinates G10, G14, G18, G20 and G24 through the use of transfer girders at the third floor level. This architectural feature decreased the number of columns along column line G at the street level by half. This feature, combined with the placement of the north exterior wall several feet to the south of column line G, created an alcove along the street, and exposed the remaining columns below the third floor elevation. This architectural feature can be seen on Figures 64 and 66.

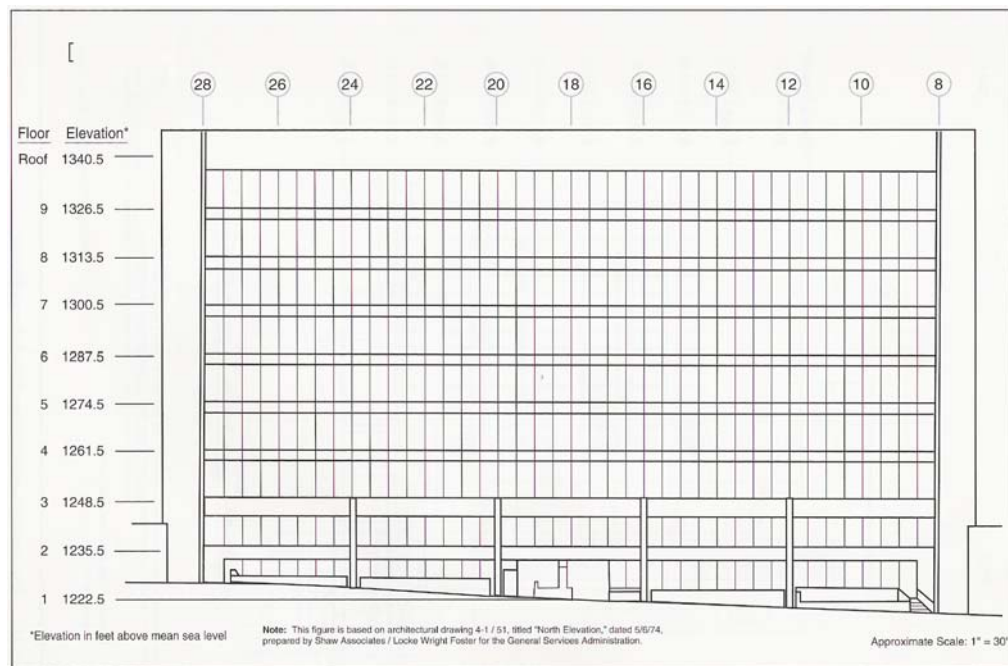


Figure 66: North Elevation Of Murrah Building (FEMA 1996)

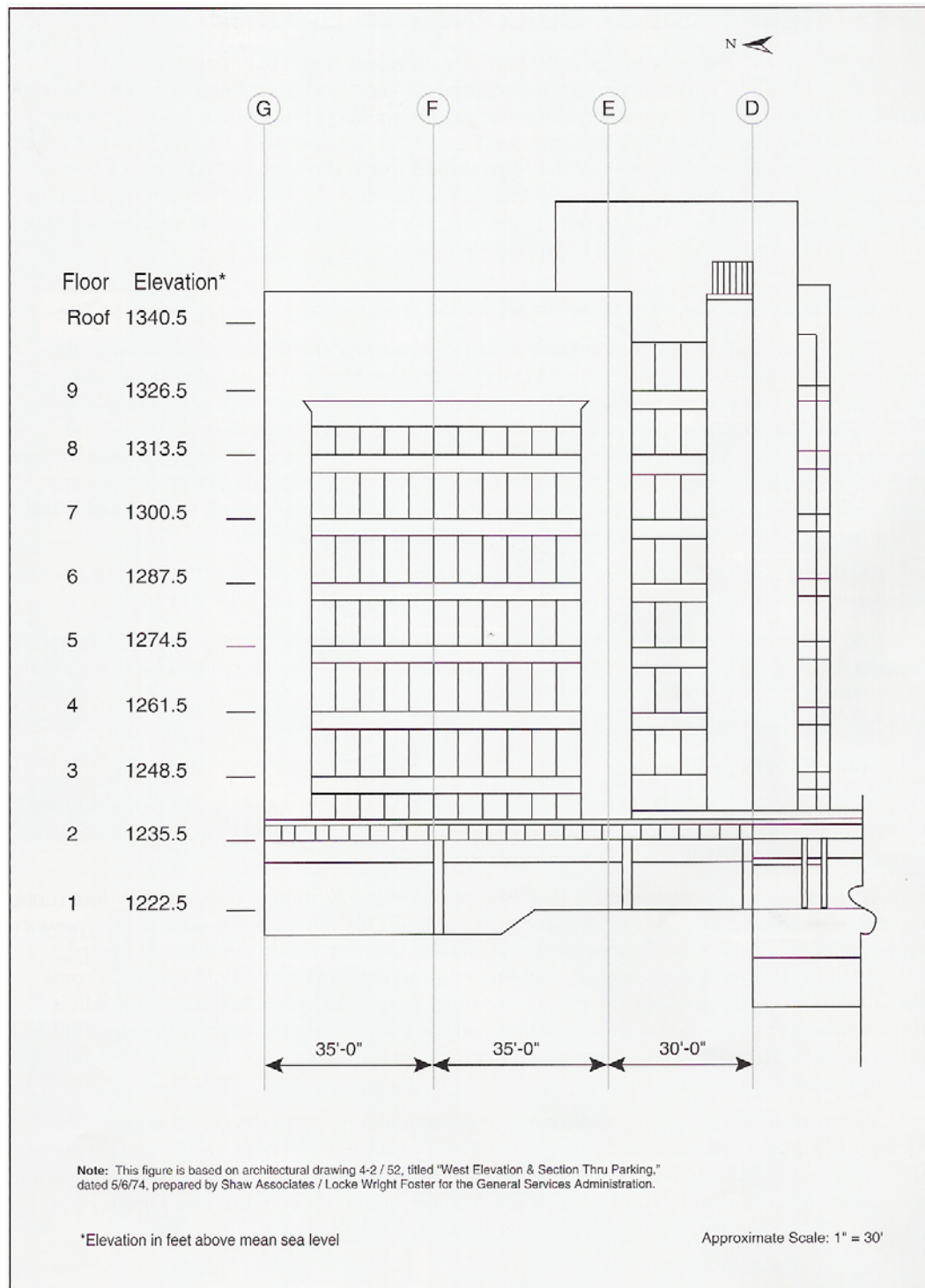


Figure 67: West Elevation Of Murrah Building (FEMA 1996)

The architectural plan consisted of ten 20-foot bays in the east-west direction and two 35-foot bays in the north-south direction, as seen in Figures 67 and 68. The floor consisted of one-way slabs which spanned in the east-west direction. Resistance to lateral and torsional displacements consisted of concrete shear walls located in the core area along the south side of the building, and in the air shafts at the four building corners. Building code provisions for this mid 70's structure, and lack of additional owner directives, resulted in wind forces controlling the design of the structure's lateral load resisting system.

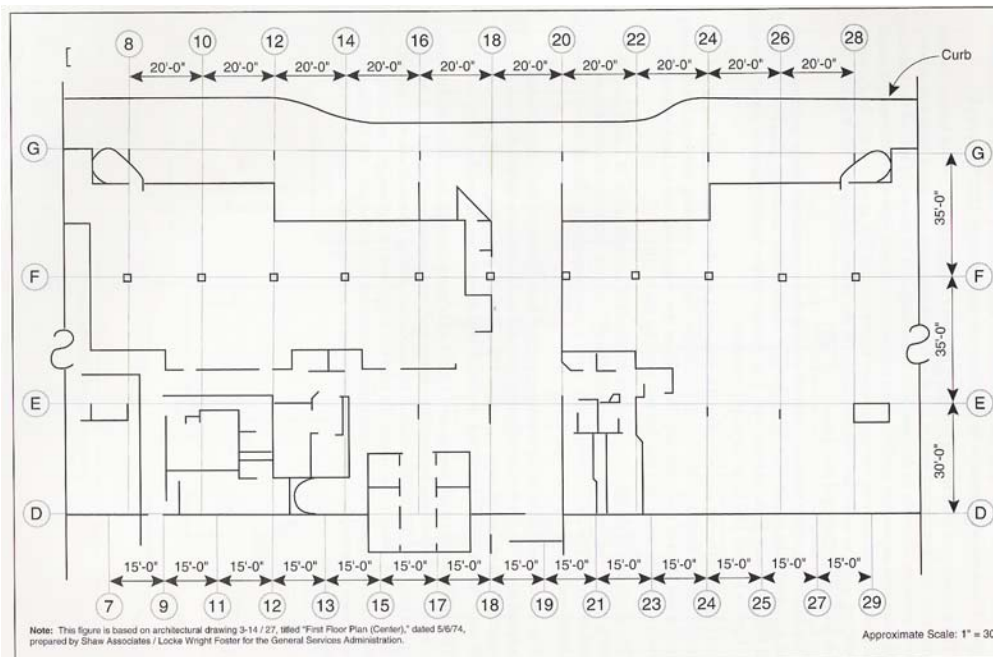


Figure 68: First Floor Plan Of Murrah Building (FEMA 1996)

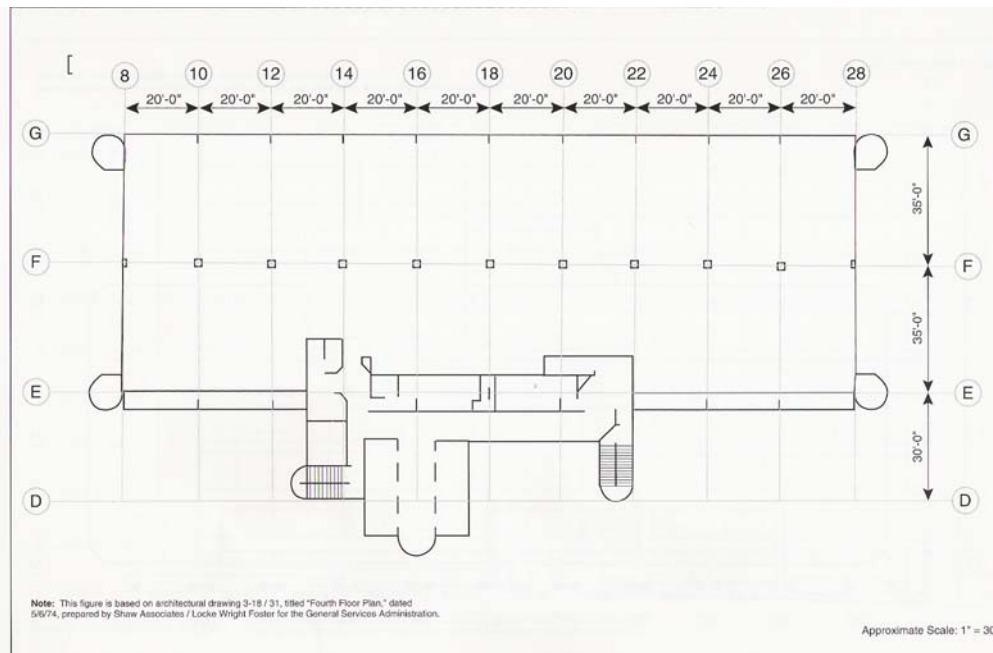


Figure 69: Fourth Thru Ninth Floor Plan Of Murrah Building (FEMA 1996)

5.3.2 BLAST WAVE FRONT PARAMETERS

The explosive was contained inside a truck parked adjacent the curb between grids 20 and 22, near column G20. From the size of the crater, the BPAT engineers estimated the quantity of explosive to be the equivalent of 4,000 pounds of TNT. The bomb crater is shown in Figures 70 and 71.

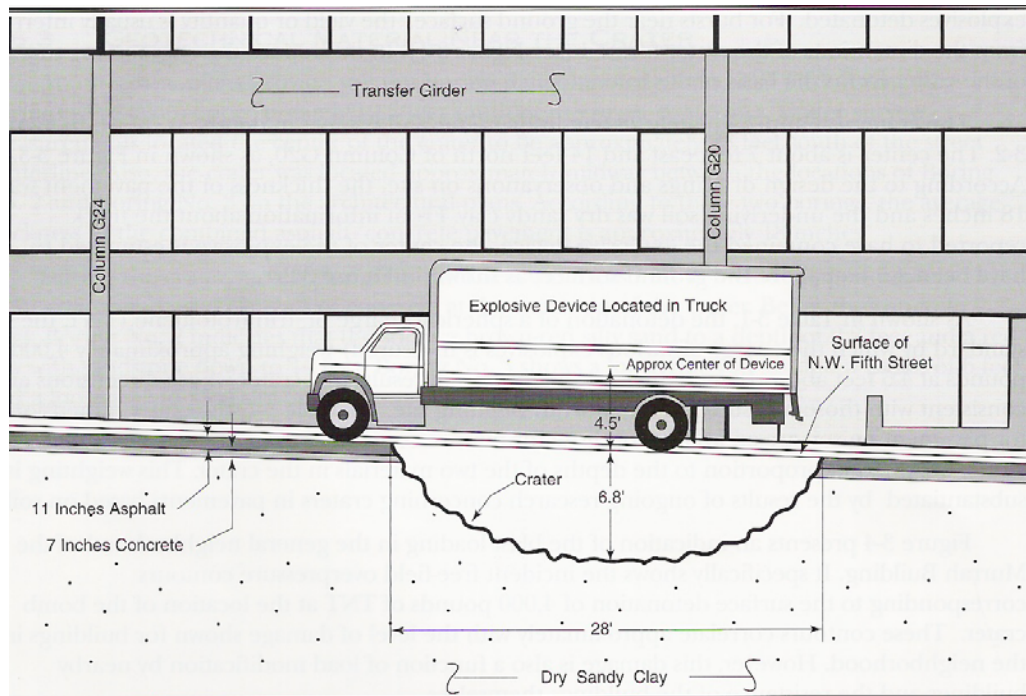


Figure 70: Location of Truck & Extent of Crater (FEMA 1996)



Figure 71: Bomb Crater Covered By Tarp (FEMA 1996)

Peak static overpressures (P_s), as shown in Figure 72, were estimated as 10,000 psi at the epicenter and 9 psi at the upper west corner. The duration of the positive pressure phase (T_s), as seen in Figure 73, was estimated at about 5 msec at the epicenter and 40 msec near the upper west corner. Peak overpressures at the adjacent structures are shown in Figure 74.

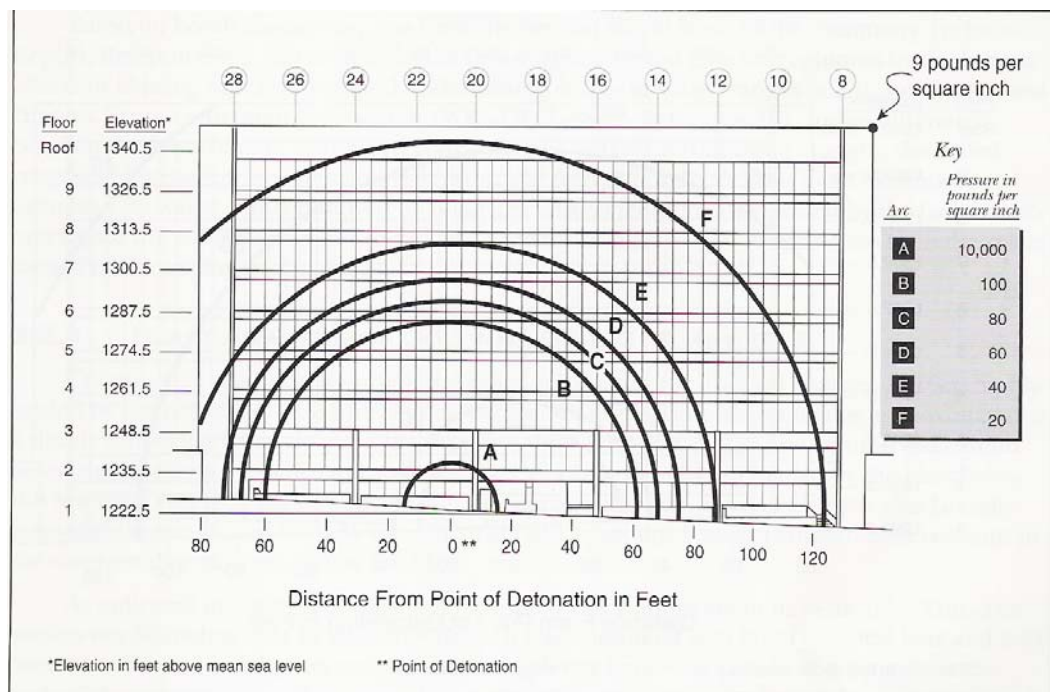


Figure 72: Peak Overpressures At North Elevation (FEMA 1996)

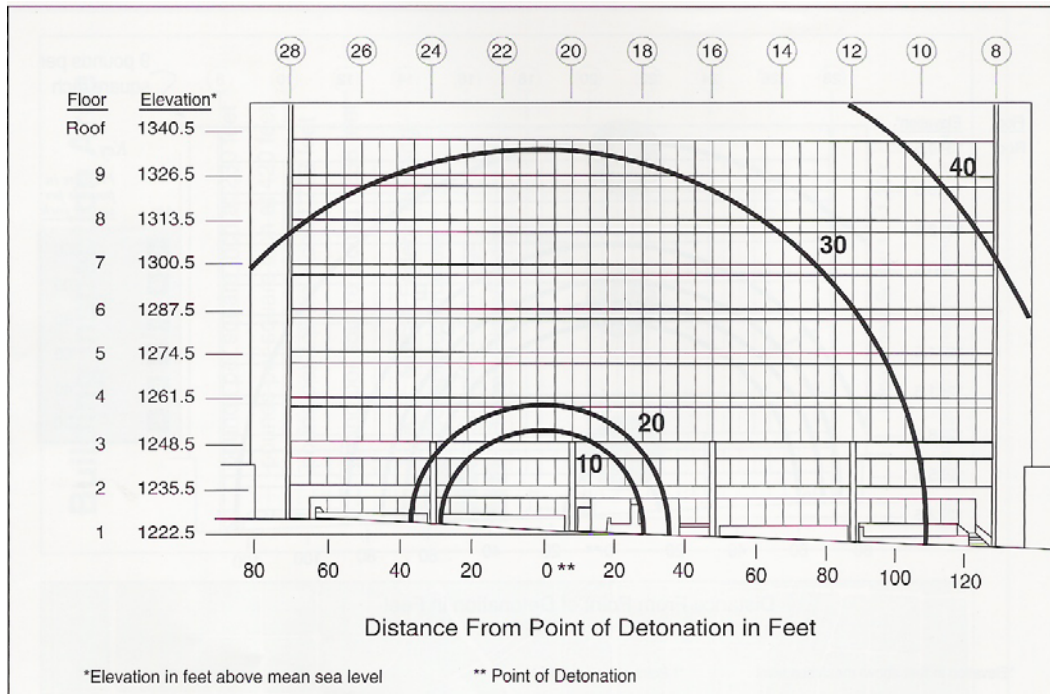


Figure 73: Positive Phase Duration At North Elevation (FEMA 1996)

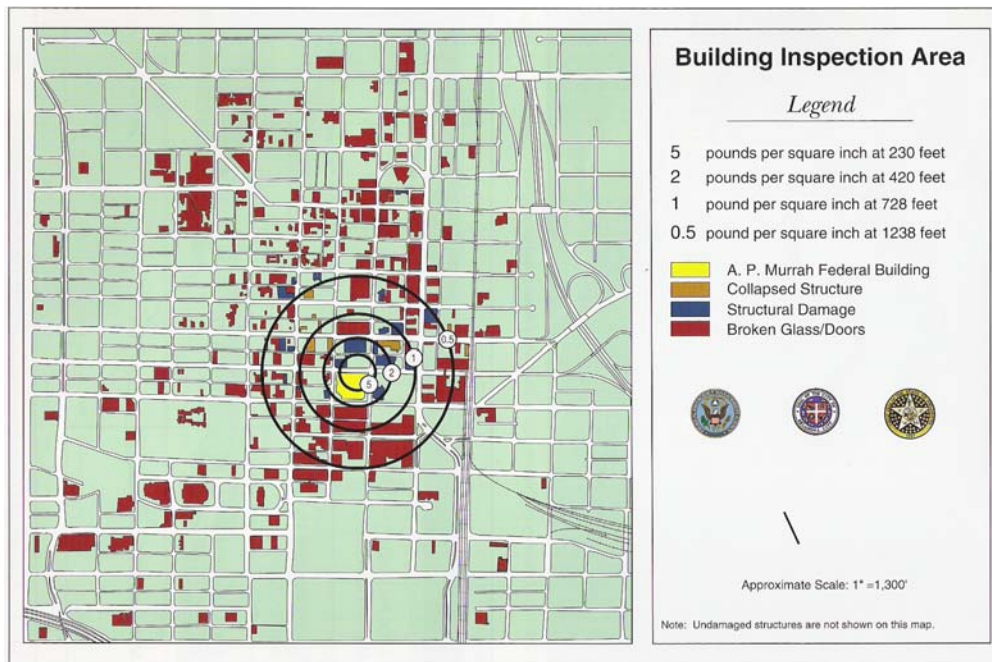


Figure 74: Peak Overpressures In Blast Vicinity (FEMA 1996)

5.3.3 BLAST EFFECTS TO STRUCTURE

Column G20 was determined by the BPAT engineers to have been destroyed by brisance from the direct effects of the blast. Column G12 was determined to have failed as a result of progressive collapse as the third floor transfer girder failed. Columns G24 and G16 could have failed either due to progressive collapse or the direct effects of the blast. Damage along column Line G is shown in the photo in Figure 76.

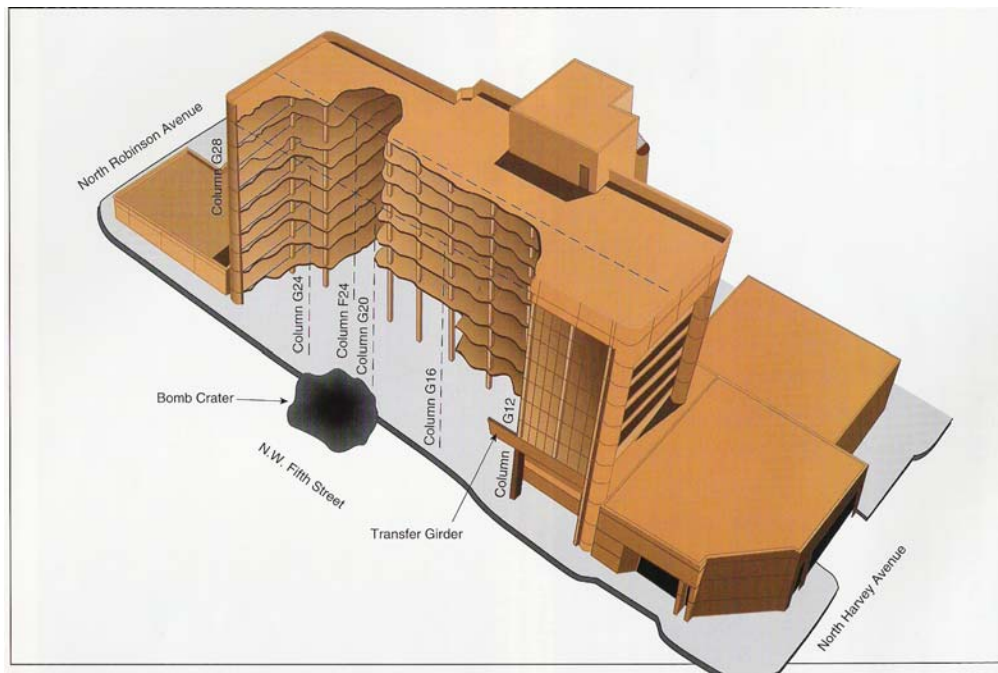


Figure 75: Failure Extent In Murrah Building (FEMA 1996)

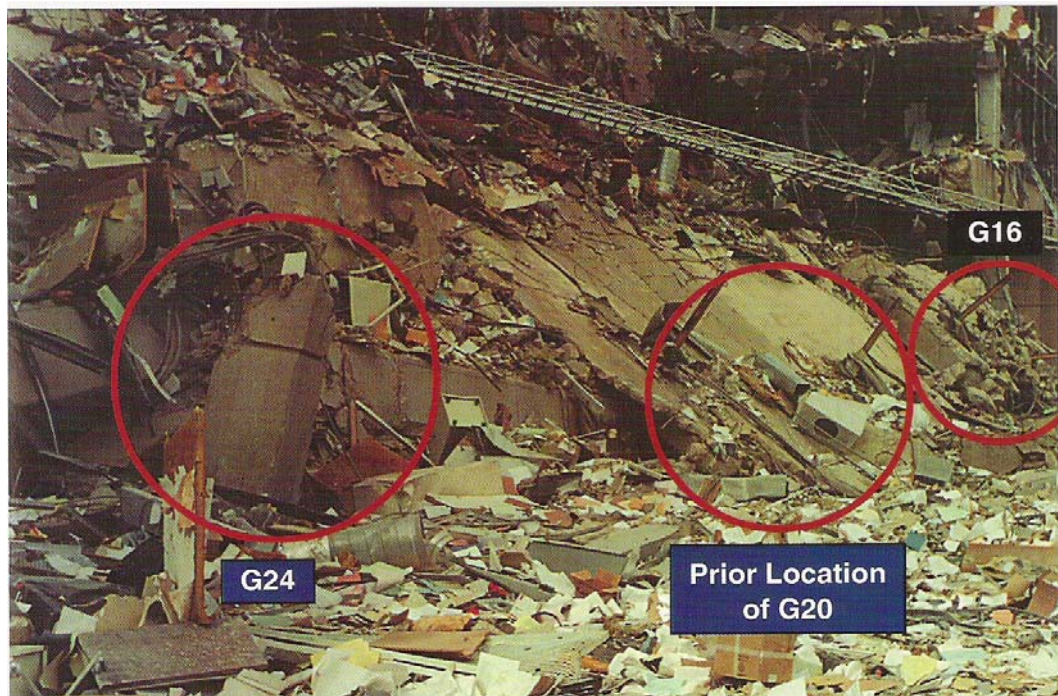


Figure 76: Damage At Column Line G (FEMA 1996)

The north façade consisted of glass and aluminum panels that offered little resistance to the blast effects. The floor slabs near the north face were directly loaded by the blast. The slabs were loaded by overpressures on both the top and bottom surfaces. The additional distance and time required for the blast wave front to reach the top surface as compared to the bottom surface, resulted in a net uplift pressure as shown in Figure 77.

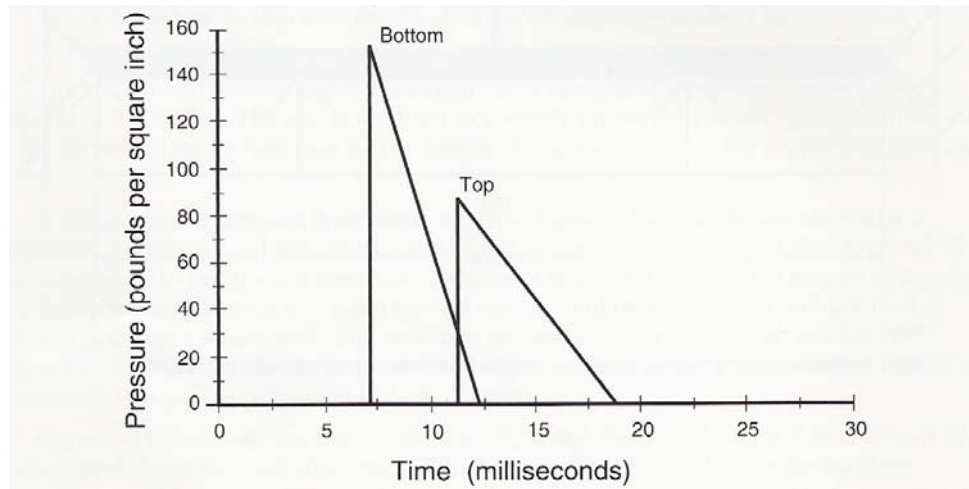


Figure 77: Blast Load Fifth Floor Slab Between Grid 20 & 22 (FEMA 1996)

The BPAT engineers analyzed the loading condition as a static uniform pressure load on a simply supported floor slab element of unit width and spanning east-west between floor beams (see Figure 78). The deflection caused by the impulsive loading was estimated at over 9 inches for the fifth floor slab in bay F-G/20-22 as shown in Figure 79.

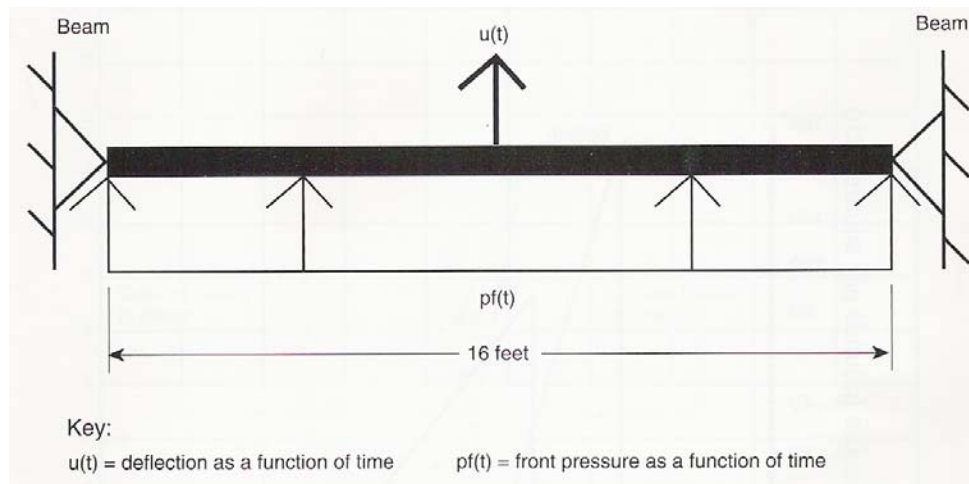


Figure 78: Model Of Floor Slab Used By BPAT Engineers (FEMA 1996)

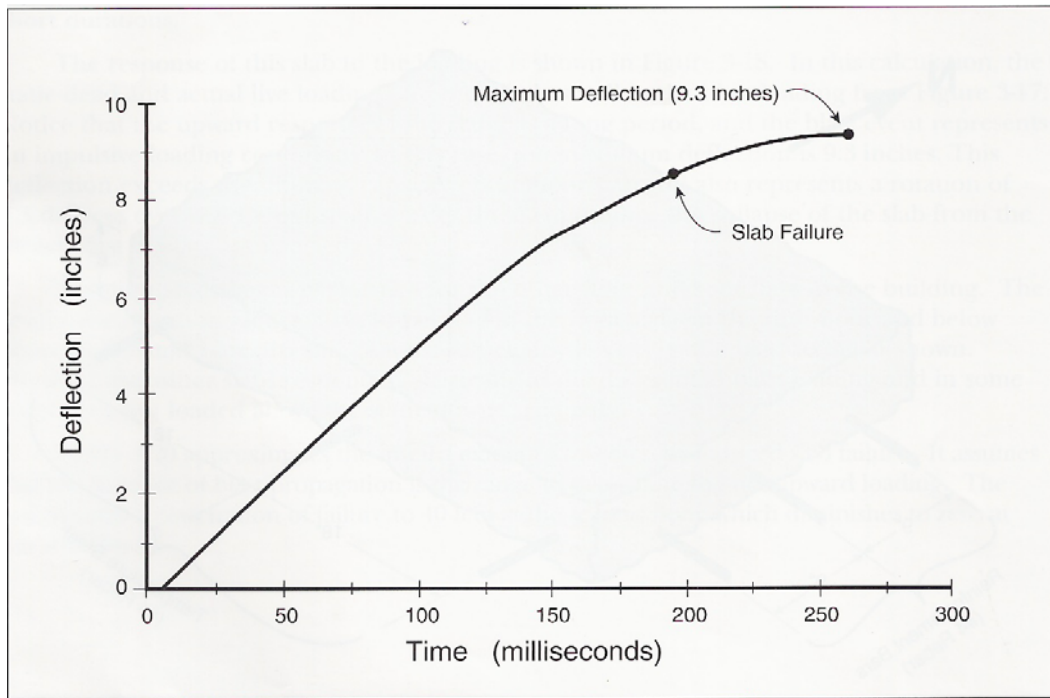


Figure 79: Fifth Floor Slab Response Predicted By BPAT (FEMA 1996)

The floor slab reinforcing consisted of temperature steel in the north-south direction, and flexural steel in the east-west direction. Flexural steel consisted of top steel over the supports and bottom steel at midspan. Neither the top steel nor the bottom steel was continuous. The floor slab was vulnerable to load reversals due to the discontinuity in the flexural steel. The positive moment and temperature reinforcing steel used in the analysis by the BPAT engineers is as shown in Figure 80.

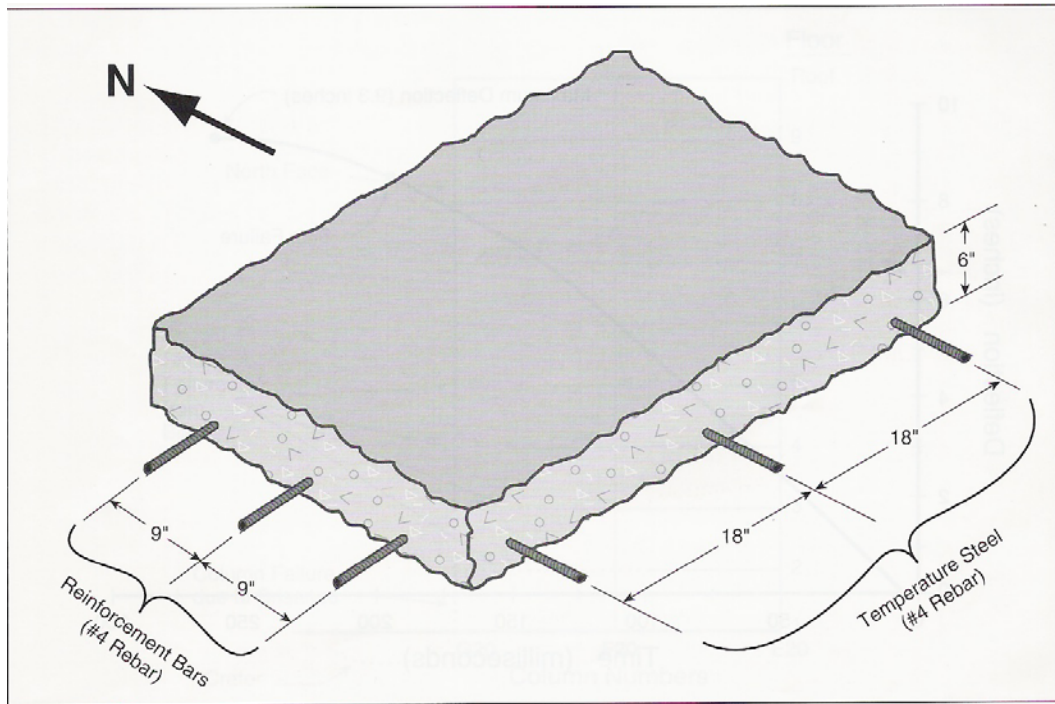


Figure 80: Floor Slab Reinforcement (FEMA 1996)

The extent of floor slab failure estimated by the BPAT engineers is shown in Figures 81 and 82. The floor slabs at the north perimeter that were expected to fail include the fifth floor slabs and below located between grid lines 18 and 24. The second floor slabs were estimated to fail up to a distance of 40 feet inside the building, while the sixth floor slabs were expected to survive.

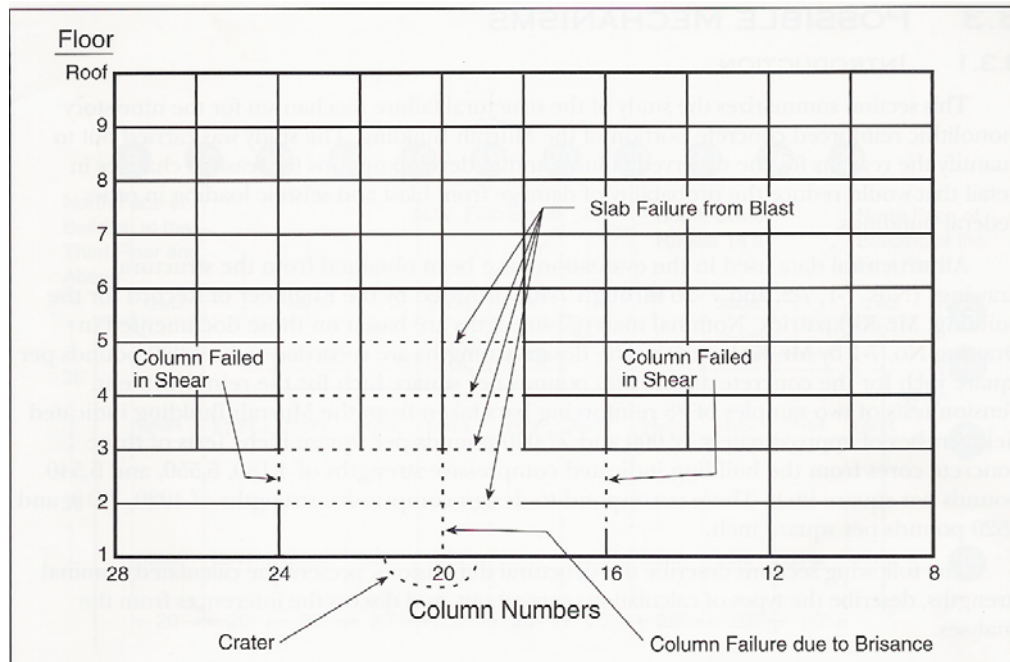


Figure 81: Slab Damage Predicted By BPAT North Elevation (FEMA 1996)

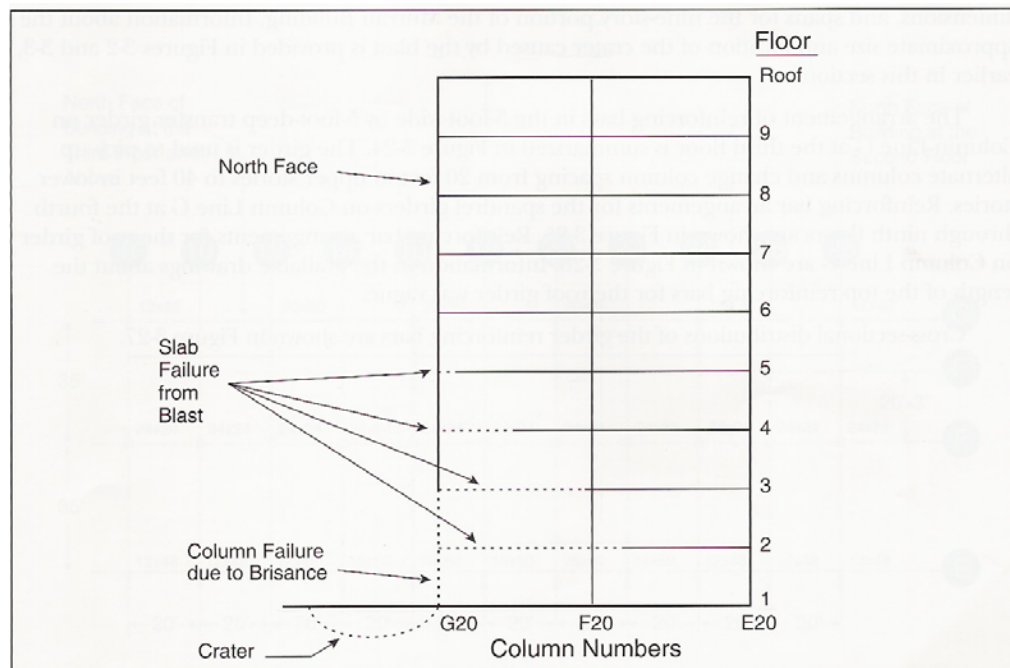


Figure 82: Extent Of Slab Damage Predicted By BPAT (FEMA 1996)

5.4 MURRAH BUILDING FIFTH FLOOR SLAB FEM ANALYSIS

The geometry, loading condition and material properties used for the reinforced concrete slab that was analyzed in this research were based on the actual conditions present in the Murrah building.

5.4.1 GEOMETRY OF FIFTH FLOOR SLAB

The two sketches in Appendix I show the framing system of the bay of interest, i.e. the fifth floor slab located in bay F-G/20-22. The floor slab modeled in this research consists of a 16 feet, 0 inches by 33 feet, 6 inches by 6 inch thick concrete slab reinforced with mild steel. The slab was fixed along the longer edges by imposing zero translations for all three degrees of freedom at the nodes along these two edges. The reinforcement is located as described in the reference FEMA, 1996. The flexural steel and the temperature steel used are #4, Grade 60 bars. The steel spacing, bar length and placement location are shown in Appendix I.

A 3D solid element mesh was used for the concrete slab. TeraDyn's steel reinforcement element was used to mesh the reinforcing steel. Reinforcing steel was modeled as a sub-element within the 3D solid concrete element. Strain compatibility was assumed between concrete and rebar, and no provision was made for bond slip between the reinforcing steel and concrete.

TeraScale provides a rebar generation capability that allows the analyst to place discrete rebar in the exact location that they are detailed in the physical structure. The rebar generator automatically computes the penetration by the rebar into the solid concrete 3D 8 node brick elements. A solid concrete element may have any number of rebar penetrating through it. This capability allows the user much more flexibility in designing the mesh. There is no need for the rebar to follow mesh lines as in the ANSYS model.

The floor system in the Murrah building was a 6 inch thick concrete one-way floor slab supported continuously along the edges by floor girders. The floor slab spanned in the east-west direction, i.e. from grid 20 to 22. The floor slabs had a clear span between floor girders of 16 feet, 0 inches. The floor girders were supported on each end by columns, and spanned from grids F to G. Along the exterior north wall at grid G, a spandrel beam was located at floors four through nine. The transfer girder was used at the third floor.

5.4.2 MESH CONFIGURATIONS

Three mesh configurations were used in the analysis. The mesh size used is 6 inches by 6 inches in the plane of the floor slab. Three mesh sizes were used through the 6 inch slab thickness; 3 elements, 6 elements and 12 elements. The mesh for the slab is shown in Figure 83. The bottom flexural steel, the top

flexural steel along the near edge of the slab, and the temperature steel are shown in Figures 84, 85, and 86, respectively. The top and bottom flexural steel consisted of alternating long and short bar lengths. Only the shorter bar lengths are shown in the figures.

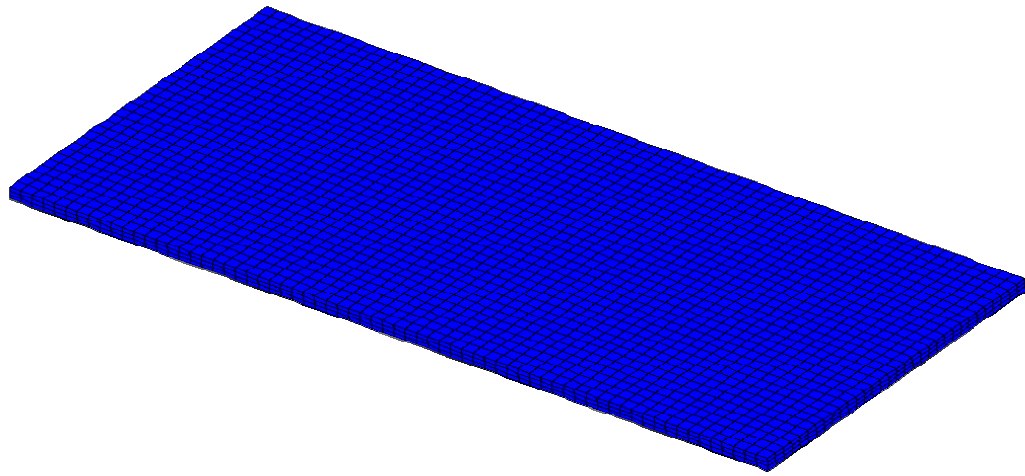


Figure 83: Murrah Fifth Floor Slab Mesh, 3 elements thick

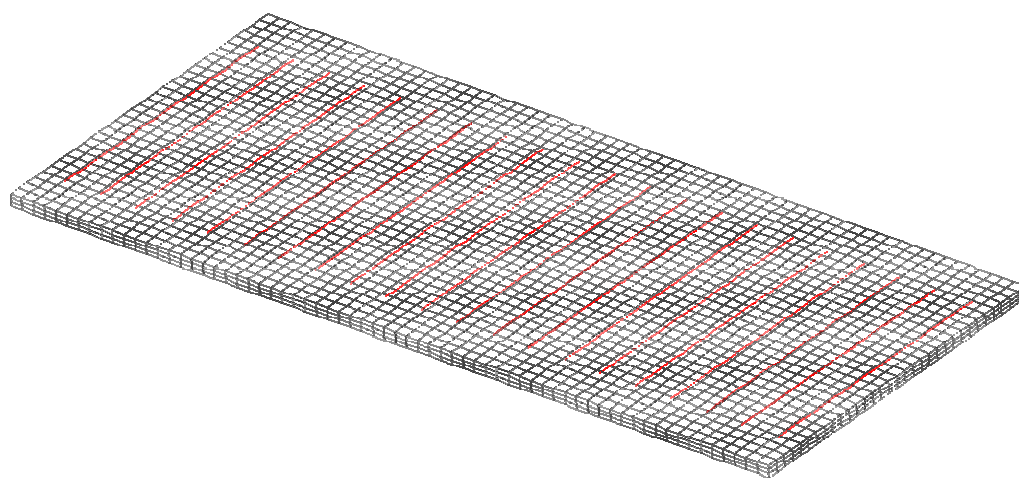


Figure 84: Murrah Slab Positive Moment Steel Mesh

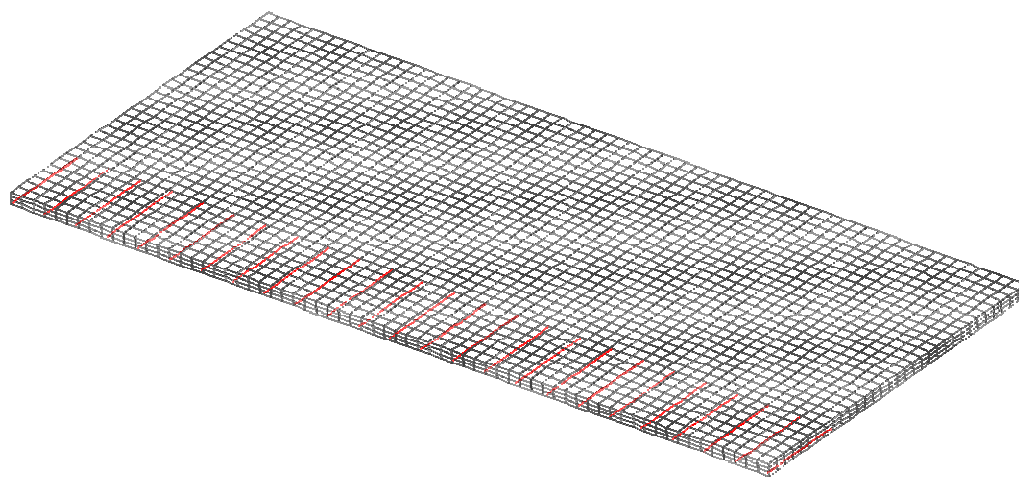


Figure 85: Murrah Slab Near Edge Negative Moment Steel Mesh

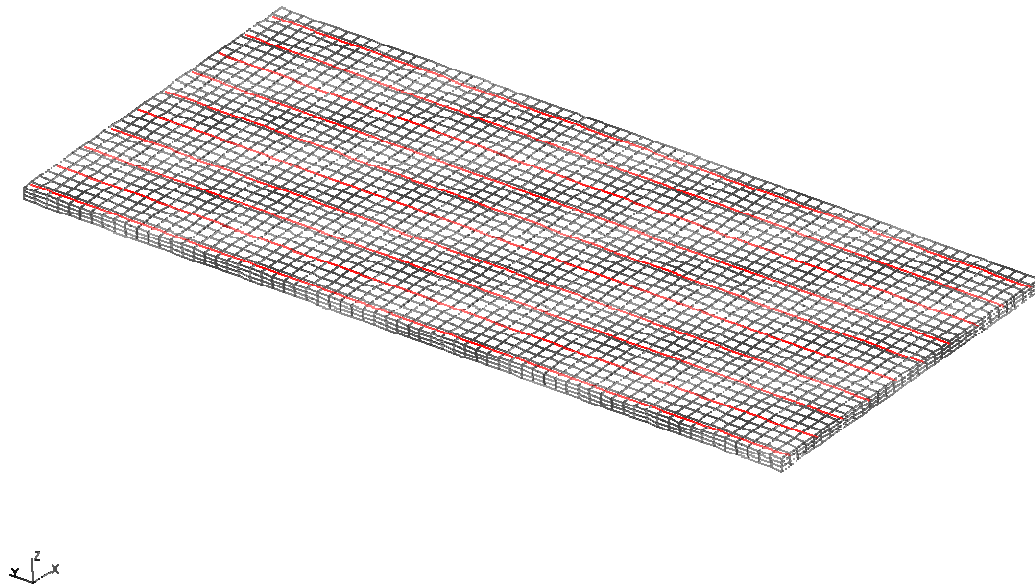


Figure 86: Murrah Slab Temperature Steel Mesh

5.4.3 MATERIAL PROPERTIES OF MURRAH SLAB

A highly nonlinear constitutive model which includes the strain softening region was used for the concrete material, as shown in Figure 46. The strain hardening ANATECH Corporation's ANAMAT constitutive model for concrete was used in TeraScale's TeraDyn FEM software for the 3D solid concrete elements. As mentioned previously in section 2.7.3, the ANAMAT constitutive model for concrete is based on smeared cracking methodology and J_2 plasticity theory (ANATECH Corp., 1998). The material nonlinearity is treated at the finite element integration points, thus the cracking and stress/strain state can vary within an element. Cracks form perpendicular to the principal strain direction, and cracking can form in three orthogonal directions. The tensile stress normal to the

crack is reduced to zero, and the stresses around the crack are redistributed. Shear stiffness is reduced upon cracking, and decreases further as cracks open. Crack directions remain fixed, i.e cracks can close but cannot “heal”.

Concrete material properties used are a concrete compressive strength of 4.0 ksi, an elastic modulus of 3,545 ksi, a Poisson’s constant of 0.18, a concrete strain at maximum compressive stress of 0.0022, and a tensile cracking strain of 0.000050.

The constitutive model for the steel characterizes the strain hardening behavior of mild steel. A bilinear stress-strain curve was used for the conventional reinforcing steel. The linear elastic portion of the curve extends to a yield strength (σ_y) of 60.0 ksi, with a modulus of elasticity (E_s) of 30,000 ksi. The linear strain hardening portion extends to 120 ksi at an equivalent plastic strain of 1.0. A Poisson’s ratio of 0.30 was used.

5.4.4 LOADING CONDITION OF MURRAH SLAB

A moving pressure load was applied to the concrete slab to replicate the wave front produced by the blast at the Murrah building. The applied loading approximates the pressure wave front produced by the blast from the 4,000 pounds of TNT. An analysis of the blast wave front parameters is contained in Appendix I. The peak static overpressure (P_s) ranges from a maximum of 80 psi

at the north edge nearest the blast epicenter to 36 psi at the south edge. The time of arrival (t_a) is 9 msec at the north edge and 13 msec at the south edge. The positive phase duration (T_s) is 24 msec. Therefore, the magnitude of the overpressure at the south edge is only about 37.5 percent of the value at the north edge, while the positive phase duration is about the same.

The blast wave front applied to the floor slab in this analysis is as shown in Figures 87 and 88. For clarity in this discussion, these figures show a magnitude of unity for the peak static overpressure at time zero and distance zero. In the analysis, a scale factor was applied to these values to represent the actual loading condition for the Murrah floor slab.

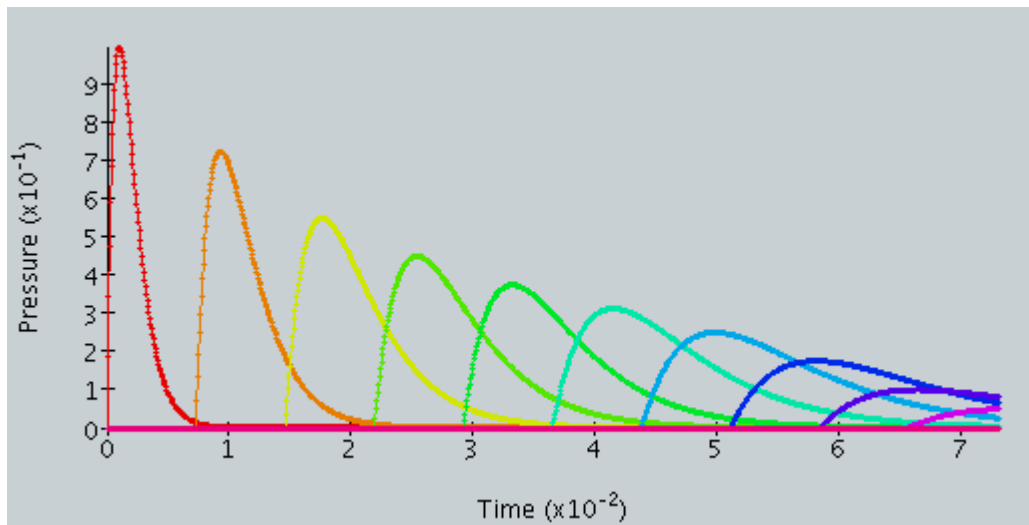


Figure 87: Pressure-Time Curve For Blast Wave Front (psi, sec)

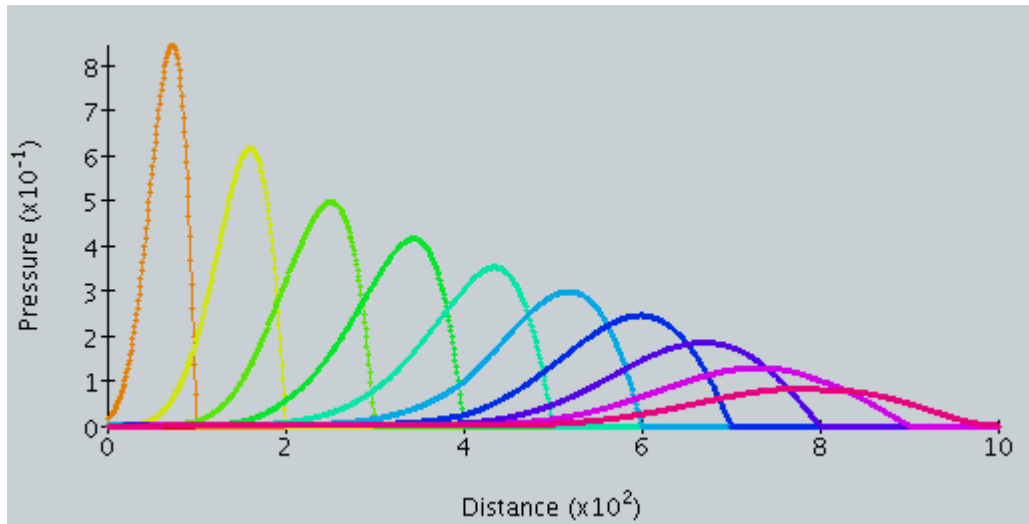


Figure 88: Pressure Distance Curve For Blast Wave Front (psi, inch)

The north edge is nearest the blast epicenter and is subjected to the blast effects first. The pressure pulse is roughly triangular with an initial magnitude of unity and duration of about 5 msec. This compares well with the impulse shown in Figure 77, which was used by the BPAT engineers in their analysis. The magnitude of the overpressure at the south edge, a distance of 402 inches from the north edge, is about 37.5 percent that at the north edge. The pressure pulse at the south edge is also nearly triangular in shape with about 10 msec duration. This compares well with the analysis in Appendix J.

From Figures 87 and 88, the blast wave reaches the south edge about 40 msec after reaching the north edge, which is longer than the 4 msec expected by the analysis in Appendix J. This difference arises from the moving pressure load model used in this analysis. The difference in the 4 msec expected time

difference and the 40 msec modeled in this analysis will influence the response of the slab to the dynamic loading.

5.5 MURRAH SLAB FEM RESULTS

Table 4 and Table 5 summarize the results of the Murrah fifth floor slab analyses. Table 4 depicts the data from analyses where the loading was applied to the bottom of the slab, producing a negative moment at midspan. Table 5 shows the data from the analyses where the loading was applied to the top of the slab. As shown in the left portion of the tables, five magnitudes of peak pressure loading were applied to three mesh configurations. The peak pressure loading values used are 1 psi, 3 psi, 5 psi, 10 psi and 20 psi. The mesh configurations are the 3, 6 and 12 element thick meshes. At the lower 1 psi peak pressure loading condition, the deflections are about 0.05 inches for the 6 and 12 element thick meshes, and about twice that for the 3 element thick mesh.

Only six of the fifteen negative moment analyses ran the entire 50 msec time duration, as shown in Table 4. Four of these six analyses are the 1 psi, 3 psi, 5 psi and 10 psi peak pressure loadings for the 3 element mesh. The other two analyses are the 1 psi peak pressure load case for the 6 and 12 element meshes. The analyses that did not run the entire 50 msec time duration are indicated in bold, and the time the analyses terminated is shown on the right portion of the table. To determine if an analysis would run the entire 50 msec duration at a

slightly lower peak pressure, an additional analysis was performed on the 6 elements thick mesh at 2 psi peak pressure. This additional analysis also terminated before the end of the 50 msec duration, at 34 msec.

MURRAH SLAB IMPULSE LOAD-DEFLECTION RESPONSE NEGATIVE MOMENT APPLIED TO POSITIVE MOMENT SECTION						
PEAK PRESSURE (psi)	FEA RESULT Elements Thru Depth					
	deflection (inches)			time step at termination (msec)		
	3 elem	6 elem	12 elem	3 elem	6 elem	12 elem
1	0.11	0.05	0.04			
2		0.06			34	
3	0.33	0.08	0.08		29	29
5	0.59	0.13	0.12		25	20
10	1.35	0.23	0.19		15	15
20	0.70	0.24	0.05	23	13	7
Note: Bold indicates run terminated as element "failed" before 50msec duration one way floor slab with 192" span with fixed ends and 402" bay width 6" slab reinf. w/ 0.27insq/ft width @ d=5" bottom steel & top steel reinf. 0.30insq/ft width @ d=5" & top temperature steel reinf. 0.135insq/ft width @ d=4.5" 4ksi concrete, Grade 60 steel 75psf/g slab mass Note: Gravity neglected in impulse load & deflection computation						

Table 4: Murrah Slab Impulsive Load Negative Moment Results

Only five of the fifteen positive moment analyses ran the entire 50 msec time duration, as shown in Table 5. Three of these five analyses are the 1 psi, 3 psi and 10 psi peak pressure loadings for the 3 element mesh. The other two

analyses are the 1 psi peak pressure load case for the 6 and 12 element meshes. The analyses that did not run the entire 50 msec time duration are indicated in bold, and the time these analyses terminated is shown on the right portion of the table. An additional analysis was performed on the 6 elements thick mesh at 2 psi peak pressure. This additional analysis also terminated before the end of the 50 msec duration, at 32 msec.

MURRAH SLAB IMPULSE LOAD-DEFLECTION RESPONSE POSITIVE MOMENT APPLIED TO POSITIVE MOMENT SECTION						
PEAK PRESSURE (psi)	FEA RESULT Elements Thru Depth					
	deflection (inches)			time step at termination (msec)		
	3 elem	6 elem	12 elem	3 elem	6 elem	12 elem
1	0.11	0.05	0.04			
2		0.05			32	
3	0.31	0.08	0.07		29	29
5	0.28	0.10	0.09	35	18	18
10	1.20	0.03	0.10		10	12
20	0.27	0.06	0.05	12	8	6
Note: Bold indicates run terminated as element "failed" before 50msec duration one way floor slab with 192" span with fixed ends and 402" bay width 6" slab reinf. w/ 0.27insq/ft width @ d=5" bottom steel & top steel reinf. 0.30insq/ft width @ d=5" & top temperature steel reinf. 0.135insq/ft width @ d=4.5" 4ksi concrete, Grade 60 steel 75psf/g slab mass Note: Gravity neglected in impulse load & deflection computation						

Table 5: Murrah Slab Impulsive Load Positive Moment Results

The analyses that did run to the end of the 50 msec analysis time duration terminated when at least one element Jacobian became zero, i.e the solution resulted in an element being subjected to a deformation that is not physically possible. The code is under development, and an element “death” option is being added to the code to allow the analysis to proceed beyond such conditions.

Figures 89 through 98 show the progression of deformation through time for the Murrah fifth floor slab. The analysis duration is 50 msec, with ten 5 msec substeps for data recording. Each figure represents the deformation at the end of a time substep. The blast epicenter is located at a point 36 inches nearer the viewer along an axis parallel to the long dimension of the slab. At time zero, the blast wave front has just reached the slab at its right short edge. The blast wave impinges on the underside of the slab, moving from right to left, along the axis parallel to the long dimension of the slab. The analysis results shown are for the 10 psi peak pressure loading on the 3 element thick mesh. Deflection is magnified by 10.

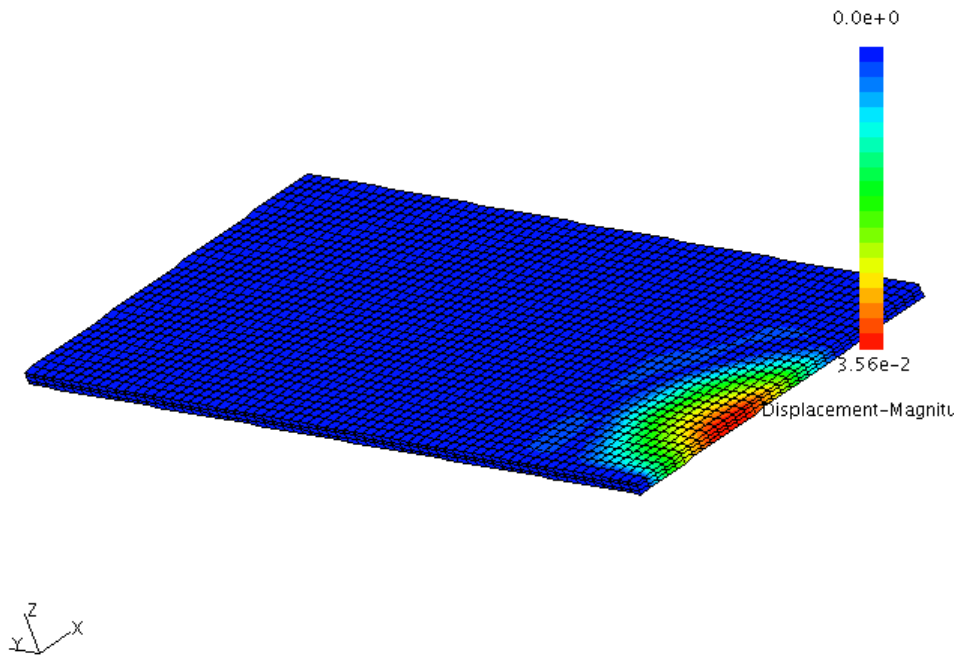


Figure 89: Murrah Slab Deflected Shape At 5 msec

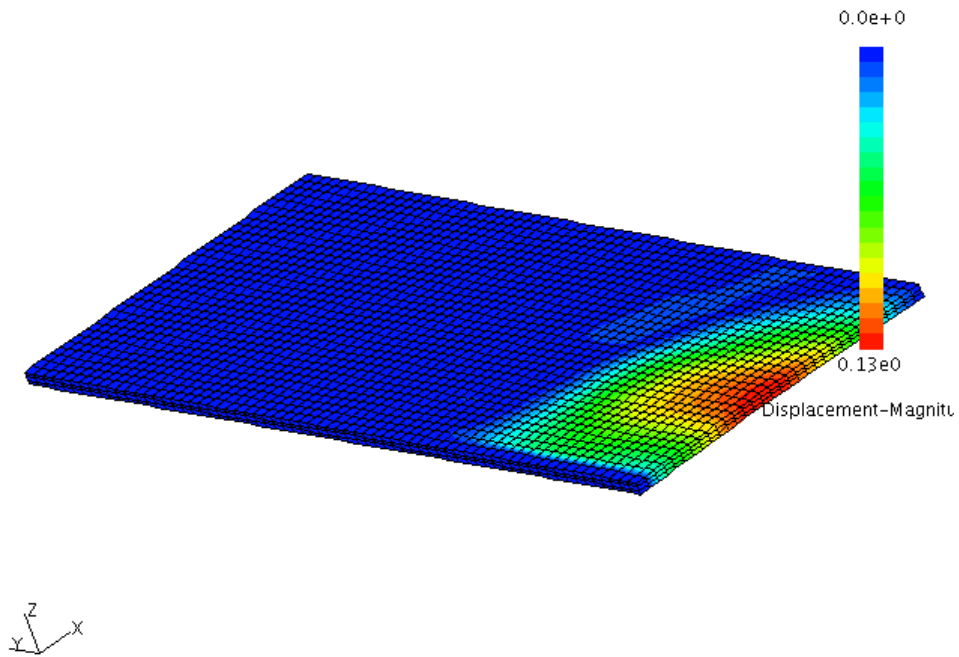


Figure 90: Murrah Slab Deflected Shape At 10 msec

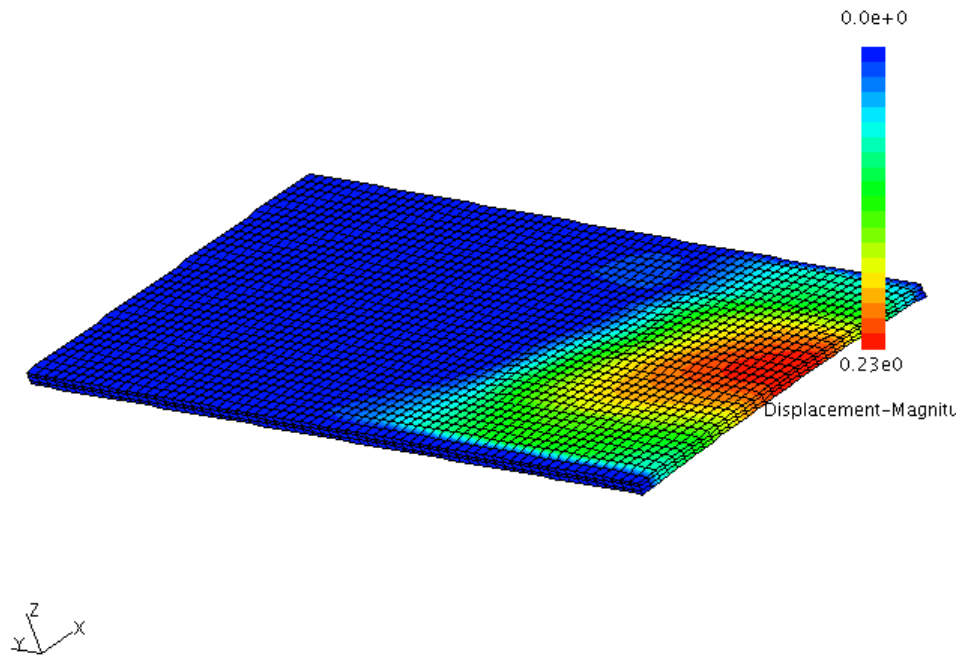


Figure 91: Murrah Slab Deflected Shape At 15 msec

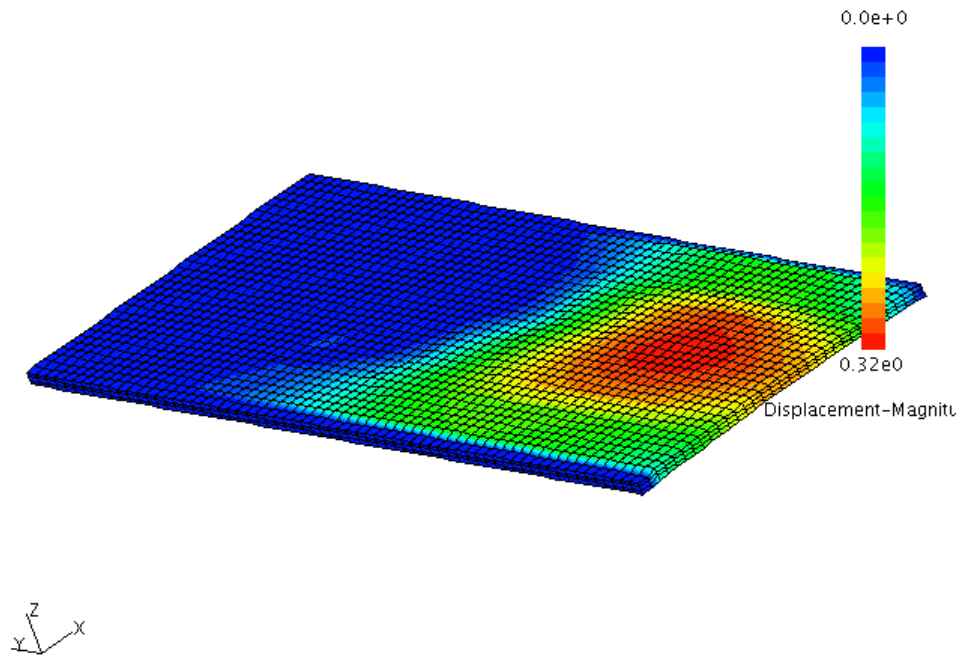


Figure 92: Murrah Slab Deflected Shape At 20 msec

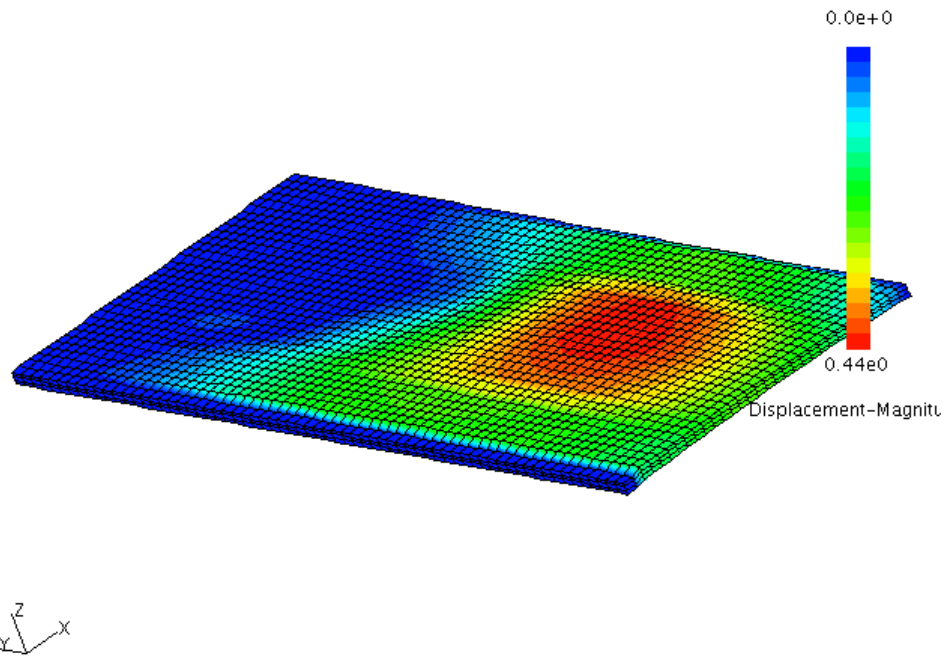


Figure 93: Murrah Slab Deflected Shape At 25 msec

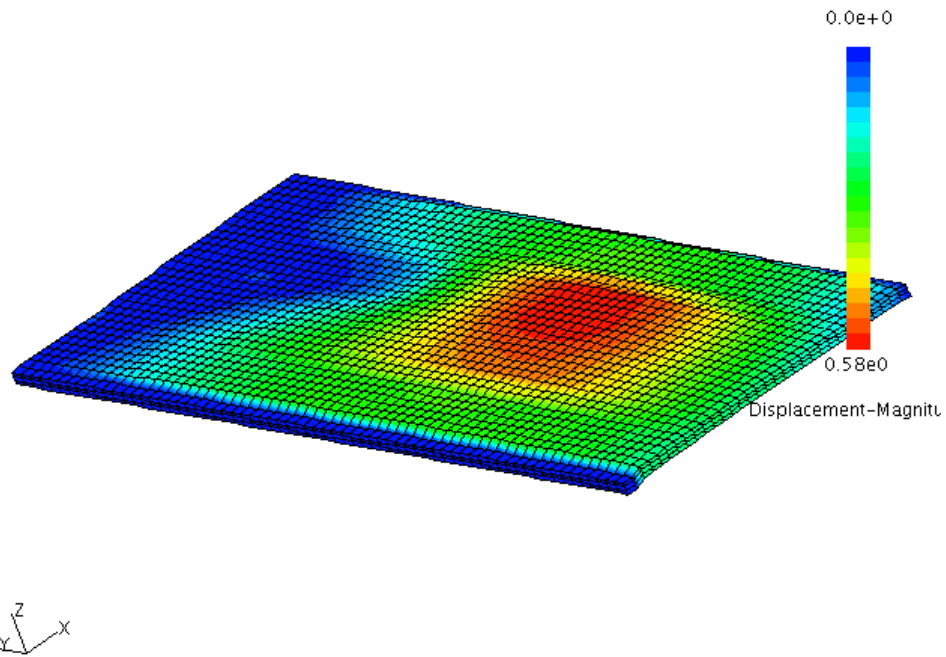


Figure 94: Murrah Slab Deflected Shape At 30 msec

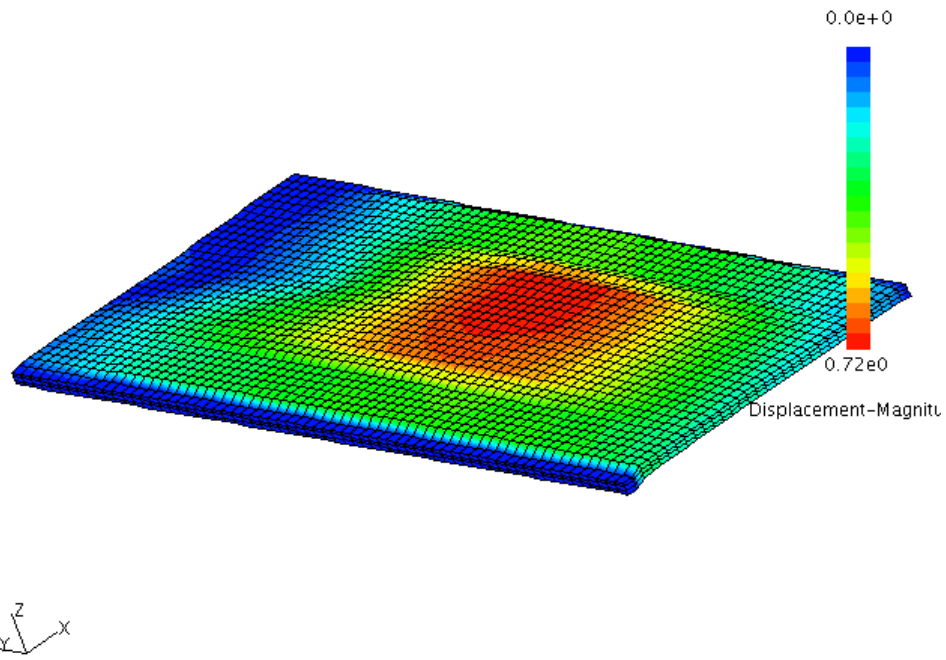


Figure 95: Murrah Slab Deflected Shape At 35 msec

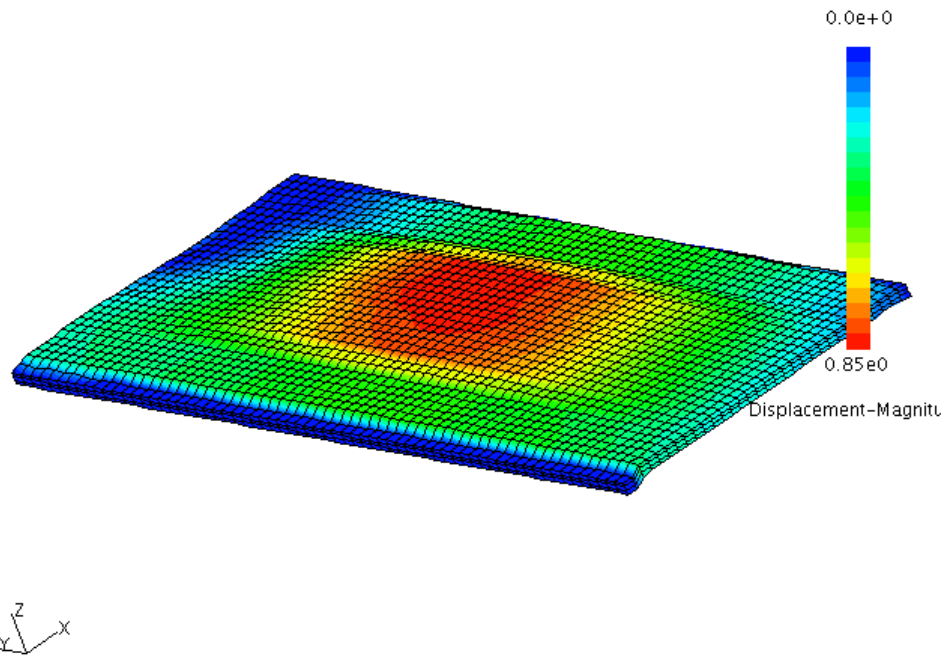


Figure 96: Murrah Slab Deflected Shape At 40 msec

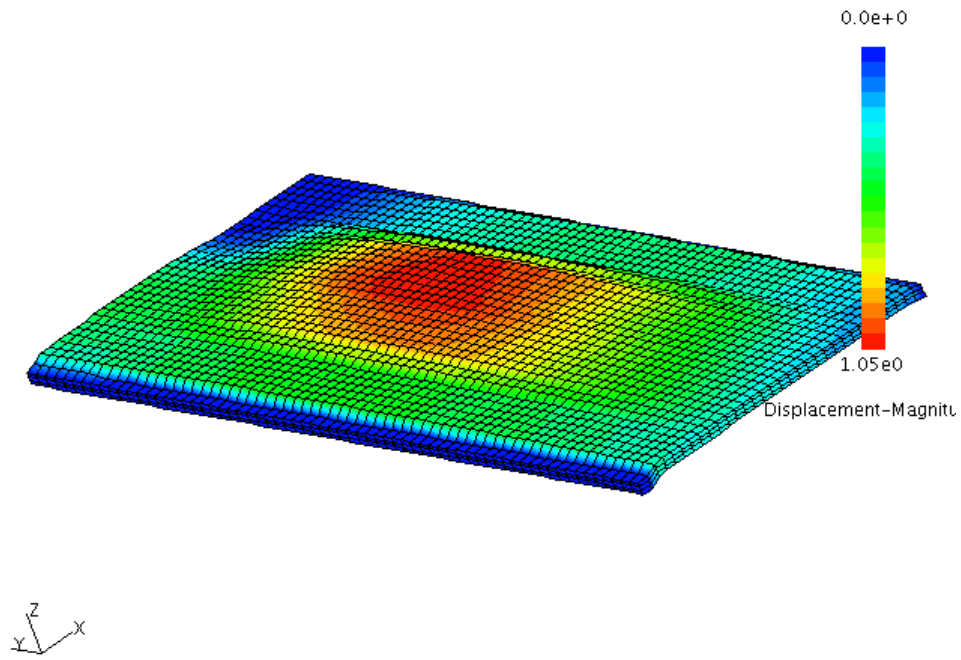


Figure 97: Murrah Slab Deflected Shape At 45 msec

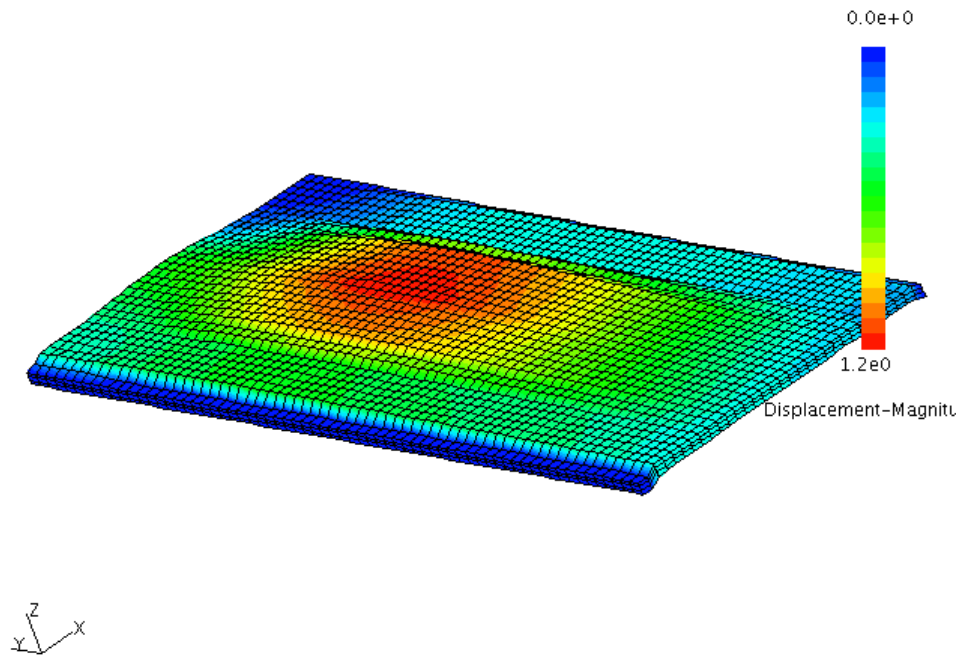


Figure 98: Murrah Slab Deflected Shape At 50 msec

Figures 99 through 108 show the crack progression through time for the Murrah fifth floor slab. The cracking initiates at the fixed end of the slab nearer the epicenter of the blast wave front. A region of high tensile flexural stress propagates with the blast wave front, and previously open cracks are closed as the deformation propagates. Cracking occurs later at the fixed edge farther from the blast epicenter. The red cracks are open cracks, while blue indicates that the cracks have closed. The analysis results shown are for the 10 psi peak pressure loading on the 3 element thick mesh. Deflection is magnified by 10.

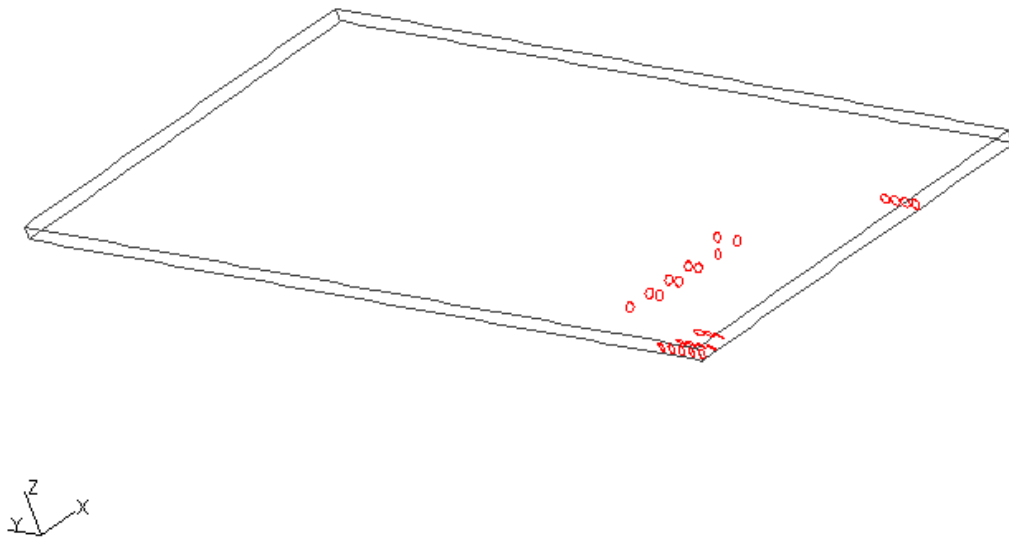


Figure 99: Murrah Slab Cracking On Deflected Shape At 5 msec

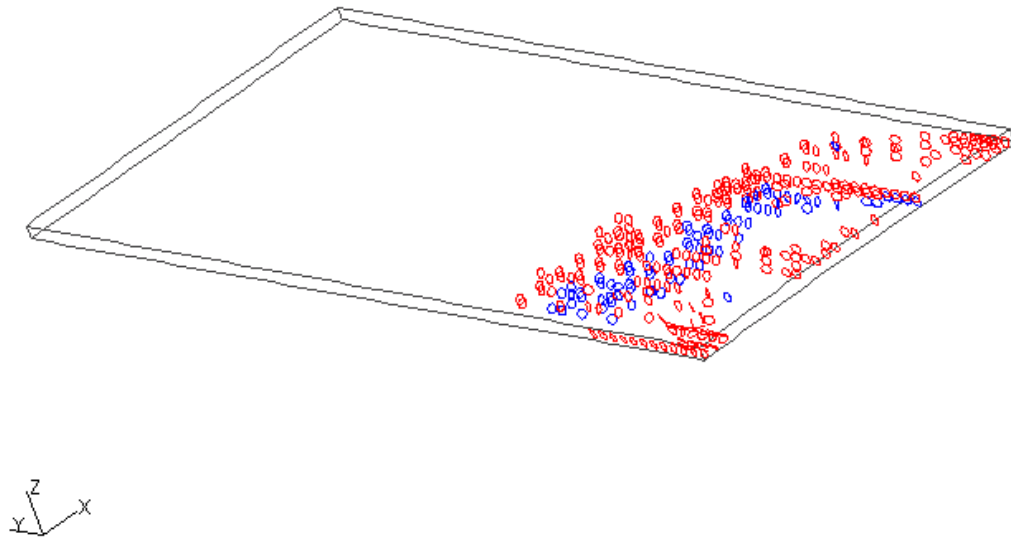


Figure 100: Murrah Slab Cracking On Deflected Shape At 10 msec

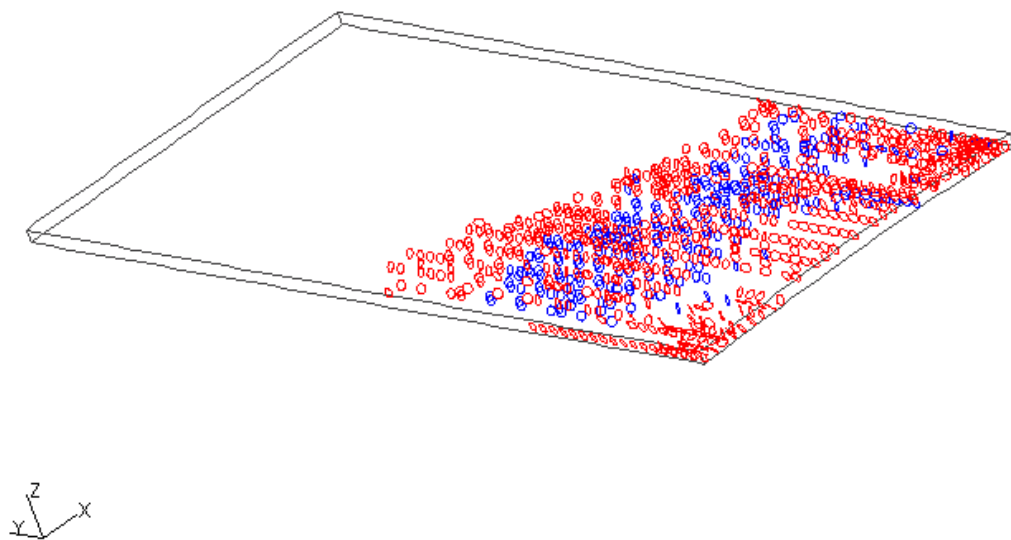


Figure 101: Murrah Slab Cracking On Deflected Shape At 15 msec

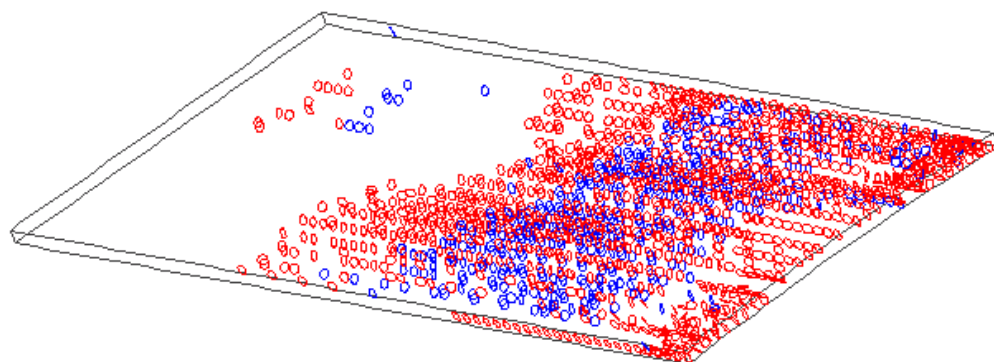


Figure 102: Murrah Slab Cracking On Deflected Shape At 20 msec

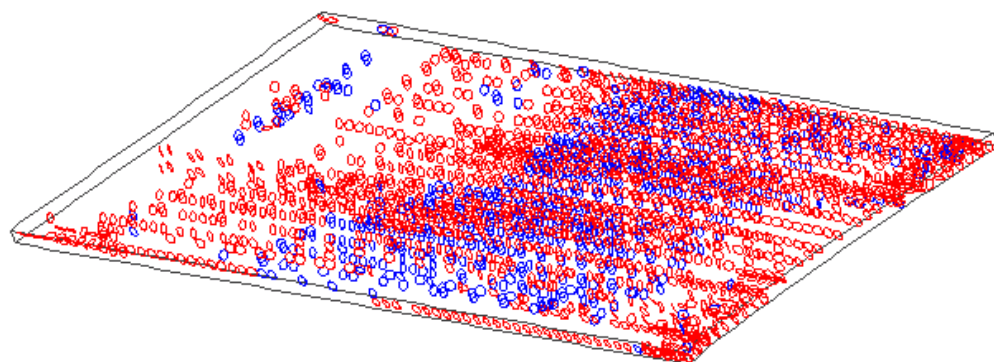


Figure 103: Murrah Slab Cracking On Deflected Shape At 25 msec

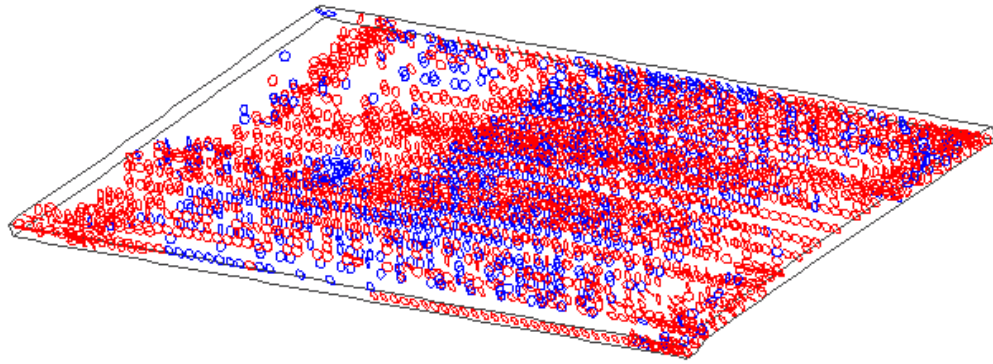


Figure 104: Murrah Slab Cracking On Deflected Shape At 30 msec

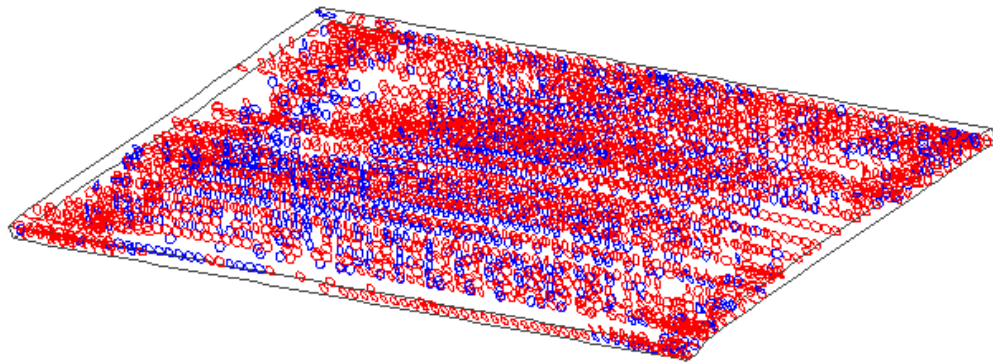


Figure 105: Murrah Slab Cracking On Deflected Shape At 35 msec

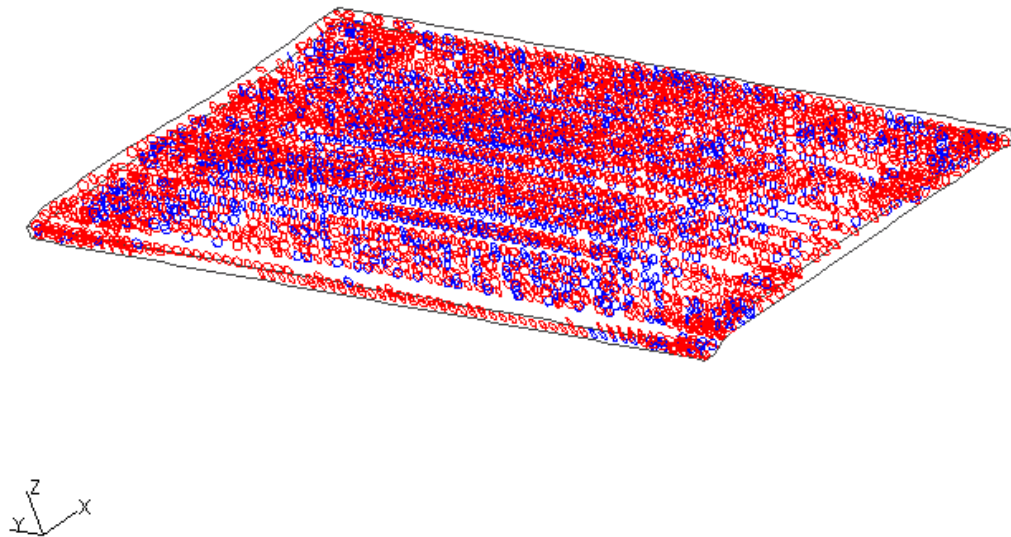


Figure 106: Murrah Slab Cracking On Deflected Shape At 40 msec

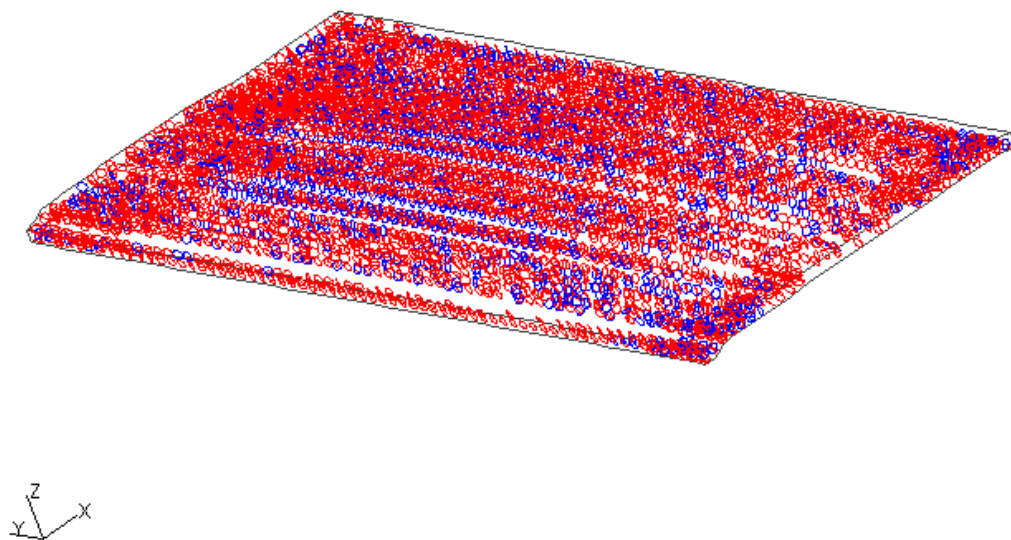


Figure 107: Murrah Slab Cracking On Deflected Shape At 45 msec

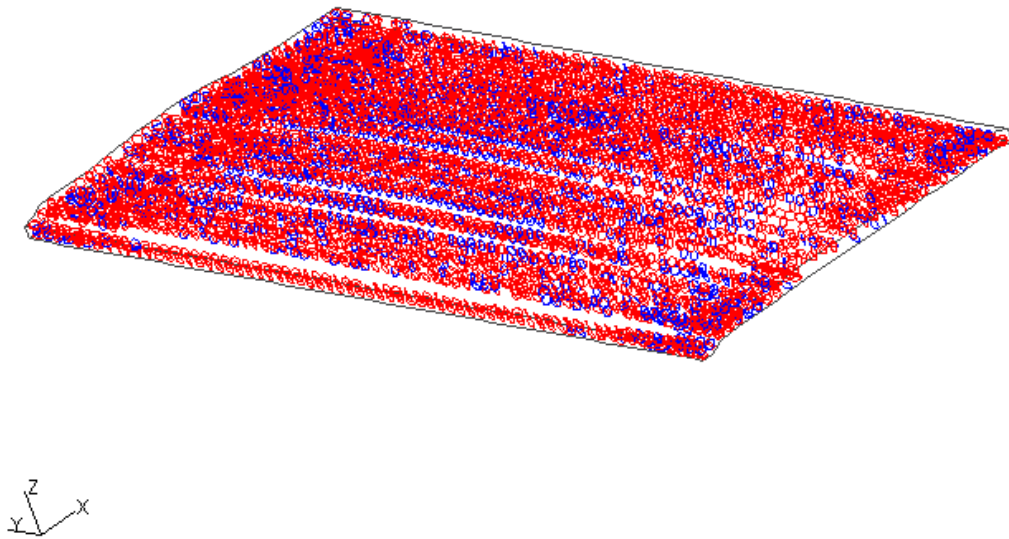


Figure 108: Murrah Slab Cracking On Deflected Shape At 50 msec

Figures showing the flexural stress contours plotted on the deflected shape of the structure are provided in Appendix L. These figures, together with the figures showing the crack progression and the deflected shape, will help the reader to visualize the upward deformation of the slab, as the blast wave moves along the underside of the slab.

5.6 MURRAH SLAB FEM DISCUSSION OF RESULTS

The Murrah slab model will be verified later in this chapter. The verification will be made by analyzing a similar structure subjected to a similar loading condition. The comparison structure will be a foot wide strip of floor slab. The results for the Murrah slab cannot be quantitatively compared to the results of the foot wide strip of floor slab subjected to a similar impulse load. The

Murrah slab is a floor bay in size, as compared to a foot wide strip. The moving pressure load originates at an edge of the Murrah slab, and takes about 40 msec to propagate across its thirty-three and a half feet bay length. The moving pressure almost immediately affects the entire foot width of the foot wide slab.

5.7 MURRAH SLAB FEM CONCLUSIONS

The Murrah slab analyses results show the need to improve the nonlinear capabilities of the software. Resolution may be increased through the use of increased computing power to model the structure with reduced time steps, finer mesh, and longer load durations and larger loadings.

5.8 VALIDATION OF MURRAH SLAB FEM ANALYSIS

A classical analysis was performed of a foot wide strip of floor slab to validate the results of the computer model for the Murrah building fifth floor slab subjected to the blast load. The expected load-deflection response was determined for both a static load and a dynamic load. The predicted dynamic response was then compared to the Murrah building floor slab finite element analysis results. Both a static analysis and a dynamic analysis were performed. The slab is assumed fixed at the ends, with negative moment resisting top steel at the ends and positive moment resisting bottom steel at center midspan.

To further evaluate the computer software, a finite element analysis was performed on the foot width of floor slab used in the classical analysis. Both a

quasi-static finite element analysis and impulsive loading finite element analyses were performed and the results compared to the response predicted by the classical analysis. The slab's simulated response to the quasi-static load condition is compared to the predicted static loading analysis results. The impulsive loading simulation results are compared to the expected strength of the slab to resist impulsive loads.

5.8.1 PREDICTED SLAB STRIP LOAD-DEFLECTION RESPONSE

The expected static load-deflection response for a foot wide strip of the Murrah Slab is shown in Figure 109. The slab will behave linear elastically until the slab cracks due to flexural tensile stresses in high moment regions. The first point beyond the origin in Figure 109 represents the point where flexural cracking first occurs for a slab with fixed supports. First cracking for a slab with fixed supports occurs over the supports, and for a load-controlled experiment the load will decrease due to a loss of stiffness as the cracks develop. After plastic hinges develop at the supports, the slab will behave as a simply supported beam. The second point in Figure 109 represents first flexural cracking at midspan of a simply supported slab. The slab can continue to resist an increase in load until ultimate flexural capacity is achieved as a third plastic hinge develops at midspan, and the concrete crushes due to flexural compressive stresses. The slab will behave similarly with or without reinforcing steel until the slab has cracked.

After cracking, the presence of reinforcing steel allows the slab to resist an increasing applied moment until flexural ultimate strength.

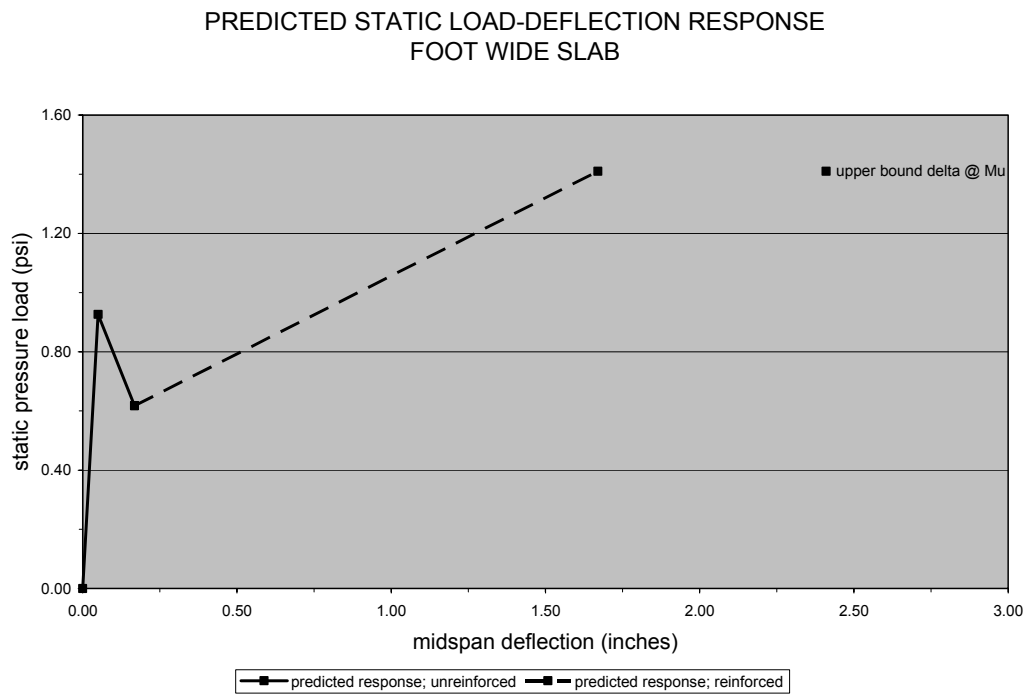


Figure 109: Slab Strip Static Load-Deflection Predicted Response

Since the impulse load duration is short compared to the natural frequency of the floor slab, the slab can withstand a peak overpressure greater than the static loading. The expected deformation response caused by an impulsive loading is shown in Figure 110.

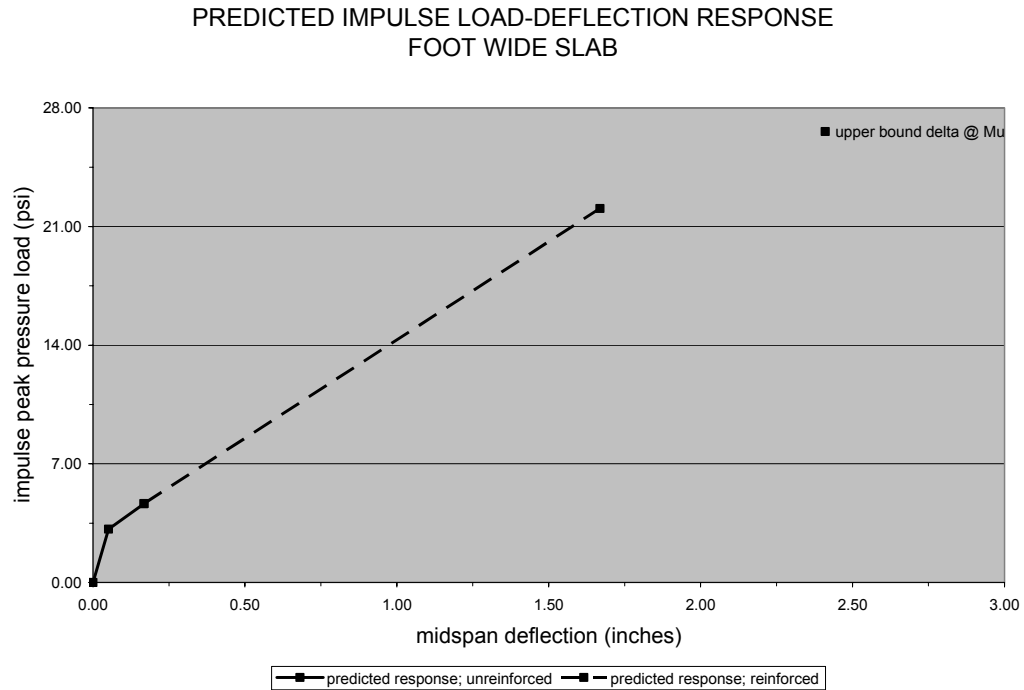


Figure 110: Slab Strip Impulse Load-Deflection Predicted Response

The classical analysis for these three load points, first cracking near the fixed ends, first cracking at midspan of a simply supported slab, and concrete crushing at midspan, are summarized in Table 6. The first five columns of Table 6 depict the static load-deflection response conditions, and the natural frequency of the structure. Note that the impulsive load conditions shown in the right three columns of Table 6 will produce the same cracking conditions as the static load conditions listed at the left. An impulsive load much greater in magnitude than the static load is required to produce the same deformation, i.e. the same cracking condition or the flexural strength condition. These impulse load-response analyses are included in Appendix K.

FOOT SLAB LOAD-DEFLECTION RESPONSE POSITIVE MOMENT APPLIED TO POSITIVE MOMENT RESISTING SECTION								
	STATIC LOAD					IMPULSE LOAD		
hinge or crushing location	static pressure (psi)	static midspan deflection (inches)	structural stiffness k (psi/inch)	natural period T _n (sec/cycle)	delta o /delta s	impulse peak pressure (psi)	impulse midspan deflection (inches)	equivalent static force (psi)
first cracking @ supports	0.93	0.05	18.00	0.05	0.30	3.14	0.05	0.93
first cracking @ midspan	0.62	0.17	3.68	0.12	0.13	4.65	0.17	0.62
ACI strength @ midspan	1.41	1.67	0.85	0.25	0.06	22.07	1.67	1.41
upper bound @ midspan	1.41	2.41	0.59	0.30	0.05	26.60	2.41	1.41
one way floor slab with 192" span with fixed ends 6" slab reinf. w/ 0.27insq/ft width @ d=5" 4ksi concrete, Grade 60 steel 75psf/g slab mass Note: Gravity neglected in impulse load & deflection computation								

Table 6: Slab Strip Load-Deflection Predicted Response

The value in the fifth column, δ_o/δ_{static} , is the ratio of the structure's impulsive response to the static response, and depends on the natural frequency of the structure and the duration of impulsive load. The values in the right three columns are the structure's dynamic response to a triangular impulse load with 5 msec duration. The impulsive peak pressure loading in the sixth column, with a magnitude much larger than the static loading in the first column, produces the same deformation response as shown in the second and seventh columns.

The impulse load-deflection response at the ultimate flexural strength condition is difficult to quantify since the extent of cracking of the Murrah slab at the moment before the blast event is not known with certainty. The natural period of the structure depends on the structural stiffness, e.g. the extent of slab cracking and the support conditions. In this response prediction, the effective moment of inertia defined in equation 9-8 of the ACI 318-02 code was used to estimate the midspan static deflection and peak impulsive pressure at ultimate flexural strength.

Both the static and dynamic load-deflection response predictions at ultimate flexural strength are sensitive to the value used for structural stiffness. To quantify this sensitivity, upper bound values of static load deflection and impulse peak pressure, shown in Figures 109 and 110 as “upper bound delta @ Mu”, were determined from a lower bound value for the cracked section moment of inertia. For this comparison, at the moment immediately prior to the blast, the slab was assumed simply supported and fully cracked, as though flexural strength had been previously reached throughout its length. This corresponds to assuming a longer natural period for the structure and lower δ_o/δ_{static} , computed from lower bound values for the structural stiffness. Conversely, a lower value for peak impulsive pressure would be expected by assuming a lower static load deflection, a shorter natural period for the structure and larger δ_o/δ_{static} through the use of a larger value for structural stiffness, e.g. a value corresponding

to twice the effective moment of inertia would predict slab failure at about $1/\sqrt{2}$ times the peak impulsive pressure.

5.8.2 FINITE ELEMENT MODEL OF SLAB STRIP

TerraScale's TeraDyn finite element analysis software, and ANATECH Corporation's ANAMAT concrete constitutive relations, were used to simulate the foot wide strip of concrete slab.

The foot wide slab model has the same reinforcement pattern as the Murrah building slab model described in Section 5.4.1, and as shown in Figure 111. Three meshes were used in the analysis; one with 3 elements through the slab depth, a second with 6 elements, and a third with 12 elements. All three meshes have 8 elements through the width and 64 elements through the length. The three meshes are shown in Figures 112, 113 and 114.

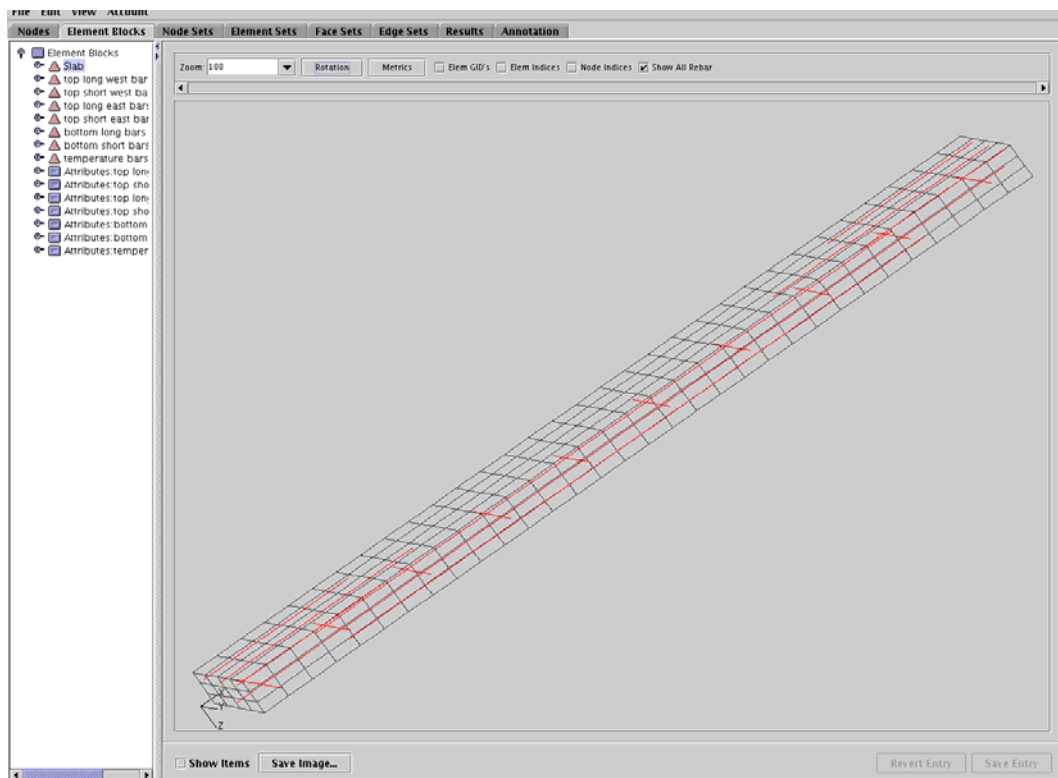


Figure 111: Slab Strip Reinforcement Pattern

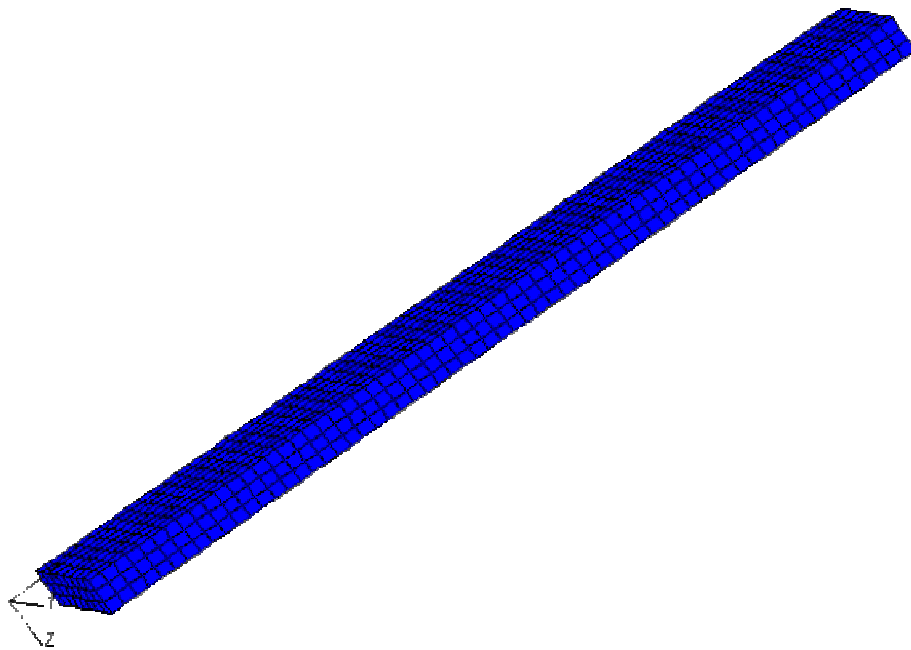


Figure 112: Slab Strip Mesh; 3 elements Through Slab Depth

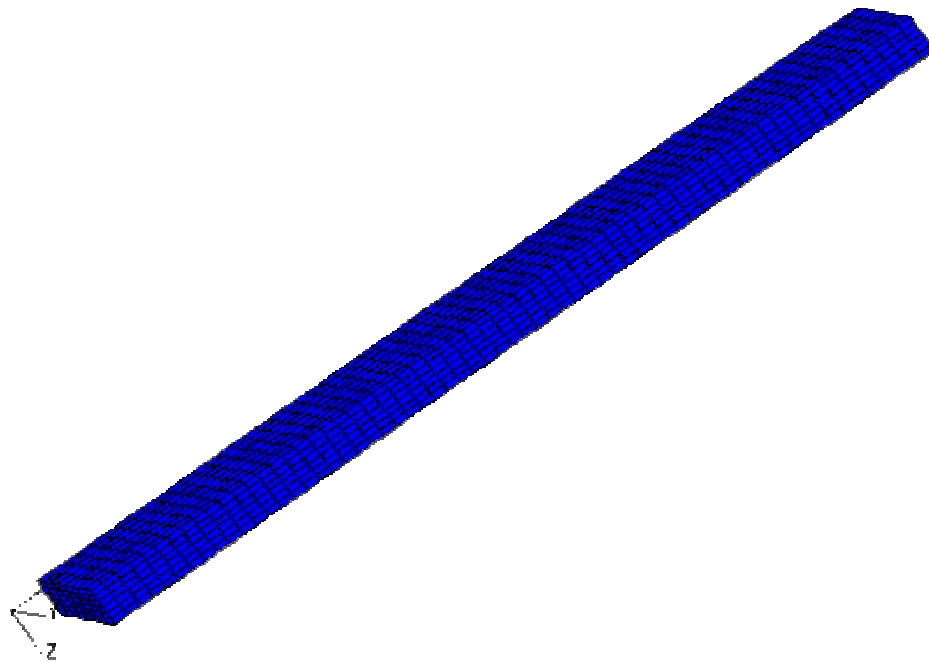


Figure 113: Slab Strip Mesh; 6 elements Through Slab Depth

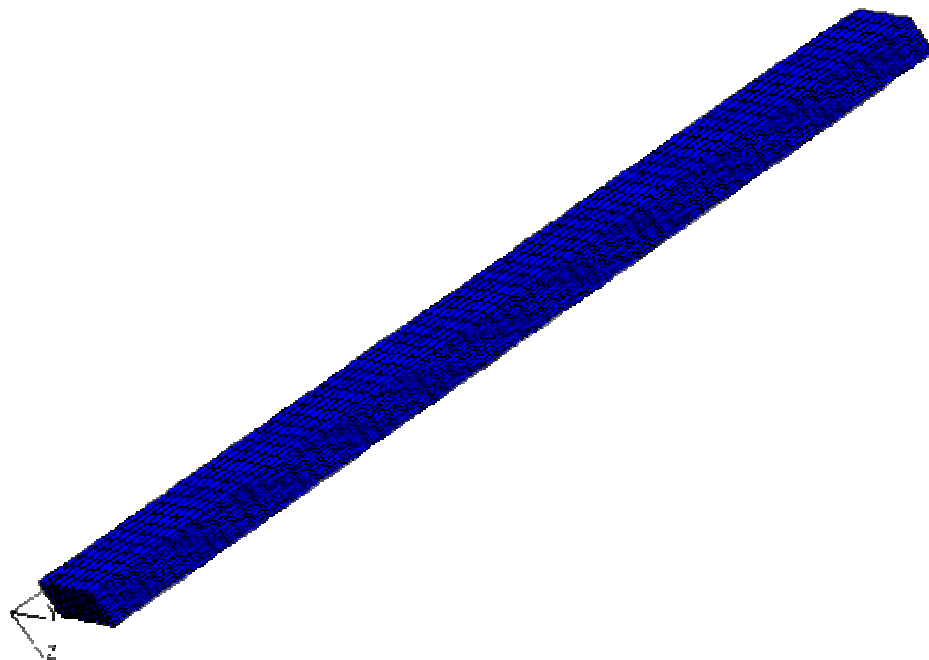


Figure 114: Slab Strip Mesh; 12 elements Through Slab Depth

5.8.3 LOADING CONDITIONS IN VALIDATION MODELS

A quasi-static and an impulse loading were performed on the foot wide slab strip to validate the computer software. In the impulsive load analysis, the slab was loaded with a 5 msec duration impulsive pressure loading. The simulations were performed at three magnitudes of peak pressure. These pressures correspond to the loading expected to initiate end region cracking, midspan cracking of a simply supported slab, and flexural failure. Two additional series of simulations were performed on more refined meshes.

In the quasi-static load analysis, the slab was loaded slowly, to prevent any inertial and damping effects in the slab response. The analyses were performed on the medium fine mesh, 6 elements through the slab depth. The value of peak load was selected as the slab's ultimate flexural strength. A second loading equal to half that value was used to investigate if additional resolution could be seen in the slab's response. The loading consisted of a linear ramp load of 0.5 sec duration. Half the loading rate, 1.0 sec load duration, was used in a second series of analysis to investigate the effect of loading rate on this explicit dynamics analysis. Half the peak load values were used in the second series. A second series of analyses were performed for the case of a simply supported floor slab, as a comparison to the results of a slab with fixed ends.

The loading rate in the quasi-static analyses were selected so that maximum load would be achieved in a length of time at least twice the predicted natural frequency of the structure. From Appendix K, the natural frequencies are 0.05 sec for the uncracked slab with fixed ends, 0.12 sec for the uncracked simply supported slab, and 0.25 sec using the ACI provisions for the effective moment of inertia of a cracked flexural member.

5.8.4 RESULTS OF FINITE ELEMENT ANALYSIS OF SLAB STRIP

The results of the impulsive loading and quasi-static loading analysis are presented in this section.

5.8.4.1 RESULTS OF IMPULSE LOADING FINITE ELEMENT ANALYSIS

Figures 115 through 123 show the cracking patterns for the three loading conditions and the two mesh refinements. The figures show that cracking occurs in the expected location, in the regions of high flexural stress. The simulations for the flexural strength loading condition for all three meshes failed to run to the end of the 50 msec time duration.

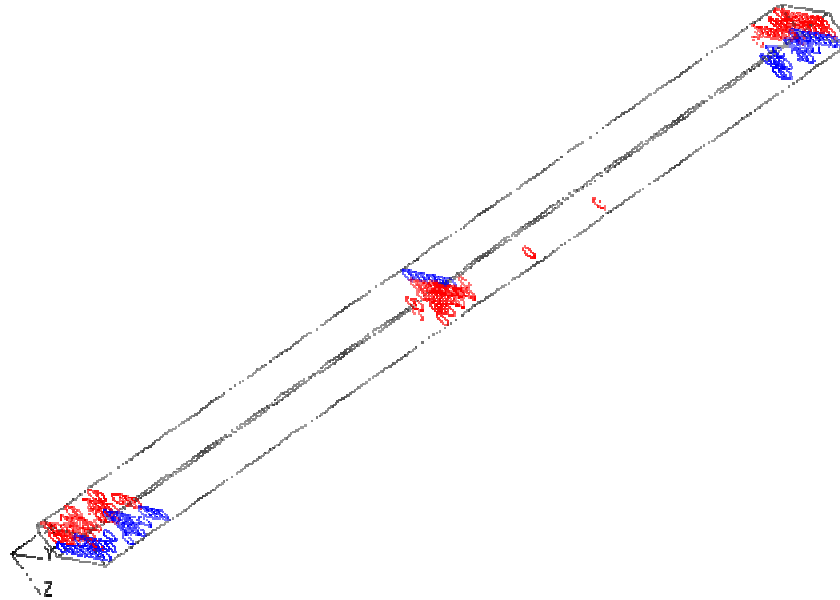


Figure 115: Slab Strip 3 Element Mesh; First Cracking At Fixed Ends

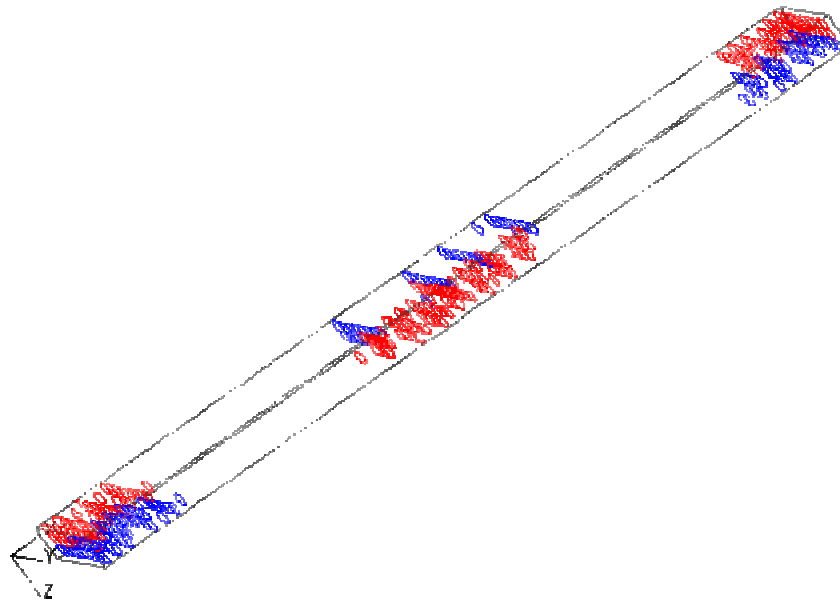


Figure 116: Slab Strip 3 Element Mesh; First Cracking At Midspan

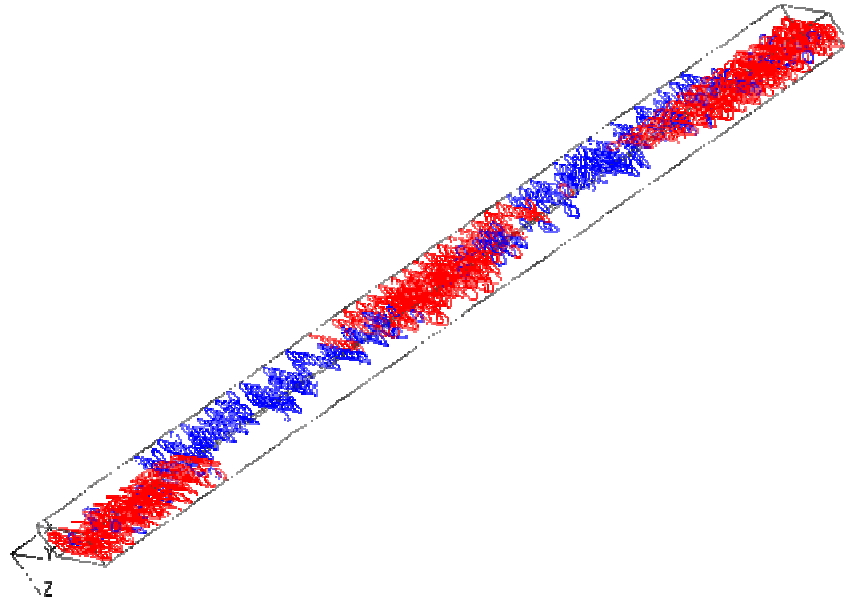


Figure 117: Slab Strip 3 Element Mesh; Flexural Strength At Midspan

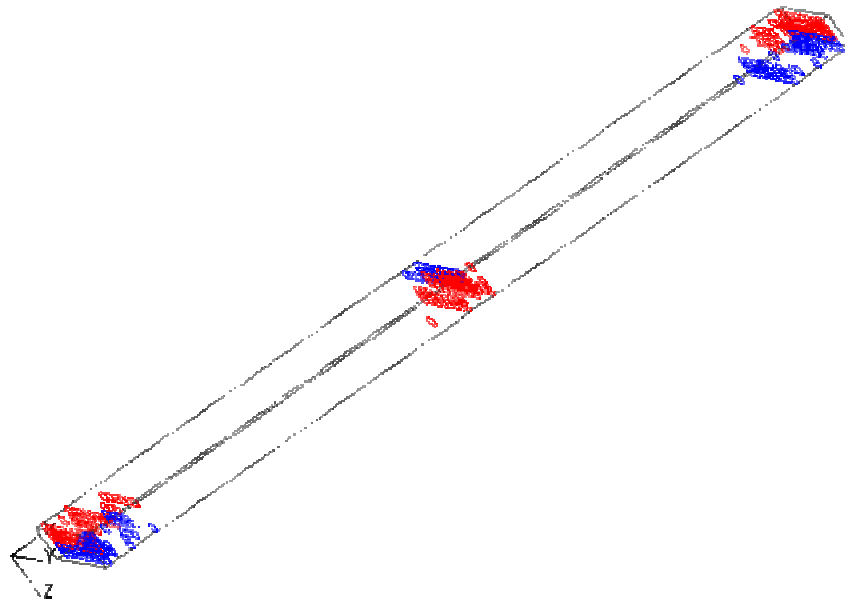


Figure 118: Slab Strip 6 Element Mesh; First Cracking At Fixed Ends

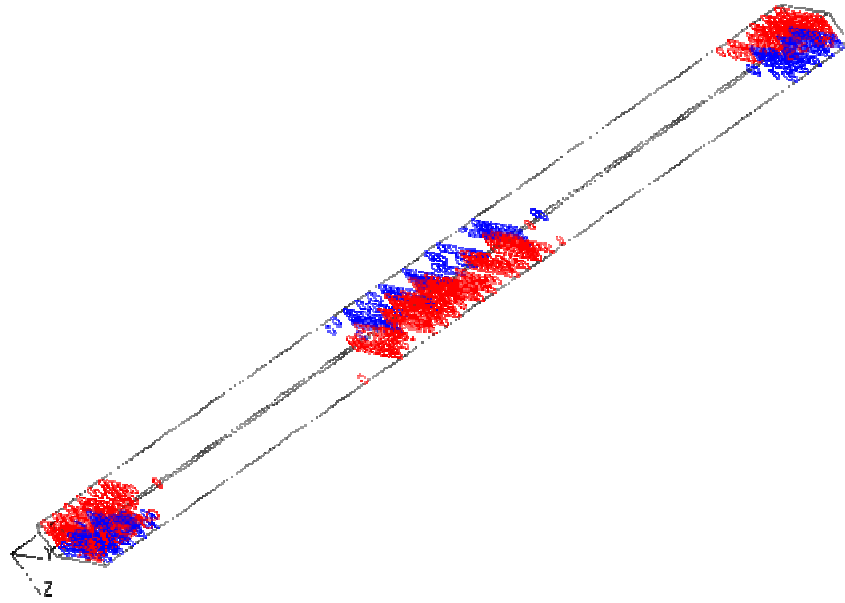


Figure 119: Slab Strip 6 Element Mesh; First Cracking At Midspan

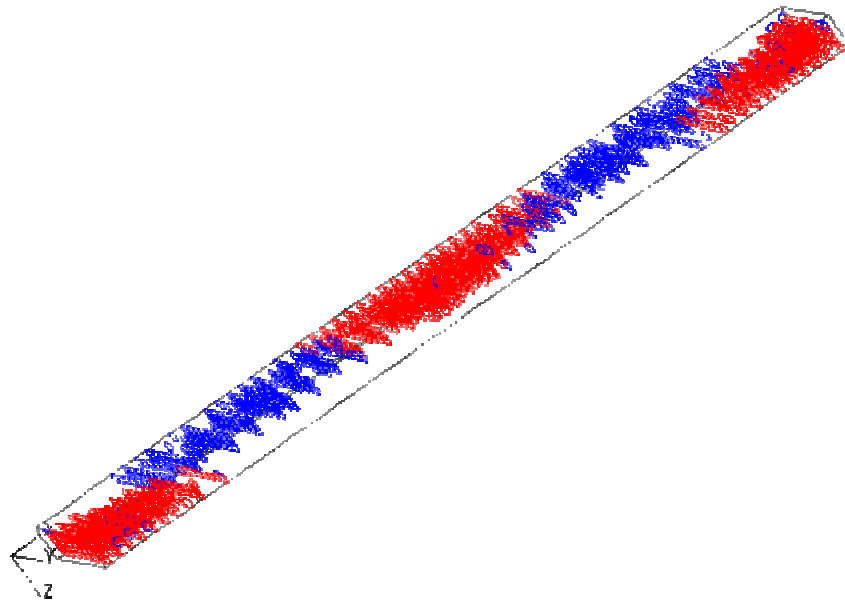


Figure 120: Slab Strip 6 Element Mesh; Flexural Strength At Midspan

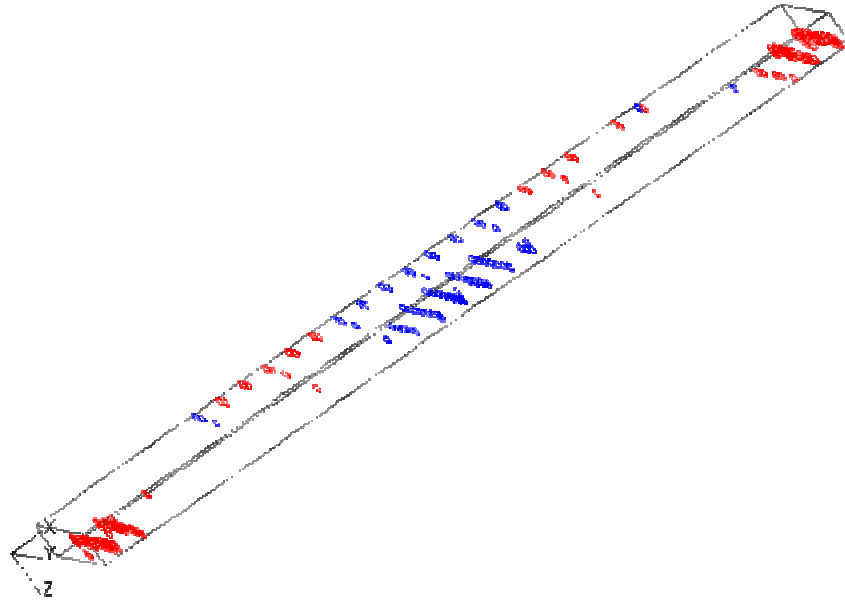


Figure 121: Slab Strip 12 Element Mesh; First Cracking At Fixed Ends

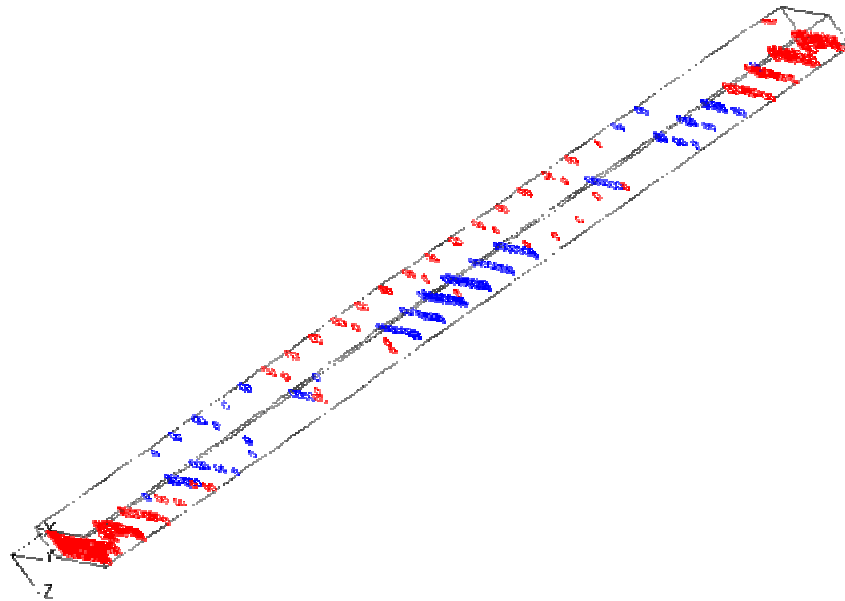


Figure 122: Slab Strip 12 Element Mesh; First Cracking At Midspan

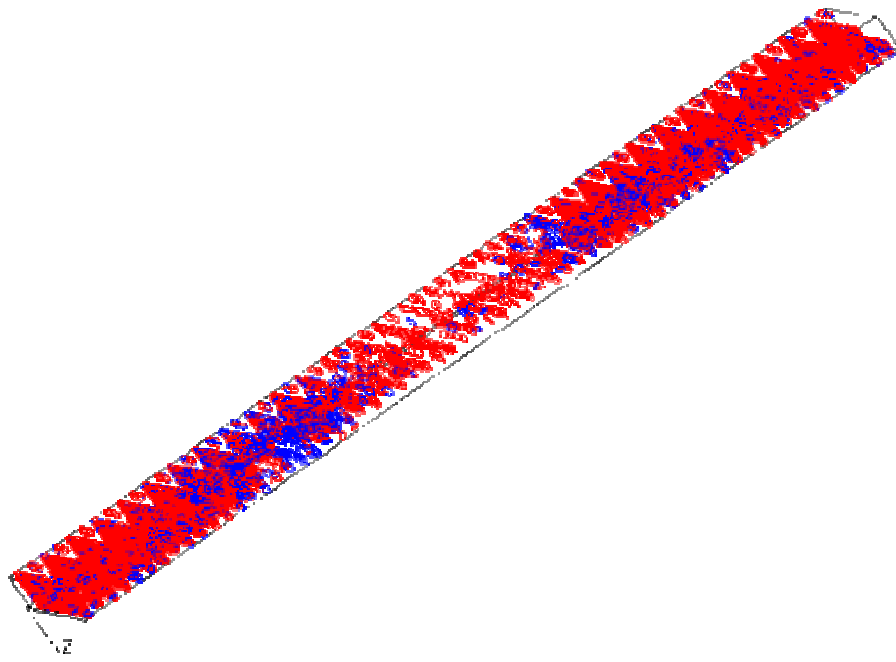


Figure 123: Slab Strip 12 Element Mesh; Flexural Strength At Midspan

5.8.4.2 RESULTS OF QUASI-STATIC LOADING FINITE ELEMENT ANALYSIS

Figures 124 through 129 show the typical results of a quasi-static load analysis of the slab with fixed ends subjected to a uniform loading. The figures illustrate the crack progression as load is increased. The deflected shape is magnified by 100. For this analysis, the mesh used has 6 elements through the slab thickness, and the loading and duration of ramp load are 1.41 psi and 0.5 sec, respectively. The figures show that cracking occurs in the expected location, in the regions of high flexural stress. As predicted, cracking first occurs on the top fiber at the fixed ends. Cracking in the end region continues and then occurs near the midspan at the bottom fiber. The analysis terminated 0.40 sec into the test at a load near that predicted to cause first cracking of a simply supported slab.

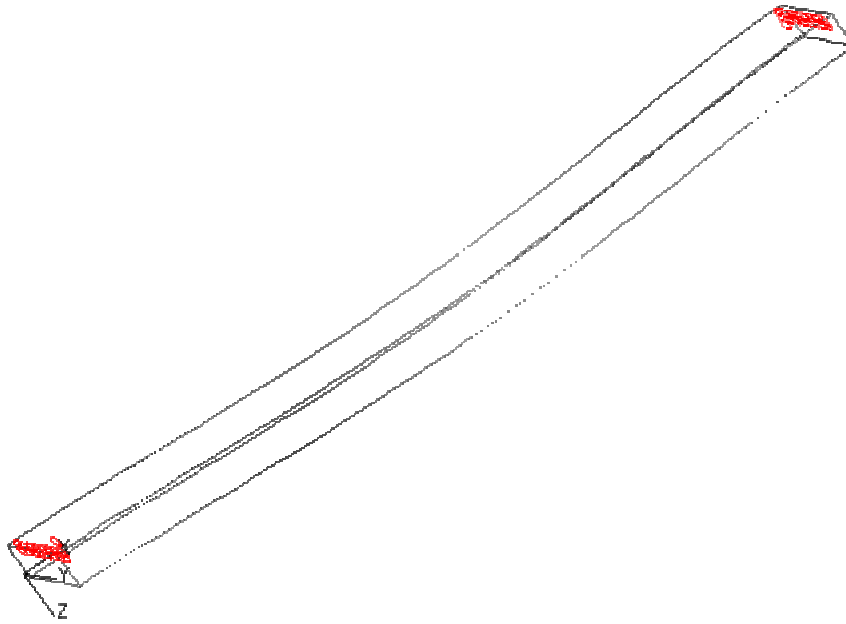


Figure 124: Slab Strip Cracking At 20 msec

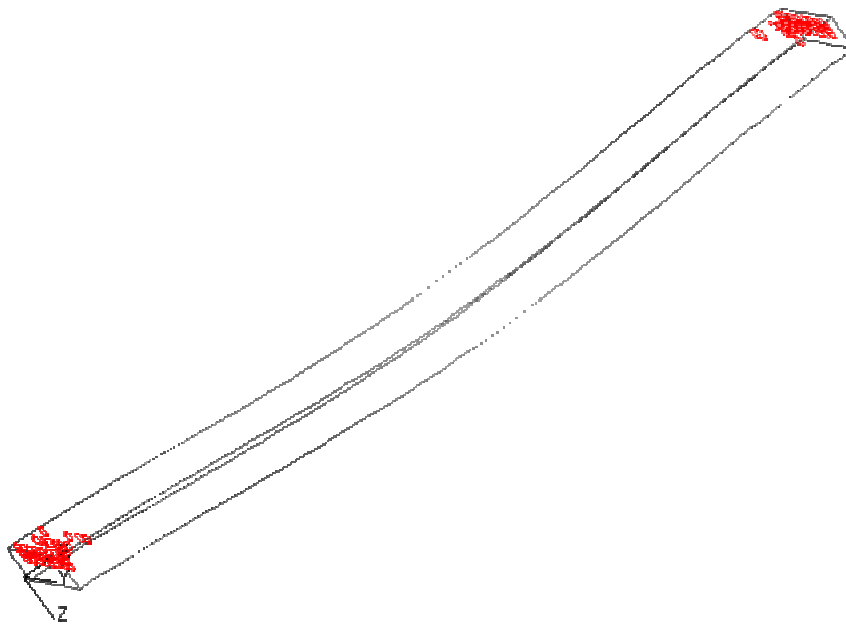


Figure 125: Slab Strip Cracking At 24 msec

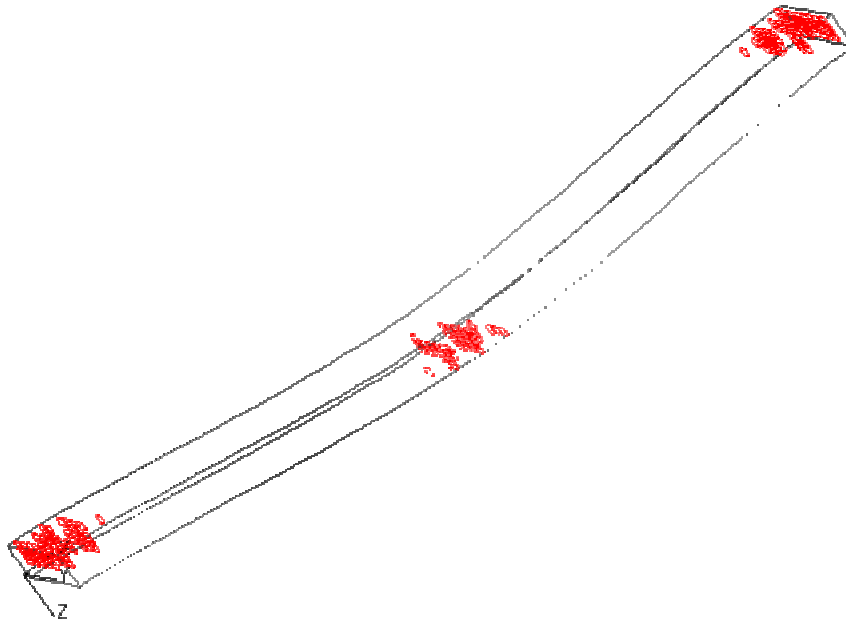


Figure 126: Slab Strip Cracking At 28 msec

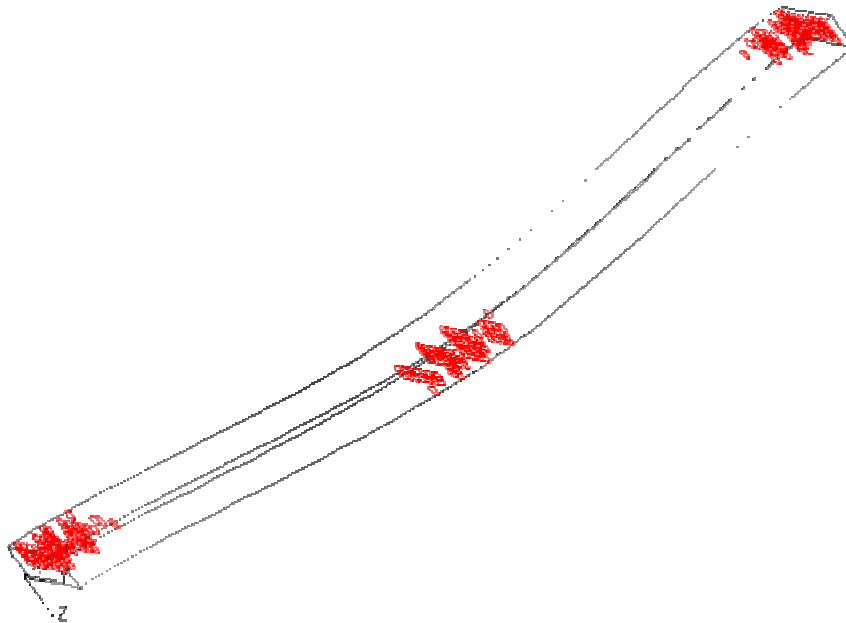


Figure 127: Slab Strip Cracking At 32 msec

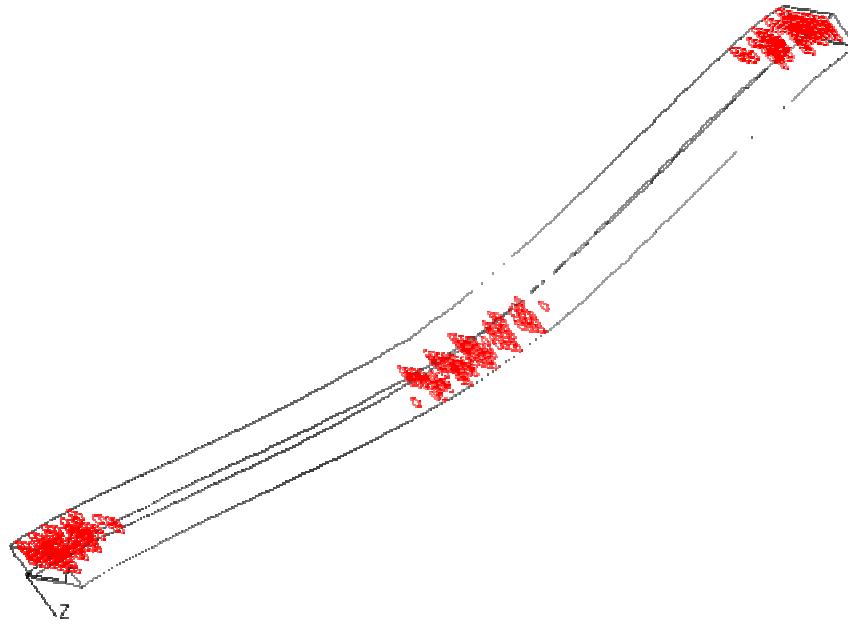


Figure 128: Slab Strip Cracking At 36 msec

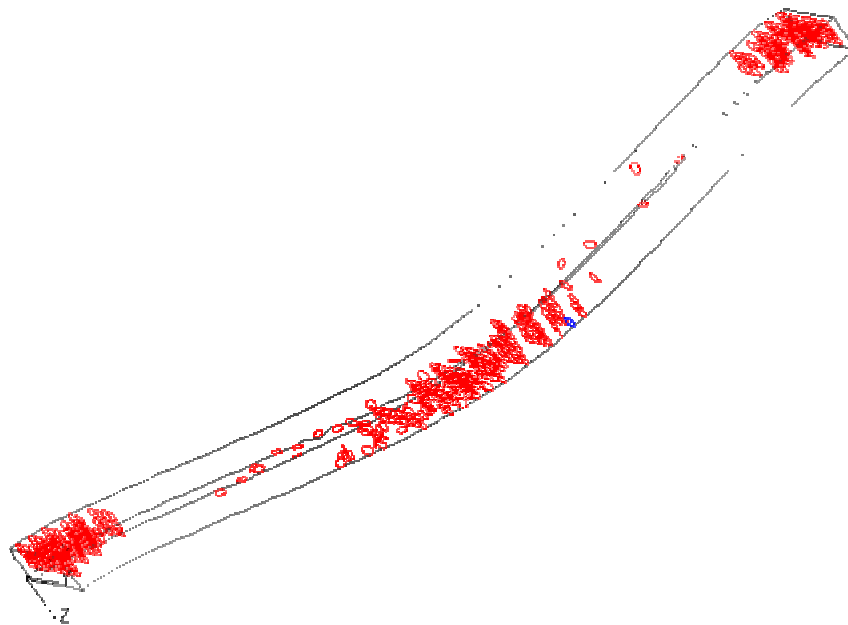


Figure 129: Slab Strip Cracking At 40 msec

5.8.5 COMPARISON OF PREDICTED AND FEA RESULTS OF SLAB STRIP

The comparison with the predicted results, both of the impulsive loading and the quasi-static loading analyses, are presented in this section.

5.8.5.1 IMPULSIVE LOADING COMPARISON OF RESULTS

The slab midspan deflection and the slab cracking pattern from the finite element analyses are compared with the predicted values. Figure 130 and Table 7 summarize the deflection values for the loading cases where the pressure loading was applied to the underside of the slab, inducing a negative moment at midspan. The loading cases that ran to the end of the 50 msec analysis duration are plotted on Figure 130. The numerical results from the loading cases that did not run to the end of the 50 msec analysis duration are indicated in bold in Table 7. From Table 7, the analyses deformation results are within a factor of about two of the predicted results, and are much closer at the first cracking value. The extent of cracking in Figures 115 through 123 compares well with the loading predicted to induce initial cracking at the ends and at midspan.

PREDICTED vs FINITE ELEMENT ANALYSIS RESULTS
IMPULSE LOAD-DEFLECTION RESPONSE
NEGATIVE MOMENT APPLIED TO FOOT SLAB WITH FIXED ENDS

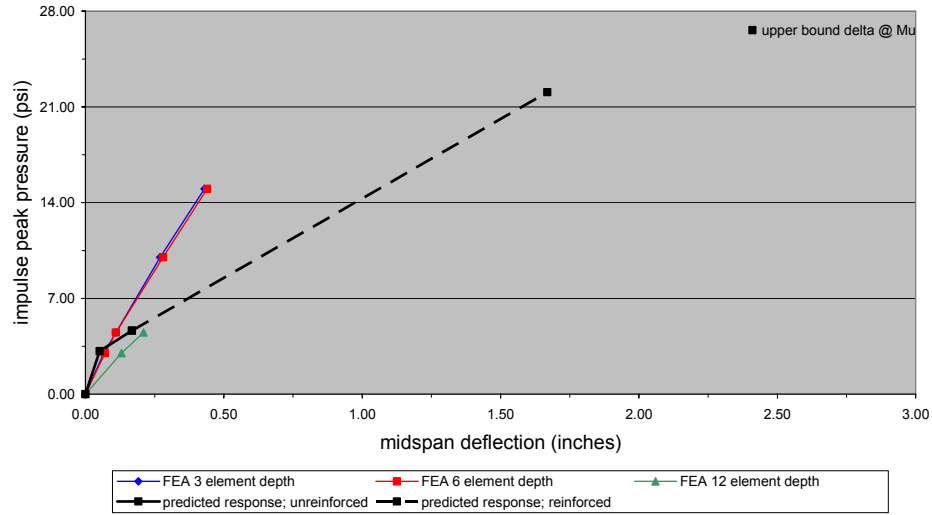


Figure 130: Slab Strip Impulsive Load Negative Moment Results

FOOT SLAB IMPULSE LOAD-DEFLECTION RESPONSE NEGATIVE MOMENT APPLIED TO POSITIVE MOMENT SECTION									
	PREDICTED			FEA RESULT					
				impulse midspan deflection (inches)			time step at termination (msec)		
hinge or crushing location	static pressure (psi)	impulse peak pressure (psi)	static midspan deflection (inches)	Elements Thru Depth					
				3 elem	6 elem	12 elem	3 elem	6 elem	12 elem
first cracking @ supports	0.93	3.14	0.05	0.07	0.07	0.13			
first cracking @ midspan	0.62	4.65	0.17	0.11	0.11	0.21			
		10.00		0.27	0.28	0.36			20
		15.00		0.43	0.44	0.28			13
ACI strength @ midspan	1.41	22.07	1.67	0.72	0.74	0.78	25	27	20
Note: Bold indicates run terminated as element "failed" before 50msec analysis duration									
one way floor slab with 192" span with fixed ends 6" slab reinf. w/ 0.27insq/ft width @ d=5" 4ksi concrete, Grade 60 steel 75psf/g slab mass									
Note: Gravity neglected in impulse load & deflection computation									

Table 7: Slab Strip Impulsive Load Negative Moment Results

Figure 131 and Table 8 summarize the deflection values for the loading cases where the pressure loading was applied to the top side of the slab, inducing a positive moment at midspan. From Table 8, the analyses deformation results are within a factor of about two of the predicted results, and are much closer at the first cracking value. The plots and deflection values are similar for either the positive or negative loading condition. This could be explained as due to the impulsive nature of the loading. The loading is applied in a short time interval, and the structure's response to the loading is more like that from a transverse shear loading, rather than from a flexural loading. Some quick hand calculations will show that the uniform static loading that will cause a shear failure in the slab is about a factor of five times that to cause a flexural loading. This could explain why the analyses for the load cases of 10 psi and 15 psi peak impulse pressure shown in Figure 130 ran the entire 50 msec analyses duration although there was no longitudinal flexural steel at the top of the slab at midspan to resist the high flexural stresses produced by the pressure applied to the bottom of the slab.

PREDICTED vs FINITE ELEMENT ANALYSIS RESULTS
IMPULSE LOAD-DEFLECTION RESPONSE
POSITIVE MOMENT APPLIED TO FOOT SLAB WITH FIXED ENDS

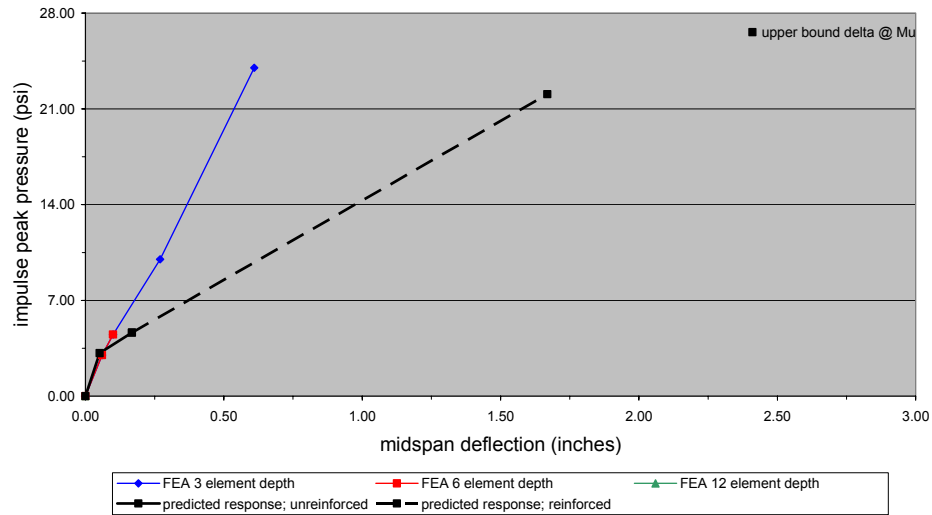


Figure 131: Slab Strip Impulsive Load Positive Moment Results

FOOT SLAB IMPULSE LOAD-DEFLECTION RESPONSE POSITIVE MOMENT APPLIED TO POSITIVE MOMENT SECTION									
	PREDICTED			FEA RESULT					
				impulse midspan deflection (inches)			time step at termination (msec)		
hinge or crushing location	static pressure (psi)	impulse peak pressure (psi)	static midspan deflection (inches)	Elements Thru Depth					
				3 elem	6 elem	12 elem	3 elem	6 elem	12 elem
first cracking @ supports	0.93	3.14	0.05	0.06	0.06	0.12	35	15	30
first cracking @ midspan	0.62	4.65	0.17	0.10	0.10	0.18			30
		10.00		0.27	0.27	0.20			10
		15.00		0.37	0.40	0.53			15
ACI strength @ midspan	1.41	22.07	1.67	0.61	0.67	0.45		15	10
<p>Note: Bold indicates run terminated as element "failed" before 50msec analysis duration</p> <p>one way floor slab with 192" span with fixed ends 6" slab reinf. w/ 0.27insq/ft width @ d=5" 4ksi concrete, Grade 60 steel 75psf/g slab mass</p> <p>Note: Gravity neglected in impulse load & deflection computation</p>									

Table 8: Slab Strip Impulsive Load Positive Moment Results

The analyses cases that failed to run to the end of the 50 msec analysis duration ended when some of the structure's elements had a zero volume, i.e. a proper and admissible displacement field could not be found since a Jacobian matrix is negative. The load cases had a zero volume element in a region of the member that had a high flexural stress. A positive Jacobian is a necessary and sufficient condition for a continuous displacement to be physically possible

5.8.5.2 QUASI-STATIC LOADING COMPARISON OF RESULTS

The slab midspan deflection and the slab cracking pattern from the finite element analyses are compared with the predicted values. Figures 132 and 133 summarize the load-deflection response for the simply supported slab and the slab with fixed ends, respectively. Note that the predicted load-deflection response for the simply supported slab does not have the load point representing first cracking at the fixed ends. The data used to create the plots is located in Appendix M. The analysis results compare qualitatively to the predicted results. Stiffness decreases as loading is increased after first cracking. The extent of cracking at the ends and at midspan in Figures 124 through 129 compares well with the predicted cracking.

PREDICTED vs FINITE ELEMENT ANALYSIS RESULTS
 QUASI STATIC LOAD-DEFLECTION RESPONSE
 POSITIVE MOMENT APPLIED TO SIMPLY SUPPORTED FOOT SLAB

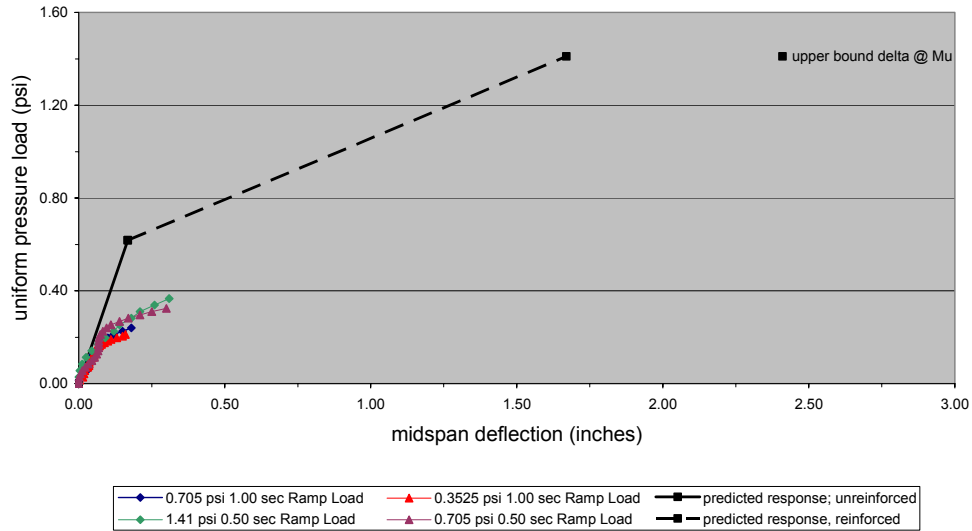


Figure 132: Simply Supported Slab Quasi-Static Loading Response

PREDICTED vs FINITE ELEMENT ANALYSIS RESULTS
 QUASI STATIC LOAD-DEFLECTION RESPONSE
 POSITIVE MOMENT APPLIED TO FOOT SLAB WITH FIXED ENDS

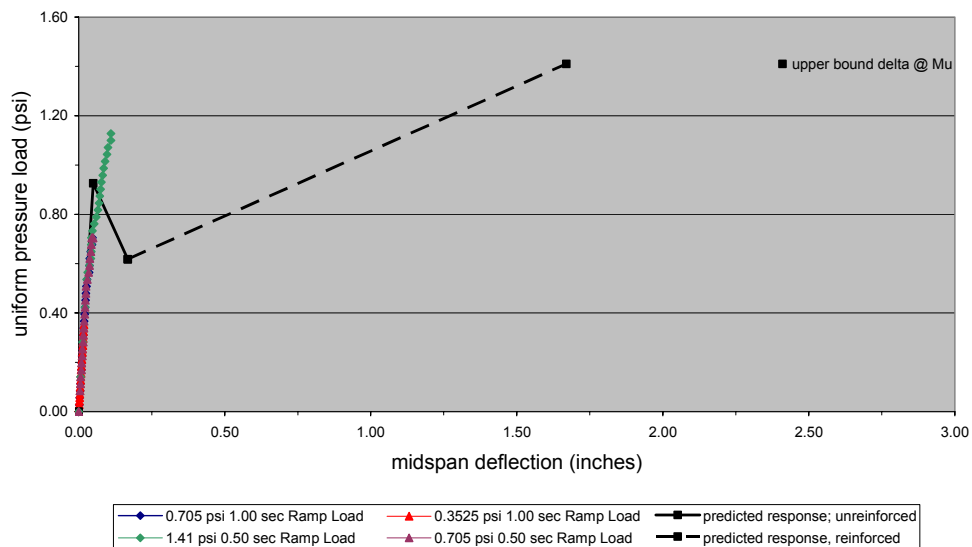


Figure 133: Fixed Ends Slab Quasi-Static Loading Response

The simply supported load cases terminated before reaching the analysis duration. The load case with a 1.0 sec duration ramp load to 0.705 psi terminated due to reaching an unstable time step. The remaining three analyses failed when some of the structure's elements had a zero volume, i.e. a proper and admissible displacement field could not be found since a Jacobian matrix is negative. The two load cases with the shorter 0.5 sec ramp time duration had a zero volume element on the bottom fiber in the middle third of the member length, a region of highest flexural stress. The remaining case had a zero volume element internal to the structure. A positive Jacobian is a necessary and sufficient condition for a continuous displacement to be physically possible.

Not all the fixed end member load cases terminated before reaching the analysis duration. The 0.5 sec duration ramp load to 1.41 psi load case terminated with a zero volume element on the top fiber at the member's fixed end, a region of highest flexural stress. The other three load cases ran their entire analysis duration.

Flexural strength has not been approached at the time the finite element analysis terminates, for the load cases that terminated prior to reaching the analysis duration. The flexural reinforcing steel stress is 8 to 11 ksi at the time of analysis termination, well below the steel's yield strength, for the analysis of the

simply supported slab loaded at 0.705 psi uniform pressure and ramp load duration of 0.5 sec.

5.8.6 CONCLUSIONS OF FINITE ELEMENT ANALYSIS OF SLAB STRIP

The TeraDyn program and the ANAMAT constitutive model for concrete can model the nonlinear behavior expected for the foot wide reinforced concrete one-way slab.

The analysis terminates before the highly nonlinear region is reached, the region near flexural ultimate strength, when some of the structure's elements in a region of highest flexural stress had a zero volume, i.e. a proper and admissible displacement field could not be found since a Jacobian matrix is negative for these elements. A positive Jacobian is a necessary and sufficient condition for a continuous displacement to be physically possible.

For the quasi-static case, additional analyses should be performed using increased duration of load to further investigate the inertial effects on the analysis results. For the 0.705 psi loaded simply supported member, the shorter 0.5 sec time duration case terminated due to inadmissible displacements (zero volume elements) while the longer 1.0 sec time duration case terminated at a lower load due to an unstable time step.

CHAPTER 6 SUMMARY OF CONCLUSIONS

6.1 INTRODUCTION

Present design practice of reinforced concrete structures is principally based on linear, elastic material properties. Deflections are generally taken as simple multiples of the elastic analysis. However, simplified linear analysis techniques are not suitable in quantifying the behavior of a reinforced concrete structure, especially approaching their failure load. The structure's response is highly load path dependent, typical of materials which exhibit plastic nonlinear stress strain behavior.

Failure analysis using the finite element analysis technique requires an understanding of the potential sources of nonlinearity. Both geometry and material behavior can be a source of nonlinearity. A geometric nonlinearity can be introduced as large deformations occur in a structure, e.g. buckling of a flexible column, or hinging at a rigid beam-column connection.

Structural engineers are becoming increasingly proficient with the finite element method since it is a useful technique in solving highly nonlinear problems in continuum mechanics. In this research commercially available software, with nonlinear concrete and steel material models, was used to model three reinforced concrete structures well beyond their linear elastic load range. The effort demonstrates the viability of using the finite element method in the strength analysis of reinforced concrete structures.

6.2 SUMMARY

This research reviews, for the benefit of a practicing structural engineer, the fundamentals of the finite element analysis method, especially as it applies in an analysis of a reinforced concrete structure. The research focuses on identifying the sources of geometric and material nonlinearity in a computational model. The research goal is to demonstrate the importance of the concrete material model, especially the strain softening region, in predicting the behavior of reinforced concrete structures.

More specifically, the research:

- Uses ANSYS to computationally model the flexural behavior of a prestressed concrete beam subjected to static load, and compares the results to experimental tests at Fears Structural Laboratory in 1995.

- Uses TeraScale's TeraDyn explicit dynamics software to computationally model an above ground reinforced concrete tornado shelter subjected to a pressure and impact load.
- Uses TeraScale's TeraDyn explicit dynamics software to computationally model a reinforced concrete one way floor slab subjected to an impact load, and compares the results to the Murrah Building blast damage on April 19, 1995.

A summary of these analyses can be found in the following section.

Analyses validation consists of a comparison with either experimental results or classical analyses. An implicit dynamic analysis was performed using ANSYS of a rectangular prestressed concrete beam subjected to point loads, and compared with experimental results. Explicit dynamic analyses were performed using TeraDyn of a tornado shelter and a one-way floor slab subjected to an impulsive pressure load, and compared to classical analyses. A quasi-static analysis was also performed using TeraDyn, of the one-way floor slab, and the results compared to a classical analysis as an additional validation of the analyses.

This engineering mechanics research utilizes the commercially available TeraDyn explicit dynamics computing software developed by TeraScale, LLC. A beta version of the TeraDyn explicit dynamics code was provided as part of a

cooperative research effort. This beta version of the code is a work in progress and this Ph.D. research provided a mechanism for validating and debugging many aspects of the reinforced concrete modeling details of the finite element application.

The constitutive model for concrete and reinforcing steel used with this explicit dynamics finite element analysis software was developed by ANATECH Corporation. The commercially available finite analysis software developed by ANSYS Corporation also includes a nonlinear concrete and reinforcing steel material model.

6.2.1 SUMMARY OF PRESTRESSED CONCRETE BEAM ANALYSIS

ANSYS version 8.0 was used in the implicit dynamic finite element analysis of the prestressed concrete rectangular beam. The concrete beam was modeled as a composite material comprised of concrete and reinforcing steel. The prestressing steel and the compression steel were idealized using line (1D) elements. The concrete was modeled using 3D solid elements. The transverse reinforcing steel was modeled using an ANSYS modeling feature that allows the steel to be “smeared” throughout the 3D solid element.

The ANSYS concrete model does not allow for strain softening, but instead the element “crushes”, and the concrete cannot resist any stress at increased strains beyond the crushing stress. The concrete “crushing” must be

“turned off” in the ANSYS concrete material model, for the concrete element to continue to resist stress at increased strains beyond the crushing stress. Similarly, once the tensile strength is reached, the element will crack, i.e. when any principal stress is tensile and reaches the tensile rupture strain. Shear transfer across the crack face is controlled by an input variable, i.e. the percentage of shear transfer across the interface can be specified for both the “crack open” and the “crack closed” condition.

A bilinear material model with an isotropic hardening rule was used for the reinforcing steel in this research. The isotropic hardening rule is suitable for this research since the loading condition is a monotonically increasing function.

The beam’s loading condition is a two point loading configuration that provides a region of constant moment and no shear stresses between the load points. This allows a more accurate measure of flexural strength and deflection, and an easier understanding of the expected cracking patterns. Flexural cracking initiates in the constant moment region. The cracking is vertical since the shear is zero. The cracking outside of the constant moment region is inclined due to shear effects. The depth the section cracks increases as the load is increased.

ANSYS has difficulty in predicting the strength and ductility of a prestressed concrete beam. The ANSYS analysis terminates due to nonconvergence before reaching the ultimate flexural strength loading condition.

ANSYS analysis loading reached about 640 kip-inches, or about 80 to 90 percent of the member's flexural strength as predicted by classical analysis or as determined from the experimental tests. The ANSYS analysis does not predict much of the ductility of the prestressed concrete flexural member. The ANSYS load versus deflection curve results of a typical analysis ends at about 0.5 inches of deflection, or only about 15 percent of the 3.5 inches exhibited during the experimental test.

The ANSYS analysis terminate as the implicit iteration strategy fails to converge. The implicit iteration strategy, Newton's method, does not work well in strain softening situations. The slope of the stress-strain relation tends to zero as the strain softening region is approached, and would actually be negative in the strain softening region. The slope of the stress-strain relation is used to estimate the solution for the next increment. This also explains why the researchers Barbosa & Ribeiro (1998) and Fanning (2001) "turned off" the concrete "crushing" in their ANSYS models in order to get numerical results that produced a plateau on the load-displacement plot, i.e. more ductile flexural behavior.

6.2.2 SUMMARY OF TORNADO SHELTER ANALYSIS

TeraScale's TeraDyn explicit dynamics finite element analysis computer software was used to analyze the reinforced concrete tornado shelter. A 3D solid element mesh was used for the concrete walls and roof slab. TeraScale's steel reinforcement element was used to mesh the reinforcing steel. Reinforcing steel

is modeled as a sub-element within the 3D solid concrete element. Strain compatibility is assumed between concrete and rebar, and no provision is made for bond slip between the reinforcing steel and concrete.

A highly nonlinear ANATECH Corporation's ANAMAT constitutive model, which includes a strain softening region, was used for the concrete material. The ANAMAT constitutive model for concrete is based on smeared cracking methodology and J_2 plasticity theory. Cracks form perpendicular to the principal strain direction, and cracking can form in three orthogonal directions. The tensile stress normal to the crack is reduced to zero, and the stresses around the crack are redistributed. Shear stiffness is reduced upon cracking, and decreases further as cracks open. Crack directions remain fixed. Cracks can open and close, but not "heal".

Concrete material properties used are a concrete compressive strength of 4.0 ksi, an elastic modulus of 3,545 ksi, a Poisson's constant of 0.18, a concrete strain at maximum compressive stress of 0.0022, and a tensile cracking strain of 0.000050.

The constitutive model for the steel characterizes the strain hardening behavior of mild steel. A bilinear stress-strain curve was used for the conventional reinforcing steel. The linear elastic portion of the curve extends to a

yield strength (σ_y) of 60.0 ksi, with a modulus of elasticity (E_s) of 30,000 ksi. The linear strain hardening portion extends to 120 ksi at an equivalent plastic strain of 1.0. A Poisson's ratio of 0.30 was used.

The reinforced concrete above ground residential tornado shelter modeled in this research is based on FEMA's minimum standard. The outside dimensions of the shelter are 8 feet, 4 inches tall by 9 feet, 0 inches wide by 6 feet, 0 inches deep. The wall thickness is 6 inches and the roof slab thickness is 4 inches, which results in a ceiling height of 8 feet, 0 inches and a roof clear span of 5 feet, 0 inches. The walls were fixed along the bottom edges by imposing zero translations for all three degrees of freedom at the nodes along these four edges. The reinforcing steel is as recommended in FEMA's standard design. The walls and ceiling were reinforced with #4 deformed steel bars in each direction at middepth spaced at 12 inches on center each way.

Projectile impact is an important shelter design consideration. FEMA's design impact load for a tornado shelter is a 2" x 4" wood stud weighing about 15 pounds, carried by a 250 mph wind. This is considered equivalent to a 10 feet to 12 feet length of 2" x 4" lumber impacting horizontally onto a vertical wall at about 100 mph, or dropping vertically onto a horizontal roof at about 67 mph.

A moving pressure impulse load was applied to the center of the back face of the tornado shelter. The loading is similar to the blast effect of 10 pounds of TNT detonated at a distance of 22 feet (see Appendix G for the classical analysis and Section 5.2 for an explanation of the blast wave front parameters). The equivalent impulse loading caused by the impact of a 15 pound length of 2 x 4 wood stud striking the shelter at 100 mph is also shown in Appendix G. This projectile, neglecting energy losses due to deformations in the wood and concrete, would be equivalent to this 10 psi pressure applied on about a quarter of the exposed tornado shelter wall. If applied over just the footprint of the stud, the pressure would be over 3,000 psi.

The impulse load used in this analysis is as shown in Figures 47 and 48. A magnitude of 10 psi was used for the peak static overpressure at time zero and distance zero. The impulse load has a duration of about 5 msec. The wave front will still have a magnitude of about 85 percent of its initial peak value after about 15 msec and traveling about 100 inches, a distance greater than the distance the wave front must travel to reach the edge of the shelter.

The analysis duration was 20 msec, with ten 2 msec substeps for data recording. Cracking in the concrete was reviewed at each of the 10 data recording intervals. Cracking initiated at the fixed ends of the wall receiving the loading, and then near the wall's center. Cracking later occurred at the fixed base opposite

the loaded wall. The structure's cracking behavior compares well with that expected for the type of load and geometry of the structure.

A review of the pressure distribution on the structure's deflected shape allows one to visualize the initial inward deformation of the rear wall, and its subsequent rebounding outward movement. The shelter can be seen to globally deflect due to the initial impulse, and then rebound. The shear resistance of the side walls can be seen in the pressure contours.

6.2.3 SUMMARY OF MURRAH BUILDING FLOOR SLAB ANALYSIS

TeraScale's TeraDyn explicit dynamics finite element analysis computer software was used to analyze a bay of the Murrah Building reinforced concrete floor slab subjected to the blast load from the malevolent bombing that occurred in Oklahoma City on April 19, 1995. A 3D solid element mesh was used for the concrete floor slab. TeraScale's steel reinforcement element was used to mesh the reinforcing steel.

ANATECH Corporation's ANAMAT constitutive model was used for the concrete material. Concrete material properties used are a concrete compressive strength of 4.0 ksi, an elastic modulus of 3,545 ksi, a Poisson's constant of 0.18, a concrete strain at maximum compressive stress of 0.0022, and a tensile cracking strain of 0.000050.

The constitutive model for the steel characterizes the strain hardening behavior of mild steel. A bilinear stress-strain curve was used for the conventional reinforcing steel. The linear elastic portion of the curve extends to a yield strength (σ_y) of 60.0 ksi, with a modulus of elasticity (E_s) of 30,000 ksi. The linear strain hardening portion extends to 120 ksi at an equivalent plastic strain of 1.0. A Poisson's ratio of 0.30 was used.

The floor system in the Murrah building was a 6 inch thick concrete one-way floor slab supported continuously along the edges by floor girders. The floor slabs had a clear span between floor girders of 16 feet, 0 inches. The bay of interest is the fifth floor slab located in bay F-G/20-22. The floor slab is a 16 feet, 0 inches by 33 feet, 6 inches by 6 inch thick concrete slab reinforced with mild steel. The slab was fixed along the longer edges by imposing zero translations for all three degrees of freedom at the nodes along these two edges.

Flexural steel and temperature steel consisted of #4, Grade 60 bars. The bottom flexural steel was placed at 9 inches on center. The top flexural steel was placed over the supports at 8 inches on center, and was not continuous at the slab midspan. Temperature steel was placed perpendicular to the flexural steel at 18 inches on center.

Three mesh configurations were used in the analysis. The mesh size used is 6 inches by 6 inches in the plane of the floor slab. Three mesh sizes were used through the 6 inch slab thickness; 3 elements, 6 elements and 12 elements.

The Murrah Building was exposed to the blast from an equivalent of about 4,000 pounds of TNT. This bay of the fifth floor slab experienced a peak static overpressure ranging from a maximum of about 80 psi at the edge nearest the blast epicenter to 36 psi at the far edge. The time of arrival was 9 msec at the near edge and 13 msec at the far edge. The positive phase duration was 24 msec. Therefore, the magnitude of the overpressure at the far edge is only about 37.5 percent of the value at the near edge, while the positive phase duration is about the same.

A moving pressure load was applied to the concrete slab to replicate the wave front experienced at the Murrah building. A difference exists between the blast wave front used in this analysis and estimates of those the Murrah building experienced. The blast wave in this analysis will reach the far edge at about 40 msec after impacting the near edge. The difference in the 4 msec expected time difference and the 40 msec modeled in this analysis will influence the response of the slab to the dynamic loading. The pressure pulse is roughly triangular in shape, with duration of about 5 msec at the near edge and about 10 msec at the far edge. The 10 msec pulse duration at the far edge differs from the 5 msec expected for

the Murrah building. The remaining features of the moving pressure load model used in this analysis are similar to those estimated for the Murrah building.

In the analysis, the slab was subjected to five magnitudes of peak pressure loading, applied to three mesh configurations. The peak pressure loading values used are 1 psi, 3 psi, 5 psi, 10 psi and 20 psi. The mesh configurations are the 3, 6 and 12 element thick meshes. The majority of the analyses terminated when an element Jacobian became zero. The code is under development and an element “death” option is being added to the code to allow the analysis to proceed beyond these occurrences.

A review of the crack progression through time from one of these analyses shows the cracking initiating at the fixed end of the slab nearer the epicenter of the blast wave front. A region of high tensile flexural stress propagates with the blast wave front, and previously open cracks are closed as the deformation propagates. Cracking occurs later at the fixed edge farther from the blast epicenter. The slab deforms upward, as the blast wave moves along the underside of the slab.

The computational results were compared to the values expected from a classical analysis of a foot wide strip of floor slab subjected to a similar impulse load. A qualitative comparison can be made between these predicted and FEM

results curves, but the differences in the applied loadings, and to a lesser extent the differences in the geometry of the structures, do not allow for a quantitative comparison to be made. Both the predicted and the FEM analysis curves illustrate the nonlinearity in the structure's load-deflection response.

6.2.4 SUMMARY OF VALIDATION OF FLOOR SLAB ANALYSIS

A classical analysis was performed of a foot wide strip of floor slab to validate the results of the computer model for the Murrah building fifth floor slab subjected to the blast load. The expected load-deflection response was determined for both a static load and a dynamic load. The predicted dynamic response was then compared to the Murrah building floor slab finite element analysis results.

To further evaluate the computer software, a finite element analysis was performed on the foot width of floor slab used in the classical analysis. Both a quasi-static finite element analysis and impulsive loading finite element analyses were performed and the results compared to the response predicted by the classical analysis.

From a classical analysis, the expected static load-deflection response of the floor slab is linear elastic until slab cracking from large flexural tensile stresses in high moment regions. The slab's load resisting capacity decreases as the cracks develop near the fixed supports. After plastic hinges develop at the

supports, the slab behaves as a simply supported beam. The slab can continue to resist an increase in load until ultimate flexural capacity is achieved as a third plastic hinge develops at midspan, and the concrete crushes due to flexural compressive stresses. The slab will behave similarly with or without reinforcing steel until the slab has cracked. After cracking, the presence of reinforcing steel allows the slab to resist an increasing applied moment until flexural ultimate strength.

Since the impulse load duration is short compared to the natural frequency of the floor slab, the slab can withstand a peak overpressure greater than the static loading. The impulse load-deflection response at the ultimate flexural strength condition is difficult to quantify since the extent of cracking of the Murrah building slab at the moment before the blast event is not known with certainty. The natural period of the structure depends on the structural stiffness, e.g. the extent of slab cracking and the support conditions. In this response prediction, the effective moment of inertia was used to estimate the midspan static deflection and peak impulsive pressure at ultimate flexural strength.

TerraScale's TeraDyn finite element analysis software, and ANATECH Corporation's ANAMAT concrete constitutive relations, were used to simulate the foot wide strip of concrete slab. The foot wide slab model has the same reinforcement pattern as the Murrah building slab. Three meshes were used in the

analysis; one with 3 elements through the slab depth, a second with 6 elements, and a third with 12 elements.

A quasi-static and an impulse loading were performed on the foot wide slab strip to validate the computer software. In the impulsive load analysis, the slab was loaded with a 5 msec duration impulsive pressure loading. The simulations were performed at three magnitudes of peak pressure. These pressures correspond to the loading expected to initiate end region cracking, midspan cracking of a simply supported slab, and flexural failure. Two additional series of simulations were performed on more refined meshes.

In the quasi-static load analysis, the slab was loaded slowly, to prevent any inertial and damping effects in the slab response. The analyses were performed on the medium fine mesh, 6 elements through the slab depth. The value of peak load was selected as the slab's ultimate flexural strength. A second loading equal to half that value was used to investigate if additional resolution could be seen in the slab's response. The loading consisted of a linear ramp load of 0.5 sec duration. Half the loading rate, 1.0 sec load duration, was used in a second series of analysis to investigate the effect of loading rate on this explicit dynamics analysis. Half the peak load values were used in the second series. A second series of analyses were performed for the case of a simply supported floor slab, as a comparison to the results of a slab with fixed ends. The loading rate in the

quasi-static analyses were selected so that maximum load would be achieved in a length of time at least twice the predicted natural frequency of the structure, so as to reduce the inertial and damping effects inherent in an explicit dynamics analysis.

A review of the impulse loading results shows cracking occurring as expected in the regions of high flexural stress.

The quasi-static analysis results compare qualitatively to the predicted results. Stiffness decreases as loading is increased after first cracking. The extent of cracking at the ends and at midspan compares well with the predicted cracking. Flexural strength has not been approached at the time the finite element analysis terminates. The flexural reinforcing steel stress at the time of analysis termination is well below the steel's yield strength.

6.3 CONCLUSIONS

This research emphasizes the importance of the concrete material model on the ability to computationally predict the nonlinear behavior of prestressed concrete flexural members. The research demonstrates the continued progress in nonlinear finite element analysis of reinforced concrete structures, and the likely future contribution for research and commerce. The research also demonstrates the need to improve the method in order to capture more ductile behavior.

Increasingly, structural engineers will use the method in their designs of complex structures, and in research into materials and systems.

6.3.1 CONCLUSIONS FROM PRESTRESSED CONCRETE BEAM ANALYSIS

ANSYS can predict the flexural strength reasonably accurately, but cannot accurately predict the ductility.

Specifically, the conclusions of the research using ANSYS are:

- The ANSYS analysis terminates due to nonconvergence at about 80 to 90 percent of the predicted flexural strength of a prestressed concrete flexural member. The ANSYS analysis terminates because the implicit iteration strategy fails to converge. The implicit iteration strategy, Newton's method, does not work well in strain softening situations. The slope of the stress-strain relation tends to zero as the strain softening region is approached, and would actually be negative in the strain softening region. The slope of the stress-strain relation is used to estimate the solution for the next increment. The ANSYS concrete material model does not have a softening region, but instead the material cannot resist any stress upon reaching the crushing stress.
- ANSYS cannot simulate the ductility of a prestressed concrete flexural member. The ANSYS analysis terminates due to nonconvergence at about 20 percent of the predicted deformation.

- The addition of a user-defined material with separate tension and compression behavior would benefit reinforced concrete modeling with ANSYS.

6.3.2 CONCLUSIONS FROM TORNADO SHELTER ANALYSIS

The TeraDyn program and the ANAMAT constitutive model for concrete can model the nonlinear behavior expected for the impulsive loading of a reinforced concrete tornado shelter structure. The analysis results depicting the structure's cracking behavior compares well with that expected for the type of load and geometry of the structure.

6.3.3 CONCLUSIONS FROM MURRAH BUILDING FLOOR SLAB ANALYSIS

The TeraDyn program and the ANAMAT constitutive model for concrete were shown to capture some of the nonlinear behavior expected for the reinforced concrete one-way slab. The Murrah slab analyses results show the need for improvements in the nonlinear analysis, especially the addition of an element "death" capability.

6.3.4 CONCLUSIONS FROM VALIDATION OF FLOOR SLAB ANALYSIS

The analysis of a one-way floor slab, using the TeraDyn program and the ANAMAT constitutive model, terminates before reaching the highly nonlinear region near the member's flexural strength.

6.4 RECOMMENDATIONS

This research demonstrates the need to improve the nonlinear capabilities of the software. Improvements in the nonlinear analysis are required to capture more ductile behavior of a reinforced concrete structure. The use of increased computing power may allow an analysis of the structure with reduced time steps, finer mesh, longer load durations and larger loadings. Increased computing power required to facilitate a more refined computational model could be obtained through enabling the software to operate on parallel processors. Another approach may be to allow the analysis of a structure to continue after the “death” of an individual element.

Additional analyses should be performed for the quasi-static analysis of the foot wide floor slab. An increased duration of load should be used to further investigate the inertial effects on the analysis results.

REFERENCES

1. ANATECH Corp., (1998), “ANACAP-U / ANAMAT Theory Manual Version 2.5”, ANATECH Corp., San Diego, CA, April.
2. ANSYS, Inc., (2003), “ANSYS 8.0 Documentation”, ANSYS, Inc., Canonsburg, PA.
3. Army, Headquarters Department of the, (1998), “Technical Manual Fundamentals Of Protective Design For Conventional Weapons”, TM 5-855-1.
4. Balan, T. A., Spacone, E. and Kwon, M., (2001), **Engineering and Structures**, Vol. 23, No. 4, pp. 333-42.
5. Barbosa, A. F., and Ribeiro, G. O. (1998), “Analysis of Reinforced Concrete Structures Using ANSYS Nonlinear Concrete Model”, **Computational Mechanics, New Trends and Applications**, CIMNE, Barcelona, Spain.
6. Bazant, Z. P., and Cedolin, L., (1991), **Stability of Structures: Elastic, Inelastic, Fracture and Damage Theories**, Oxford University Press, New York, New York.
7. Benson, D. J., (1991), “Computational Methods In Lagrangian and Eulerian Hydrocodes”, **Computer Methods in Applied Mechanics and Engineering**, (1992), pp. 235-394.
8. Bittnar, Z., and Sejnoha, J., (1996), **Numerical Methods in Structural Mechanics**, ASCE Press, New York, New York.
9. Boresi, A. P., and Chong, K. P., (1987), **Elasticity in Engineering Mechanics**, Elsevier Science Publishing Co., Inc, New York, New York.
10. Chen, W. F., and Han, D. J., (1995), **Plasticity for Structural Engineers**, Gau Lih Nook Co., Ltd., Taipei, Taiwan.
11. Chin, M. P., (2001), “Laboratory Testing and Constitutive Modeling of High Performance Concrete (HPC)”, Masters Thesis, University of Oklahoma, Norman, OK, August.

12. Dowell, R. K., and Dunham, R. S., (2000), "Application of a Confined Concrete Model to Passively Confined Concrete Columns", 14th Engineering Mechanics Conference, Austin, Texas, May.
13. Fanning, P., (2001), "Nonlinear Models of Reinforced and Post-Tensioned Concrete Beams", **Electronic Journal of Structural Engineering**, Vol. 2, pp. 111-119.
14. Federal Emergency Management Agency, (1996), "The Oklahoma City Bombing: Improving Building Performance Through Multi-Hazard Mitigation", FEMA Publication 277, August.
15. Federal Emergency Management Agency, (1999), "National Performance Criteria for Tornado Shelters", May.
16. Federal Emergency Management Agency, (2000), "Design and Construction Guidance for Community Shelters", FEMA Publication 361, July
17. Federal Emergency Management Agency, (2003), "Tornado Protection: Selecting Refuge Areas in Buildings", FEMA Publication 431, November.
18. Federal Emergency Management Agency, (2004), "Taking Shelter from the Storm: Building a Safe Room Inside Your House", FEMA Publication 330, March.
19. Fujita, T. T., (1971), "Proposed Characterization of Tornadoes and Hurricanes by Area and Intensity", SMRP No. 91, University of Chicago, Chicago, IL,
20. Gerstle, K. H., (1981), "Simple Formulation of Biaxial Concrete Behavior", **Journal of the American Concrete Institute**, Vol. 78, No. 1, pp. 62-8.
21. Han, D. J., and Chen, W. F., (1986), "On Strain-Space Plasticity Formulation for Hardening-Softening Materials with Elasto-Plastic Coupling", **International Journal of Solids and Structures**, Vol. 22, No. 8, pp. 935-950.
22. Horowitz, B., (1997), "Singularities in Elastic Finite Element Analysis", **Concrete International**, Vol. 19, No. 12, December, pp. 33-36.
23. Jirasek, M., and Bazant, Z. P., (2002), **Inelastic Analysis of Structures**, John Wiley & Sons, Inc., New York, New York.

24. Kubischta, K. E., Rashid, Y. R., and Dunham, R. S., (2003), "Predictive Analysis of a 1/3 - Scale Reinforced Concrete Building, Report to CAMUS International Benchmark", ANATECH Corp., San Diego, CA., May 30.
25. Kwon, M., & Spacone, E. (2002), "Three-Dimensional Finite Element Analysis of Reinforced Concrete Columns", **Computers and Structures**, Vol. 80, pp. 199-212.
26. Mander, J. B., Priestly, M. J. N., and Park, R., (1984), "Seismic Design of Bridge Piers", Report 84-2, Department of Civil Engineering, University of Canterbury, Christchurch, New Zealand, February.
27. Mander, J. B., Priestly, M. J. N., and Park, R., (1988), "Observed Stress-Strain Behavior of Confined Concrete", **Journal of Structural Engineering**, ASCE, Vol. 114, No. 8, pp. 1827-1849, August.
28. Monroe, J. S., and Dobmeier, J, (2003), "Cost Savings with Finite Element Modeling, The Structural Design of the Hill Seaton Reservoir Riser", **Structural Engineer**, Vol.4, No. 2, pp. 30-32.
29. Nawy, E. G., (1996), **Prestressed Concrete**, Prentice-Hall, Inc., Upper Saddle River, New Jersey.
30. Paulsgrove, G. A., (1996), "Fundamental Mechanisms for the Development of Pretensioned Strands", Masters Thesis, University of Oklahoma, Norman, OK, January.
31. Rashid, Y. R., (1968), "Ultimate Strength Analysis of Prestressed Concrete Pressure Vessels", **Nuclear Engineering and Design**, Vol. 7, pp. 334-344.
32. Rose, D. R., (1995), "Measurement of Bond Performance; Correlation of Pull-Out Strength with Transfer Length", Masters Thesis, University of Oklahoma, Norman, OK, April.
33. Smith, P. D., and Hetherington, J. G., (1994), **Blast and Ballistic Loading of Structures**, Butterworth-Heinemann, Ltd., Oxford.
34. Willam, K. J., and Warnke, E. P., (1975), "Constitutive Model for the Triaxial Behavior of Concrete", Proceedings of the International Association of Bridge and Structural Engineers, Vol. 19, pp. 1-30.

LIST OF APPENDICES

	Page
APPENDIX A RECTANGULAR BEAM CA3-S TEST DATA	213
APPENDIX B RECTANGULAR BEAM ANSYS TEST DATA	222
APPENDIX C PLAIN CONCRETE RECTANGULAR BEAM	237
APPENDIX D FUJITA TORNADO DAMAGE SCALE	239
APPENDIX E USING TERASCALE'S MESHER PROGRAM	241
APPENDIX F USING TERASCALE'S TERADYN PROGRAM	256
APPENDIX G TORNADO SHELTER IMPACT LOAD PROPERTIES	259
APPENDIX H TORNADO SHELTER HYDROSTATIC PRESSURE	262
APPENDIX I MURRAH FLOOR SLAB MEMBER PROPERTIES	268
APPENDIX J MURRAH SLAB MOVING PRESSURE LOADING	271
APPENDIX K MURRAH SLAB LOAD-DEFLECTION RESPONSE	283
APPENDIX L MURRAH SLAB FLEXURAL STRESS	303
APPENDIX M FOOT SLAB QUASI-STATIC LOAD-DEFLECTION	309
APPENDIX N LITERATURE REVIEW	312

APPENDIX A RECTANGULAR BEAM CA3-S TEST DATA

This appendix contains a summary of the experimental flexural test on a prestressed concrete rectangular beam, Beam CA3-S (Paulsgrove 1996).

	Page
Beam CA3-S Experimental Test Diary	214
Beam CA3-S Load-Deflection And Crack Pattern Data	215
Beam CA3-S Load Diagram Computation	216
Beam CA3-S Moment-Curvature Relation	217
Beam CA3-S Geometry And Reinforcement	218
Beam CA3-S Predicted Deflection	219
Prestressed Beam Flexural Failure	220
Prestressed Beam Bond Failure	221

BEAM CA3-S

Test Parameters:

Lt = 19.2 inches
Ld Predicted = 41.1 inches
Le = 60 inches
Span = 192 inches
Failure Mode: Flexural
Maximum Moment: 703 kip-inches

Test Summary:

Loaded beam to 13 kips in increments of 500 pounds. Took electronic data measurements of load, deflection and end slips.

DEMEC readings taken at:

0.0 kips 6.5 kips 10.0 kips 11.5 kips 13.0 kips

First cracking observed at beam station 75 at 11.5 kips (411 kip-inches). Unloaded beam and took electronic data at 500 pound increments. Loaded beam and took electronic data at 500 pound increments.

DEMEC readings taken at:

0.0 kips	2.5 kips	5.0 kips	7.5 kips
10.0 kips	12.5 kips	14.0 kips	16.0 kips
18.0 kips	18.5 kips		
3.00 inches deflection	3.35 inches deflection	3.6 inches	

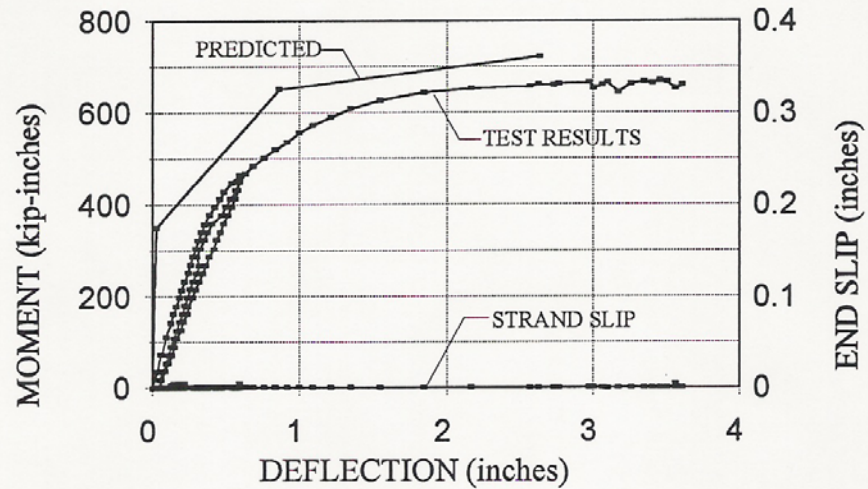
deflection

Crack Patterns: Flexural cracking was first observed at beam station 75 in the constant moment region under the load spreader beam at 11.5 kips (411 kip-inches).. As loading was increased, the cracking progressed up the cross section. Additional cracks developed along the length at beam stations 43, 50, 56, 60, 67, 80, 83, 91, 101, 111 and 120, progressing from the region of highest moment towards the supports. The average crack spacing is 7.0 inches. The flexural cracks which initiated in the shear region of the beam inclined toward the load points. Concrete crushing was observed between the load points

End Slips: No end slips observed.

Failure Mode: The failure mode was determined to be flexural. Moment at failure was measured at 703 kip-inches. The predicted nominal moment is 723 kip-inches. Concrete crushing was observed between load points. No end slips were measured. Note that flexural failure was predicted since the predicted development length (Ld) of 41.1 inches is much less than the tested embedment length (Le) of 60 inches.

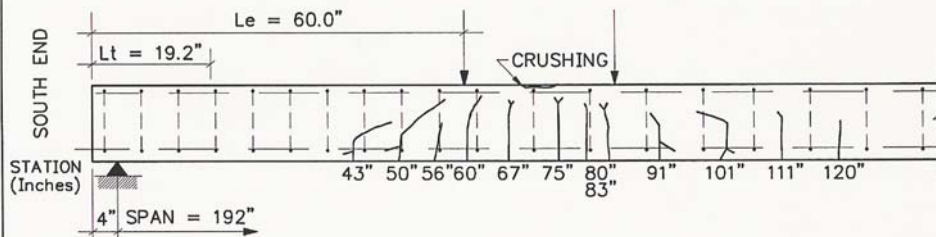
FLEXURAL FAILURE



1 kip-inch = 0.1130 kN·m

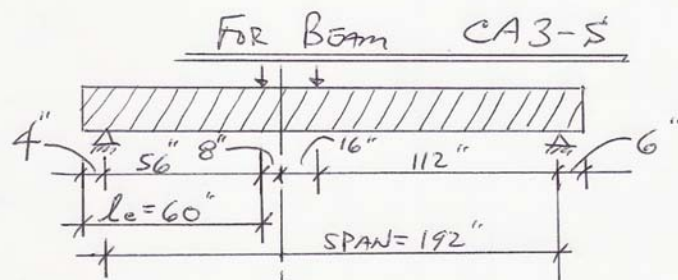
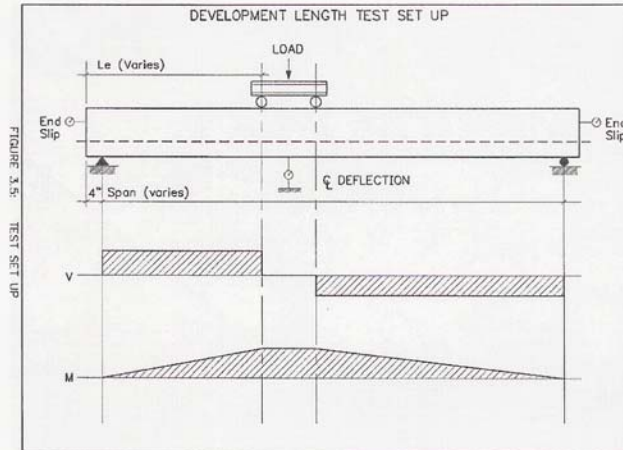
1 inch = 25.4 mm

BEAM CA3-S MOMENT vs. DEFLECTION AND END SLIPS



CRACKING PATTERN
BEAM CA3-S EAST ELEV

1" = 25.4 mm



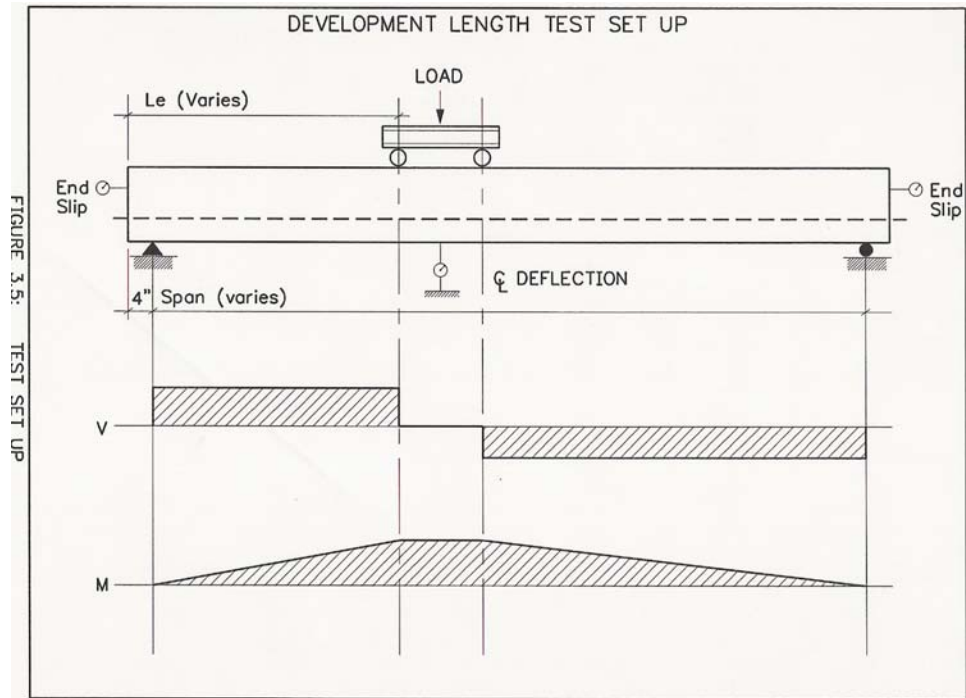
$$M_u = 742,700 \text{ #-in} = V_L (l_e - 4) = V_L (60 - 4)$$

$$V_L = \frac{742,700}{56} = 13,263 \text{ #}$$

$$P_u = \frac{V_L (24)}{b} = \frac{13,263 (24)}{16} = 19,890 \text{ #}$$

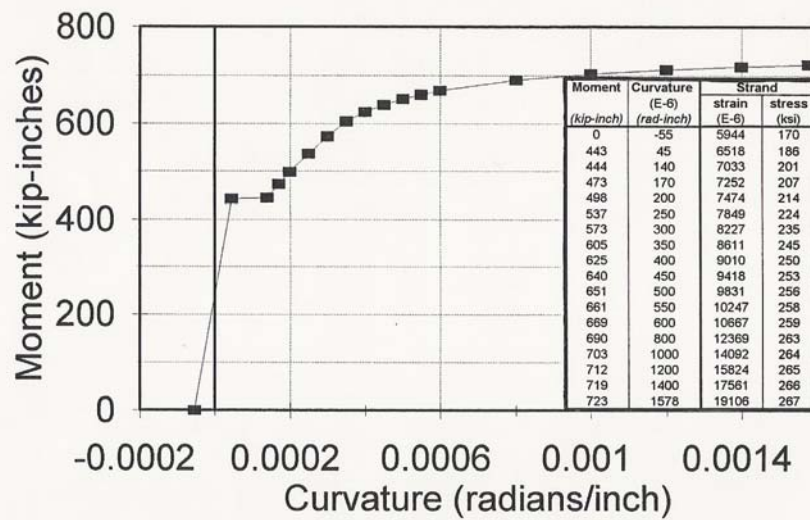
$$V_R = \frac{P_u}{24} = \frac{19,890 (8)}{24} = 6,630 \text{ #}$$

$$a = \left(\frac{l_e - 4}{l - 24} \right) 24 = \left(\frac{60 - 4}{192 - 24} \right) 24 = 8.0 ; b = 24 - 8$$



MOMENT - CURVATURE

Figure 2.10: Moment vs Curvature



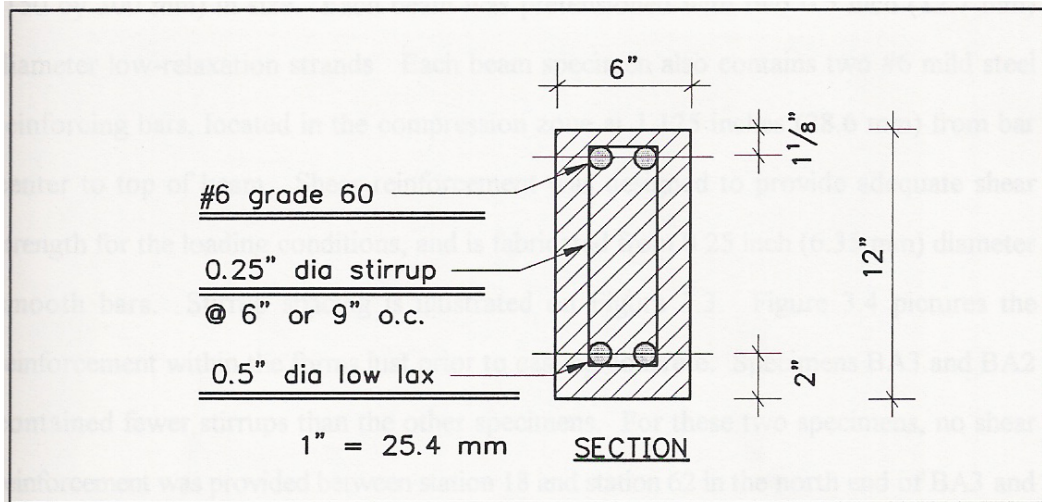


FIGURE 3.2: BEAM CROSS SECTION

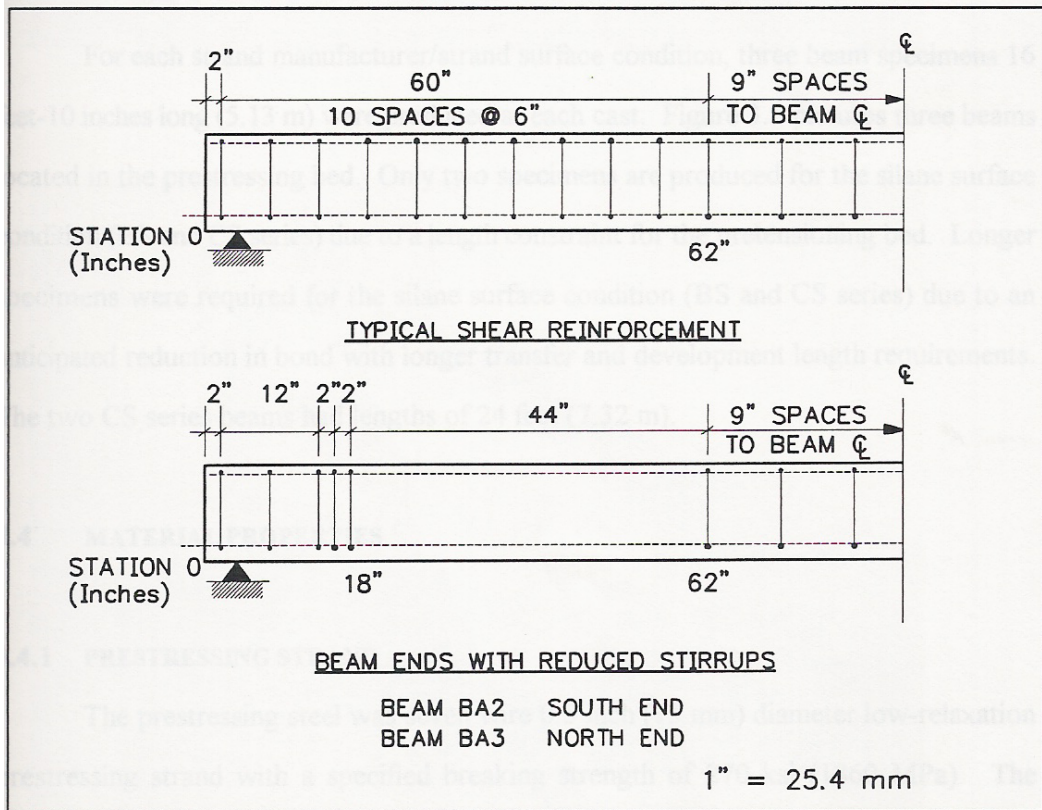


FIGURE 3.3: SHEAR REINFORCEMENT

DEFLECTIONS				
SPAN (inches)	Le (inches)	Mo (inches)	$\phi = 0.0005$ M (inches)	Mn (inches)
112	32	0.014	0.276	1.108
112	36	0.014	0.269	1.148
112	40	0.159	0.750	1.161
112	42	0.015	0.252	1.183
112	44	0.015	0.244	1.188
112	46	0.015	0.236	1.190
112	48	0.015	0.227	1.188
142	52	0.019	0.433	1.705
192	52	0.025	0.866	2.491
192	60	0.026	0.862	2.636
280	120	0.208	3.041	5.986

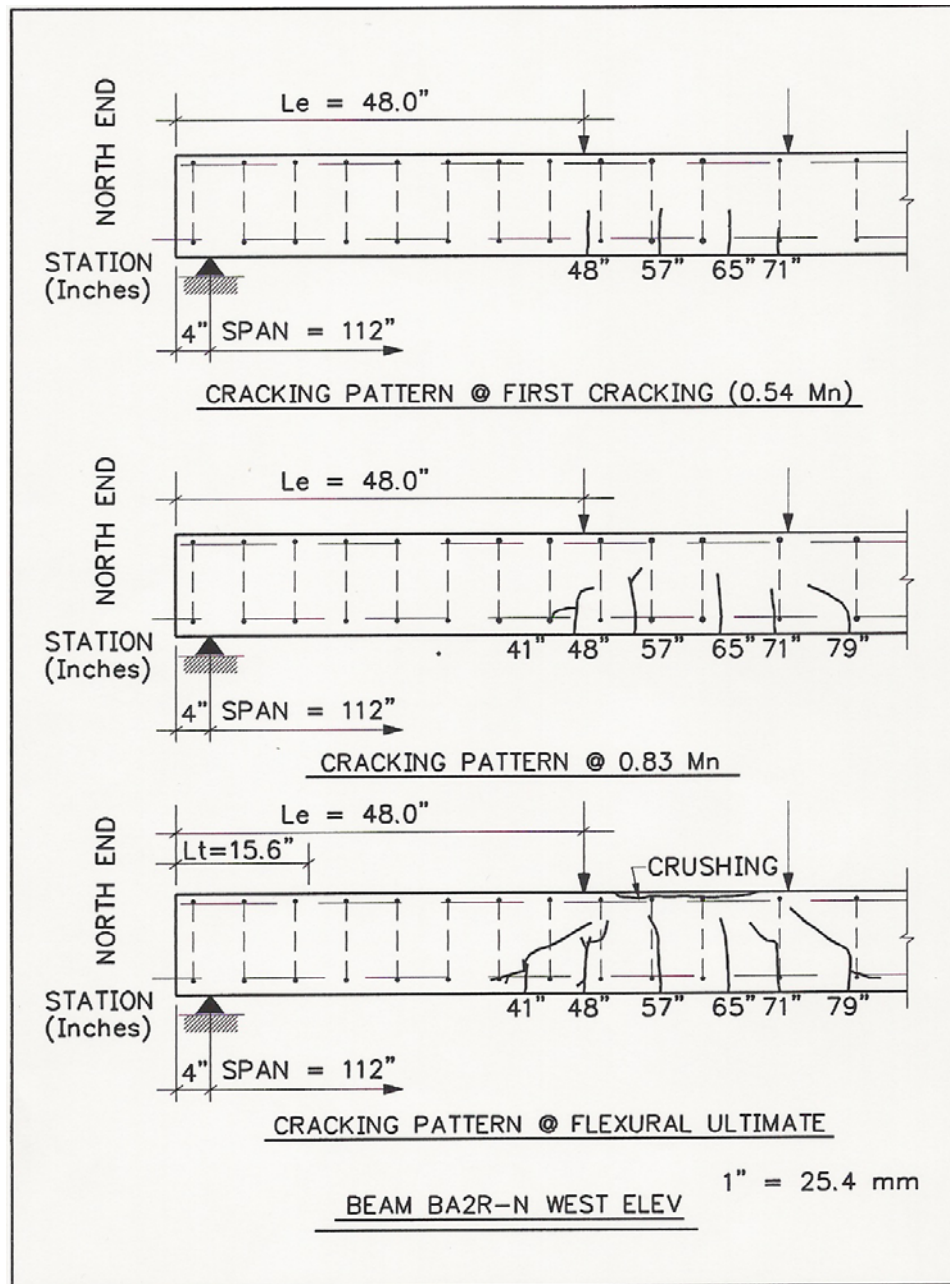


FIGURE 4.2: CRACKING PROGRESSION OF FLEXURAL FAILURE

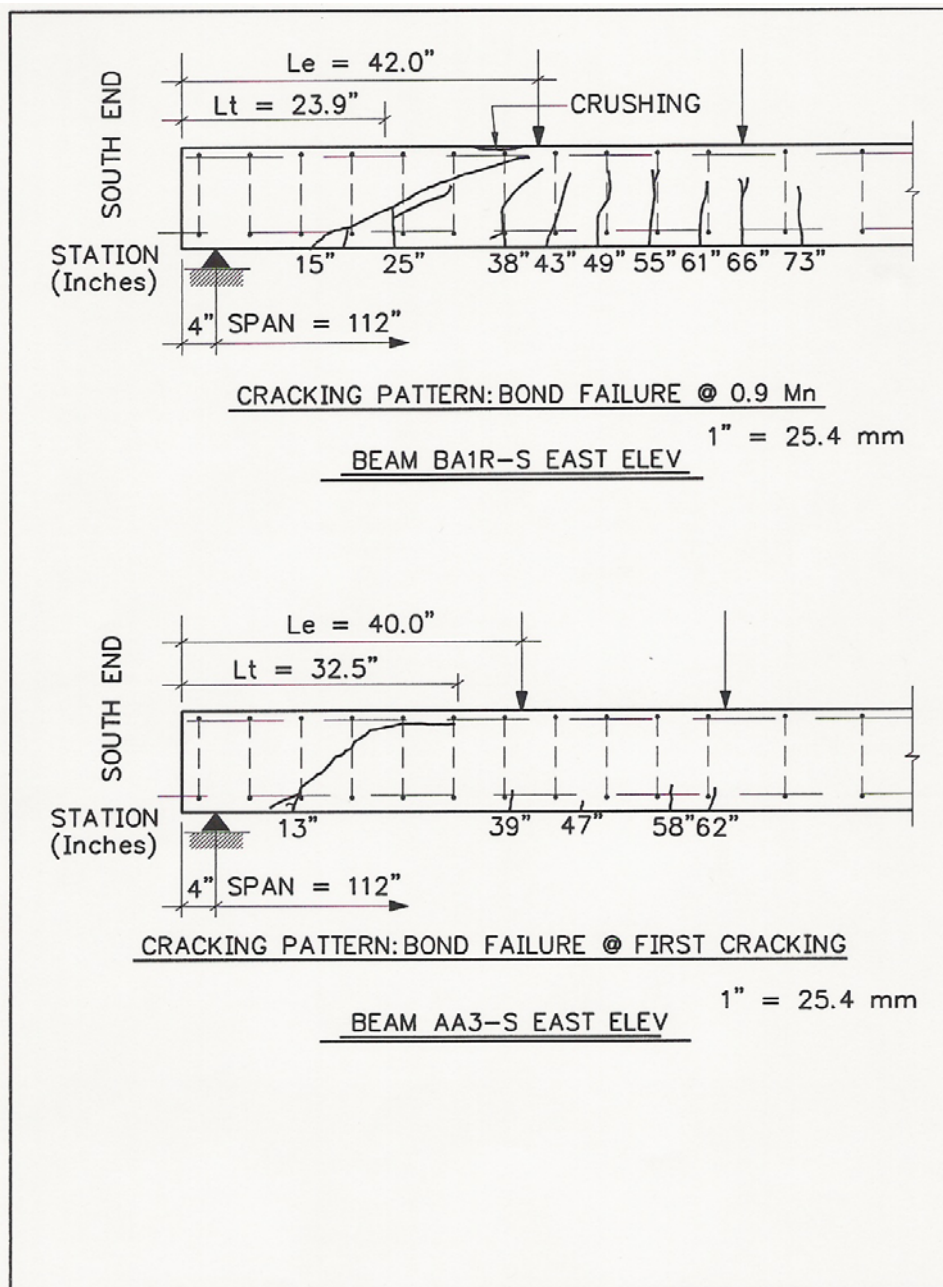


FIGURE 4.3: CRACKING PROGRESSION OF BOND FAILURE

APPENDIX B RECTANGULAR BEAM ANSYS TEST DATA

This appendix contains a copy of the ANSYS “*.lgw” implicit dynamics finite element analysis input file prepared to compute the load-deflection response of a prestressed concrete rectangular beam. An initial time step was used to transfer the prestress force from the prestressing steel strands to the concrete. The implicit dynamics solution followed after completion of the initial time step.

ANSYS “ *.lgw ” FILE

```

/FILNAME,psbeam,0
/TITLE,Prestressed Concrete Beam
!*
/NOPR
/PMETH,OFF,0
KEYW,PR_SET,1
KEYW,PR_STRUC,1
KEYW,PR_THERM,0
KEYW,PR_FLUID,0
KEYW,PR_ELMAG,0
KEYW,MAGNOD,0
KEYW,MAGEDG,0
KEYW,MAGHFE,0
KEYW,MAGELC,0
KEYW,PR_MULTI,0
KEYW,PR_CFD,0
/GO
/PREP7
!*
!*
!*
ET,1,SOLID65
!*
ET,2,LINK180
!*
ET,3,PRETS179
!*
!*
!*
R,1,,,,,
RMORE,,,,,
!*
R,2,2,0.00272,90,0,0,0,
RMORE,0,0,0,0,0,
!*
R,3,,44,,000323,
!*
R,4,0.153,0.000112,
!*
!*
!*
MPTEMP,,,,,,,,
MPTEMP,1,0
MPDATA,EX,1,,4415000
MPDATA,PRXY,1,,2
TB,CONC,1,1,9,
TBTEMP,0
TBDATA,,9,,95,581,6000,,
TBDATA,,,,,,,,
MPTEMP,,,,,,,,
MPTEMP,1,0
MPDATA,DENS,1,,000216
!*
!*
MPTEMP,,,,,,,,
MPTEMP,1,0
MPDATA,EX,2,,29000000
MPDATA,PRXY,2,,3
TB,BISO,2,1,2,
TBTEMP,0
TBDATA,,50000,290000,,,
MPTEMP,,,,,,,,
MPTEMP,1,0

```

```

MPDATA,DENS,2,,.000734
!*
!*
MPTEMP,,,,,,,,
MPTEMP,1,0
MPDATA,EX,3,,29000000
MPDATA,PRXY,3,,.3
TB,BISO,3,1,2,
TBTEMP,0
TBDATA,,60000,290000,,,,
MPTEMP,,,,,,,,
MPTEMP,1,0
MPDATA,DENS,3,,.000734
!*
!*
MPTEMP,,,,,,,,
MPTEMP,1,0
MPDATA,EX,4,,28600000
MPDATA,PRXY,4,,.3
TB,BISO,4,1,2,
TBTEMP,0
TBDATA,,270000,28600,,,,
MPTEMP,,,,,,,,
MPTEMP,1,0
MPDATA,DENS,4,,.000734
!*
!*
!*
*SET,a,6
*SET,b,12
*SET,c,202
*SET,d,8
*SET,e,16
*SET,f,60
*SET,g,4
*SET,h,192
*SET,x1,2
*SET,x2,4
*SET,y1,2
*SET,y2,10.875
!*
!*
!*
K,1,x1,y1,0,,,,
K,2,x1,y1,g,,,,
K,3,x1,y1,f,,,,
K,4,x1,y1,f+d,,,,
K,5,x1,y1,f+d+e,,,,
K,6,x1,y1,g+h,,,,
K,7,x1,y1,c,,,,
!*
K,8,x2,y1,0,,,,
K,9,x2,y1,g,,,,
K,10,x2,y1,f,,,,
K,11,x2,y1,f+d,,,,
K,12,x2,y1,f+d+e,,,,
K,13,x2,y1,g+h,,,,
K,14,x2,y1,c,,,,
!*
KSEL,S,KP,,1,14,,
CM,STRANDKP,KP
KATT, 4, 4, 2, 0
!*
/REPLOT,RESIZE
/VIEW,1,1,1,1
/ANG,1

```

```

/REP,FAST
!*
!*
K,15,x2,y2,0,,,
K,16,x2,y2,g,,,
K,17,x2,y2,f,,,
K,18,x2,y2,f+d,,,
K,19,x2,y2,f+d+e,,,
K,20,x2,y2,g+h,,,
K,21,x2,y2,c,,,
!*
K,22,x1,y2,0,,,
K,23,x1,y2,g,,,
K,24,x1,y2,f,,,
K,25,x1,y2,f+d,,,
K,26,x1,y2,f+d+e,,,
K,27,x1,y2,g+h,,,
K,28,x1,y2,c,,,
!*
KSEL,S,KP,,15,28,,,
CM,REBARKP,KP
KATT, 3, 3, 2, 0
!*
/REPLOT,RESIZE
/VIEW,1,1,1,1
/ANG,1
/REP,FAST
!*
!*
!*
KSEL,S,MAT,,4
!*
LSTR, 1, 2
LSTR, 2, 3
LSTR, 3, 4
LSTR, 4, 5
LSTR, 5, 6
LSTR, 6, 7
!*
LSTR, 8, 9
LSTR, 9, 10
LSTR, 10, 11
LSTR, 11, 12
LSTR, 12, 13
LSTR, 13, 14
!*
LSEL,S,LINE,,1,12,,,
CM,STRANDL,LINE
LATT, 4, 4, 2, 0, , ,
!*
LESIZE, 1, , , 2, , , , 0
LESIZE, 2, , , 28, .5, , , , 0
LESIZE, 3, , , 4, , , , , 0
LESIZE, 4, , , 8, , , , , 0
LESIZE, 5, , , 56, 2, , , , 0
LESIZE, 6, , , 3, , , , , 0
!*
LESIZE, 7, , , 2, , , , , 0
LESIZE, 8, , , 28, .5, , , , 0
LESIZE, 9, , , 4, , , , , 0
LESIZE, 10, , , 8, , , , , 0
LESIZE, 11, , , 56, 2, , , , 0
LESIZE, 12, , , 3, , , , , 0
!*
/REPLOT,RESIZE
/VIEW,1,1,1,1

```

```

/ANG,1
/REP,FAST
!*
!*
KSEL,S,MAT,,3
!*
LSTR, 15, 16
LSTR, 16, 17
LSTR, 17, 18
LSTR, 18, 19
LSTR, 19, 20
LSTR, 20, 21
!*
LSTR, 22, 23
LSTR, 23, 24
LSTR, 24, 25
LSTR, 25, 26
LSTR, 26, 27
LSTR, 27, 28
!*
LSEL,S,LINE,,13,24,,
CM,REBARL,LINE
LATT, 3, 3, 2, 0, , ,
!*
LESIZE, 13, , , 2, , , , 0
LESIZE, 14, , , 28, .5, , , , 0
LESIZE, 15, , , 4, , , , 0
LESIZE, 16, , , 8, , , , 0
LESIZE, 17, , , 56, 2, , , , 0
LESIZE, 18, , , 3, , , , , 0
!*
LESIZE, 19, , , 2, , , , , 0
LESIZE, 20, , , 28, .5, , , , 0
LESIZE, 21, , , 4, , , , , 0
LESIZE, 22, , , 8, , , , , 0
LESIZE, 23, , , 56, 2, , , , 0
LESIZE, 24, , , 3, , , , , 0
!*
/REPLOT,RESIZE
/VIEW,1,1,1,1
/ANG,1
/REP,FAST
!*
!*
!*
CMSEL,S,STRANDL,LINE
LMESH,STRANDL,,
!*
/REPLOT,RESIZE
/VIEW,1,1,1,1
/ANG,1
/REP,FAST
!*
!*
CMSEL,S,REBARL,LINE
LMESH,REBARL,,
!*
/REPLOT,RESIZE
/VIEW,1,1,1,1
/ANG,1
/REP,FAST
!*
!*
BLOCK,0,a,0,y1,0,g,
BLOCK,0,a,y1,y2,0,g,

```

```

BLOCK,0,a,y2,b,0,g,
BLOCK,0,a,0,y1,g,f,
BLOCK,0,a,y1,y2,g,f,
BLOCK,0,a,y2,b,g,f,
BLOCK,0,a,0,y1,f,f+d,
BLOCK,0,a,y1,y2,f,f+d,
BLOCK,0,a,y2,b,f,f+d,
BLOCK,0,a,0,y1,f+d,f+d+e,
BLOCK,0,a,y1,y2,f+d,f+d+e,
BLOCK,0,a,y2,b,f+d,f+d+e,
BLOCK,0,a,0,y1,f+d+e,g+h,
BLOCK,0,a,y1,y2,f+d+e,g+h,
BLOCK,0,a,y2,b,f+d+e,g+h,
BLOCK,0,a,0,y1,g+h,c,
BLOCK,0,a,y1,y2,g+h,c,
BLOCK,0,a,y2,b,g+h,c,
GPLOT
!*
!*
!*
VSEL,ALL
!*
/REPLOT,RESIZE
/VIEW,1,1,1,1
/ANG,1
/REP,FAST
!*
!*
!*
VGLUE,ALL
!*
!*
VSEL,ALL
!*
VATT, 1, 2, 1, 0
!*
!*
/REPLOT,RESIZE
/VIEW,1,1,1,1
/ANG,1
/REP,FAST
!*
!*
!*
LSEL,S,LINE,,25,308,,
CM,CONCRETEL,LINE
CMSEL,,CONCRETEL
!*
LATT, 1, 2, 1, 0, , ,
!*
!*
LSEL,S,LINE,,33,36,,
CM,CONCRETELA,LINE
LESIZE,CONCRETELA, , , 2, , , , 0
!*
LSEL,S,LINE,,47,48,,
CM,CONCRETELB,LINE
LESIZE,CONCRETELB, , , 2, , , , 0
!*
LSEL,S,LINE,,59,60,,
CM,CONCRETELC,LINE
LESIZE,CONCRETELC, , , 2, , , , 0
!*
LSEL,S,LINE,,241,244,,
CM,CONCRETELD,LINE
LESIZE,CONCRETELD, , , 28, .5, , , , 0

```



```

!*
LSEL,S,LINE,,269,270,,,
CM,CONCRETELE,LINE
LESIZE,CONCRETELE, , , 28, .5, , , , 0
!*
LSEL,S,LINE,,273,274,,,
CM,CONCRETELF,LINE
LESIZE,CONCRETELF, , , 28, .5, , , , 0
!*
LSEL,S,LINE,,253,256,,,
CM,CONCRETELG,LINE
LESIZE,CONCRETELG, , , 4, , , , , 0
!*
LSEL,S,LINE,,277,278,,,
CM,CONCRETELH,LINE
LESIZE,CONCRETELH, , , 4, , , , , 0
!*
LSEL,S,LINE,,281,282,,,
CM,CONCRETELI,LINE
LESIZE,CONCRETELI, , , 4, , , , , 0
!*
LSEL,S,LINE,,257,260,,,
CM,CONCRETELJ,LINE
LESIZE,CONCRETELJ, , , 8, , , , , 0
!*
LSEL,S,LINE,,285,286,,,
CM,CONCRETELK,LINE
LESIZE,CONCRETELK, , , 8, , , , , 0
!*
LSEL,S,LINE,,289,290,,,
CM,CONCRETELL,LINE
LESIZE,CONCRETELL, , , 8, , , , , 0
!*
LSEL,S,LINE,,261,264,,,
CM,CONCRETELM,LINE
LESIZE,CONCRETELM, , , 56, 2, , , , 0
!*
LSEL,S,LINE,,293,294,,,
CM,CONCRETELN,LINE
LESIZE,CONCRETELN, , , 56, 2, , , , 0
!*
LSEL,S,LINE,,297,298,,,
CM,CONCRETELO,LINE
LESIZE,CONCRETELO, , , 56, 2, , , , 0
!*
LSEL,S,LINE,,265,268,,,
CM,CONCRETELP,LINE
LESIZE,CONCRETELP, , , 3, , , , , 0
!*
LSEL,S,LINE,,301,302,,,
CM,CONCRETELQ,LINE
LESIZE,CONCRETELQ, , , 3, , , , , 0
!*
LSEL,S,LINE,,305,306,,,
CM,CONCRETELR,LINE
LESIZE,CONCRETELR, , , 3, , , , , 0
!*
!*
LSEL,S,LINE,,26,,,,
CM,CONCRETELAA,LINE
LESIZE,CONCRETELAA, , , 3, , , , , 0
!*
LSEL,S,LINE,,28,,,,
CM,CONCRETELB,LINE
LESIZE,CONCRETELB, , , 3, , , , , 0
!*

```

```

LSEL,S,LINE,,38,,,,
CM,CONCRETELCC,LINE
LESIZE,CONCRETELCC, , , 3, , , , 0
!*
LSEL,S,LINE,,50,,,,
CM,CONCRETELDD,LINE
LESIZE,CONCRETELDD, , , 3, , , , 0
!*
LSEL,S,LINE,,29,,,,
CM,CONCRETELEE,LINE
LESIZE,CONCRETELEE, , , 3, , , , 0
!*
LSEL,S,LINE,,31,,,,
CM,CONCRETELFF,LINE
LESIZE,CONCRETELFF, , , 3, , , , 0
!*
LSEL,S,LINE,,43,,,,
CM,CONCRETELGG,LINE
LESIZE,CONCRETELGG, , , 3, , , , 0
!*
LSEL,S,LINE,,55,,,,
CM,CONCRETELHH,LINE
LESIZE,CONCRETELHH, , , 3, , , , 0
!*
LSEL,S,LINE,,65,,,,
CM,CONCRETELII,LINE
LESIZE,CONCRETELII, , , 3, , , , 0
!*
LSEL,S,LINE,,67,,,,
CM,CONCRETELJJ,LINE
LESIZE,CONCRETELJJ, , , 3, , , , 0
!*
LSEL,S,LINE,,79,,,,
CM,CONCRETELKK,LINE
LESIZE,CONCRETELKK, , , 3, , , , 0
!*
LSEL,S,LINE,,91,,,,
CM,CONCRETELLL,LINE
LESIZE,CONCRETELLL, , , 3, , , , 0
!*
LSEL,S,LINE,,101,,,,
CM,CONCRETEMMM,LINE
LESIZE,CONCRETEMMM, , , 3, , , , 0
!*
LSEL,S,LINE,,103,,,,
CM,CONCRETELNN,LINE
LESIZE,CONCRETELNN, , , 3, , , , 0
!*
LSEL,S,LINE,,115,,,,
CM,CONCRETELOO,LINE
LESIZE,CONCRETELOO, , , 3, , , , 0
!*
LSEL,S,LINE,,127,,,,
CM,CONCRETELPP,LINE
LESIZE,CONCRETELPP, , , 3, , , , 0
!*
LSEL,S,LINE,,137,,,,
CM,CONCRETELQQ,LINE
LESIZE,CONCRETELQQ, , , 3, , , , 0
!*
LSEL,S,LINE,,139,,,,
CM,CONCRETELRR,LINE
LESIZE,CONCRETELRR, , , 3, , , , 0
!*
LSEL,S,LINE,,151,,,,
CM,CONCRETESSS,LINE

```

```

LESIZE,CONCRETELSS, , , 3, , , , 0
!*
LSEL,S,LINE,,163,,,,
CM,CONCRETELTT,LINE
LESIZE,CONCRETELTT, , , 3, , , , 0
!*
LSEL,S,LINE,,173,,,,
CM,CONCRETELUU,LINE
LESIZE,CONCRETELUU, , , 3, , , , 0
!*
LSEL,S,LINE,,175,,,,
CM,CONCRETELVV,LINE
LESIZE,CONCRETELVV, , , 3, , , , 0
!*
LSEL,S,LINE,,187,,,,
CM,CONCRETELWW,LINE
LESIZE,CONCRETELWW, , , 3, , , , 0
!*
LSEL,S,LINE,,199,,,,
CM,CONCRETELXX,LINE
LESIZE,CONCRETELXX, , , 3, , , , 0
!*
LSEL,S,LINE,,209,,,,
CM,CONCRETELYY,LINE
LESIZE,CONCRETELYY, , , 3, , , , 0
!*
LSEL,S,LINE,,211,,,,
CM,CONCRETELZZ,LINE
LESIZE,CONCRETELZZ, , , 3, , , , 0
!*
LSEL,S,LINE,,223,,,,
CM,CONCRETELZ,LINE
LESIZE,CONCRETELZ, , , 3, , , , 0
!*
LSEL,S,LINE,,235,,,,
CM,CONCRETELY,LINE
LESIZE,CONCRETELY, , , 3, , , , 0
!*
!*
LSEL,S,LINE,,25,,,,
CM,CONCRETELA AAA,LINE
LESIZE,CONCRETELA AAA, , , 1, , , , 0
!*
LSEL,S,LINE,,27,,,,
CM,CONCRETELBBB,LINE
LESIZE,CONCRETELBBB, , , 1, , , , 0
!*
LSEL,S,LINE,,30,,,,
CM,CONCRETELCCC,LINE
LESIZE,CONCRETELCCC, , , 1, , , , 0
!*
LSEL,S,LINE,,32,,,,
CM,CONCRETELD D D D,LINE
LESIZE,CONCRETELD D D D, , , 1, , , , 0
!*
LSEL,S,LINE,,66,,,,
CM,CONCRETELEEEE,LINE
LESIZE,CONCRETELEEEE, , , 1, , , , 0
!*
LSEL,S,LINE,,68,,,,
CM,CONCRETELFFF,LINE
LESIZE,CONCRETELFFF, , , 1, , , , 0
!*
LSEL,S,LINE,,102,,,,
CM,CONCRETELG G G,LINE
LESIZE,CONCRETELG G G, , , 1, , , , 0

```

```

!*
LSEL,S,LINE,,104,,,
CM,CONCRETELHHH,LINE
LESIZE,CONCRETELHHH, , , 1, , , , 0
!*
LSEL,S,LINE,,138,,,
CM,CONCRETELIII,LINE
LESIZE,CONCRETELIII, , , 1, , , , 0
!*
LSEL,S,LINE,,140,,,
CM,CONCRETELJJJ,LINE
LESIZE,CONCRETELJJJ, , , 1, , , , 0
!*
LSEL,S,LINE,,174,,,
CM,CONCRETELKKK,LINE
LESIZE,CONCRETELKKK, , , 1, , , , 0
!*
LSEL,S,LINE,,176,,,
CM,CONCRETELLLL,LINE
LESIZE,CONCRETELLLL, , , 1, , , , 0
!*
LSEL,S,LINE,,210,,,
CM,CONCRETELMMM,LINE
LESIZE,CONCRETELMMM, , , 1, , , , 0
!*
LSEL,S,LINE,,212,,,
CM,CONCRETELNNN,LINE
LESIZE,CONCRETELNNN, , , 1, , , , 0
!*
!*
LSEL,S,LINE,,245,246,,,
CM,CONCRETELAAAA,LINE
LESIZE,CONCRETELAAAA, , , 3, , , , 0
!*
LSEL,S,LINE,,247,248,,,
CM,CONCRETELBBBB,LINE
LESIZE,CONCRETELBBBB, , , 3, , , , 0
!*
LSEL,S,LINE,,271,272,,,
CM,CONCRETELCCCC,LINE
LESIZE,CONCRETELCCCC, , , 3, , , , 0
!*
LSEL,S,LINE,,279,280,,,
CM,CONCRETELDDDD,LINE
LESIZE,CONCRETELDDDD, , , 3, , , , 0
!*
LSEL,S,LINE,,287,288,,,
CM,CONCRETELEEEE,LINE
LESIZE,CONCRETELEEEE, , , 3, , , , 0
!*
LSEL,S,LINE,,295,296,,,
CM,CONCRETELFFFF,LINE
LESIZE,CONCRETELFFFF, , , 3, , , , 0
!*
LSEL,S,LINE,,303,304,,,
CM,CONCRETELGGGG,LINE
LESIZE,CONCRETELGGGG, , , 3, , , , 0
!*
!*
LSEL,S,LINE,,249,250,,,
CM,CONCRETELAAAAA,LINE
LESIZE,CONCRETELAAAAA, , , 4, , , , 0
!*
LSEL,S,LINE,,251,252,,,
CM,CONCRETELBBBBB,LINE
LESIZE,CONCRETELBBBBB, , , 4, , , , 0

```

```

!*
LSEL,S,LINE,,275,276,,,
CM,CONCRETELCCCCC,LINE
LESIZE,CONCRETELCCCCC, , , 4, , , , 0
!*
LSEL,S,LINE,,283,284,,,
CM,CONCRETELDDDDD,LINE
LESIZE,CONCRETELDDDDD, , , 4, , , , 0
!*
LSEL,S,LINE,,291,292,,,
CM,CONCRETELEEEEE,LINE
LESIZE,CONCRETELEEEEE, , , 4, , , , 0
!*
LSEL,S,LINE,,299,300,,,
CM,CONCRETELFFFFFF,LINE
LESIZE,CONCRETELFFFFFF, , , 4, , , , 0
!*
LSEL,S,LINE,,307,308,,,
CM,CONCRETELGGGGG,LINE
LESIZE,CONCRETELGGGGG, , , 4, , , , 0
!*
!*
VSEL,ALL
!*
CM,CONCRETEV,VOLU
CMSEL,S,CONCRETEV,VOLU
MSHAPE,0,3d
MSHKEY,1
VMESH,CONCRETEV
!*
!*
ALLSEL,ALL
!*
/REPLOT,RESIZE
/VIEW,1,1,1,1
/ANG,1
/REP,FAST
!*
!*
NUMMRG,NODE,,00001, , ,LOW
!*
!*
/REPLOT,RESIZE
/VIEW,1,1,1,1
/ANG,1
/REP,FAST
!*
!*
NSEL,S,NODE,,417,420,,,
CM,LEFTSUPPORT,NODE
CMSEL,S,LEFTSUPPORT,NODE
D,LEFTSUPPORT,UY,0, , , , , ,
D,LEFTSUPPORT,UZ,0, , , , , ,
!*
/REPLOT,RESIZE
/VIEW,1,1,1,1
/ANG,1
/REP,FAST
!*
!*
NSEL,S,NODE,,837,840,,,

```

```

CM,RIGHTSUPPORT,NODE
CMSEL,S,RIGHTSUPPORT,NODE
D,RIGHTSUPPORT,UY,0,,,,,,
!*
/REPLOT,RESIZE
/VIEW,1,1,1,1
/ANG,1
/REP,FAST
!*
!*
NSEL,S,NODE,,837,,,
CM,ONERIGHTSUPPORT,NODE
CMSEL,S,ONERIGHTSUPPORT,NODE
D,ONERIGHTSUPPORT,UX,0,,,,,,
!*
!*
NSEL,S,NODE,,417,,,
CM,ONELEFTSUPPORT,NODE
CMSEL,S,ONELEFTSUPPORT,NODE
D,ONELEFTSUPPORT,UX,0,,,,,,
!*
/REPLOT,RESIZE
/VIEW,1,1,1,1
/ANG,1
/REP,FAST
!*
!*
!*
NSEL,S,NODE,,1650,1651,,,
CM,LEFTLOADINNERPOINT,NODE
CMSEL,S,LEFTLOADINNERPOINT,NODE
F,ALL,FY,-4000,
!*
/REPLOT,RESIZE
/VIEW,1,1,1,1
/ANG,1
/REP,FAST
!*
!*
NSEL,S,NODE,,1645,,,
NSEL,A,NODE,,1649,,,
CM,LEFTLOADOUTERPOINT,NODE
CMSEL,S,LEFTLOADOUTERPOINT,NODE
F,ALL,FY,-2000,
!*
/REPLOT,RESIZE
/VIEW,1,1,1,1
/ANG,1
/REP,FAST
!*
!*
NSEL,S,NODE,,2306,2307,,,
CM,RIGHTLOADINNERPOINT,NODE
CMSEL,S,RIGHTLOADINNERPOINT,NODE
F,ALL,FY,-2000,
!*
/REPLOT,RESIZE
/VIEW,1,1,1,1
/ANG,1
/REP,FAST
!*
!*
NSEL,S,NODE,,2301,,,
NSEL,A,NODE,,2305,,,
CM,RIGHTLOADOUTERPOINT,NODE
CMSEL,S,RIGHTLOADOUTERPOINT,NODE

```

```

F,ALL,FY,-1000,
!*
/REPLOT,RESIZE
/VIEW,1,1,1,1
/ANG,1
/REP,FAST
!*
!*
!*
NSEL,S,NODE,,741,744,,
CM,CENTERLINEDEFLECTION,NODE
CMSEL,S,CENTERLINEDEFLECTION,NODE
!*
/REPLOT,RESIZE
/VIEW,1,1,1,1
/ANG,1
/REP,FAST
!*
!*
!*
ALLSEL,ALL
!*
/REPLOT,RESIZE
/VIEW,1,1,1,1
/ANG,1
/REP,FAST
!*
!*
!*
FINISH
!*
!*
!*
/SOL
!*
!*
!*
ESEL,S,MAT,,4
!*
ISTRESS,202000, , , ,
!*
/REPLOT,RESIZE
/VIEW,1,1,1,1
/ANG,1
/REP,FAST
!*
!*
!*
ALLSEL,ALL
!*
/REPLOT,RESIZE
/VIEW,1,1,1,1
/ANG,1
/REP,FAST
!*
!*
!*
ANTYPE,0
NSUBST,10,1000,10
OUTRES,ERASE
OUTRES,ALL,ALL
PSTRES,1
RESCONTRL,DEFINE,ALL,NONE,0
TIME,1
!*
/STATUS,SOLU

```

```

!*
SOLVE
!*
!*
!*
FINISH
!*
/POST1
!*
/SHOW,WIN32C
INRES,ALL
FILE,'psbeam','rst','.'
SET,LAST
SET,FIRST
/PLOPTS,INFO,3
/CONTOUR,ALL,18
/PNUM,MAT,1
/NUMBER,1
/REPLOT,RESIZE
!/UIS,ABORT,1
/SHOW,WIN32
/REPLOT,RESIZE
FINISH
/POST26
FINISH
/POST1
INRES,BASIC
FILE,'psbeam','rst','.'
SET,LAST
FINISH
/POST26
FILE,'psbeam','rst','.'
/UI,COLL,1
NUMVAR,200
SOLU,191,NCMIT
STORE,MERGE
FILLDATA,191,,,1,1
REALVAR,191,191
!*
NSOL,2,744,U,Y, UY744
STORE,MERGE
FILLDATA,192,,,0,0
FILLDATA,193,,,1,0
FILLDATA,194,,,1,0
FILLDATA,195,,,1,1
VARNAME,195,NSET
!
! Name: Delta
! ID: 3
! Function: abs({UY744})
ABS,3,2,,,Delta
!
STORE,MERGE
FILLDATA,192,,,0,0
FILLDATA,193,,,1,0
FILLDATA,194,,,1,0
FILLDATA,195,,,1,1
VARNAME,195,NSET
!
! Name: Load
! ID: 4
! Function: {TIME}*18000
FILLDATA,199,,,18000,0
REALVAR,199,199
PROD,4,1,199,,Load
!

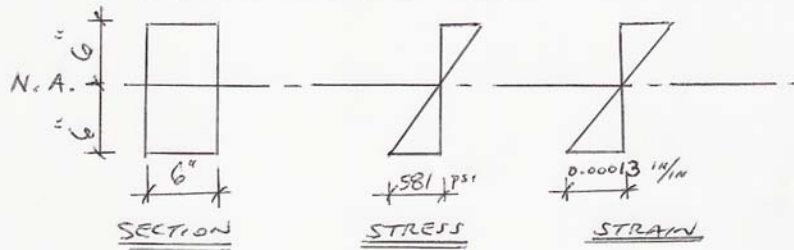
```


STORE,MERGE
XVAR,3
PLVAR,4,
!*

APPENDIX C PLAIN CONCRETE RECTANGULAR BEAM

This appendix contains a summary of the classical analysis computations for the deflection of a plain concrete rectangular beam.

PLAIN CONCRETE BEAM



SECTION & MATERIAL PROPERTIES

$$F_t = 7.5 \sqrt{F'_c} = 7.5 \sqrt{6000} = 581 \text{ psi}$$

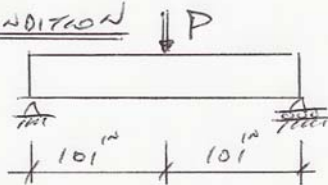
$$E_c = 57,000 \sqrt{F'_c} = 57,000 \sqrt{6000} = 4,415,000 \text{ psi}$$

$$I = \frac{1}{12} b h^3 = \frac{1}{12} (6)(12)^3 = 864 \text{ in}^4$$

$$M_{CR} = F_t \frac{I}{c} = 581 \text{ psi} \left(\frac{864 \text{ in}^4}{6 \text{ in}} \right) = 83,700 \text{ in} \cdot \text{lb}$$

$$\epsilon = \frac{F_t}{E} = \frac{581 \text{ psi}}{4,415,000 \text{ psi}} = 0.00013 \text{ in/in}$$

LOADING CONDITION



$$\delta = \frac{P l^3}{48 E I} = \frac{4 \left(\frac{P l}{4} \right) l^2}{48 E I} = \frac{4 M l^2}{48 E I}$$

$$\delta = \frac{(4)(83,700 \text{ in} \cdot \text{lb})(20 \text{ ft})^2}{48 (4,415,000 \text{ psi}) 864 \text{ in}^4} = 0.0746 \text{ in}$$

$$\boxed{\delta = 0.0746 \text{ in} @ M_{CR} = 83,700 \text{ in} \cdot \text{lb}}$$

APPENDIX D FUJITA TORNADO DAMAGE SCALE

This appendix contains the tornado damage scale as characterized by its area and intensity (Fujita 1971).

Fujita Tornado Damage Scale

Developed in 1971 by T. Theodore Fujita of the University of Chicago

SCALE	WIND ESTIMATE *** (MPH)	TYPICAL DAMAGE
F0	< 73	<u>Light damage.</u> Some damage to chimneys; branches broken off trees; shallow-rooted trees pushed over; sign boards damaged.
F1	73-112	<u>Moderate damage.</u> Peels surface off roofs; mobile homes pushed off foundations or overturned; moving autos blown off roads.
F2	113-157	<u>Considerable damage.</u> Roofs torn off frame houses; mobile homes demolished; boxcars overturned; large trees snapped or uprooted; light-object missiles generated; cars lifted off ground.
F3	158-206	<u>Severe damage.</u> Roofs and some walls torn off well-constructed houses; trains overturned; most trees in forest uprooted; heavy cars lifted off the ground and thrown.
F4	207-260	<u>Devastating damage.</u> Well-constructed houses leveled; structures with weak foundations blown away some distance; cars thrown and large missiles generated.
F5	261-318	<u>Incredible damage.</u> Strong frame houses leveled off foundations and swept away; automobile-sized missiles fly through the air in excess of 100 meters (109 yds); trees debarked; incredible phenomena will occur.

*** **IMPORTANT NOTE ABOUT F-SCALE WINDS:** Do not use F-scale winds literally. These precise wind speed numbers are actually guesses and have never been scientifically verified. Different wind speeds may cause similar-looking damage from place to place -- even from building to building. *Without a thorough engineering analysis of tornado damage in any event, the actual wind speeds needed to cause that damage are unknown.*

APPENDIX E USING TERASCALE'S MESHER PROGRAM

This appendix contains a mesh generation example using TeraScale's software Mesher. The example used is a mesh of a tornado shelter. The shelter is a prismatic structure consisting of four walls and a roof slab. The walls and roof contain reinforcing steel at middepth, in orthogonal directions.

A finite element mesh is generated using TeraScale's mesh generation program, Mesher. An input file, which has a filename of “*-recipe.xml”, is required for the Mesher program. Mesher generates an output file with a filename of “*.tsm.xml”. The filename for the tornado shelter is “shelter-recipe.xml”.

The data input fields for the Mesher input file are accessible from the five folders located at the top of the screen, as shown in Figure E-1. The first folder is the “Sketches” folder, which has input data fields for the definition of nodes, edges, and regions. The image shown in Figure E-2 was created from the data entries shown in Figure E-1. Attributes such as material properties can be assigned to “regions” during the preparation of the TeraDyn input file.

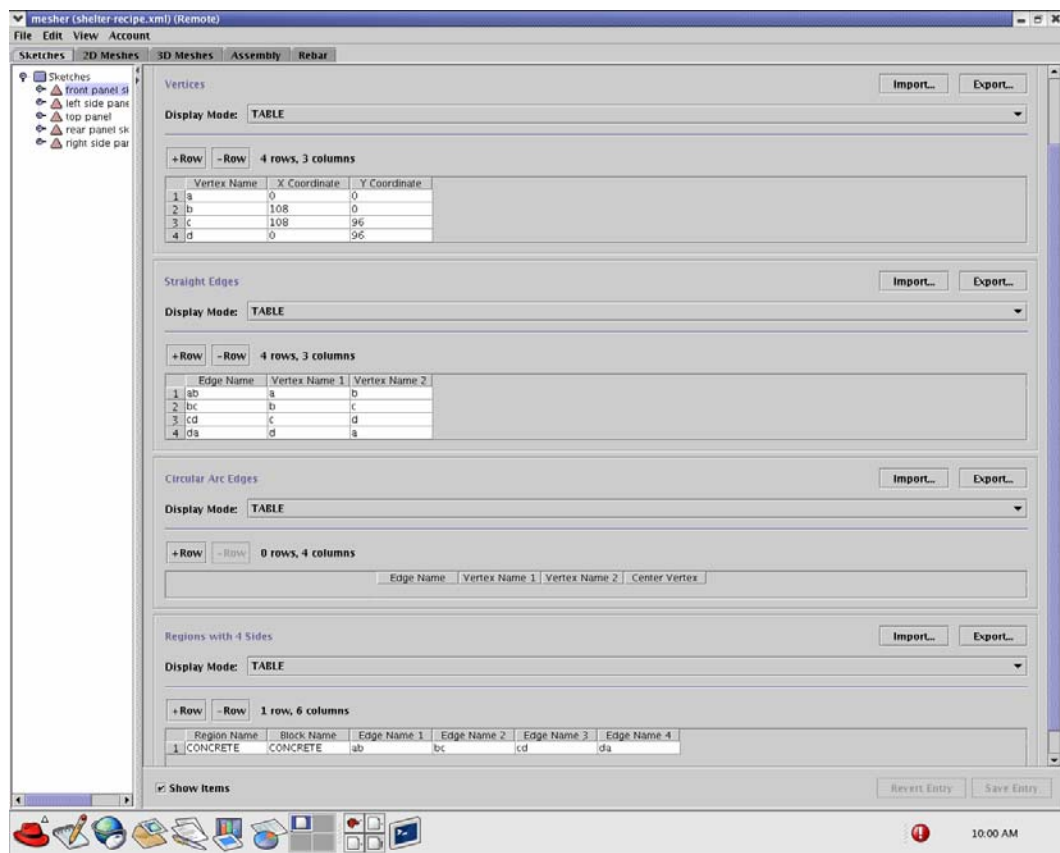


Figure E-1: Sketches Tab For Mesher Input File

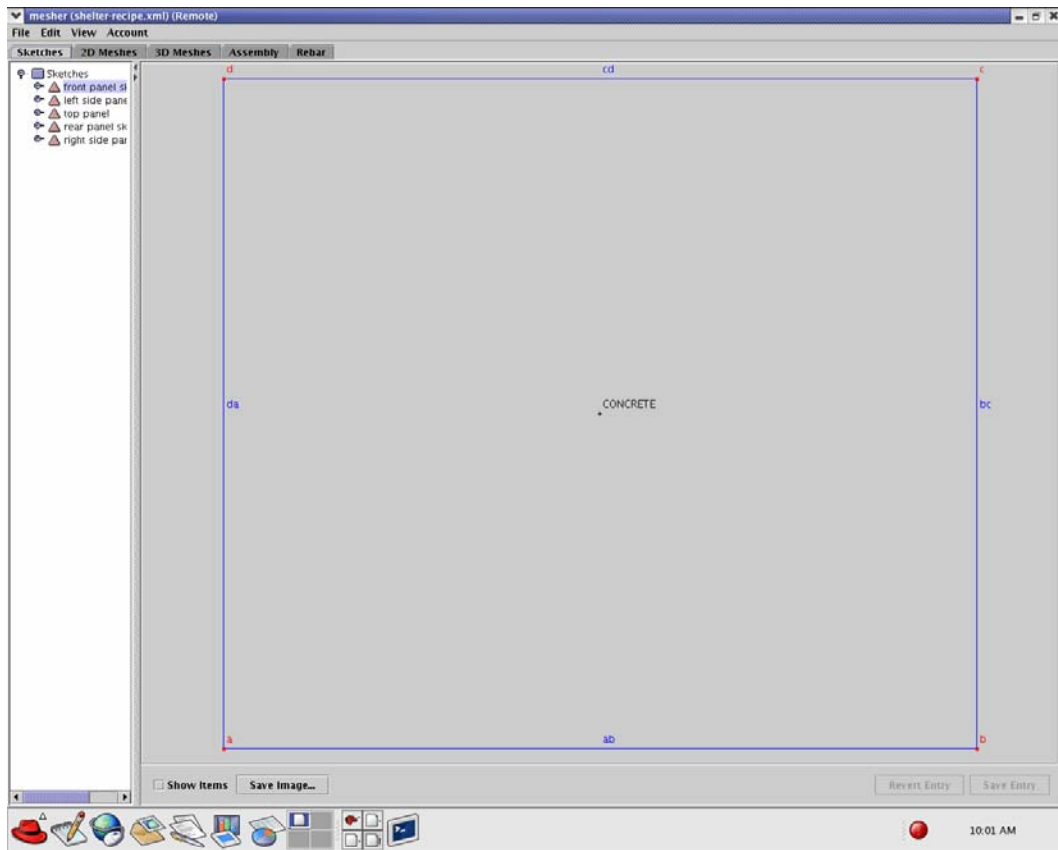


Figure E-2: Sketch Generated For Mesher Input File

A 2D mesh of the sketch is created using the data entry fields in the “2D Meshes” folder, shown in Figure E-3. On this screen, the number of nodes along each edge, and the spacing interval between nodes, are defined. Figure E-4 shows the mesh “seeds” along the edges created from the previous screens. The purpose of “node sets” will be shown later.

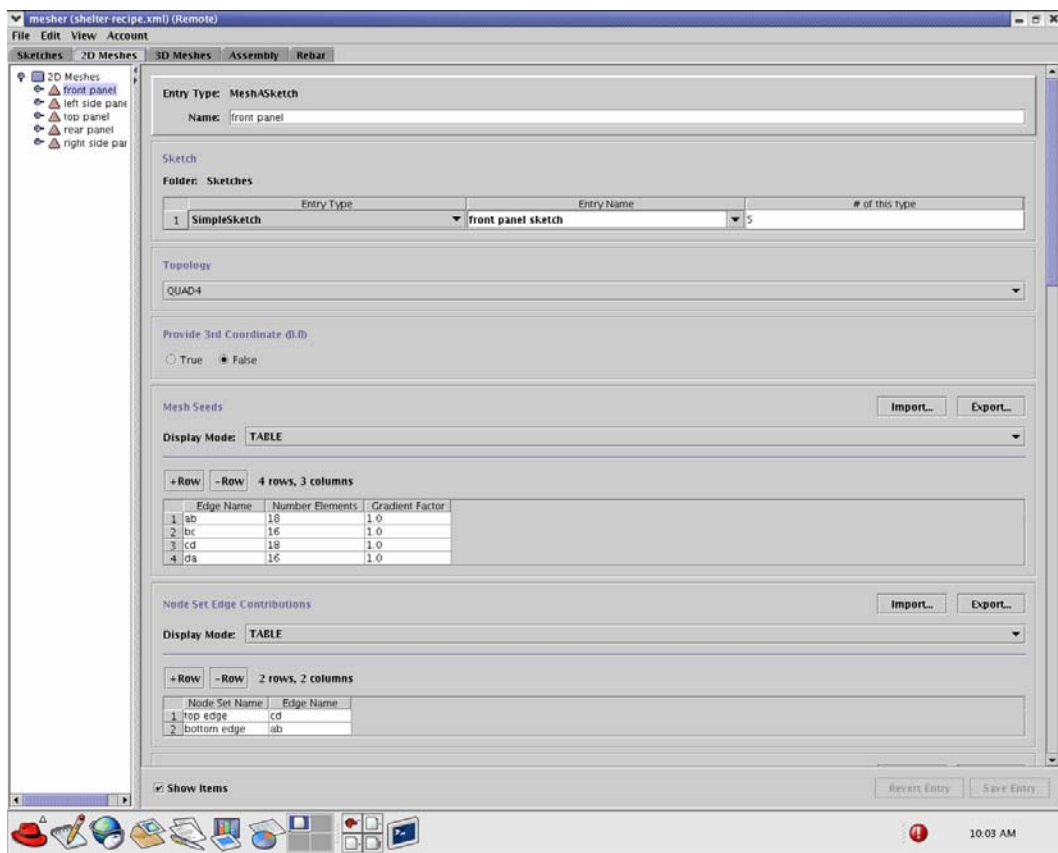


Figure E-3: 2D Meshes Tab For Mesher Input File

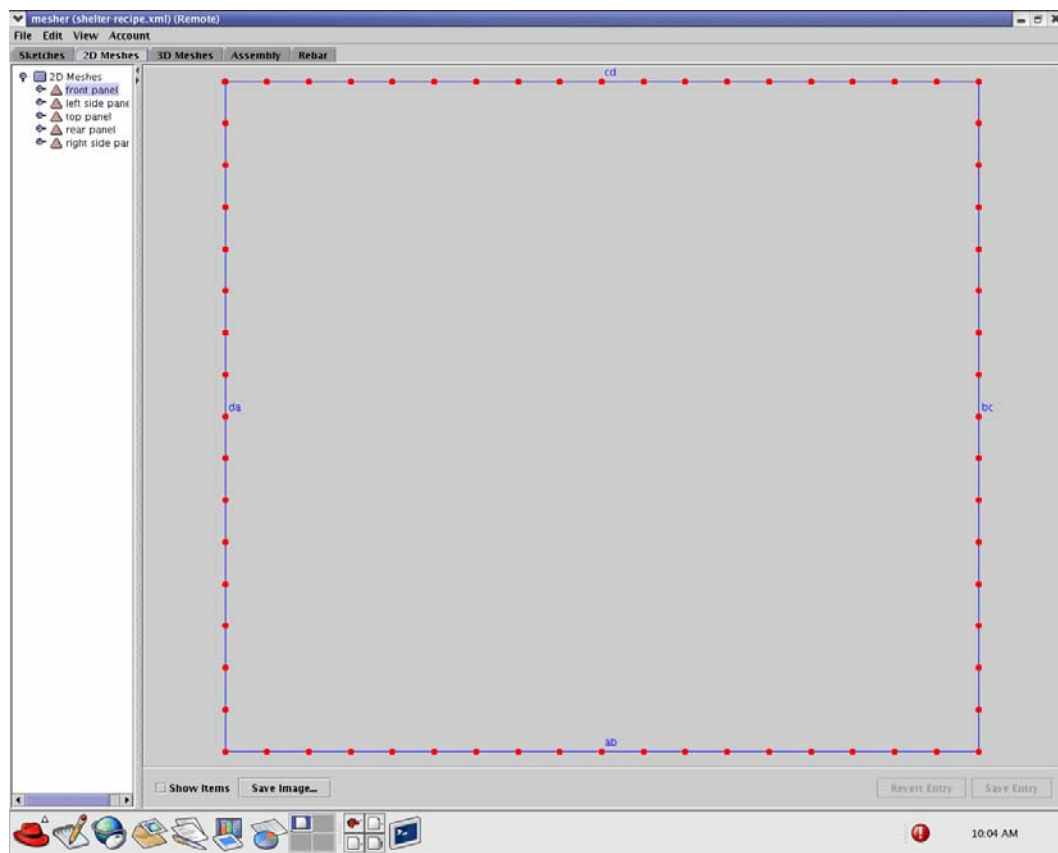


Figure E-4: 2D Mesh Data For Mesher Input File

If a 3D mesh is needed, the 3D mesh of the 2D Mesh is created using the data entry fields in the “3D Meshes” folder, shown in Figure E-5. On this screen, the distance that the 2D Mesh will be “extruded” into the +Z direction is defined. The number of nodes along the extruded edges, and the spacing interval between these nodes, are defined. Figure E-6 shows the mesh “seeds” along the edges created from this and previous screens.

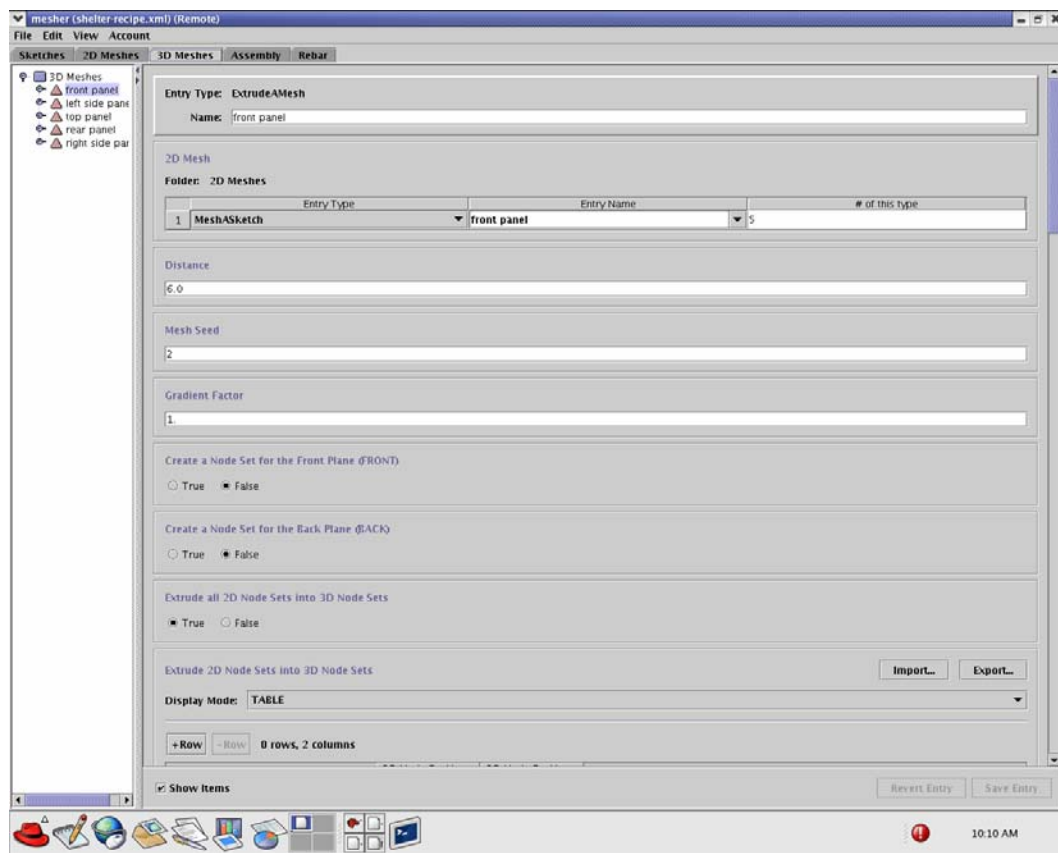


Figure E-5: 3D Meshes Tab For Mesher Input File

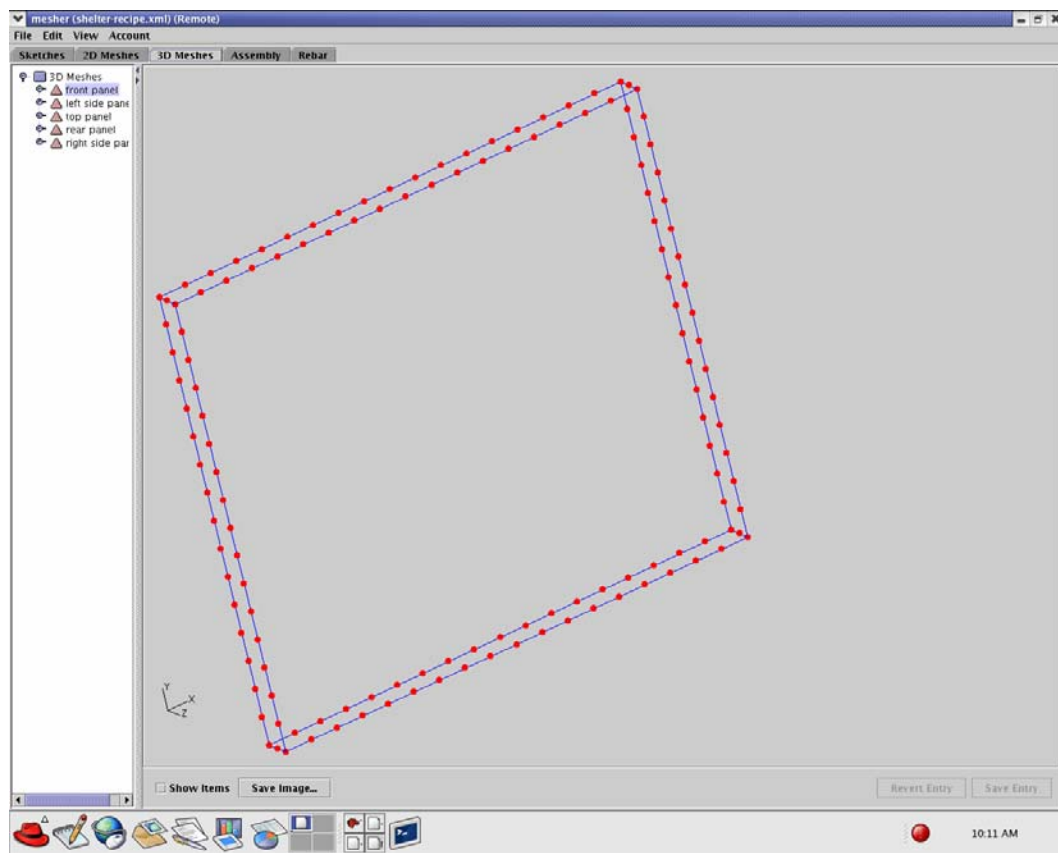


Figure E-6: 3D Mesh Data For Mesher Input File

Rebar is meshed using the data entry fields in the “Rebar” folder, shown in Figure E-7. On this screen, a rebar is defined as a series of coordinates connected into a line. Additional similar bars can be included into the rebar sketch by using the “number of bars along sweep” data entry. For the case shown, 9 rectangular ties are equally spaced in 96 inches. The rebar “instance” defined earlier can be translated and rotated using the data fields shown in Figure E-8. An “assembly” of rebar can be created using the data fields shown in Figure E-9.

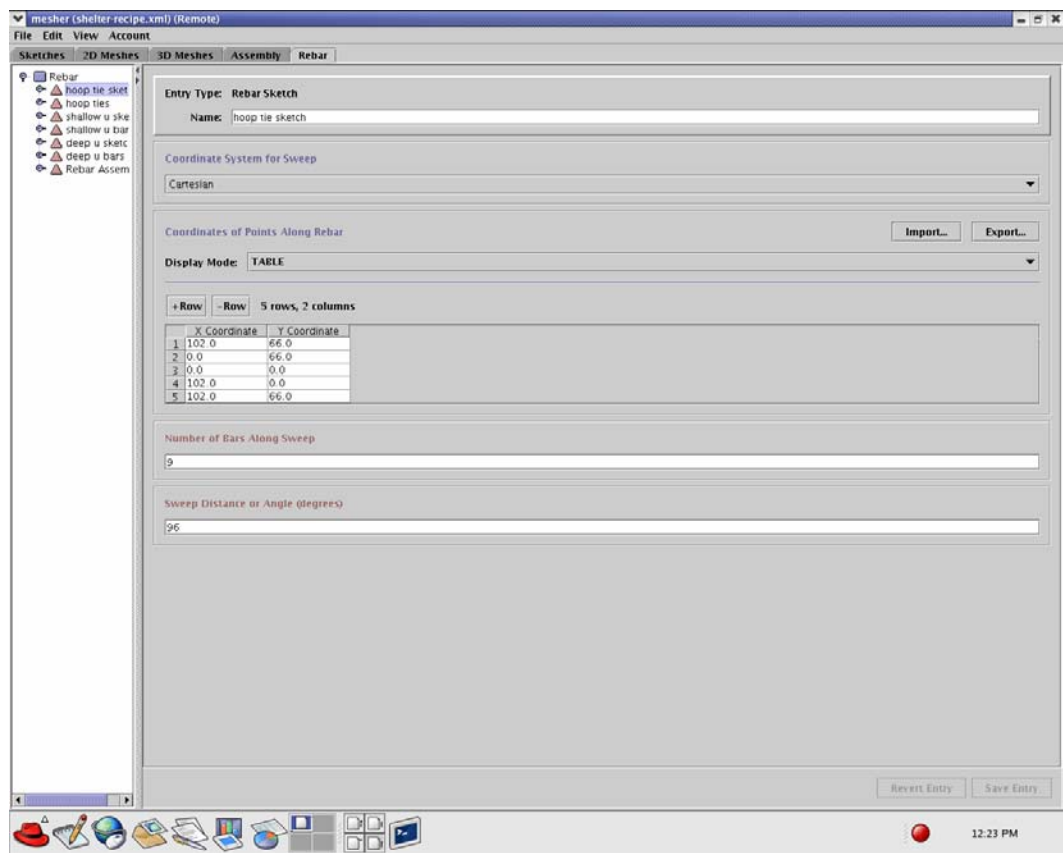


Figure E-7: Rebar Tab For Mesher Input File

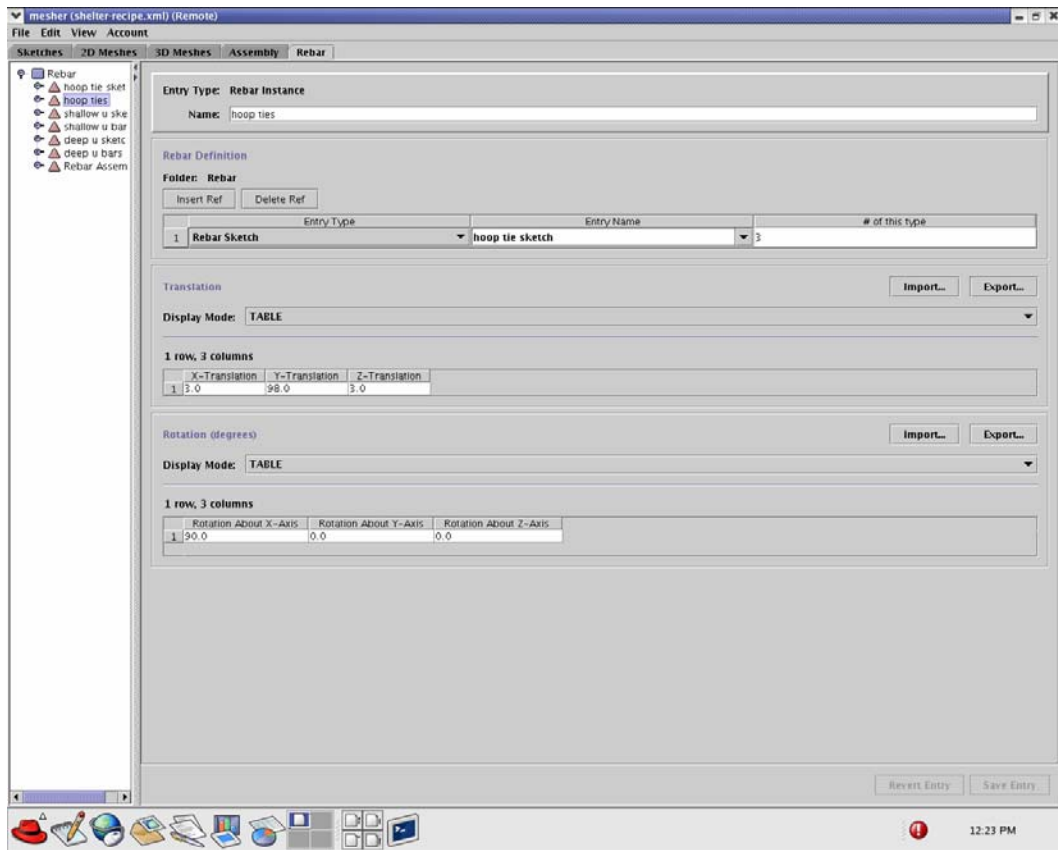


Figure E-8: Rebar Instance Data For Mesher Input File

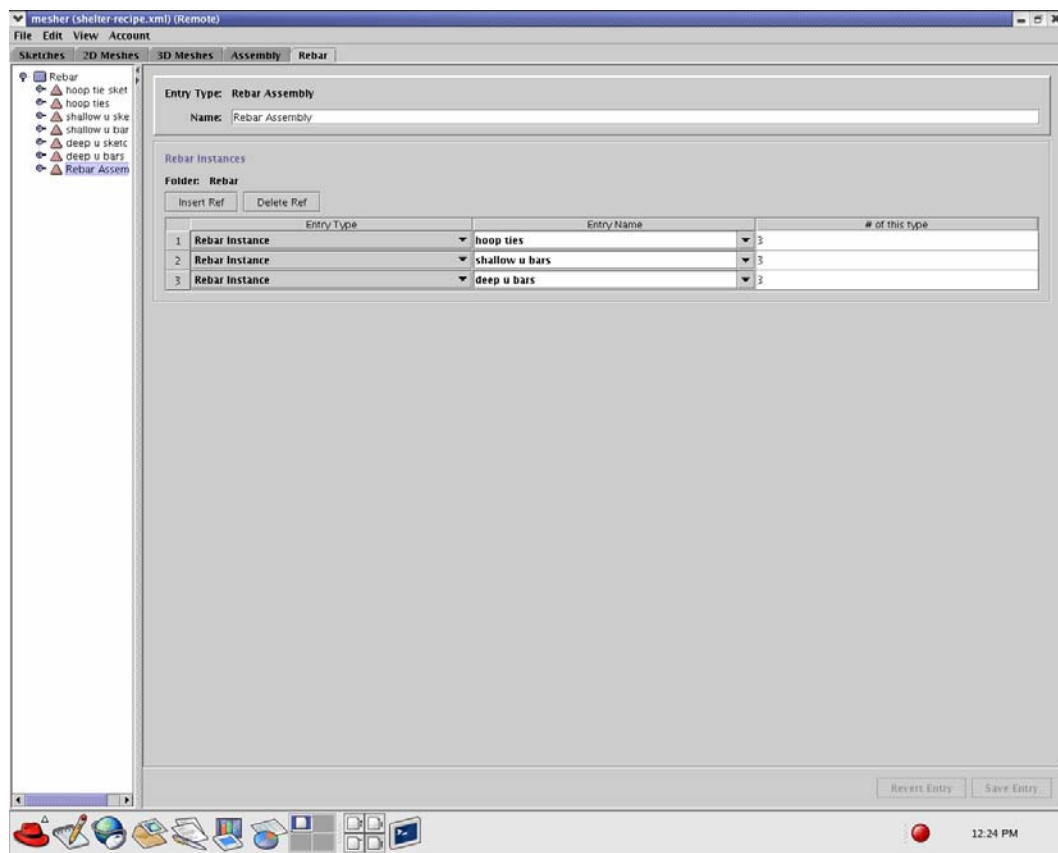


Figure E-9: Rebar Assembly Data For Mesher Input File

An “assembly” of either 2D meshes or 3D meshes can be created using the data entry fields in the “Assembly” folder. First, the meshes are translated and rotated as required as shown in Figure E-10. Second, the data fields shown on Figure E-11 are used to combine the meshes, including the rebar meshes.

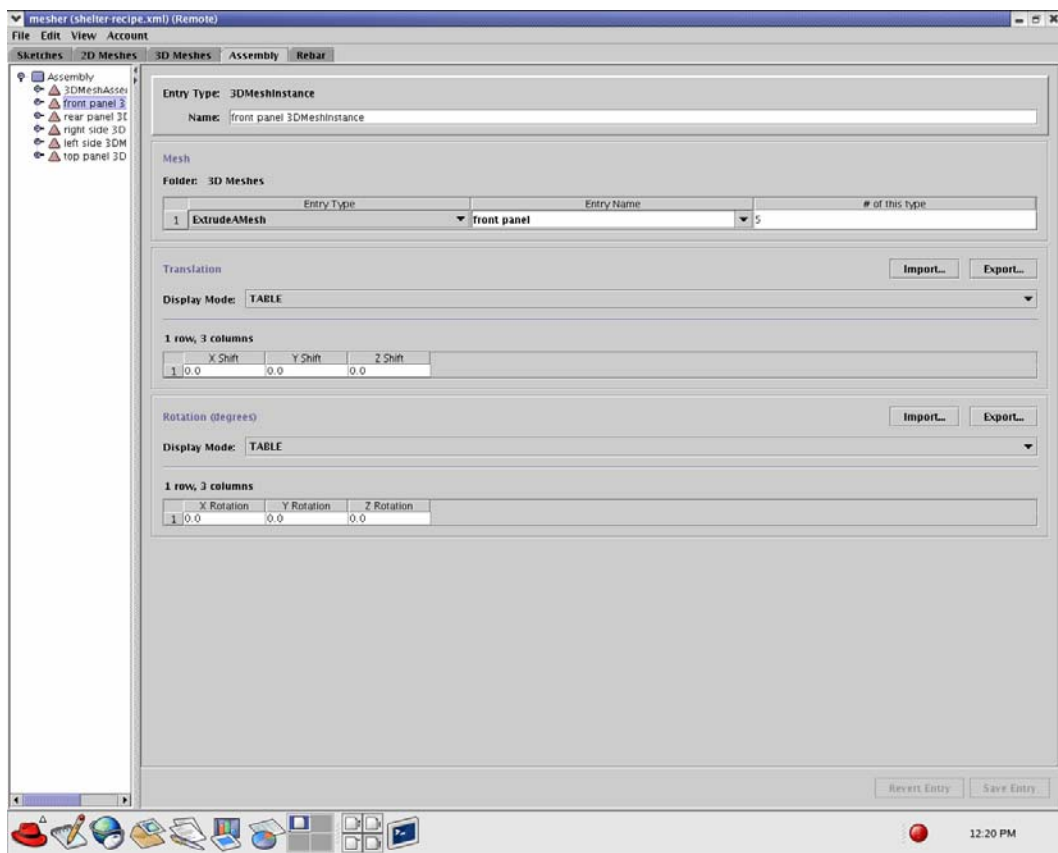


Figure E-10: Assembly Tab For Mesher Input File

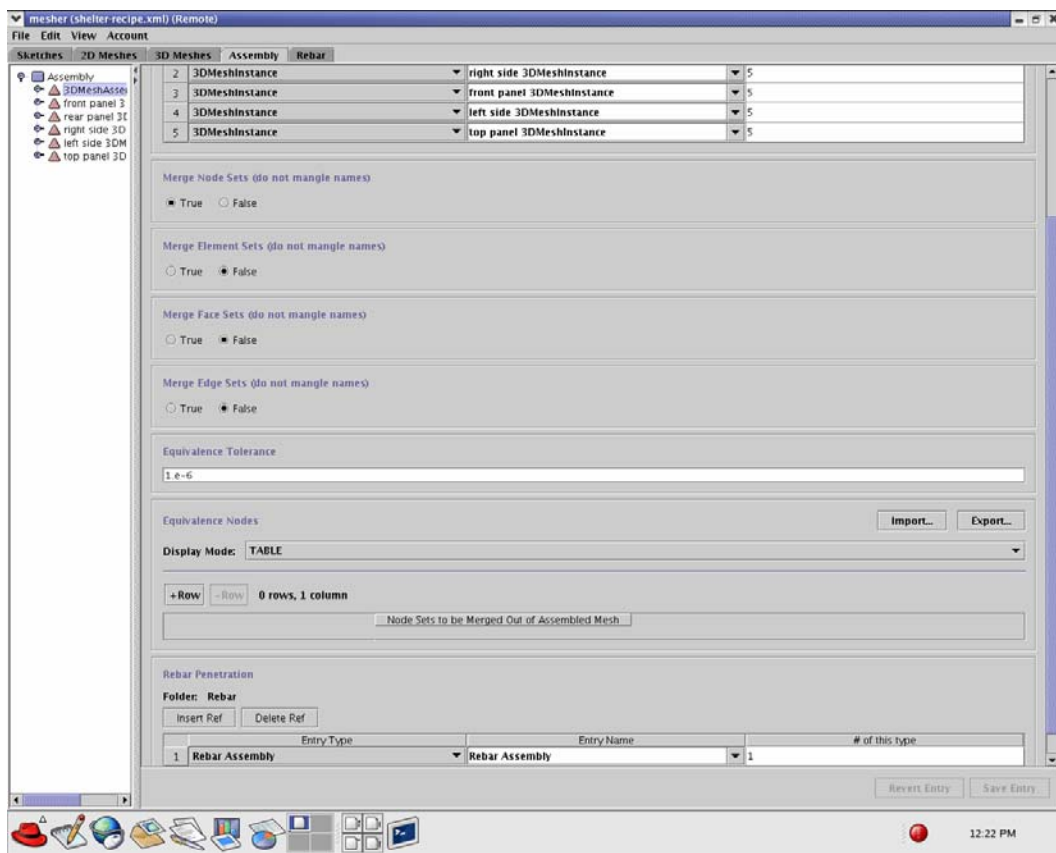


Figure E-11: Assembly Data For Mesher Input File

The resulting mesh for the tornado shelter is shown in Figures E-12 and E-13. The mesh was generated by TeraScale’s Mesher software. The Mesher output filename for the tornado shelter is “shelter.tsm.xml”. In the preceding discussion, the data input fields were shown for the “front panel” of the tornado shelter. The roof slab and the three remaining walls have similar data entries. The data input fields were also shown for the “hoop ties”, which are the horizontal bars that extend at middepth inside the four perimeter walls. The

vertical bars and roof slab bars were generated as “U” shaped bars that extended at middepth thru the opposite walls and roof slab.

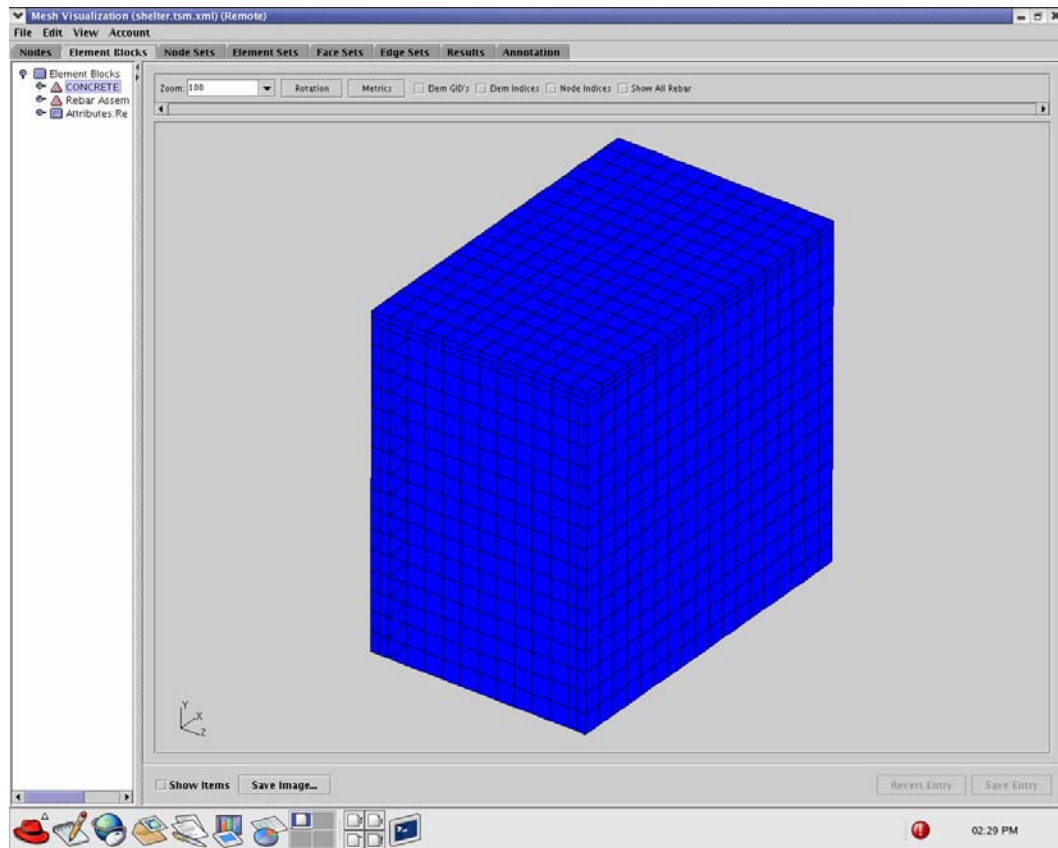


Figure E-12: Tornado Shelter Mesh

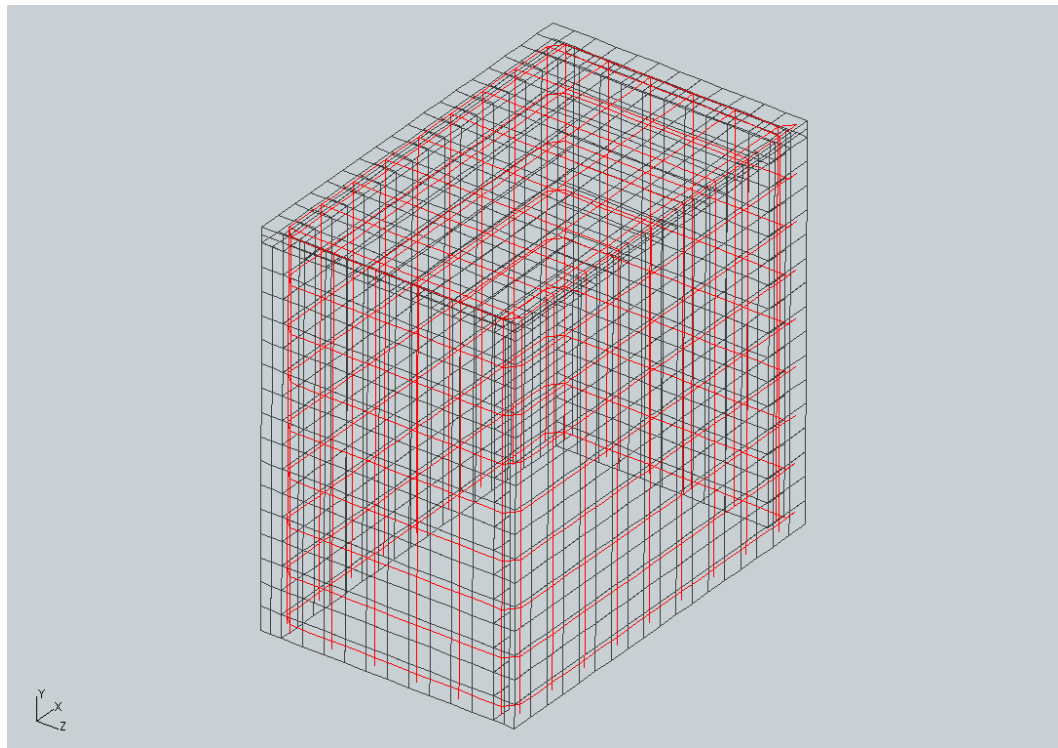


Figure E-13: Tornado Shelter Rebar Mesh

APPENDIX F USING TERASCALE'S TERADYN PROGRAM

This appendix contains an explicit dynamics finite element analysis example using TeraScale's software TeraDyn. The analysis example used is an impulsive load on a mesh of a reinforced concrete tornado shelter.

The finite element analysis is accomplished using TeraScale's explicit dynamics finite element analysis software program, TeraDyn. An input file, which has a filename of "*.xml", is required for the TeraDyn program. TeraDyn generates an output file with a filename of "*-results.tsm.xml". The filename for the tornado shelter is "shelter-results.tsm.xml".

The data input fields for the TeraDyn input file are accessible from the eleven folders located at the top of the screen, as shown in Figure F-1. The first folder is the "Analysis" folder, which has input data fields for the selection of the mesh and analysis time duration. Other tabs contain data entry fields for the material properties, boundary conditions, and output requests.

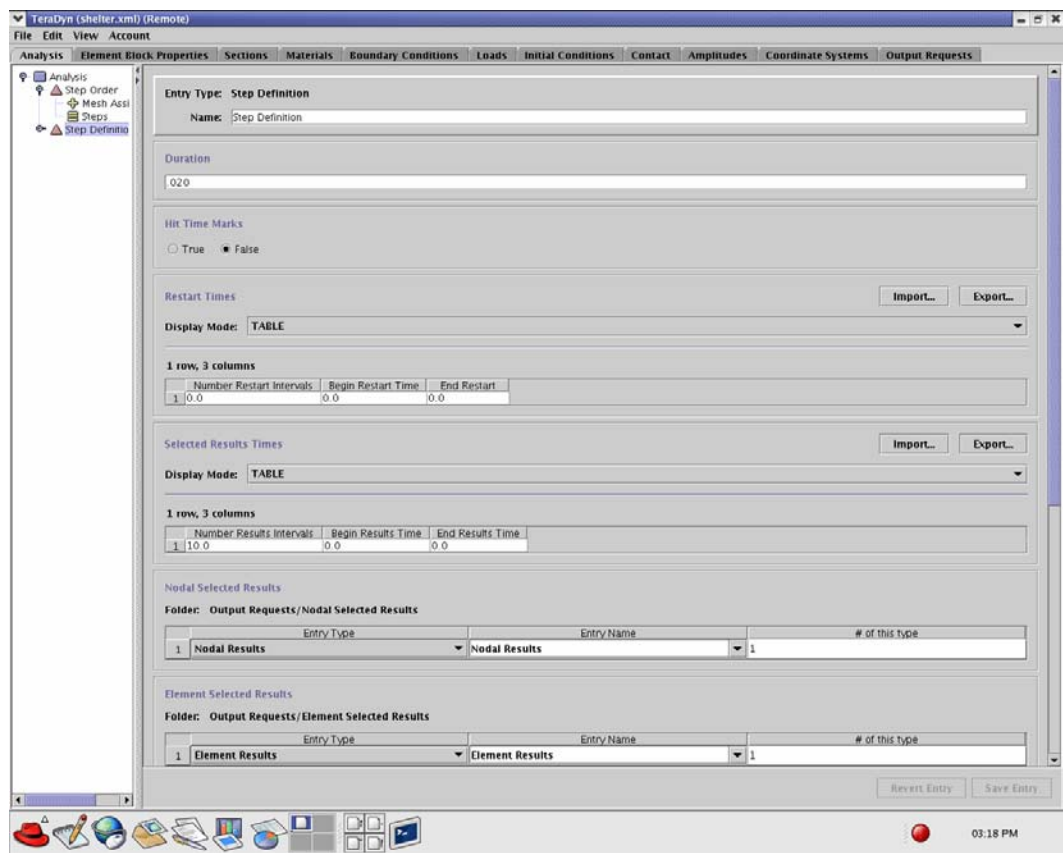
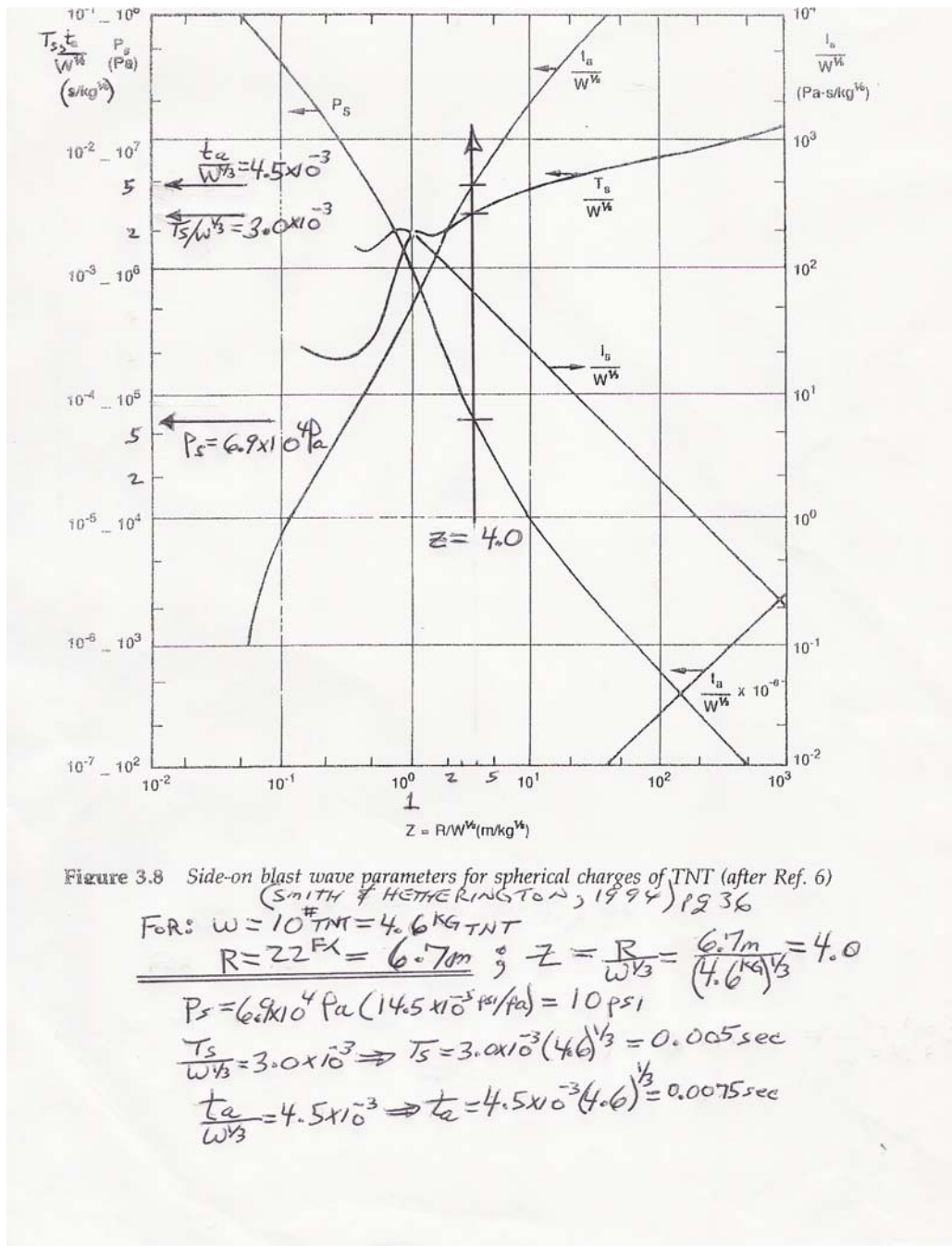


Figure F-1: Data Entry Tabs For TeraDyn Input File

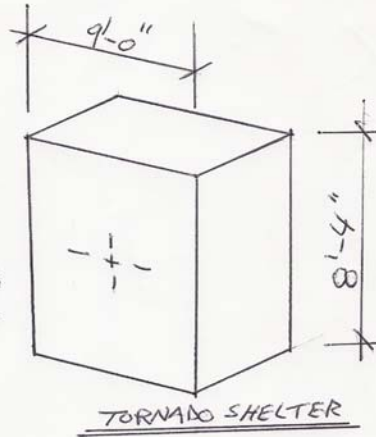
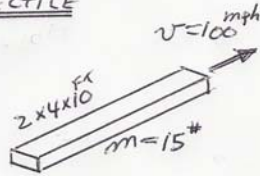
APPENDIX G TORNADO SHELTER IMPACT LOAD PROPERTIES

This appendix contains blast loading computations used to calibrate the moving pressure impulse loading used in the tornado shelter analysis.

	Page
Blast Wave Parameters vs. Scaled Distance; 10# TNT @ Range = 22 ft	260
Equivalent Impulse Loading On Tornado Shelter	261



PROJECTILE



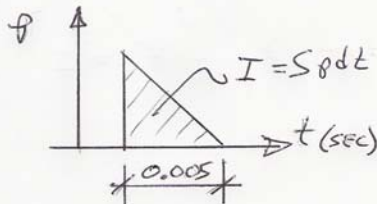
MOMENTUM

$$m = \frac{15 \#}{32.2 \text{ ft/sec}^2} = 0.46 \# \cdot \text{sec}^2 / \text{ft}$$

$$mv = 0.46 \# \cdot \text{sec}^2 / \text{ft} (100 \text{ mi/hr}) \left(\frac{5280 \text{ ft/mi}}{3600 \text{ sec/hr}} \right)$$

$$mv = 68 \# \cdot \text{sec}$$

IMPULSE



$$\int f dt = \frac{1}{2} (0.005 \text{ sec}) f \text{ Area}$$

$$\int f dt = 0.0025 \text{ sec } f \text{ Area}$$

IMPULSE = Δmv

$$0.0025 \text{ sec } f \text{ Area} = 68 \# \cdot \text{sec}$$

$$f \text{ Area} = 27,300 \#$$

LOADING

f (psf)	Area (INSQ)	
3400	8	PROJECTILE FOOTPRINT
340	80	CONCRETE SHEAR CONE
10	2730	ONE QUARTER SHELTER AREA

APPENDIX H TORNADO SHELTER HYDROSTATIC PRESSURE

This appendix contains results from the finite element analysis of the tornado shelter subjected to an impulsive loading. The figures show the hydrostatic pressure contours plotted on the deflected shape of the structure in 2 msec intervals for the 20 msec analysis duration. Deflection is magnified by 400.

	Page
Tornado Shelter Hydrostatic Pressure On Deflected Shape At 2 msec	263
Tornado Shelter Hydrostatic Pressure On Deflected Shape At 4 msec	263
Tornado Shelter Hydrostatic Pressure On Deflected Shape At 6 msec	264
Tornado Shelter Hydrostatic Pressure On Deflected Shape At 8 msec	264
Tornado Shelter Hydrostatic Pressure On Deflected Shape At 10 msec	265
Tornado Shelter Hydrostatic Pressure On Deflected Shape At 12 msec	265
Tornado Shelter Hydrostatic Pressure On Deflected Shape At 14 msec	266
Tornado Shelter Hydrostatic Pressure On Deflected Shape At 16 msec	266
Tornado Shelter Hydrostatic Pressure On Deflected Shape At 18 msec	267
Tornado Shelter Hydrostatic Pressure On Deflected Shape At 20 msec	267

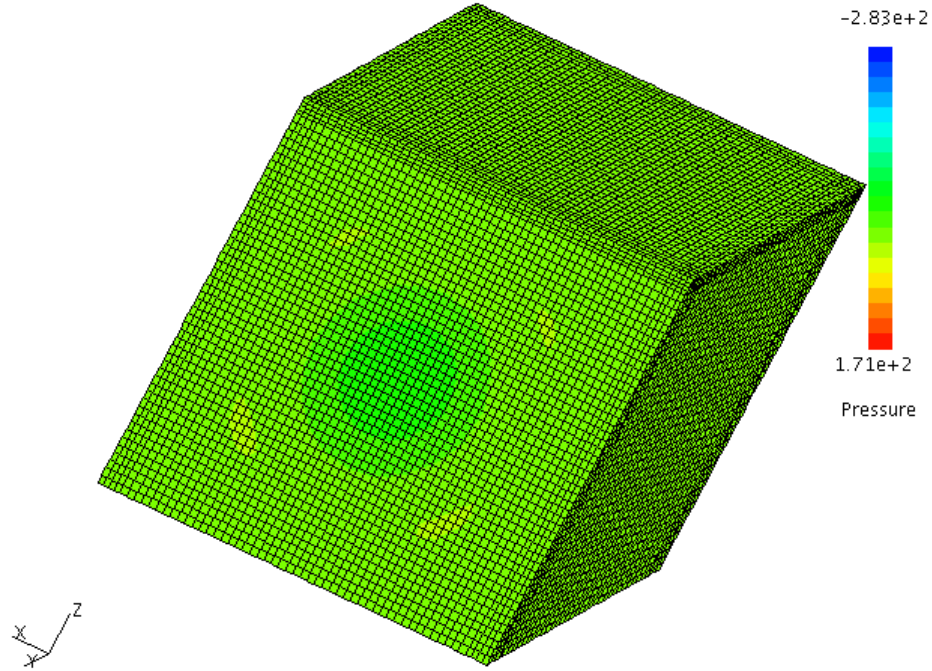


Figure G-1: Tornado Shelter Hydrostatic Pressure On Deflected Shape At 2 msec

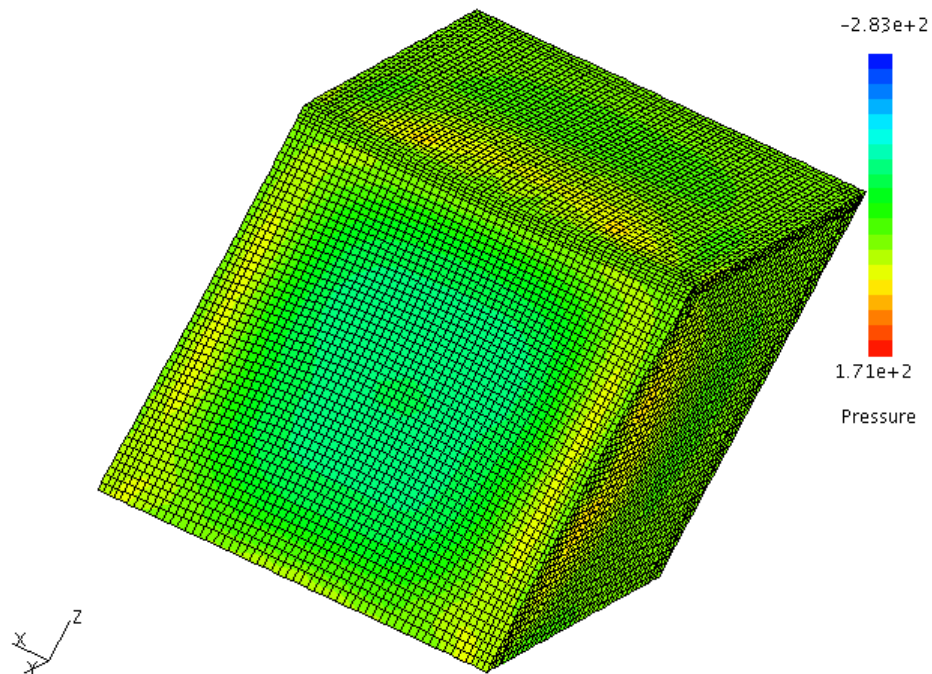


Figure G-2: Tornado Shelter Hydrostatic Pressure On Deflected Shape At 4 msec

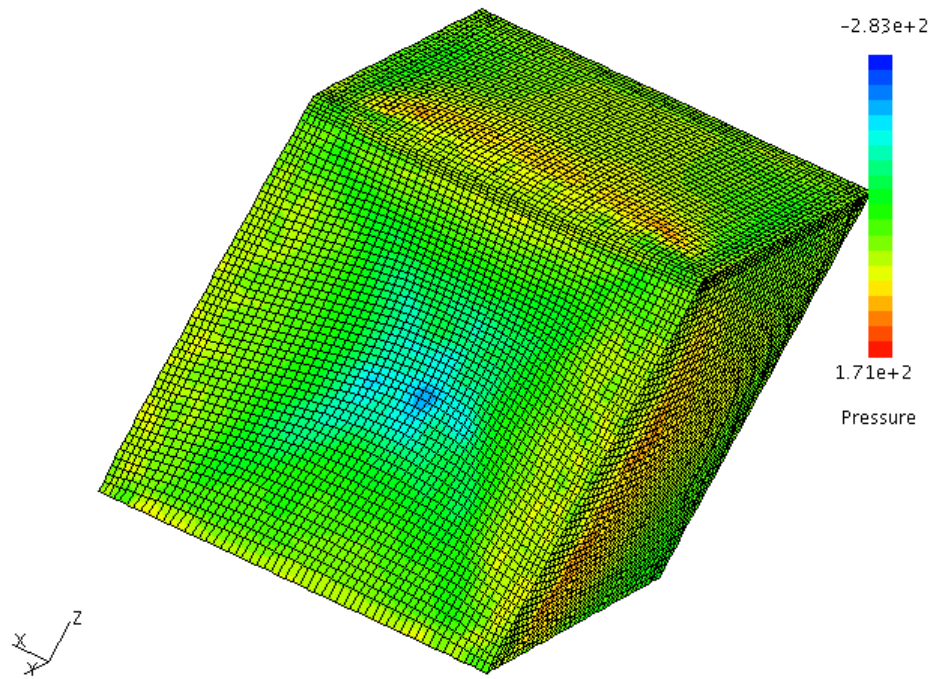


Figure G-3: Tornado Shelter Hydrostatic Pressure On Deflected Shape At 6 msec

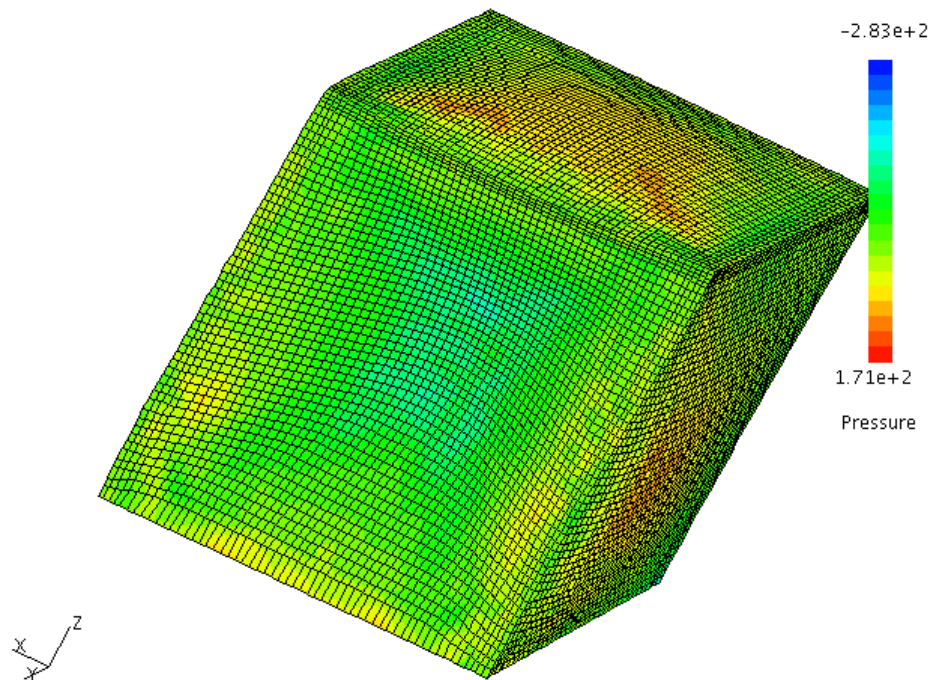


Figure G-4: Tornado Shelter Hydrostatic Pressure On Deflected Shape At 8 msec

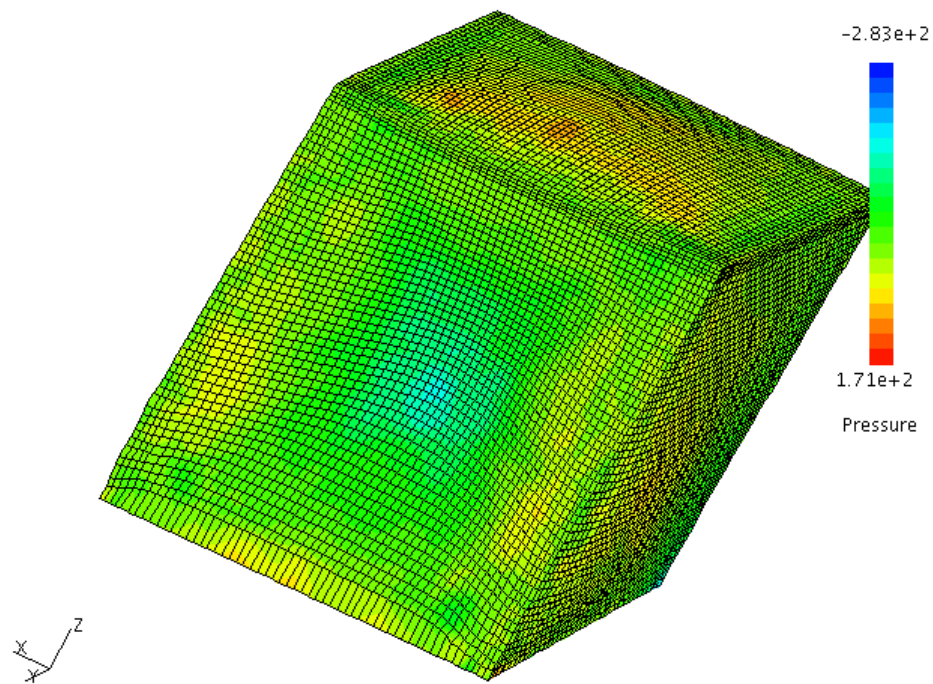


Figure G-5: Tornado Shelter Hydrostatic Pressure On Deflected Shape At 10 msec

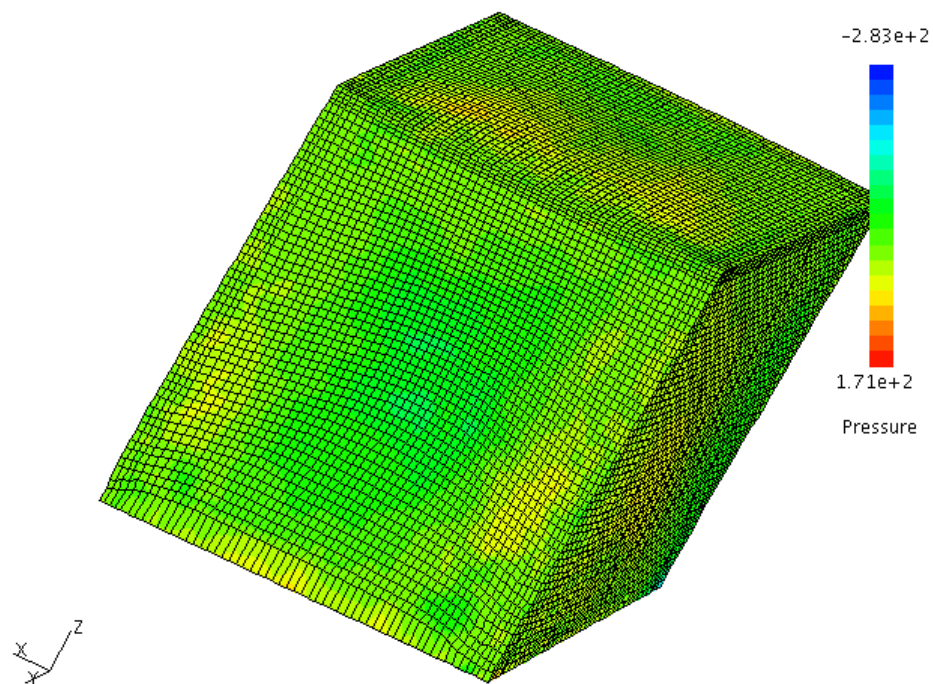


Figure G-6: Tornado Shelter Hydrostatic Pressure On Deflected Shape At 12 msec

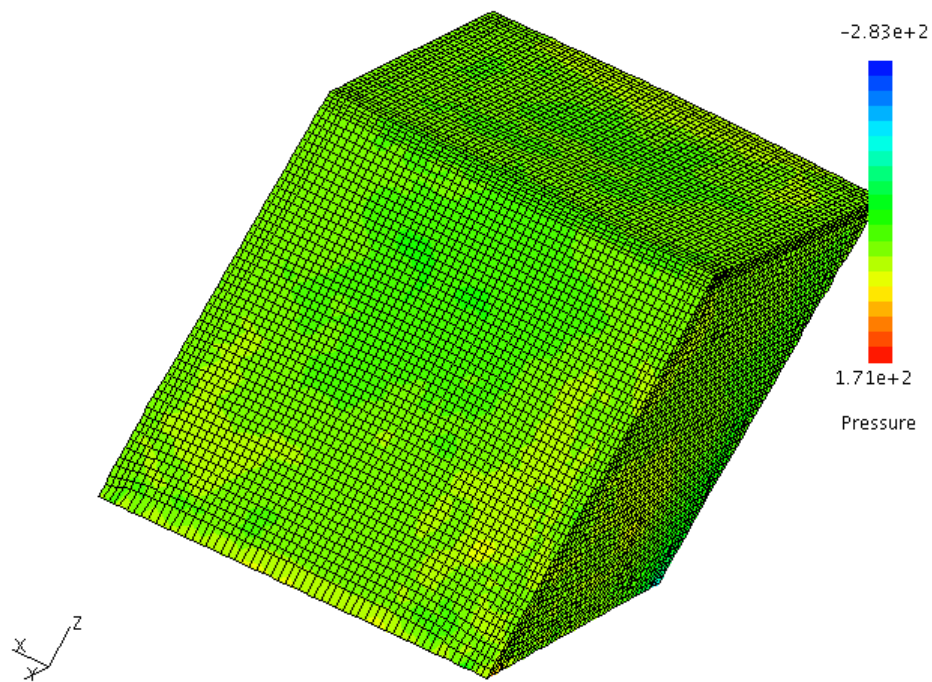


Figure G-7: Tornado Shelter Hydrostatic Pressure On Deflected Shape At 14 msec

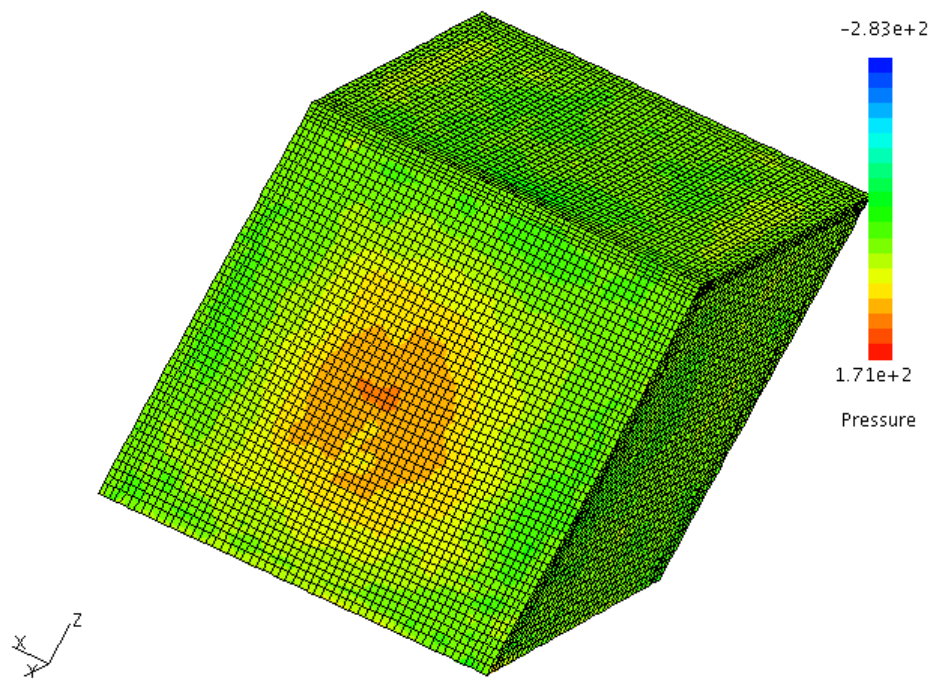


Figure G-8: Tornado Shelter Hydrostatic Pressure On Deflected Shape At 16 msec

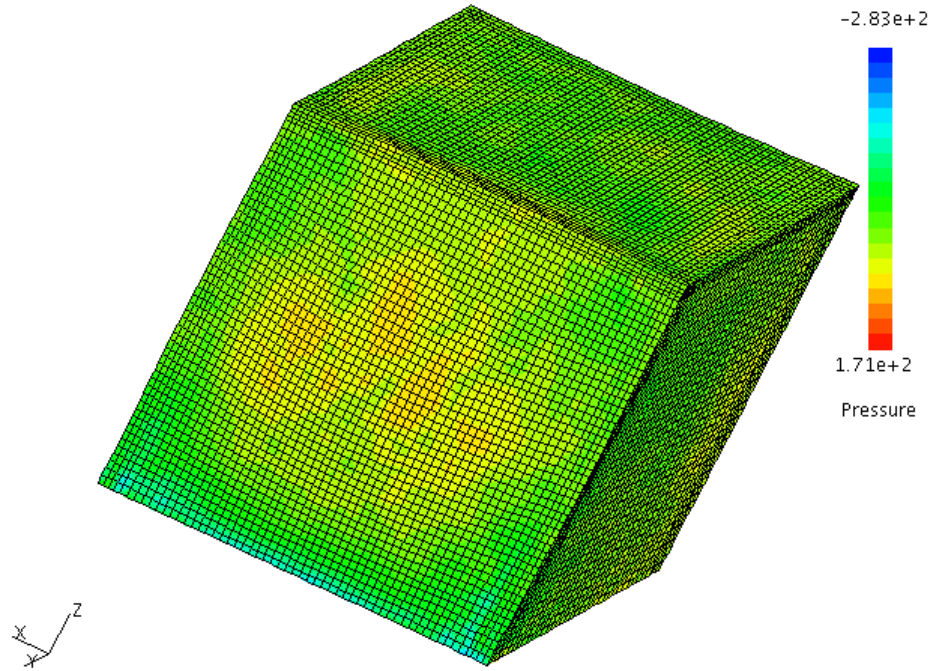


Figure G-9: Tornado Shelter Hydrostatic Pressure On Deflected Shape At 18 msec

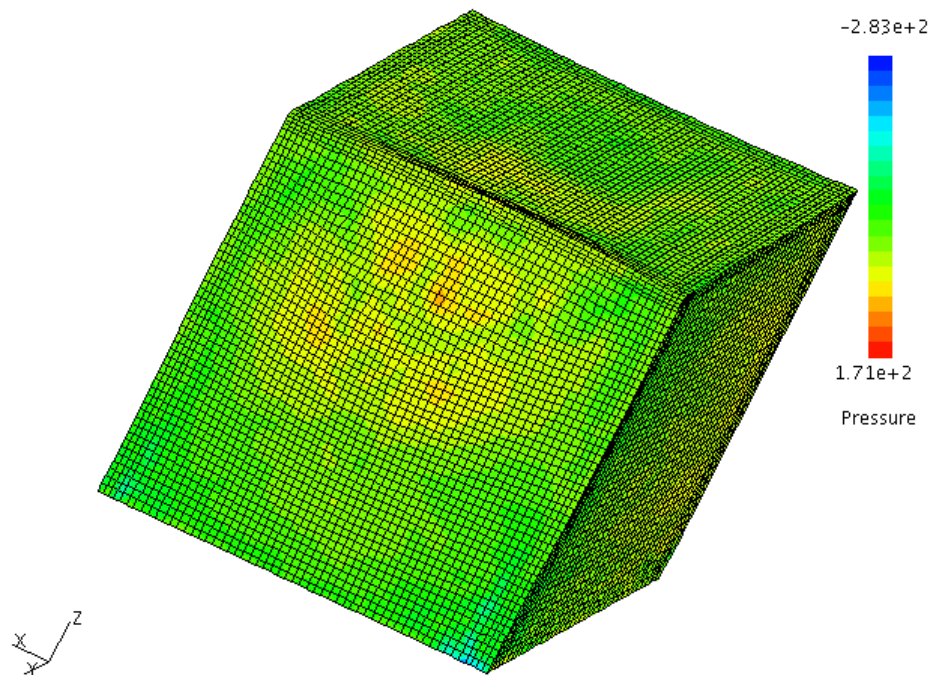


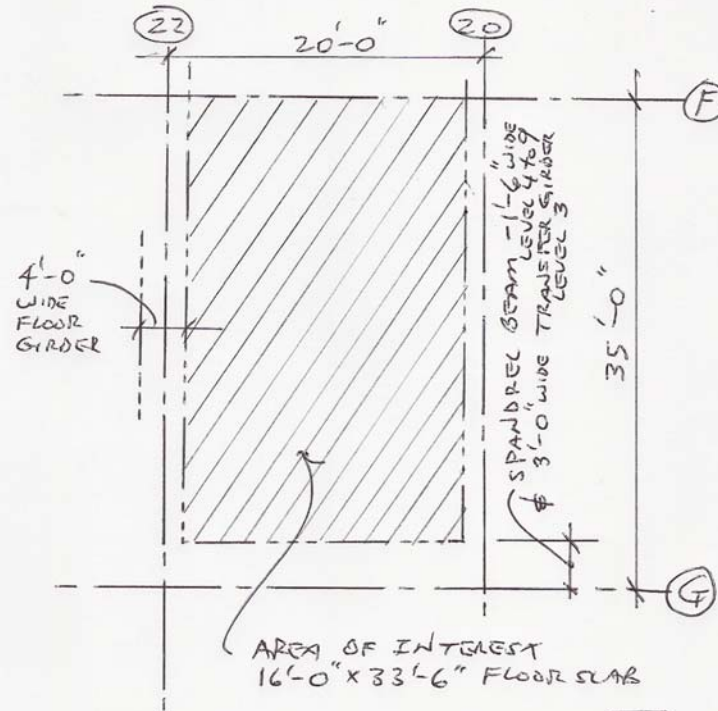
Figure G-10: Tornado Shelter Hydrostatic Pressure On Deflected Shape At 20 msec

APPENDIX I MURRAH FLOOR SLAB MEMBER PROPERTIES

This appendix contains section and member properties used in the blast loading analysis of the fifth floor slab in the Murrah Building.

	Page
Murrah Building Floor Framing Plan	269
Murrah Building Floor Slab Section Properties	270

MURRAY BUILDINGS FLOOR SLAB



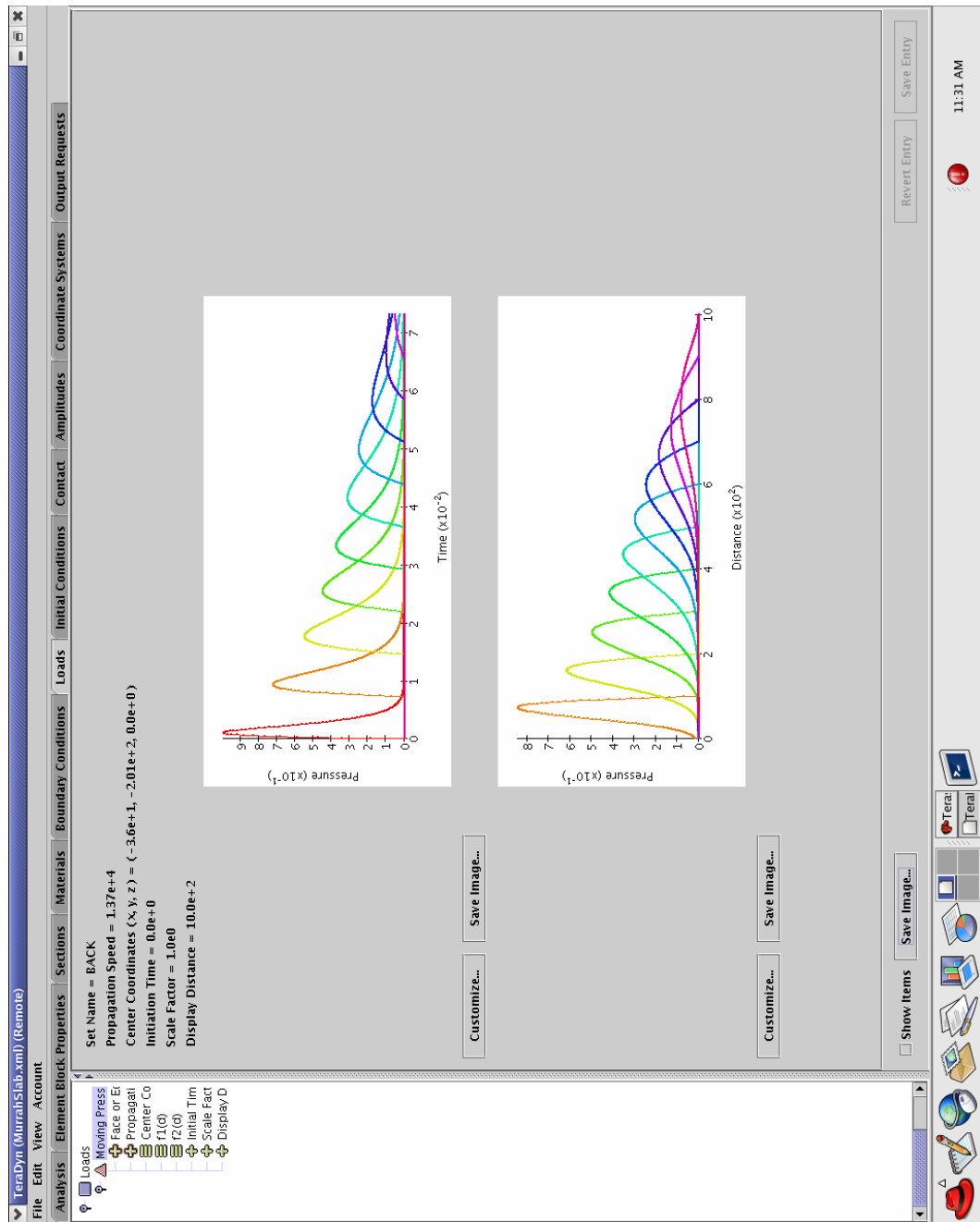
FLOOR FRAMING PLAN



APPENDIX J MURRAH SLAB MOVING PRESSURE LOADING

This appendix documents the computations used to calibrate the moving pressure load used in TeraScale's TeraDyn analysis software for the Murrah Slab.

	Page
TeraDyn Input Screen; Moving Pressure Load	272
TeraDyn Input Screen; Moving Pressure Load Input Values	273
TeraDyn Moving Pressure Load Function Definition	274
Range from Blast Epicenter to Murrah Slab	275
Summary of Blast Wave Parameters P_s , T_a and T_s Computations	276
Example Computation Using Scaled Distance Parameter Z	277
Blast Wave Parameters vs. Scaled Distance @ Range = 48ft	278
Blast Wave Parameters vs. Scaled Distance @ Range = 55ft	279
Blast Wave Parameters vs. Scaled Distance @ Range = 60ft	280
Blast Wave Parameters vs. Scaled Distance @ Range = 100ft	281
Moving Pressure Load Propagation Speed; Speed of Sound in Air	282





Moving Pressures – A Spatially and Temporally Varying Pressure Distribution on a Flat Surface

The moving pressure load is intended to model a blast loading on a flat surface where the magnitude of the peak pressure, and the rise time to the peak pressure is a function of distance from the epicenter of the blast. We define the pressure at any point on the surface as a function of the distance, d , of the point from the epicenter of the blast as:

$$p(\tau, d) = a\tau e^{-b\tau} \quad (1.1)$$

where τ is the time measured from the arrival of the pressure wave at the point and a and b are functions of distance, which are defined below. If ω is the propagation wave speed of the pressure wave along the surface, then τ is given by:

$$\tau = \max(0, t - t_0 - \frac{d}{\omega}) \quad (1.2)$$

where t is the current value of time and t_0 is the pressure initiation time at the epicenter. We see that τ is simply time measured from the point where the pressure wave applies and Equation (1.1) evaluates to zero until the pressure wave arrives.

The time at which the peak pressure occurs is given by

$$\tau_{\max} = \frac{1}{b} \quad (1.3)$$

which we refer to as the “rise time” and the peak pressure at that time is given by

$$p_{\max} = \frac{a}{b} e^{-1} \quad (1.4)$$

We allow the user to define two functions of distance from the epicenter, which describe the behavior of the pressure wave. If we define a and b as functions of distance:

$$\begin{aligned} a(d) &= \frac{f_1(d)}{f_2(d)} e^{+1} \\ b(d) &= \frac{1}{f_2(d)} \end{aligned} \quad (1.5)$$

Upon substitution of equation (1.5) into equations (1.3) & (1.4)

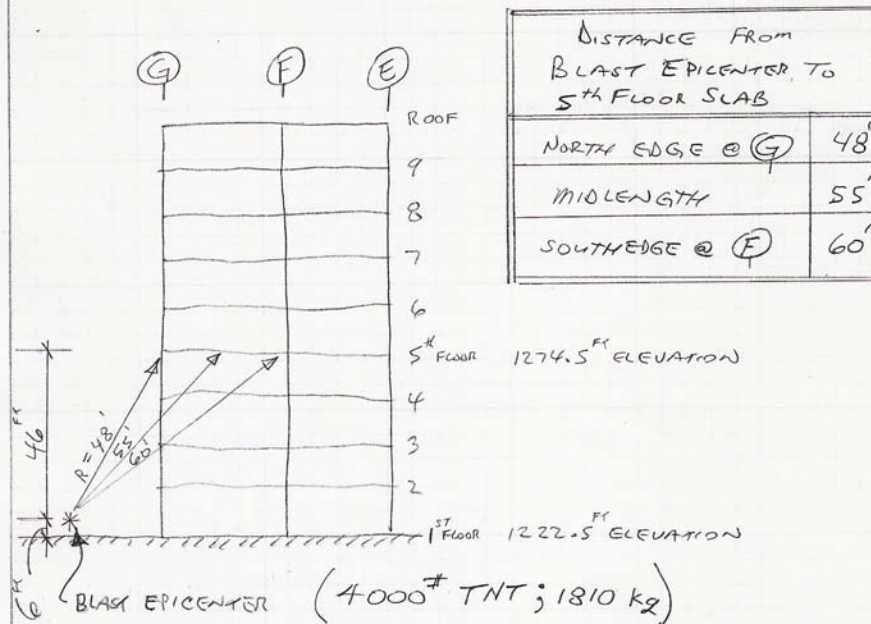
$$\begin{aligned} \tau_{\max} &= f_2(d) \\ p_{\max} &= f_1(d) \end{aligned} \quad (1.6)$$

22-141 50 SHEETS
22-142 100 SHEETS
22-144 200 SHEETS

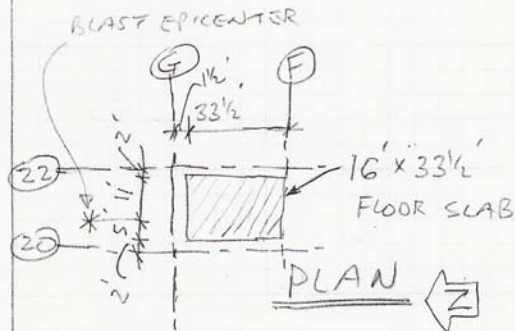
MURRAH BUILDING OKLAHOMA CITY BOMBING 19 April 1995

REFERENCE : FEMA 277, Aug 1996

PAGES 36-38 & APPENDIX B
FIGURE 3-6, FIGURE 3-21



ELEVATION SECTION: LOOKING EAST

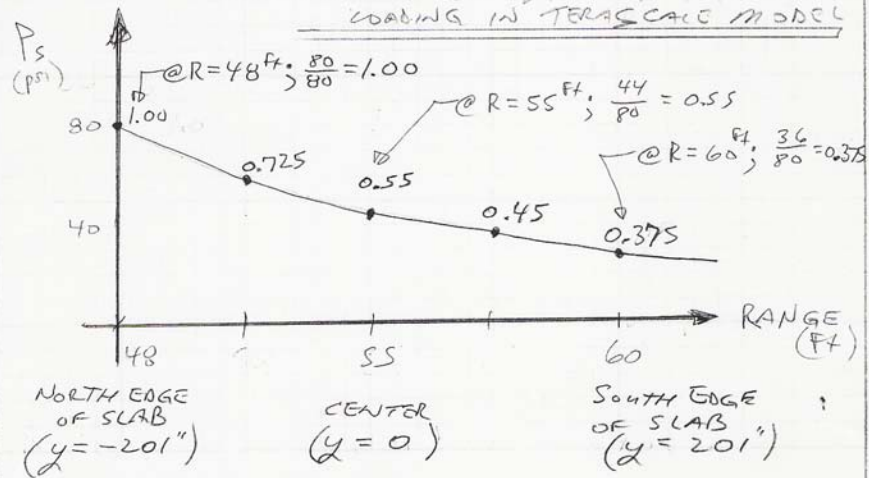


MURRAY BUILDING
OKLAHOMA CITY BOMBING 19 APRIL 1995

Blast Pressure Wave Computations Summary

R Range (ft)	P _s Peak Static Pressure (psi)	T _s Positive Phase Duration (millisecond)	T _a Time of Arrival (millisecond)
48 (North Edge of Slab)	80	24	9
55 (Center)	44	24	12
60 (South Edge of Slab)	36	24	13
100	13	30	43

CALIBRATION OF MOWING PRESSURE
LOADING IN TERAS CALC MODEL



MURRAY BUILDING
OKLAHOMA CITY BOMBING 19 APRIL 1995

REFERENCE: BLAST & BALLISTIC LOADING OF STRUCTURES
SMITH & HETHERINGTON, 1994

QUANTITY & TYPE OF EXPLOSIVE

$$W = 4000^{\#} \text{ TNT EQUIVALENT}$$

$$m = \frac{W}{Z} = \frac{4000^{\#}}{32.2 \text{ ft/sec}^2} = 124^{\#} \text{ sec}^2/\text{ft} = 124 \text{ slugs}$$

$$124 \text{ slugs} (14.594 \text{ kg/slug}) = 1810 \text{ kg TNT}$$

SCALED DISTANCE (Z) (REFER SECTION 15.3 ^{PG 296 TEXT} EXAMPLE 1)

$$Z = \frac{R}{W^{1/3}} = \frac{14.6^{\text{m}}}{(1810)^{1/3}} = \frac{14.6}{12.2} = 1.2 \text{ @ } R = 48 \left(\frac{\text{ft}}{3.281 \text{ ft}} \right) = 14.6^{\text{m}}$$

$$\text{From Fig 3.8 @ } Z = 1.2 \Rightarrow P_s = 5.5 \times 10^5 \text{ Pa}$$

$$5.5 \times 10^5 \text{ Pa} (14.5 \times 10^{-2} \frac{\text{psi}}{\text{Pa}}) = 80 \text{ psi}$$

$$\text{From Fig 3.8 @ } Z = 1.2 \Rightarrow T_s/W^{1/3} = 2 \times 10^{-3}$$

$$\frac{T_s}{W^{1/3}} = 2 \times 10^{-3} \Rightarrow T_s = 2 \times 10^{-3} (12.2) = 24 \text{ msec}$$

$$\text{From Fig 3.8 @ } Z = 1.2 \Rightarrow t_a/W^{1/3} = 7 \times 10^{-4}$$

$$\frac{t_a}{W^{1/3}} = 7 \times 10^{-4} \Rightarrow t_a = 7 \times 10^{-4} (12.2) = 9 \text{ msec}$$

SUMMARY: @ $R = 48^{\text{ft}}$

peak static overpressure is 80 psi

the arrival time is 9 msec

and the positive phase duration is 24 msec

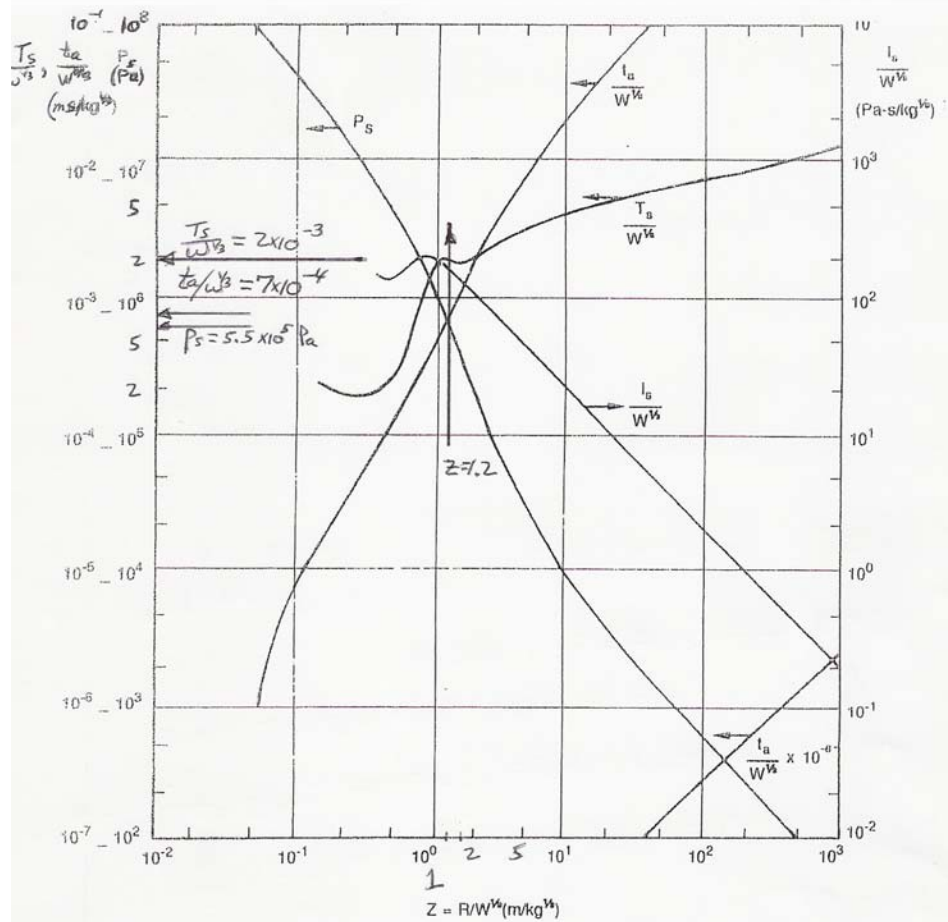


Figure 3.8 Side-on blast wave parameters for spherical charges of TNT (after Ref. 6)

(Smith & Hetherington, 1994) p236

For $R = 48^{\text{ft}} = 14.6 \text{ m}$; $Z = \frac{R}{W^{1/3}} = \frac{14.6}{12.2} = 1.2$

$P_s = 5.5 \times 10^5 \text{ Pa}$ ($14.5 \times 10^{-5} \text{ psi/Pa}$) = 80 psi

$\frac{T_s}{W^{1/3}} = 2 \times 10^{-3} \Rightarrow T_s = 2 \times 10^{-3} (12.2) = 24 \text{ msec}$

$\frac{t_a}{W^{1/3}} = 7 \times 10^{-4} \Rightarrow t_a = 7 \times 10^{-4} (12.2) = 9 \text{ msec}$

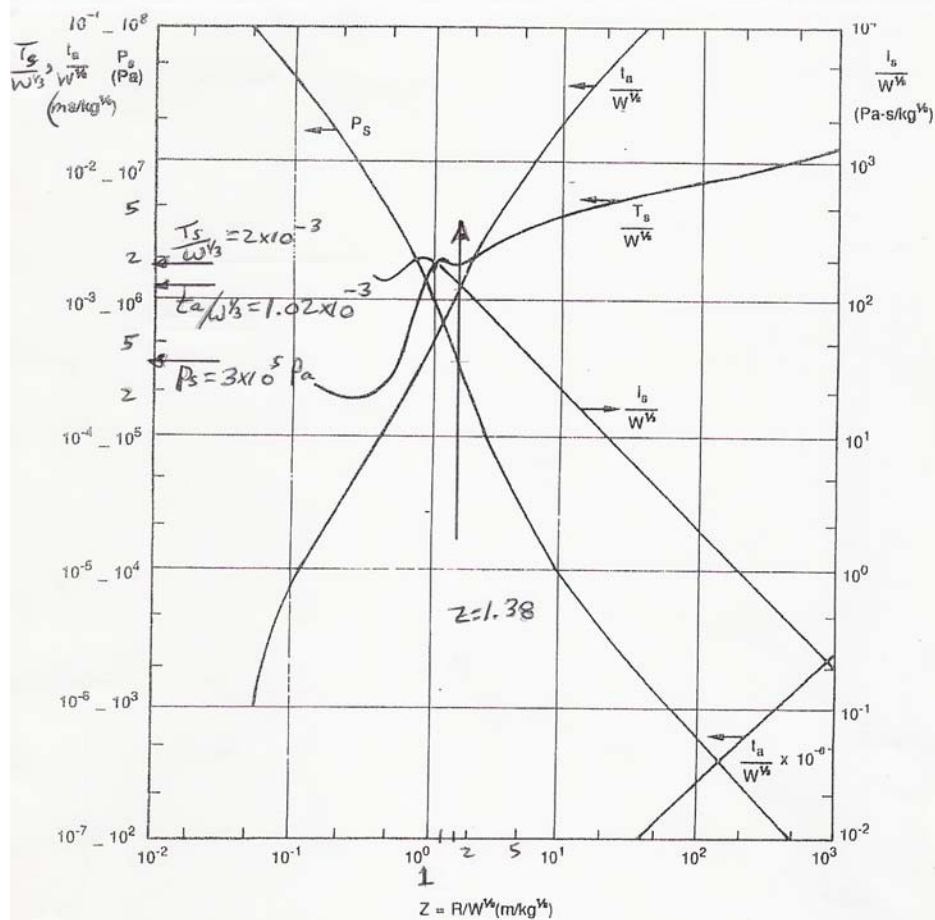


Figure 3.8 Side-on blast wave parameters for spherical charges of TNT (after Ref. 6)

(SMITH & HETHERINGTON, 1994) pg 36

For $R = 55 \text{ ft} = 16.9 \text{ m}$; $z = \frac{R}{W^{1/3}} = \frac{16.9}{12.2} = 1.38$

$P_s = 3 \times 10^5 \text{ Pa}$ ($14.5 \times 10^{-5} \frac{\text{Pa}}{\text{Pa}}$) = 43.5 psi

$\frac{T_s}{W^{1/3}} = 2 \times 10^{-3} \Rightarrow T_s = 2 \times 10^{-3} (12.2) = 24 \text{ msec}$

$\frac{t_a}{W^{1/3}} = 1.02 \times 10^{-3} \Rightarrow t_a = 1.02 \times 10^{-3} (12.2) = 12 \text{ msec}$

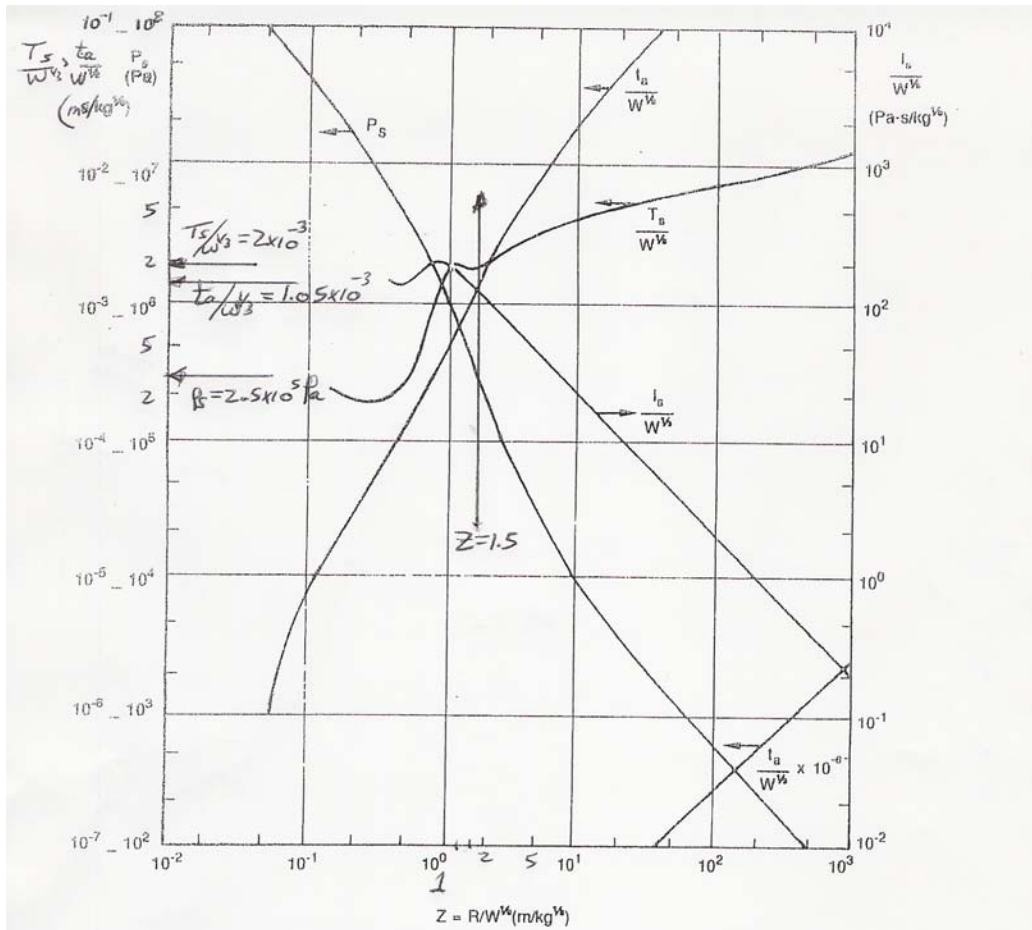


Figure 3.8 Side-on blast wave parameters for spherical charges of TNT (after Ref. 6)
(Smith & Hetherington, 1994) p236

For $R = 60 \text{ m} = 18.3 \text{ m}$; $z = \frac{R}{W^{1/3}} = \frac{18.3}{12.2} = 1.50$

$p_s = 2.5 \times 10^5 \text{ Pa} (14.5 \times 10^{-5} \text{ Pa/Pa}) = 36.3 \text{ psi}$

$T_s/W^{1/3} = 2 \times 10^{-3} \Rightarrow T_s = 2 \times 10^{-3} (12.2) = 24 \text{ msec}$

$t_a/W^{1/3} = 1.05 \times 10^{-3} \Rightarrow t_a = 1.05 \times 10^{-3} (12.2) = 13 \text{ msec}$

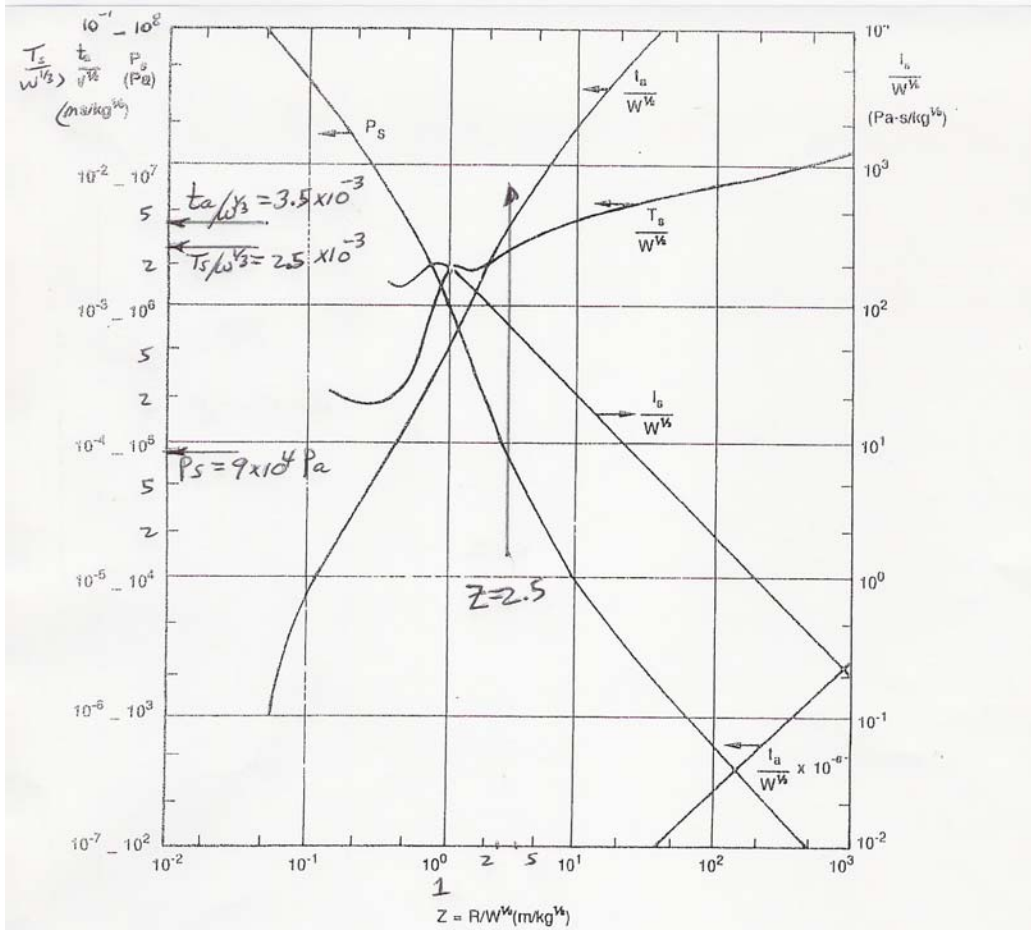


Figure 3.8 Side-on blast wave parameters for spherical charges of TNT (after Ref. 6)
(Smith & Hetherington, 1994) p. 36

For $R = 100 \text{ m}$, $F_x = 30.5 \text{ m}$; $Z = \frac{R}{W^{1/3}} = \frac{30.5}{12.2} = 2.50$

$P_s = 9 \times 10^4 \text{ Pa} (14.5 \times 10^{-5} \text{ psi/Pa}) = 13 \text{ psi}$

$\frac{T_s}{W^{1/3}} = 2.5 \times 10^{-3} \Rightarrow T_s = 2.5 \times 10^{-3} (12.2) = 30 \text{ msec}$

$\frac{t_a}{W^{1/3}} = 3.5 \times 10^{-3} \Rightarrow t_a = 3.5 \times 10^{-3} (12.2) = 43 \text{ msec}$

Speed of Sound in Air

The speed of sound in dry air is given approximately by

$$v_{\text{sound in air}} \approx 331.4 + 0.6T_C \text{ m/s}$$

where T_C is the celsius temperature,

so that at temperature $26.66666^\circ\text{C} = 80^\circ\text{F}$,

the speed of sound is $347.6666 \text{ m/s} = 1140.638 \text{ ft/s} = 778.7733 \text{ mi/hr}$.

This calculation is usually accurate enough, but for great precision one must examine the more general relationship for sound speed in gases. This sound speed does not apply to gases other than air, for example the helium from a balloon.

It is important to note that the sound speed in air is determined by the air itself. It is not dependent upon the sound amplitude, frequency or wavelength.

Sound speeds in other gases Wave speeds in other media

Relation to frequency and wavelength

Breaking the sound barrier with an aircraft

Index

Traveling
wave
concepts

Sound
propagation
concepts

HyperPhysics***** Sound

R
Nave

Go Back

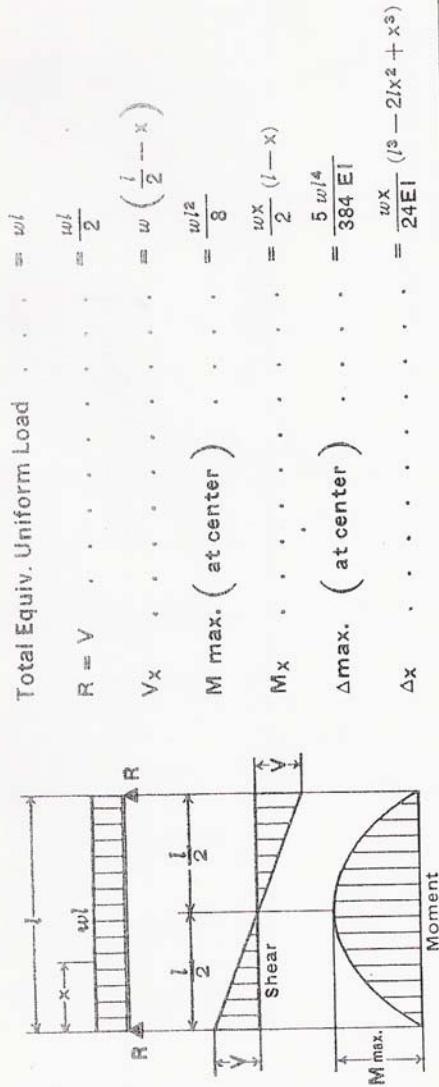
$$S_a = 779 \text{ m/hr} \left(\frac{5280 \text{ (ft) m/mile}}{3600 \text{ sec/hr}} \right) = 13,700 \text{ m/sec}$$

APPENDIX K MURRAH SLAB LOAD-DEFLECTION RESPONSE

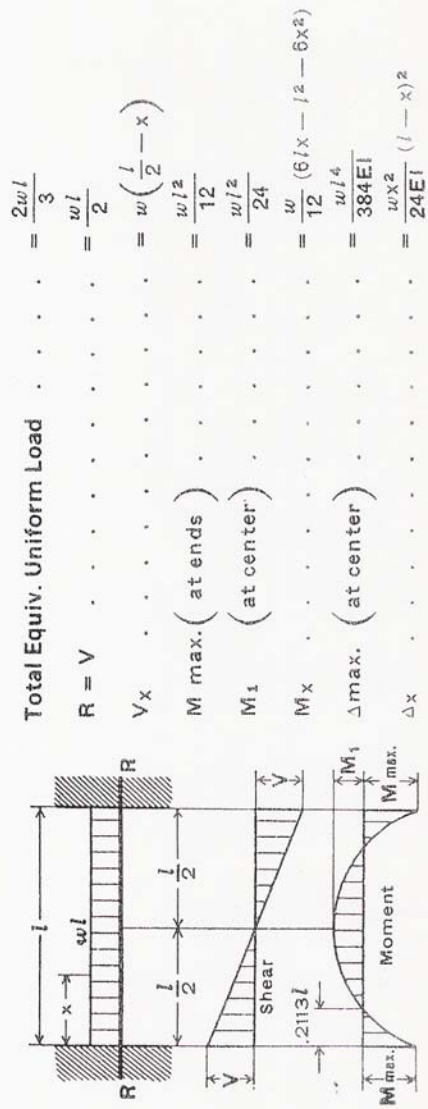
This appendix documents the computations used to estimate the magnitude of the impulsive load required to fail the fifth floor slab of the Murrah building.

	Page
Diagrams Of Uniformly Loaded Beams	284
Murrah Slab Cracking Moment	285
Murrah Slab Design Flexural Strength	286
Murrah Slab Cracked Section Properties	287
Murrah Slab Load At First Cracking At Fixed Ends	289
Murrah Slab Load At First Cracking At Midspan	290
Murrah Slab Load At Design Flexural Strength	291
Murrah Slab Deflections At First Cracking	292
Murrah Slab Deflections At Design Flexural Strength	293
Undamped Free Vibration Single Degree Of Freedom	294
Triangular Impulsive Load	295
Impulsive Load Required To Cause First Cracking At Fixed Ends	296
Impulsive Load Required To Cause First Cracking At Midspan	297
Impulsive Load Required To Reach Flexural Strength	300
ACI Estimated Deflection And Peak Pressure	302

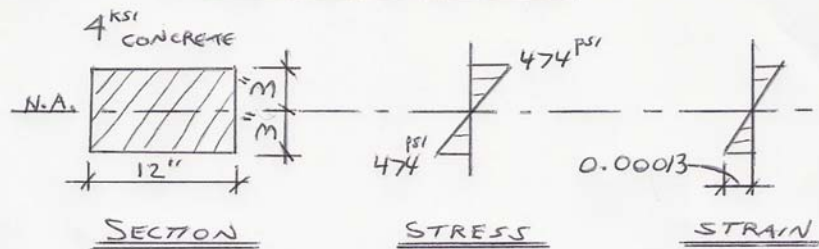
1. SIMPLE BEAM—UNIFORMLY DISTRIBUTED LOAD



15. BEAM FIXED AT BOTH ENDS—UNIFORMLY DISTRIBUTED LOADS



CRACKING MOMENT



$$E_c = 57 \sqrt{f'_c} = 57 \sqrt{4000} = 3,605,000 \text{ psi}$$

$$f_r = 7.5 \sqrt{f'_c} = 7.5 \sqrt{4000} = 474 \text{ psi}$$

$$I = \frac{1}{12} b h^3 = \frac{1}{12} (12) (12)^3 = 216 \text{ in}^4$$

$$M_{CR} = f_r \frac{I}{c} = 474 \frac{\text{psi}}{6 \text{ in}} \frac{216 \text{ in}^4}{6 \text{ in}} = 34,150 \text{ in-lbs}$$

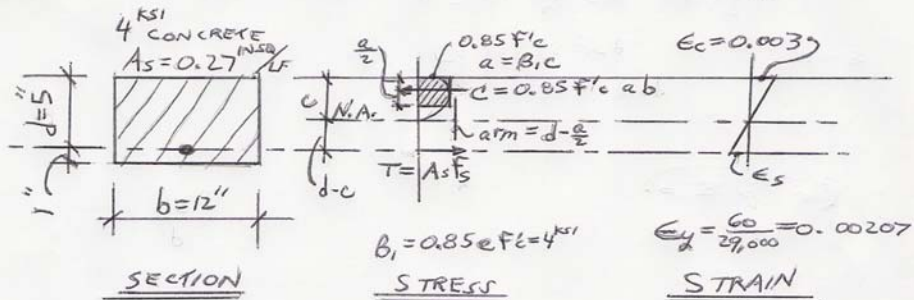
$$\epsilon = \frac{f_r}{E} = \frac{474 \text{ psi}}{3,605,000 \text{ psi}} = 0.00013 \text{ in/in}$$

$M_{CR} = 34,150 \text{ in-lb}$

CRACKING MOMENT

DESIGN STRENGTH

REFERENCE
REINFORCED CONCRETE 2ND ED
MAC GREGOR 1992



EQUILIBRIUM: $T = C$

$$A_s F_s = 0.85 F'_c a b$$

$$a = \frac{A_s F_s}{0.85 F'_c b}$$

@ yield $\Rightarrow a = \frac{A_s F_y}{0.85 F'_c b}$

EQ 1

INTERNAL COUPLE = EXTERNAL MOMENT

$$M_n = T \cdot d = A_s F_s \left(d - \frac{a}{2} \right)$$

@ yield $\Rightarrow M_n = A_s F_y \left(d - \frac{a}{2} \right)$

EQ 2

EQ 1

$$a = \frac{A_s F_y}{0.85 F'_c b}$$

$$a = \frac{0.27 \text{ IN}^2 (60 \text{ KSI})}{0.85 (4 \text{ KSI}) 12 \text{ IN}}$$

$$a = 0.397 \text{ IN}$$

EQ 2

$$M_n = A_s F_y \left(d - \frac{a}{2} \right)$$

$$M_n = 0.27 (60 \text{ KSI}) \left(5 - \frac{0.397}{2} \right) \text{ IN}$$

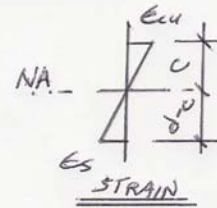
$$M_n = 77.8 \text{ K-IN}$$

STRAIN COMPATIBILITY

$$\epsilon_{cy} = 0.003$$

$$c = \frac{a}{\beta_1} = \frac{0.397 \text{ in}}{0.85} = 0.467$$

$$\frac{\epsilon_s}{d-c} = \frac{\epsilon_{cy}}{c}$$



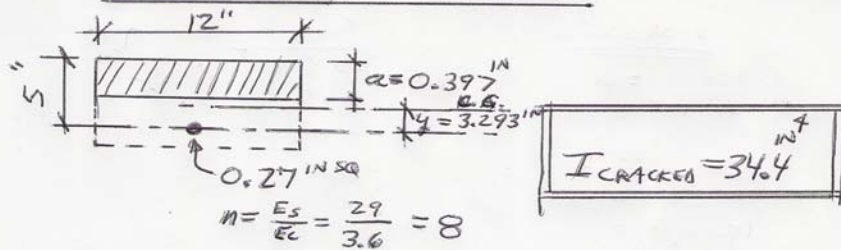
$$\epsilon_s = \frac{\epsilon_{cy}}{c} (d-c)$$

$$\epsilon_s = \frac{0.003}{0.467} (5 - 0.467) = 0.0029 \text{ in/in}$$

$\epsilon_s > \epsilon_y = 0.00207 \therefore$ STEEL YIELDS
ASSUMPTION VALID

\therefore DUCTILE DESIGN

CRACKED SECTION PROPERTIES



	A	y	Ay	I _o	d	Ad ²
1	4.76	4.80	22.85	0.06	1.51	10.8
2	2.18	0	0	0	3.293"	23.6

$$\sum A = 6.939$$

$$\sum Ay = 22.85$$

$$\bar{y} = \frac{\sum Ay}{\sum A} = \frac{22.85}{6.939} = 3.293 \text{ in ABOVE REBAR ELEVATION}$$

$$I = I_o + Ad^2 = 34.4 \text{ in}^4$$

SOME COMPUTED QUANTITIES

CONCRETE

$$A_{\text{CONCRETE}} = 0.397(12) = 4.76 \text{ in}^2$$

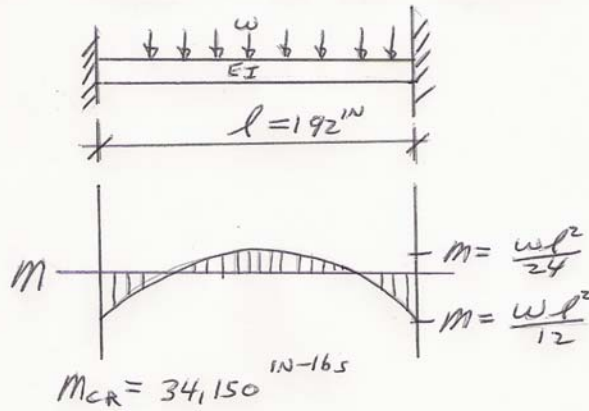
$$I_o = \frac{1}{12} b d^3 = \frac{1}{12} (12) (0.397)^3 = 0.06 \text{ in}^4$$

$$d = 5 - \frac{0.397}{2} - 3.293 = 1.51 \text{ in}$$

STEEL

$$A_{\text{STEEL}} = n A_s = 8(0.27) = 2.18 \text{ in}^2$$

LOAD @ FIRST CRACKING



@ FIXED ENDS

$$M = \frac{wl^2}{12} \Rightarrow w = \frac{12M}{l^2}$$

$$w = \frac{12(34,150 \text{ in-lb})}{(192 \text{ in})^2} = 11.1 \text{ #/in}$$

$$P_{\text{STATIC}} = \frac{11.1 \text{ #/in}}{12 \text{ in}}$$

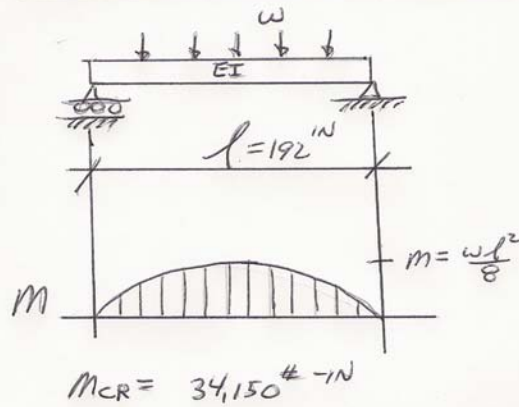
CONTROLS $\Rightarrow \boxed{P_{\text{STATIC}} = 0.926 \text{ PSI} \quad \text{FIRST CRACKING @ FIXED ENDS}}$

@ MIDSPAN

$$M = \frac{wl^2}{24} \Rightarrow w = \frac{24M}{l^2}$$

$\boxed{P_{\text{STATIC}} = 1.85 \text{ PSI} \quad \text{@ MIDSPAN}}$
 DOES NOT CONTROL

LOAD @ FIRST CRACKING



@ MIDSPAN

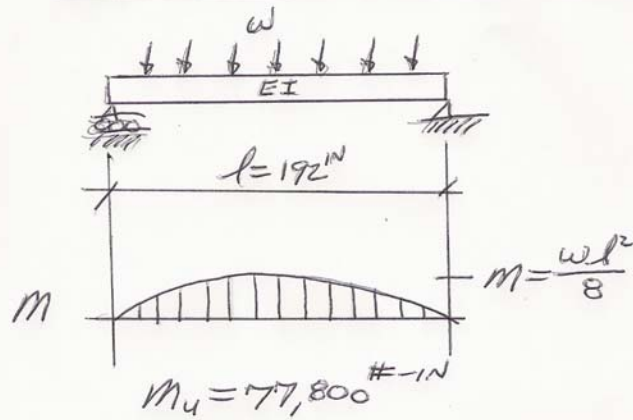
$$m = \frac{wl^2}{8} \Rightarrow w = \frac{8m}{l^2}$$

$$w = \frac{8(34,150 \text{ #-in})}{(192 \text{ in})^2} = 7.41 \text{ #/in}$$

$f_{\text{STATIC}} = 0.618 \text{ PSI}$	FIRST CRACKING @ MIDSPAN
---	-----------------------------

SLAB BEHAVES AS SIMPLY SUPPORTED
BEAM AFTER HINGES FORM AT
FIXED ENDS

LOAD @ FLEXURAL STRENGTH



@ MIDSPAN

$$M = \frac{w l^2}{8} \Rightarrow w = \frac{8M}{l^2}$$

$$w = \frac{8(77800 \text{ #-in})}{(192 \text{ in})^2} = 16.88 \text{ #/in}$$

$$f_{\text{STATIC}} = \frac{16.88 \text{ #/in}}{12 \text{ in}}$$

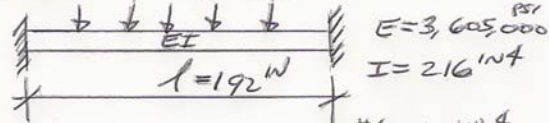
$f_{\text{STATIC}} = 1.41 \text{ PSI FLEXURAL STRENGTH @ MIDSPAN}$
--

DEFLECTIONS

FIRST CRACKING

$$p = 0.926 \text{ PSI}$$

$$w = 11.1 \text{ #/IN}$$



$$\Delta_{\text{STATIC}} = \frac{w l^4}{384 EI} = \frac{(0.926)(12) \text{ #/IN} (192 \text{ IN})^4}{384 (3,605,000 \text{ PSI}) (216 \text{ IN}^4)}$$

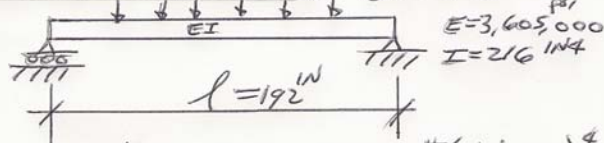
$$\Delta_{\text{STATIC}} = 0.051 \text{ IN} \quad @ \quad p_{\text{STATIC}} = 0.926 \text{ PSI}$$

FIRST CRACKING OCCURS @ FIXED ENDS

FIRST CRACKING @ MIDSPAN

$$p = 0.618 \text{ PSI}$$

$$w = 7.42 \text{ #/IN}$$



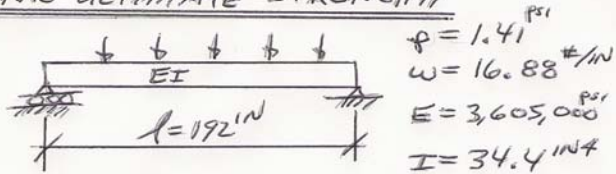
$$\Delta_{\text{STATIC}} = \frac{5 w l^4}{384 EI} = \frac{5 (0.618)(12) \text{ #/IN} (192 \text{ IN})^4}{384 (3,605,000 \text{ PSI}) (216 \text{ IN}^4)}$$

$$\Delta_{\text{STATIC}} = 0.168 \text{ IN} \quad @ \quad p_{\text{STATIC}} = 0.618 \text{ PSI}$$

FIRST CRACKING @ MIDSPAN ASSUMING
BEAM BEHAVES AS SIMPLY SUPPORTED
BEAM AFTER FIRST CRACKING @ BEAM
ENDS

DEFLECTIONS

FLEXURAL ULTIMATE STRENGTH



$$\delta_{\text{STATIC}} = \frac{5 w l^4}{384 EI} = \frac{5 (1.41 \text{ psi}) (12 \text{ \#/in}) (192 \text{ in})^4}{384 (3,605,000 \text{ psi}) (34.4 \text{ in}^4)}$$

$$\delta_{\text{STATIC}} = 2.41 \text{ in} \quad @ \quad p_{\text{STATIC}} = 1.41 \text{ psi}$$

CONCRETE CRUSHING @ MIDSPAN
 ASSUMING BEAM BEHAVES AS SIMPLY
 SUPPORTED BEAM AT FLEXURAL ULTIMATE
 AND ASSUMING FULLY CRACKED SECTION
 FULL BEAM LENGTH

UNDAMPED FREE VIBRATION SINGLE DEGREE OF FREEDOM

$$\omega_n = \sqrt{\frac{k}{m}} \quad \text{EQ 2.1.4}$$

REFERENCE: DYNAMICS
OF STRUCTURES
CHOPRA 1995

$$T_n = \frac{2\pi}{\omega_n} = 2\pi \sqrt{\frac{m}{k}} \quad \text{EQ 2.1.5}$$

$$m = \frac{W}{g}$$

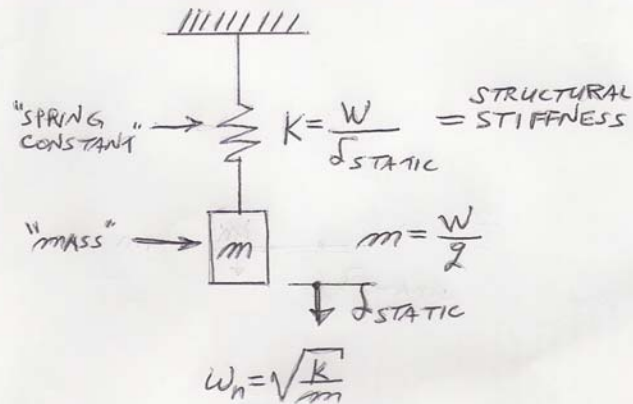
$$k = \frac{W}{\delta_{\text{STATIC}}}$$

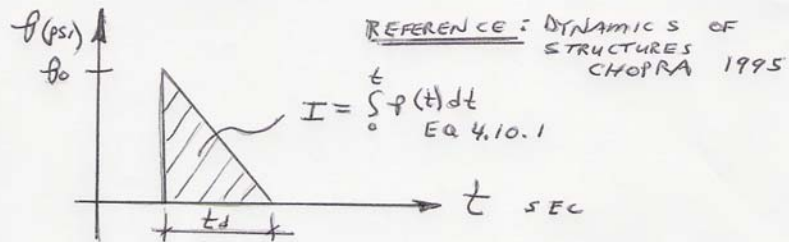
$$\therefore T_n = 2\pi \sqrt{\frac{W/g}{W/\delta_{\text{STATIC}}}} = 2\pi \sqrt{\frac{\delta_{\text{STATIC}}}{g}} \quad \text{EQ 2.1.8}$$

$$T_n = 2\pi \sqrt{\frac{\delta_{\text{STATIC}}}{g}} \quad \text{NATURAL PERIOD (SEC)}$$

$$\omega_n = \frac{2\pi}{T_n} = \sqrt{\frac{g}{\delta_{\text{STATIC}}}} \quad \text{CIRCULAR NATURAL FREQUENCY (RAD/SEC)}$$

$$f_n = \frac{1}{T_n} = \frac{1}{2\pi} \sqrt{\frac{g}{\delta_{\text{STATIC}}}} \quad \text{NATURAL FREQUENCY (HZ)}$$





$$I = \int_0^{t_d} p(t) dt$$

WHEN $\frac{t_d}{T_n} < 0.25$; THE FORCING FUNCTION MAY BE TREATED AS PURE IMPULSE
SINCE PULSE DURATION IS SHORT
COMPARED TO NATURAL PERIOD OF STRUCTURE
(Pg 146)

$$\Delta_0 = \frac{I}{m\omega_n} = \frac{I}{K} \frac{2\pi}{T_n} \quad \text{EQ 4.10.3}$$

FOR TRIANGULAR IMPULSE

$$I = \frac{1}{2} t_d p_0$$

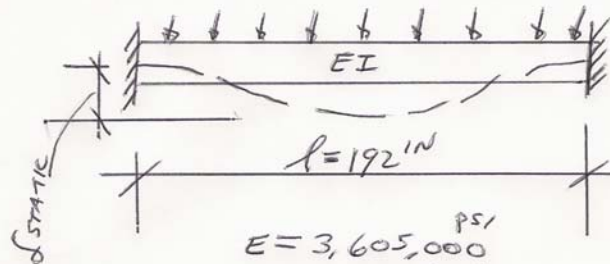
$$K = \frac{p_0}{\Delta_{\text{STATIC}}}$$

$$\Delta_0 = \frac{\frac{1}{2} t_d p_0}{p_0 / \Delta_{\text{STATIC}}} \frac{2\pi}{T_n} = \pi \frac{t_d}{T_n} \Delta_{\text{STATIC}}$$

$\frac{\Delta_0}{\Delta_{\text{STATIC}}} = \pi \frac{t_d}{T_n} \quad \text{FOR TRIANGULAR IMPULSE}$

EQ 4.10.6

COMPUTE IMPULSE LOAD REQUIRED
TO CAUSE FIRST CRACKING AT
FIXED ENDS



$$E = 3,605,000 \text{ PSI}$$

$$I = 216 \text{ in}^4 \text{ (UNCRACKED SECTION)}$$

$$\Delta_{\text{STATIC}} = 0.051 \text{ in}$$

$$\phi = 0.926 \text{ PSI} \text{ (} w = 11.1 \text{ \#/in)} \text{ } \phi_{\text{STATIC}}$$

ASSUME ONLY DEAD LOAD ON SLAB
AT TIME OF IMPULSIVE LOADING

$$W = \frac{144 \text{ PCF}}{6/12 \text{ Ft}} \approx 72 \text{ PSF} = 0.5 \text{ PSI}$$

$$m = \frac{W}{g} = \frac{0.5 \text{ PSI}}{32.2 (12) \text{ in/sec}^2} = 1.294 \times 10^{-3} \text{ \#-sec}^2/\text{in}^2$$

$$K = \frac{\phi}{\Delta} = \frac{0.926 \text{ PSI}}{0.051 \text{ in}} = 18 \text{ PSI/in}$$

$$\omega_n = \sqrt{\frac{K}{m}} = \sqrt{\frac{18 \text{ PSI/in}}{1.294 \times 10^{-3} \text{ \#-sec}^2/\text{in}^2}} = \sqrt{13910/\text{sec}^2}$$

$$\omega_n = 118 \text{ RAD/SEC} \quad f_n = \frac{\omega_n}{2\pi} = 18.8 \text{ cycle/sec}$$

$$T_n = \frac{1}{f_n} = 0.053 \text{ sec/cycle}$$

$$\frac{t_d}{T_n} = \frac{0.005}{0.053} = 0.094 < 0.25$$

∴ CAN USE APPROXIMATION

$$\frac{f_o}{f_{static}} = \pi \frac{t_d}{T_n} = 3.14(0.094)$$

$$\boxed{\frac{f_o}{f_{static}} = 0.295}$$

FOR UNCRACKED
SLAB WITH
FIXED ENDS
WITH 75 PSF
SELF WEIGHT
 $f_{static} \leq 0.926 \text{ psi}$
 $m = \frac{75 \text{ psf}}{2}$

FIND IMPULSIVE LOAD REQUIRED TO CRACK
SLAB; i.e. $f_{static} = 0.051 \text{ in}$

EQ 4.10.3 $f_o = \frac{I}{K} \frac{2\pi}{T_n}$ — TRIANGULAR IMPULSE
 $I = \frac{1}{2} t_d f_o = \frac{1}{2} (0.005 \text{ sec}) f_o$
 $K = 18 \text{ psi/in}$
 $T_n = 0.053 \text{ sec/cycle}$

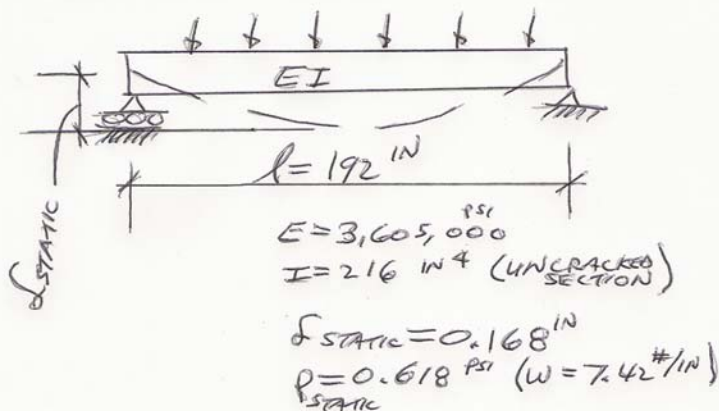
$$0.051 \text{ in} = f_o = \frac{\frac{1}{2} (0.005 \text{ sec}) f_o 2\pi}{(18 \text{ psi/in})(0.053 \text{ sec/cycle})}$$

$$\boxed{f_o = 3.10 \text{ psi}}$$

IMPULSE REQ'D
TO CRACK SLAB
AT FIXED ENDS
(SELF WT = 0.5 psi)

NOTE: BEAM SELF WT
PROVIDES INERTIA FORCE
TO RESIST IMPULSE, BUT
IS NEGLECTED IN
DEFLECTION & IMPULSE
COMPUTATION

COMPUTE IMPULSE LOAD REQUIRED
TO CAUSE FIRST CRACKING AT
MIDSPAN (ASSUME CRACKING AT
FIXED ENDS ALLOWS SLAB TO ACT
AS SIMPLY SUPPORTED BEAM)



ASSUME ONLY DEAD LOAD ON SLAB AT
TIME OF IMPULSIVE LOADING

$$W = 72 \text{ psf} = 0.5 \text{ psi}$$

$$m = 1.294 \times 10^{-3} \text{ #} \cdot \frac{\text{sec}^2}{\text{in}}$$

$$K = \frac{p}{\delta} = \frac{0.618}{0.168} = 3.68 \text{ psi/in}$$

$$\omega_n = \sqrt{\frac{K}{m}} = \sqrt{\frac{3.68 \text{ psi/in}}{1.294 \times 10^{-3} \text{ #} \cdot \frac{\text{sec}^2}{\text{in}}}} = \sqrt{2843} \text{ /sec}$$

$$\omega_n = 53 \text{ RAD/sec} \quad f_n = \frac{\omega_n}{2\pi} = 8.49 \text{ cycles/sec}$$

$$T_n = \frac{1}{f_n} = 0.118 \text{ sec/cycle}$$

$$\frac{t_d}{T_n} = \frac{0.005}{0.118} = 0.0424 < 0.25$$

∴ CAN USE APPROXIMATION

$$\frac{f_o}{f_{\text{static}}} = \pi \frac{t_d}{T_n} = 3.14 (0.0424)$$

$$\boxed{\frac{f_o}{f_{\text{static}}} = 0.133}$$

FOR UNCRACKED
SLABS SIMPLY
SUPPORTED WITH
75 PSF SELF WT
 $f_{\text{static}} = 0.618 \text{ psi}$
 $m = \frac{75 \text{ PSF}}{2}$

FIND ~~IMPULSIVE~~ LOAD REQUIRED TO CRACK
SLAB AT MIDSPAN

Eq 4.10.3
$$f_o = \frac{I}{K} \frac{2\pi}{T_n}$$

$$I = \frac{1}{2} (0.005) f_o$$

$$K = 3.68 \text{ psi/in}$$

$$T_n = 0.118 \text{ sec/cycle}$$

$$f_o = 0.168 = \frac{\frac{1}{2} (0.005 \text{ sec}) 8.02\pi}{(3.68 \text{ psi/in}) (0.118 \text{ sec/cycle})}$$

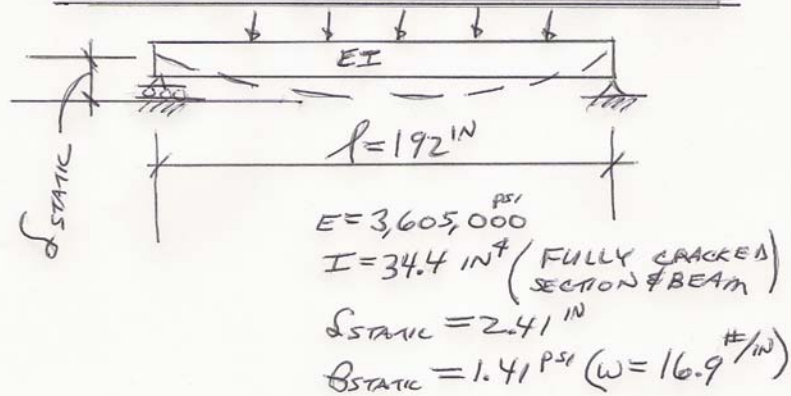
$$\boxed{P_o = 4.64 \text{ psi}}$$

"GRAVITY" IS
"TURNED OFF"
WHEN IMPULSE
STRIKES BEAM
WITH MASS $\frac{W}{2}$

IMPULSE PRESSURE
REQ'D TO CRACK
SLAB AT MIDSPAN
SIMPLY SUPPORTED
SELF WT = 0.5 psi

NOTE: BEAM SELF WT RESISTS
INERTIA FORCE BUT IS
NEGLECTED TO COMPUTE
DEFLECTION & IMPULSE

COMPUTE IMPULSE LOAD REQUIRED
TO REACH ULTIMATE FLEXURAL LOAD



ASSUME ONLY DEAD LOAD ON SLAB AT TIME OF
IMPULSIVE LOADING

$$W = 72 \text{ psf} = 0.5 \text{ psi}$$

$$m = \frac{W}{g} = 1.294 \times 10^{-3} \frac{\text{#} \cdot \text{sec}^2/\text{in}}{\text{in}^2}$$

$$k = \frac{B}{\delta} = \frac{1.41 \text{ psi}}{2.41 \text{ in}} = 0.585 \frac{\text{psi}}{\text{in}}$$

$$\omega_n = \sqrt{\frac{k}{m}} = \sqrt{\frac{0.585 \text{ psi/in}}{1.294 \times 10^{-3} \text{ #sec}^2/\text{in}^2}} = \sqrt{452/\text{sec}^2}$$

$$\omega_n = 21.3 \text{ RAD/sec} \quad f_n = 3.38 \text{ CYCLE/SEC}$$

$$T_n = 0.295 \text{ sec/cycle}$$

$$\frac{t_d}{T_n} = \frac{0.005}{0.295} = 0.0169 < 0.25$$

∴ CAN USE APPROXIMATION

$$\frac{L_0}{L_{\text{STATIC}}} = \pi \frac{t_d}{T_n} = 3.14 (0.0169)$$

$$\frac{L_0}{L_{\text{STATIC}}} = 0.053$$

FOR FULLY CRACKED
BEAM SIMPLY SUPPORTED
WITH 75 PSF SELF WT.

$$P_{\text{STATIC}} \leq 1.41 \text{ PSI}$$

$$m = \frac{75 \text{ PSF}}{g}$$

FIND IMPULSIVE LOAD TO REACH FLEXURAL
STRENGTH

$$\text{EQ 4.10.3} \quad L_0 = \frac{I}{K} \frac{2\pi}{T_n}$$

$$I = \frac{1}{2} (0.005) P_0$$

$$K = 0.585 \text{ PSI/IN}$$

$$T_n = 0.295 \text{ sec/cycle}$$

$$L_0 = 2.41 = \frac{\frac{1}{2} (0.005) P_0 \cdot 2\pi}{(0.585 \text{ PSI/IN}) (0.295 \text{ sec/cycle})}$$

$$P_0 = 26.5 \text{ PSI}$$

IMPULSE REQ'D
TO REACH
FLEXURAL ULTIMATE
STRENGTH

NOTE: BEAM SELF WT
RESISTS IMPULSE BUT
IS NEGLECTED IN
COMPUTATION OF I

GRAVITY IS "TURNED OFF"
WHEN IMPULSE STRIKES BEAM
WITH MASS = $\frac{W}{g}$

ACI ESTIMATED DEFLECTIONS & Peak Pressure

REFERENCE: ACI 318-02

§ 9.5.2

$$\text{EQ 9-8: } I_e = \left(\frac{m_{cr}}{m_u} \right)^3 I_g + \left[1 - \left(\frac{m_{cr}}{m_u} \right)^3 \right] I_{cr}$$

$$\frac{m_{cr}}{m_u} = \frac{34150 \text{ in}^4}{77800 \text{ in}^4} = 0.439$$

$$I_e = (0.439)^3 216 \text{ in}^4 + (1 - (0.439)^3) 34.4 \text{ in}^4$$

$$I_e = 18.27 \text{ in}^4 + 31.49 \text{ in}^4$$

$$\boxed{I_e = 49.8 \text{ in}^4} \quad \text{ACI 318-02 § 9.5.2.3}$$

$$\Delta_{static} = \frac{5wL^4}{384EI} = \frac{5(1.41)(12)^4(192)}{384(3605000)(49.8 \text{ in}^4)}$$

$$\boxed{\Delta_{static} = 1.67 \text{ in}} \quad \left\{ \begin{array}{l} @ P = 1.41 \text{ psi} \quad I_e = 49.8 \text{ in}^4 \\ \text{CONCRETE CRACKING @ MIDSPAN} \\ \text{SIMPLY SUPPORTED BEAM} \end{array} \right.$$

$$k = \frac{P}{\Delta} = \frac{1.41 \text{ psi}}{1.67 \text{ in}} = 0.845 \text{ psi/in}$$

$$\omega_n = \sqrt{\frac{k}{m}} = \sqrt{\frac{0.845 \text{ psi/in}}{1.294 \times 10^{-3} \text{ sec}^2/\text{in}}} = \sqrt{653/\text{sec}^2} = 25.6 \text{ rad/sec}$$

$$F_n = 4.07 \text{ cycles/sec} \quad T_n = 0.246 \text{ sec/cycle}$$

$$\frac{\Delta_0}{\Delta_{static}} = \pi \frac{0.005}{0.246} = 0.06 \neq 0.25 \geq \frac{0.06}{\pi} \text{ OK}$$

$$\Delta_0 = 1.67 = \frac{1/2 (0.005 \text{ sec}) f_0 2\pi}{(0.845 \text{ psi/in}) (0.246 \text{ sec/cycle})} \Rightarrow \boxed{f_0 = 22.1 \text{ psi}}$$

APPENDIX L MURRAH SLAB FLEXURAL STRESS

This appendix contains results from the finite element analysis of the Murrah building fifth floor slab subjected to an impulsive loading. The figures show the flexural stress contours plotted on the deflected shape of the structure in 5 msec intervals for the 50 msec analysis duration. The load case is 10 psi peak pressure and the mesh is 3 elements through the slab depth. Deflection is magnified by 10.

	Page
Murrah Slab Flexural Stress On Deflected Shape At 5 msec	304
Murrah Slab Flexural Stress On Deflected Shape At 10 msec	304
Murrah Slab Flexural Stress On Deflected Shape At 15 msec	305
Murrah Slab Flexural Stress On Deflected Shape At 20 msec	305
Murrah Slab Flexural Stress On Deflected Shape At 25 msec	306
Murrah Slab Flexural Stress On Deflected Shape At 30 msec	306
Murrah Slab Flexural Stress On Deflected Shape At 35 msec	307
Murrah Slab Flexural Stress On Deflected Shape At 40 msec	307
Murrah Slab Flexural Stress On Deflected Shape At 45 msec	308
Murrah Slab Flexural Stress On Deflected Shape At 50 msec	308

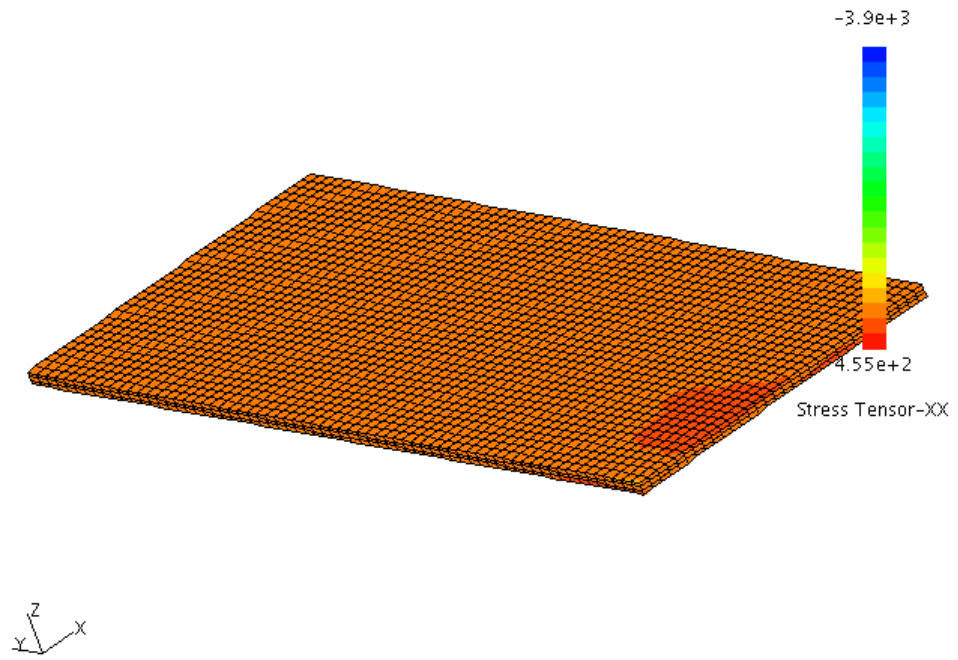


Figure K-1: Murrah Slab Flexural Stress On Deflected Shape At 5 msec

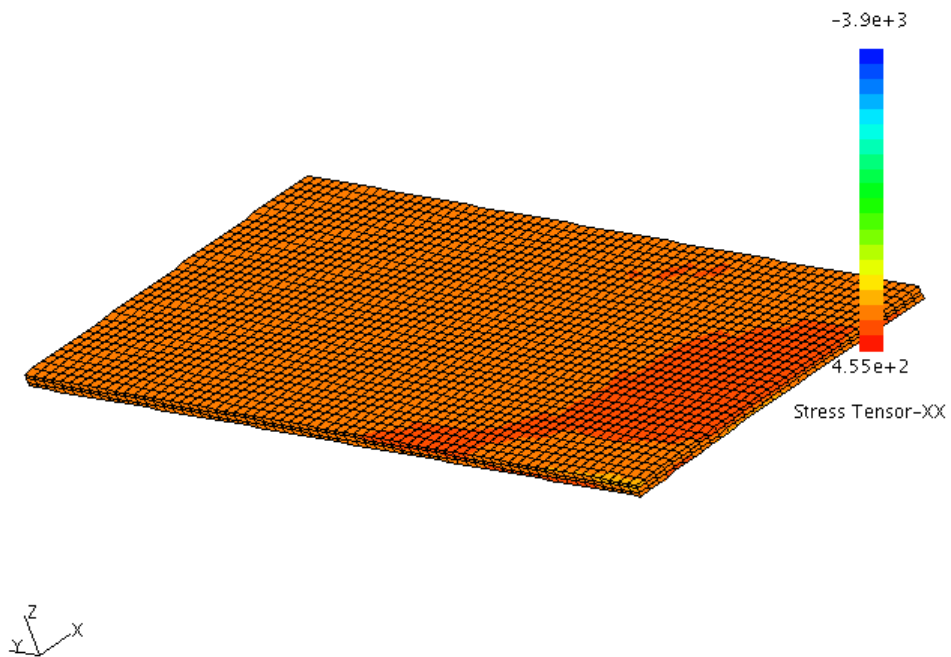


Figure K-2: Murrah Slab Flexural Stress On Deflected Shape At 10 msec

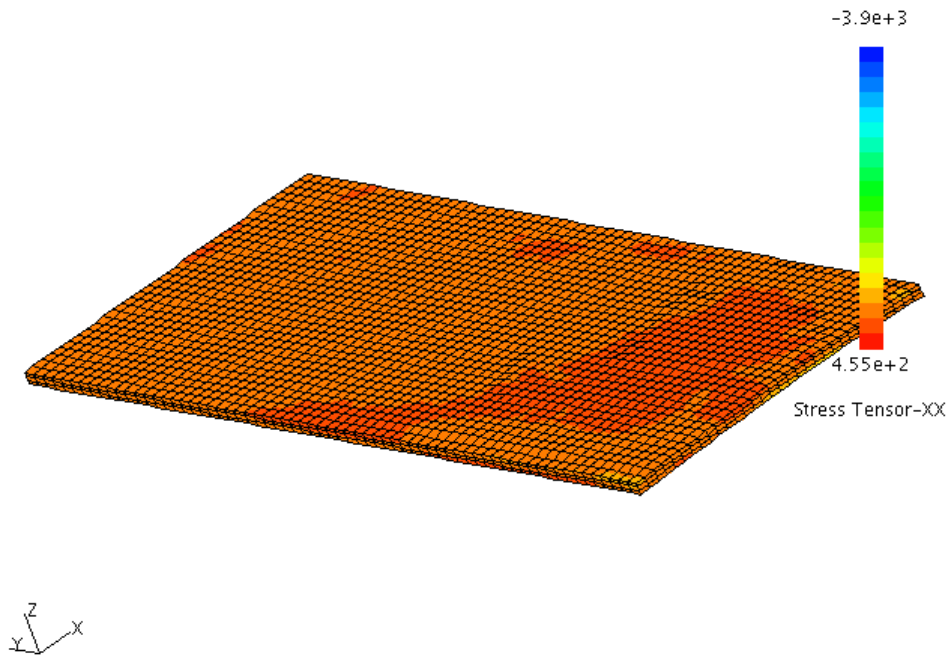


Figure K-3: Murrah Slab Flexural Stress On Deflected Shape At 15 msec

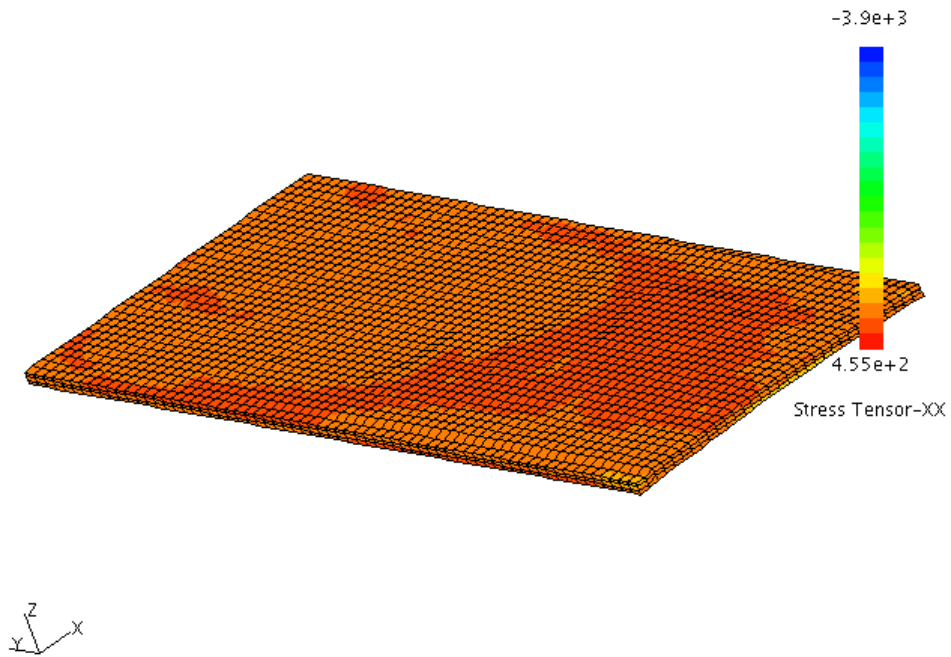


Figure K-4: Murrah Slab Flexural Stress On Deflected Shape At 20 msec

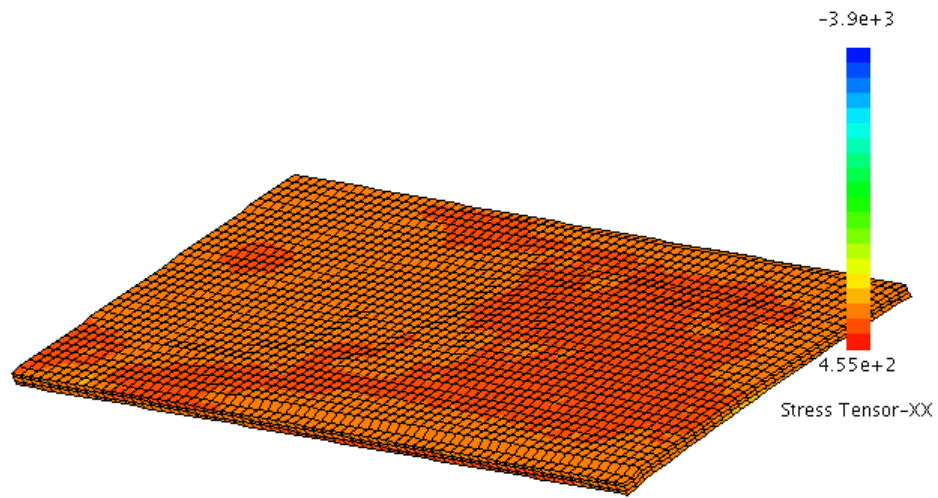


Figure K-5: Murrah Slab Flexural Stress On Deflected Shape At 25 msec

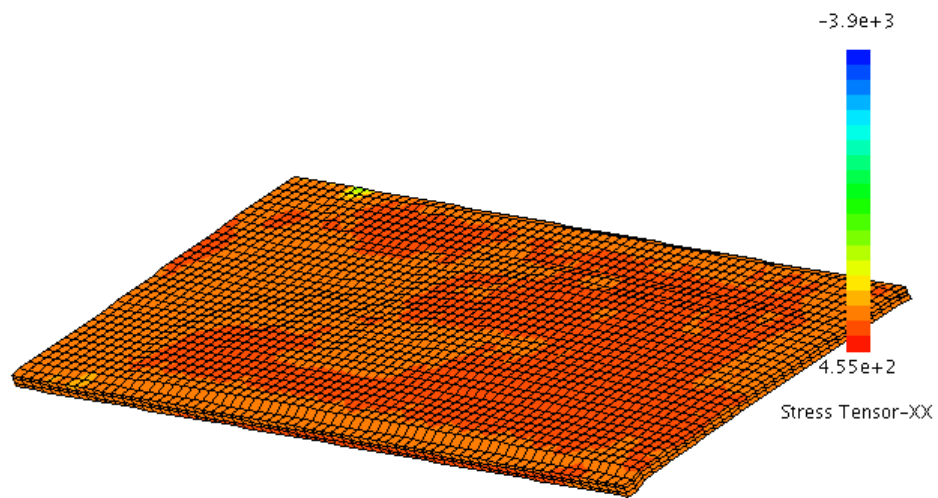


Figure K-6: Murrah Slab Flexural Stress On Deflected Shape At 30 msec

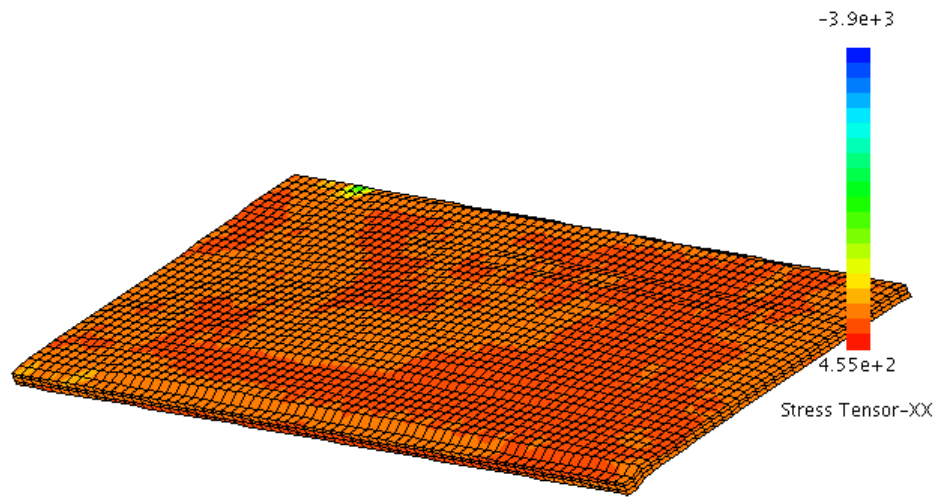


Figure K-7: Murrah Slab Flexural Stress On Deflected Shape At 35 msec

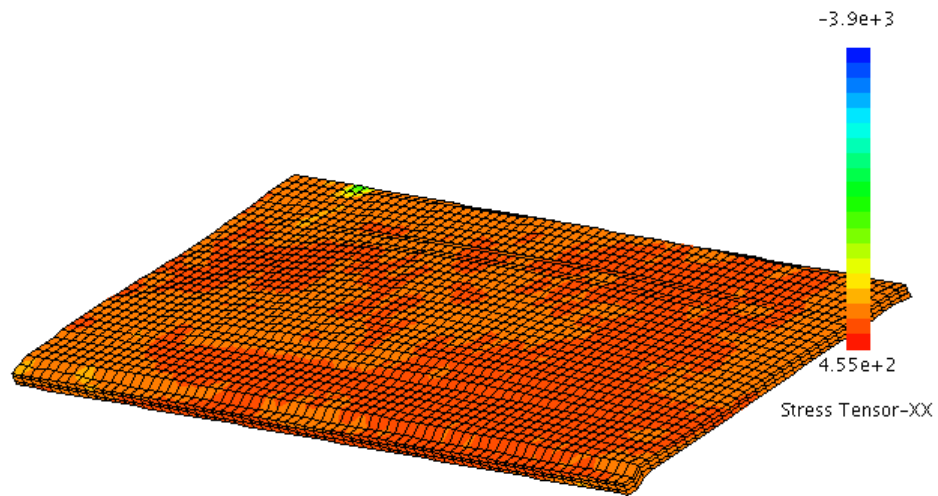


Figure K-8: Murrah Slab Flexural Stress On Deflected Shape At 40 msec

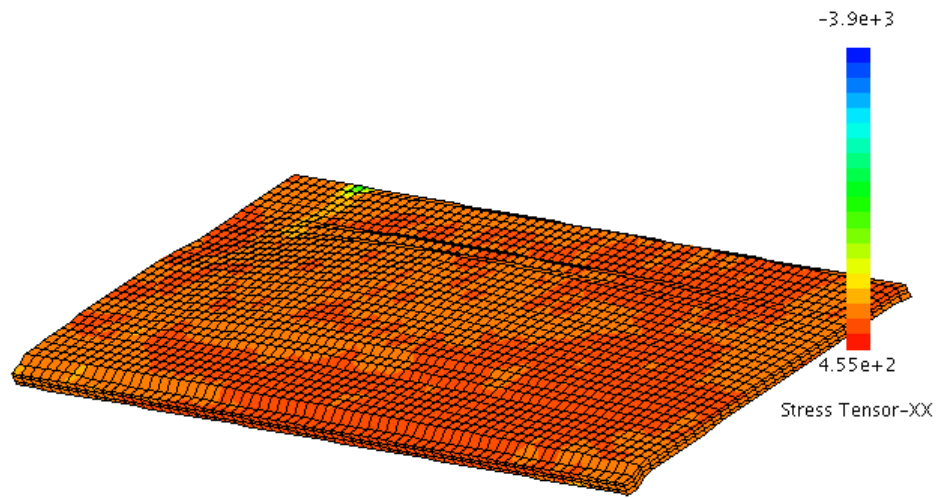


Figure K-9: Murrah Slab Flexural Stress On Deflected Shape At 45 msec

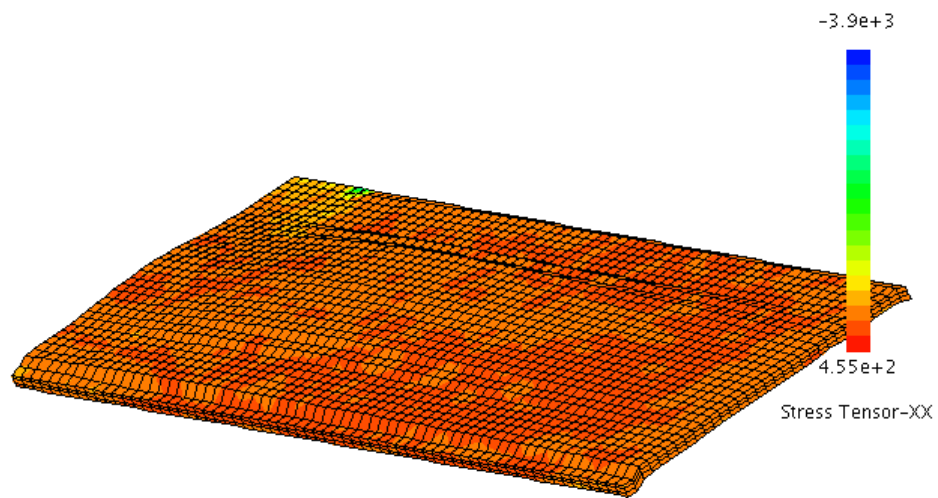


Figure K-10: Murrah Slab Flexural Stress On Deflected Shape At 50 msec

APPENDIX M FOOT SLAB QUASI-STATIC LOAD-DEFLECTION

This appendix contains results data from the quasi-static finite element analysis of the foot wide strip of floor slab. Mesh used was 6 elements through the slab thickness.

	Page
Simply Supported Slab Quasi-Static Loading Response Data	310
Fixed Ends Slab Quasi-Static Loading Response Data	311

QUASI STATIC LOAD-DEFLECTION RESPONSE
POSITIVE MOMENT APPLIED TO POSITIVE MOMENT RESISTING SECTION
SIMPLY SUPPORTED FOOT WIDE SLAB STRIP

DURATION OF RAMP LOAD
(sec)

0.50						1.00					
time step (sec)	load 0.705 (psi)	midspan deflection (inches)	time step (sec)	load 1.41 (psi)	midspan deflection (inches)	time step (sec)	load 0.353 (psi)	midspan deflection (inches)	time step (sec)	load 0.705 (psi)	midspan deflection (inches)
0.00	0.00	0.0000	0.00	0.00	0.0000	0.00	0.00	0.0000	0.00	0.00	0.0000
0.01	0.01	0.0002	0.01	0.03	0.0004	0.04	0.01	0.0032	0.02	0.01	0.0009
0.02	0.03	0.0019	0.02	0.06	0.0037	0.08	0.03	0.0139	0.04	0.03	0.0065
0.03	0.04	0.0059	0.03	0.08	0.0118	0.12	0.04	0.0180	0.06	0.04	0.0169
0.04	0.06	0.0128	0.04	0.11	0.0256	0.16	0.06	0.0206	0.08	0.06	0.0278
0.05	0.07	0.0222	0.05	0.14	0.0444	0.20	0.07	0.0311	0.10	0.07	0.0344
0.06	0.08	0.0332	0.06	0.17	0.0663	0.22	0.08	0.0349	0.12	0.08	0.0360
0.07	0.10	0.0443	0.07	0.20	0.0909	0.24	0.08	0.0360	0.14	0.10	0.0365
0.08	0.11	0.0542	0.08	0.23	0.1200	0.26	0.09	0.0361	0.16	0.11	0.0410
0.09	0.13	0.0617	0.09	0.25	0.1400	0.28	0.10	0.0380	0.18	0.13	0.0507
0.10	0.14	0.0663	0.10	0.28	0.1800	0.30	0.11	0.0424	0.20	0.14	0.0620
0.11	0.16	0.0684	0.11	0.31	0.2100	0.32	0.11	0.0481	0.22	0.16	0.0705
0.12	0.17	0.0688	0.12	0.34	0.2600	0.34	0.12	0.0524	0.24	0.17	0.0767
0.13	0.18	0.0689	0.13	0.37	0.3100	0.36	0.13	0.0539	0.26	0.18	0.0853
0.14	0.20	0.0702				0.38	0.13	0.0540	0.28	0.20	0.0997
0.15	0.21	0.0742				0.40	0.14	0.0554	0.30	0.21	0.1200
0.16	0.23	0.0824				0.42	0.15	0.0595	0.32	0.23	0.1500
0.17	0.24	0.0954				0.44	0.16	0.0651	0.34	0.24	0.1800
0.18	0.25	0.1100				0.46	0.16	0.0711			
0.19	0.27	0.1400				0.48	0.17	0.0781			
0.20	0.28	0.1700				0.50	0.18	0.0877			
0.21	0.30	0.2100				0.52	0.18	0.0995			
0.22	0.31	0.2500				0.54	0.19	0.1100			
0.23	0.32	0.3000				0.56	0.20	0.1300			
						0.58	0.20	0.1500			
						0.60	0.21	0.1600			
<p style="text-align: center;">one way floor slab with 192" span and simply supported ends 6" slab reinf. w/ 0.27insq/ft width @ d=5" 4ksi concrete, Grade 60 steel 75psf/g slab mass</p> <p style="text-align: center;">Note: Gravity neglected in impulse load & deflection computation</p>											

QUASI STATIC LOAD-DEFLECTION RESPONSE
POSITIVE MOMENT APPLIED TO POSITIVE MOMENT RESISTING SECTION
FOOT WIDE SLAB STRIP WITH FIXED ENDS

DURATION OF RAMP LOAD
(sec)

0.50						1.00					
time step (sec)	load 0.705 (psi)	midspan deflection (inches)	time step (sec)	load 1.41 (psi)	midspan deflection (inches)	time step (sec)	load 0.353 (psi)	midspan deflection (inches)	time step (sec)	load 0.705 (psi)	midspan deflection (inches)
0.00	0.00	0.0000	0.00	0.00	0.0000	0.00	0.00	0.0000	0.00	0.00	0.0000
0.06	0.08	0.0040	0.05	0.14	0.0064	0.04	0.01	0.0078	0.04	0.03	0.0155
0.08	0.11	0.0062	0.10	0.28	0.0135	0.08	0.03	0.0154	0.08	0.06	0.0308
0.10	0.14	0.0068	0.15	0.42	0.0215	0.12	0.04	0.0229	0.12	0.08	0.0458
0.12	0.17	0.0092	0.19	0.54	0.0270	0.16	0.06	0.0301	0.16	0.11	0.0602
0.14	0.20	0.0096	0.20	0.56	0.0310	0.20	0.07	0.0371	0.20	0.14	0.0741
0.16	0.23	0.0120	0.21	0.59	0.0365	0.24	0.08	0.0439	0.24	0.17	0.0877
0.18	0.25	0.0125	0.22	0.62	0.0417	0.28	0.10	0.0506	0.28	0.20	0.1010
0.20	0.28	0.0148	0.23	0.65	0.0433	0.32	0.11	0.0573	0.32	0.23	0.1114
0.22	0.31	0.0156	0.24	0.68	0.0425	0.36	0.13	0.0641	0.36	0.25	0.1128
0.24	0.34	0.0175	0.25	0.71	0.0432	0.40	0.14	0.0710	0.40	0.28	0.1142
0.26	0.37	0.0187	0.26	0.73	0.0473	0.44	0.16	0.0783	0.44	0.31	0.1156
0.28	0.39	0.0202	0.27	0.76	0.0533	0.48	0.17	0.0857	0.48	0.34	0.1171
0.30	0.42	0.0218	0.28	0.79	0.0601	0.52	0.18	0.0933	0.52	0.37	0.1187
0.32	0.45	0.0229	0.29	0.82	0.0654	0.56	0.20	0.1010	0.56	0.39	0.1202
0.34	0.48	0.0248	0.30	0.85	0.0696	0.60	0.21	0.1010	0.60	0.42	0.1218
0.36	0.51	0.0256	0.31	0.87	0.0723	0.64	0.23	0.1116	0.64	0.45	0.1233
0.38	0.54	0.0295	0.32	0.90	0.0747	0.68	0.24	0.1124	0.68	0.48	0.1248
0.40	0.56	0.0340	0.33	0.93	0.0779	0.72	0.25	0.1131	0.72	0.51	0.1268
0.42	0.59	0.0372	0.34	0.96	0.0818	0.76	0.27	0.1138	0.76	0.54	0.1281
0.44	0.62	0.0381	0.35	0.99	0.0857	0.80	0.28	0.1145	0.80	0.56	0.1357
0.46	0.65	0.0417	0.36	1.02	0.0905	0.84	0.30	0.1152	0.84	0.59	0.1368
0.48	0.68	0.0436	0.37	1.04	0.0970	0.88	0.31	0.1158	0.88	0.62	0.1380
0.50	0.71	0.0448	0.38	1.07	0.1000	0.92	0.32	0.1165	0.92	0.65	0.1410
0.52	0.71	0.0486	0.39	1.10	0.1100	0.96	0.34	0.1172	0.96	0.68	0.1453
0.53	0.71	0.0490	0.40	1.13	0.1100	1.00	0.35	0.0179	1.00	0.71	0.1470
<p style="text-align: center;">one way floor slab with 192" span and fixed ends 6" slab reinf. w/ 0.27insq/ft width @ d=5" 4ksi concrete, Grade 60 steel 75psf/g slab mass</p> <p style="text-align: center;">Note: Gravity neglected in impulse load & deflection computation</p>											

APPENDIX N LITERATURE REVIEW

This appendix contains additional literature review on concrete and reinforcing steel constitutive relations and on the finite element analysis technique.

APPENDIX N LITERATURE REVIEW

TABLE OF CONTENTS

	Page
LIST OF FIGURES	315
APPENDIX N LITERATURE REVIEW	316
2.1 INTRODUCTION	316
2.2 GENERAL THEORY	316
2.2.1 STIFFNESS METHOD	318
2.2.2 FLEXIBILITY METHOD	318
2.2.3 EQUILIBRIUM, COMPATIBILITY AND CONSTITUTIVE RELATIONS	320
2.2.4 RITZ NUMERICAL APPROXIMATION METHOD	320
2.2.5 CONVERGENCE	321
2.3 NONLINEARITY	321
2.3.1 SOURCES OF NONLINEARITY	322
2.3.2 GEOMETRIC NONLINEARITY	323
2.3.3 MATERIAL NONLINEARITY	325
2.3.3.1 LINEAR ELASTIC MATERIAL	325
2.3.3.2 ELASTIC VERSUS INELASTIC MATERIAL	326
2.3.3.3 NONLINEAR INELASTIC MATERIAL	328
2.4 CONSTITUTIVE MODEL	329
2.4.1 FAILURE THEORY	332
2.4.1.1 PRESSURE INSENSITIVE MODEL	333
2.4.1.2 PRESSURE SENSITIVE MODEL	335
2.4.1.3 MAXIMUM TENSILE STRESS MODEL	340
2.4.2 FLOW RULE	342
2.4.2.1 ASSOCIATED FLOW RULE	345
2.4.2.2 NONASSOCIATED FLOW RULE	345
2.4.3 WORK HARDENING	346
2.4.3.1 ISOTROPIC HARDENING	347
2.4.3.2 KINEMATIC HARDENING	348
2.4.3.3 MIXED HARDENING	349
2.4.4 STRAIN SOFTENING	350
2.4.5 CONCRETE	351
2.4.6 MILD STEEL AND PRESTRESSING STRAND	357
2.4.7 CRACK MODEL	358
2.4.8 BOND MODEL	359
2.5 NUMERICAL ANALYSIS	359
2.5.1 CONSISTENT TANGENT STIFFNESS	361
2.5.2 SOLUTION METHODS	362
2.5.2.1 h-METHOD	362

2.5.2.2	p-METHOD	363
2.6	APPLICATIONS OF FINITE ELEMENT ANALYSES	363
2.6.1	STATIC ANALYSIS	364
2.6.2	MODAL ANALYSIS	364
2.6.3	HARMONIC RESPONSE ANALYSIS	365
2.6.4	TRANSIENT DYNAMIC ANALYSIS	365
2.6.5	SPECTRUM ANALYSIS	366
2.6.6	BUCKLING ANALYSIS	366
2.6.7	EXPLICIT DYNAMIC ANALYSES	367

LIST OF FIGURES

	Page
Figure 1: Potential Energy (Bittnar and Sejnoha 1996).....	318
Figure 2: Complementary Energy (Chen 1995).....	319
Figure 3: Geometric Nonlinearity (ANSYS, Inc., 2003).....	323
Figure 4: Snap-Back & Bifurcation (ANSYS, Inc., 2003)	324
Figure 5: Nonlinear Material (Chen and Han 1995).....	327
Figure 6: Material Models (Chen 1995)	329
Figure 7: Haigh Westergaard Stress Space (Chen 1995).....	332
Figure 8: Maximum Shear Stress Models (Bittnar 1996).....	334
Figure 9: Maximum Shear Stress Deviatoric Plane (Chen 1995).....	335
Figure 10: Mohr-Coulomb Model (Chen 1995)	336
Figure 11: Mohr-Coulomb 3D Space (Chen 1995)	337
Figure 12: Mohr Coulomb Plane Stress (Chen 1995).....	338
Figure 13: Drucker-Prager 3D Space (Chen 1995).....	339
Figure 14: Mohr-Coulomb & Drucker-Prager (Chen 1995).....	340
Figure 15: Rankine Maximum Principal Stress (Chen 1995).....	341
Figure 16: Tension Cut Off (Chen 1995).....	342
Figure 17: Loading (Chen 1995).....	346
Figure 18: Isotropic Hardening (Chen 1995).....	347
Figure 19: Bauschinger Effect (Chen 1995)	348
Figure 20: Kinematic Hardening (Chen 1995)	349
Figure 21: Mixed Hardening (Chen 1995).....	350
Figure 22: Hardening and Softening (Bittnar 1996).....	351
Figure 23: Concrete Biaxial Failure Surface (Jirasek 2002).....	352
Figure 24: Concrete Uniaxial Hardening & Softening (Jirasek 2002)	353
Figure 25: Concrete Biaxial Failure Surface (Jirasek 2002).....	354
Figure 26: Concrete Models in 3D Space (Chen 1995).....	355
Figure 27: Concrete Yield Surface (Jirasek 2002).....	356
Figure 28: Mild Steel Material Model (Boresi 1987)	357
Figure 29: Prestressing Steel Model (Nawy 1996).....	358
Figure 30: Solution Methods (Bittnar 1996).....	362

APPENDIX N LITERATURE REVIEW

2.1 INTRODUCTION

The most common application of the finite element method is in solving problems in structural mechanics. In fact, the method was invented by structural engineers to solve problems in elasticity and structural mechanics. The finite element analysis method is increasingly used as an analysis technique by structural design engineers. The current state of development of commercial software in combination with the power of personal computers, allow both researchers and practitioners the benefit of increasing their knowledge of the behavior of concrete structures through the use of finite element analysis.

2.2 GENERAL THEORY

The finite element method obtains an approximation of the solution of a continuum problem in structural mechanics. The structure is modeled as an assemblage of elements, interconnected at their joints, or nodes. Thus, the finite element model is a discretization of the real, continuous, structure. Known are the initial geometry of the structure, the structural stiffness of the elements, and the structure's support conditions. The structure is loaded, and the displacements of

the node points are determined approximately through numeric computations. A balance is obtained between the internal strain energy contained within the structure's elements as the internal nodes displace due to the loads, and the external work exerted on the structure as the external nodal loads act through their nodal displacements. The additional terms, kinetic energy and viscous dissipation energy, must also be considered in a dynamic analysis. The stresses in the structure's elements are then determined from the nodal displacements and the corresponding constitutive laws.

The finite element method can be used to solve many problems in structural mechanics. The theoretical basis for the analysis method is the principle of virtual work, and the variational principles of mechanics (Bittnar and Sejnoha, 1996). The method is based upon the first law of thermodynamics, which states that energy is conserved. Therefore, the external work performed to deform a structural system must equal the structure's internal strain energy. The laws of thermodynamics also state that for a process to be reversible, any deformations in the process must be reversible, i.e. in an elastic deformation the external work equals the change in internal strain energy. But a real deformation is often an irreversible process that dissipates energy, i.e. in an inelastic deformation, the external work must equal the internal strain energy plus any energy losses due to the plastic deformation of the material. The additional terms,

kinetic energy and viscous dissipation energy, must also be considered in a dynamic analysis.

2.2.1 STIFFNESS METHOD

The principle of virtual displacements leads to the Lagrange variational principle, and is the basis for the displacement, equilibrium, or stiffness, method used in structural analysis. The Lagrange variational principle states that the solution minimizes the potential energy of the system. The minimum potential energy principle leads to the Cauchy equilibrium equations and the natural, or Neumann, boundary conditions. A displacement field is approximated using the structural stiffness matrix while enforcing compatibility. The variation of the potential energy of the structural system is shown in Figure 1.

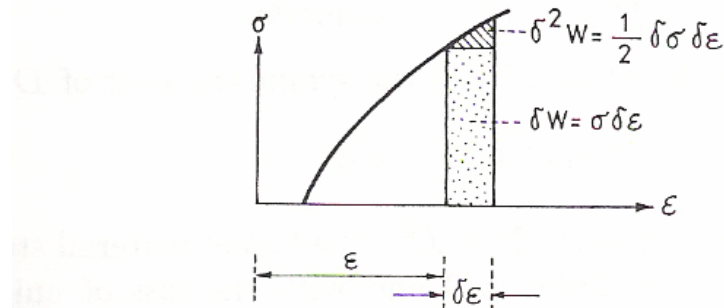


Figure 134: Potential Energy (Bittnar and Sejnoha 1996)

2.2.2 FLEXIBILITY METHOD

The principle of virtual work leads to the Castigliano variational principle, and is the basis for the force, compatibility, or flexibility, method used in

structural analysis. The Castigliano variational principle states that the solution minimizes the complementary energy of the system. The minimum complementary energy principle leads to the strain-displacement relations and the compatibility equations, and the essential, kinematic, or Dirichlet, boundary conditions. A stress field is approximated using the structural flexibility matrix while enforcing equilibrium. A variation in the complementary energy for the structural system is shown as the shaded area to the left of the stress strain curve in Figure 2.

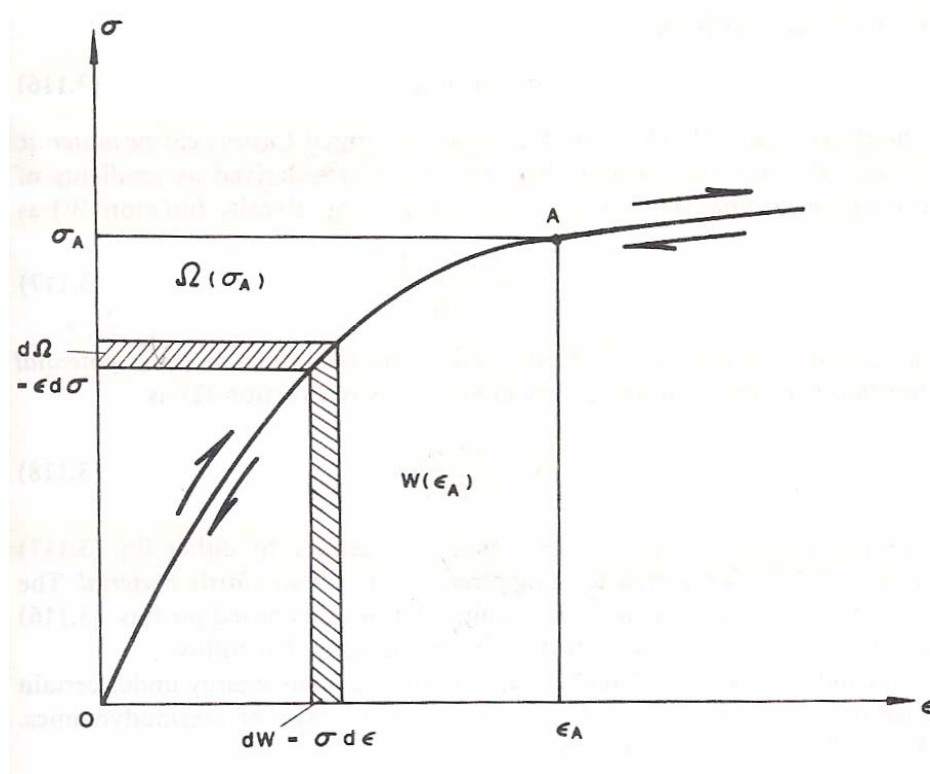


Figure 135: Complementary Energy (Chen 1995)

2.2.3 EQUILIBRIUM, COMPATIBILITY AND CONSTITUTIVE RELATIONS

In both the equilibrium and compatibility approaches, the material properties, or constitutive relations, are used in the solution. Thus, as required to solve any problem in structural mechanics, equilibrium, compatibility, and constitutive laws are satisfied.

2.2.4 RITZ NUMERICAL APPROXIMATION METHOD

The stiffness method is the dominant solution form used in finite element analysis. This is likely due to the relative ease in formulating the structure's stiffness matrix as compared to the flexibility matrix. The stresses can be solved for directly using the equilibrium method, avoiding the difficulty of inverting the structure's stiffness matrix. The solution is reached iteratively, using approximated displacements, until the desired accuracy is reached, i.e. the solution converges. Then the structure's mesh is refined, and another converged solution is obtained. The solution is determined from a comparison of the converged solutions from mesh refinements.

The stiffness method of finite element analysis is based upon the Ritz numerical approximation technique. For a continuum problem, the structure is discretized. Shape functions that only have nonzero values near their corresponding nodes, are introduced into the interpolation. The displacements are adjusted iteratively, until the total potential energy functional is minimized, and the convergence requirements for the problem are met.

2.2.5 CONVERGENCE

Convergence is affected by mesh and element selection. The mesh must be adequately fine and must approximate the boundary. A study of the solution values for successive refinements in the mesh will demonstrate convergence to a solution. The approximate solution determined using the finite element method will approach the exact solution as the mesh is refined further. Additional refinements in the mesh will no longer be required once the required accuracy is reached.

The approximate solution will monotonically approach the exact solution provided the elements used are “conforming” elements. The approximation functions associated with the selected element must satisfy continuity and completeness requirements, for the element to be a “conforming” element. Continuity ensures there are no gaps or overlaps in the displacement field on the boundary between elements, or within the element. Completeness ensures that for the case of zero strain in the element, the displacement of the element will be a rigid body rotation or translation. Completeness also ensures that the element can represent a state of constant strain.

2.3 NONLINEARITY

Failure analysis using the finite element analysis technique requires an understanding of the potential sources of nonlinearity. The assumptions used to

develop the computational model must reasonably address the problem's nonlinearities, in order to obtain accurate results. The load-response history of the structure must be carefully modeled, with adequate attention given to the size of the load increment. Near failure, large deformations can occur, and sources of nonlinearity can cause inaccuracies and instabilities in the analysis.

Linearity is exhibited when the load-displacement curve is linear throughout the range of loading and displacements. Thus, linearity occurs only when the structural stiffness remains constant for each increment of displacement. A constant structural stiffness requires a linear strain-displacement relation and a linear stress-strain relation. Stated more simply, linearity only occurs when geometry and material properties are linear.

However, many real problems are not linear problems, and use of linear approximations may lead to inaccurate results. Nonlinear structural behavior is characterized as a nonlinear load-deflection curve, and a varying structural stiffness. Geometry and material behavior are the predominant sources of nonlinearity.

2.3.1 SOURCES OF NONLINEARITY

Nonlinearity can be introduced by geometric nonlinearity and material nonlinearity. A third form of nonlinearity, “changing status” nonlinearity, occurs

when a structural behavior is dependent on a status or condition that can change during the loading (ANSYS, Inc., 2003). Examples of “changing status” nonlinearity are a tension-only axial member such as a cable, a bearing-only roller support which provides a reaction only when the structure is in contact with the support, a gap within the structure that can open and close as the structure deforms with loading, and a contact problem where the contact area and the contact stress can vary with the loading. These examples clearly result in changes to the structural stiffness during loading.

2.3.2 GEOMETRIC NONLINEARITY

Geometric nonlinearity is characterized by a changing geometric configuration resulting from large deformations during loading. Large rotations and displacements in the structure can produce significant changes in structural stiffness. Figure 3 is an example of a nonlinear load displacement relation resulting from a geometric nonlinearity. Any changes in the structural stiffness during loading caused by geometry, is a geometric nonlinearity.

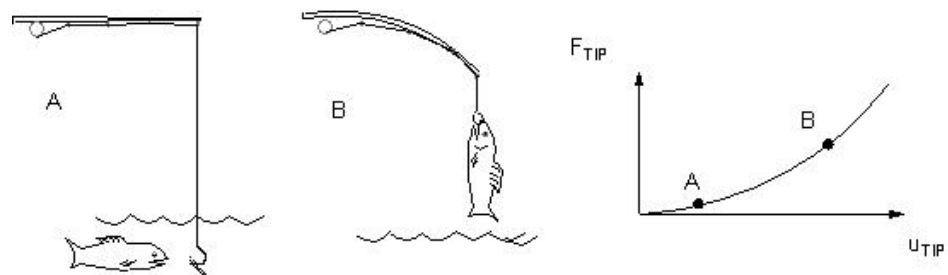


Figure 136: Geometric Nonlinearity (ANSYS, Inc., 2003)

Common forms of geometric nonlinearity include *bifurcation* due to buckling of a slender column, and *snap-through* or *snap-back* due to buckling of a thin plate or shell structure. Figure 4 shows these nonlinear loading paths.

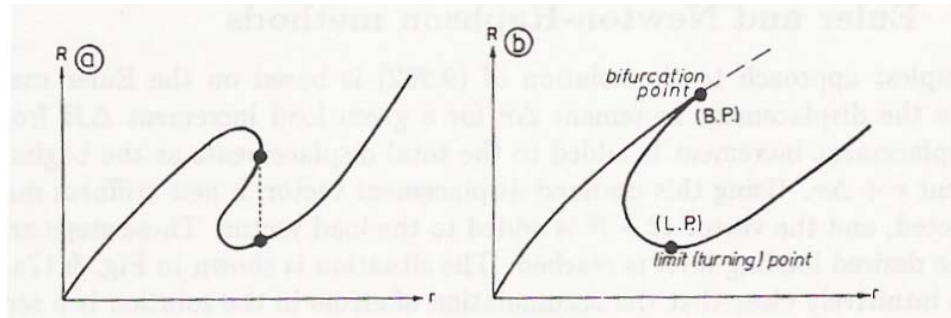


Figure 137: Snap-Back & Bifurcation (ANSYS, Inc., 2003)

A geometric nonlinearity can also occur for applied loads at the structure's boundary. For example, consider pressure on the surface of a structure; the applied surface load is normal to the surface of an element of the structure, and the direction will change as the structure deforms during loading.

Large deformations occur in portions of the structure, as the loading approaches the failure load. In classical small displacement theory, for each increment of deformation, strains and angles of rotation are assumed small, and the rotations are assumed small compared to the strains. Then the quadratic terms of the second order strain tensor can be neglected. These higher order terms are retained in large strain problems and we use the Lagrangian or Eulerian

definitions of strain. Nonlinearity is introduced when retaining these higher order terms in the derivation and use of the strain-displacement relation to improve accuracy for large strain problems.

2.3.3 MATERIAL NONLINEARITY

Temperature effects, and time dependent effects such as volumetric changes from creep and shrinkage, are potential sources of material nonlinearity. A material can exhibit other nonlinearities, such as a dependency on the rate of loading, cyclic loading, or the magnitude of stress.

Materials can be assumed to behave either linearly or nonlinearly, and either elastically or inelastically. A linear elastic material exhibits a constant material stiffness throughout the load path, and the current stress and strain state can be uniquely determined from the current loading condition. In contrast, the stress and strain state for a nonlinear inelastic material cannot be uniquely determined from the current loading, but rather is dependent upon the load path. Additional information on material properties and material nonlinearity is provided in the following paragraphs.

2.3.3.1 LINEAR ELASTIC MATERIAL

A linear material exhibits a linear stress strain relationship. In other words, the material stiffness is constant throughout the loading range.

2.3.3.2 ELASTIC VERSUS INELASTIC MATERIAL

A material behaves elastically only when the load path is reversible. The external work expended by loading an elastic material is converted into internal strain energy within the material, as the material deforms under the loading. Both the deformations and the energy are fully recovered upon unloading the structure. The state of strain can be determined uniquely from the current state of stress and is not dependent on the load path. Conversely, the state of stress can be determined uniquely from the current state of strain and is not dependent on the load path. The principal stress axes coincide with the principal strain axes.

Elastic materials can behave either linearly or nonlinearly. A linear elastic material will exhibit a reversible, linear, stress-strain relation. A nonlinear elastic material model will exhibit a nonlinear but reversible stress-strain relationship, i.e. reversible dilation and distortion (Chen and Han, 1995). Although the material stiffness is nonlinear, the loading is unique, and the deformations and the internal strain energy are fully recoverable. Figure 5 shows a nonlinear material stress strain curve. A reversible, elastic behavior is depicted in the left portion of Figure 5. An irreversible, inelastic behavior is shown on the right, and the elastic and plastic strain components are shown.

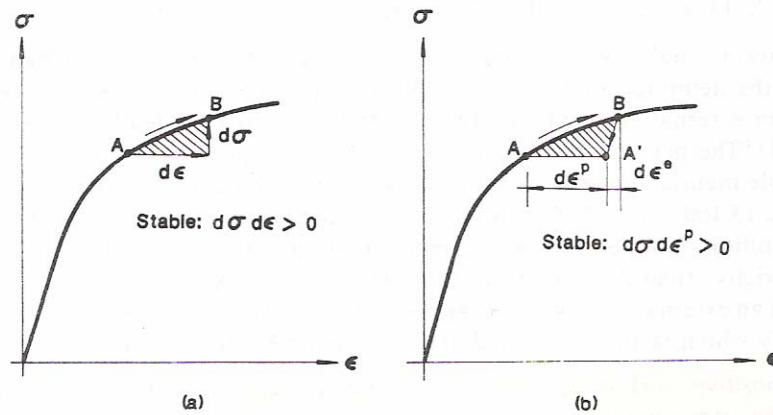


Figure 138: Nonlinear Material (Chen and Han 1995)

All real materials exhibit nonlinear inelastic behavior, although some materials exhibit nearly linear elastic behavior in a portion of the range of their stress-strain relation. Therefore, an elastic material is an idealized material, since any real deformation dissipates energy, and results in at least some permanent deformation.

All real materials deform in an irreversible process, i.e. the deformations cannot be fully reversed without expending additional energy. The second law of thermodynamics states that entropy is a monotonically increasing function. It further states that a process cannot yield a negative internal entropy increment. A process that yields constant internal entropy is a reversible process. A reversible process only occurs in theory. All real processes are irreversible, i.e. heat is generated as a result of the process.

2.3.3.3 NONLINEAR INELASTIC MATERIAL

Material nonlinearity and inelasticity are observed for most materials, especially near the failure load. A nonlinear material exhibits a changing material stiffness upon loading. The deformations and internal strain energy of an inelastic material under loading are not fully recoverable upon unloading, and some permanent deformations remain in the material. For inelastic materials, knowledge of the load history is required to determine the current state of stress and strain; i.e. the current stress state is dependent upon the load path.

Figure 6 shows four inelastic material models. Linear elastic material behavior occurs initially for the first three models, followed by inelastic behavior. The fourth model is entirely nonlinear. The upper left model depicts linear elastic behavior followed by perfectly plastic behavior. Linear work hardening behavior follows the linear elastic region for the model in the upper right. Work hardening behavior is the ability of a material to withstand an increased amount of stress after yielding. An exponential function models the work hardening region in the lower left. The nonlinear model in the lower right is the Ramberg-Osgood model.

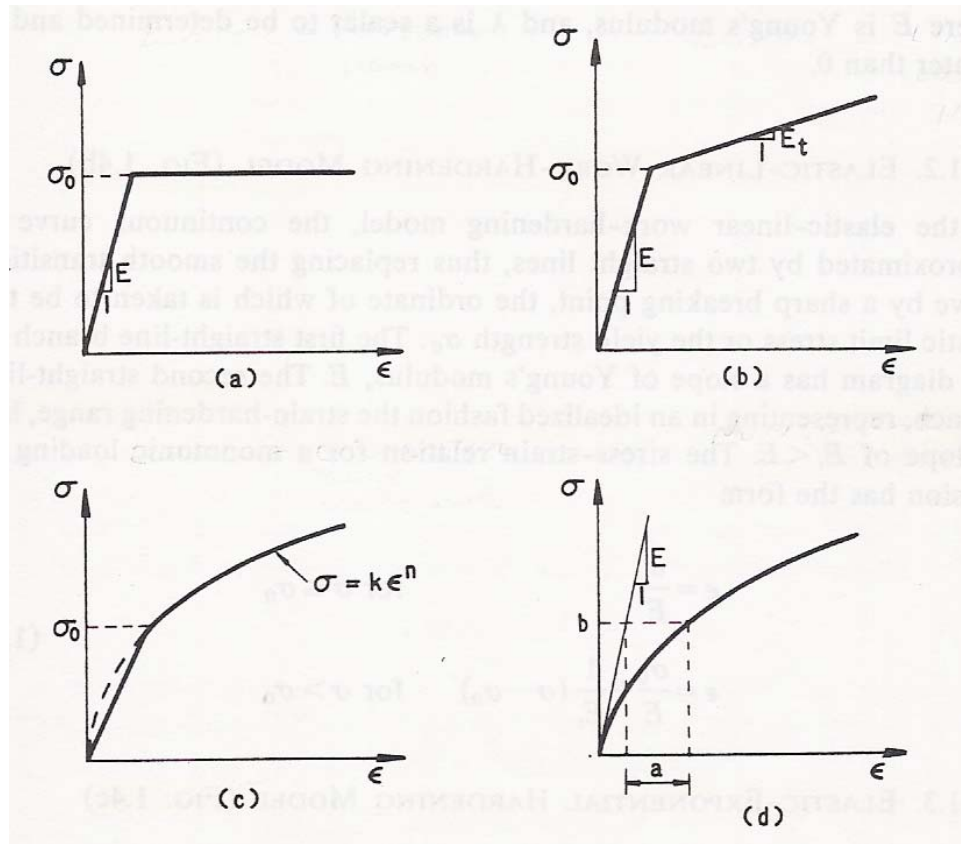


Figure 139: Material Models (Chen 1995)

2.4 CONSTITUTIVE MODEL

A constitutive model is a mathematical formulation for the material's stress strain relationship during loading, in three dimensional stress space. The model describes the relationship both before initial yielding, and after yielding. These mathematical models have been developed for both linear and nonlinear materials, exhibiting either elastic or inelastic behavior.

Constitutive relations must be derived from experimental observations. Thus material stiffness is derived from stress-strain data obtained by experimental research. Experimentalists have recorded the data after performing tension, compression, pure shear (torsion), and other tests on material specimens. For isotropic materials, Young's modulus and Poisson's ratio are obtained from uniaxial loading tests. Pure shear loading tests provide the shear modulus. The bulk modulus is obtained from a three dimensional, hydrostatic, compression test. Additional material parameters are empirically derived for use in constitutive relations that model plastic material behavior.

Constitutive relations mathematically specify the behavior of materials, both in the material's elastic region before the stresses exceed the elastic limit, and in the material's work hardening region after the material yields. These relations specify the initial yield surface (failure theory), the subsequent yield surface as loading at the yield condition produces plastic deformation in the material (hardening rule), and the elastic and plastic strain increments for the stress increment at the yield condition (flow rule). These relations are discussed in the following paragraphs. The material behavior that occurs in the strain softening region, beyond the material's work hardening region, will also be discussed.

A three dimensional stress state can be decomposed into a hydrostatic stress and a deviatoric stress. The hydrostatic part is equivalent to a uniform pressure on the material; i.e. the shear stresses are zero, and the three normal stresses are equal. The remaining stresses are called the deviatoric stresses, and generally consist of both shear and normal stress components. The hydrostatic stresses cause either dilation, for the tensile case, or contraction, for the compression case. Since the deviatoric stresses consist of normal and shear stresses, these stress components cause the associated distortional strains in the material.

These decomposed stress components, the hydrostatic and deviatoric stress components, can be plotted in the Haigh-Westergaard stress space as shown in Figure 7. In the figure, point P represents the stress state in 3D principal stress space. The hydrostatic axis represents all possible hydrostatic stress conditions, and is a line through the origin and oriented equidistant from the three principal stress axes. A deviatoric plane is a plane normal to the hydrostatic axis. Thus for any stress state, the vector from the origin to the deviatoric plane represents the hydrostatic stress, and the vector in the deviatoric plane from the hydrostatic stress to the 3D principal stress point represents the deviatoric stress. A meridian plane is a plane containing the hydrostatic axes. The meridian planes are identified with a counterclockwise angle within the deviatoric plane from the vertical principal stress axis, σ_1 , to the point representing the stress state. The

tensile meridian is $\Theta = 0^\circ$. The compressive meridian is $\Theta = 60^\circ$. These meridians represent a hydrostatic stress state, along with their respective tensile or compressive stress superimposed in one direction.

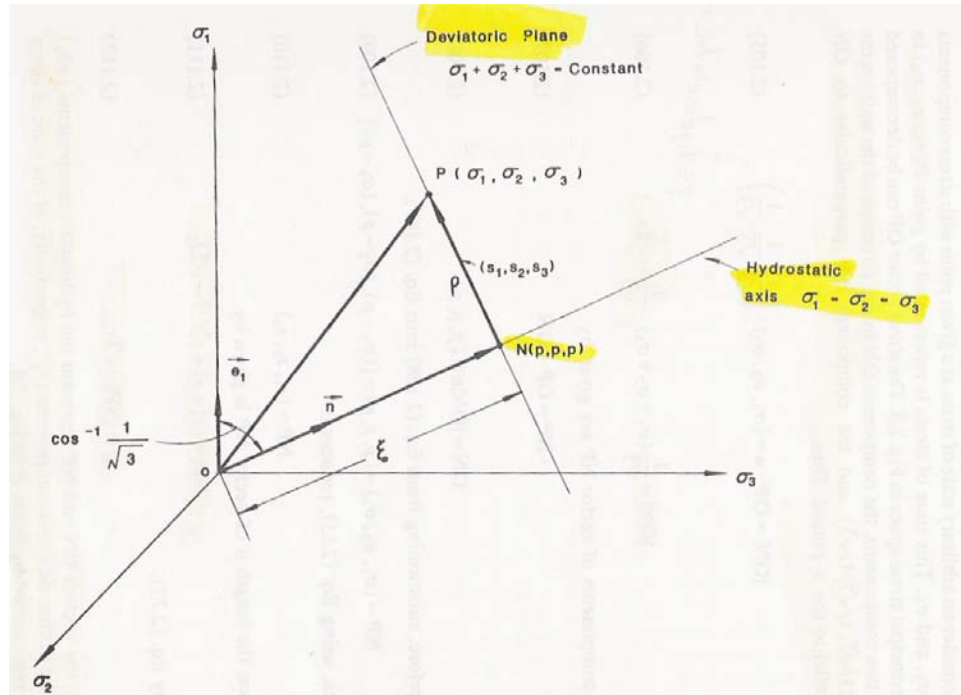


Figure 140: Haigh Westergaard Stress Space (Chen 1995)

2.4.1 FAILURE THEORY

For elastic materials, either linear or nonlinear, the failure, or yield, surface remains constant for all loading conditions. The failure surface can expand for inelastic materials that can strain harden; i.e. materials that can withstand an increase in stress beyond initial yielding. The initial failure surface will remain constant for an elastic, perfectly plastic, material, since the material

cannot withstand an increase in stress after initial yield. Damage theory is commonly used to model the behavior of strain softening; i.e. the behavior of a material to withstand only a reduced stress, once a certain loading condition is reached. Damage models have the effect of contracting the failure surface, the opposite as occurs in the case of strain hardening, where the failure surface is expanding.

2.4.1.1 PRESSURE INSENSITIVE MODEL

Some material behavior, such as steel, is pressure insensitive. Early constitutive models were based upon material behavior which neglects the effect of pressure on the material. These failure theories are dependent upon only one parameter, maximum shear stress. These failure theories are based only on the distortional part of the material behavior, and neglect the hydrostatic pressure.

Tresca and St. Venant, in the 1870's, developed a yield criterion for metals based upon maximum shear stress. Von Mises published another pressure insensitive yield criteria in 1913, today called the J_{2D} theory. J_{2D} is the second invariant of the stress deviator tensor. Von Mises based the yield criterion on the octahedral shear stress.

These models are shown in the right of Figure 8 for the plane stress, 2D, stress state, where $\sigma_3 = 0$. Tresca's hexagon failure surface is inscribed into the von Mises ellipse. The left of Figure 8 shows these models plotted in 3D

principal stress space. The models continue indefinitely along the hydrostatic axes, since the models are pressure insensitive models.

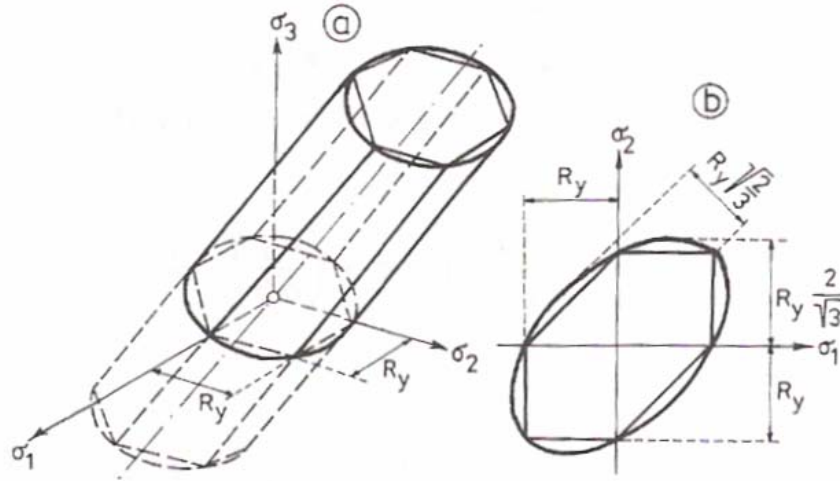


Figure 141: Maximum Shear Stress Models (Bittnar 1996)

Figure 9 shows these models plotted in the deviatoric plane. For isotropic materials, which have the same material properties in each of the three mutually orthogonal directions, the failure surface is symmetric, and the model is completely defined by the properties of the first 60°, i.e. the material properties from the tensile meridian to the compressive meridian completely define the remaining 240°.

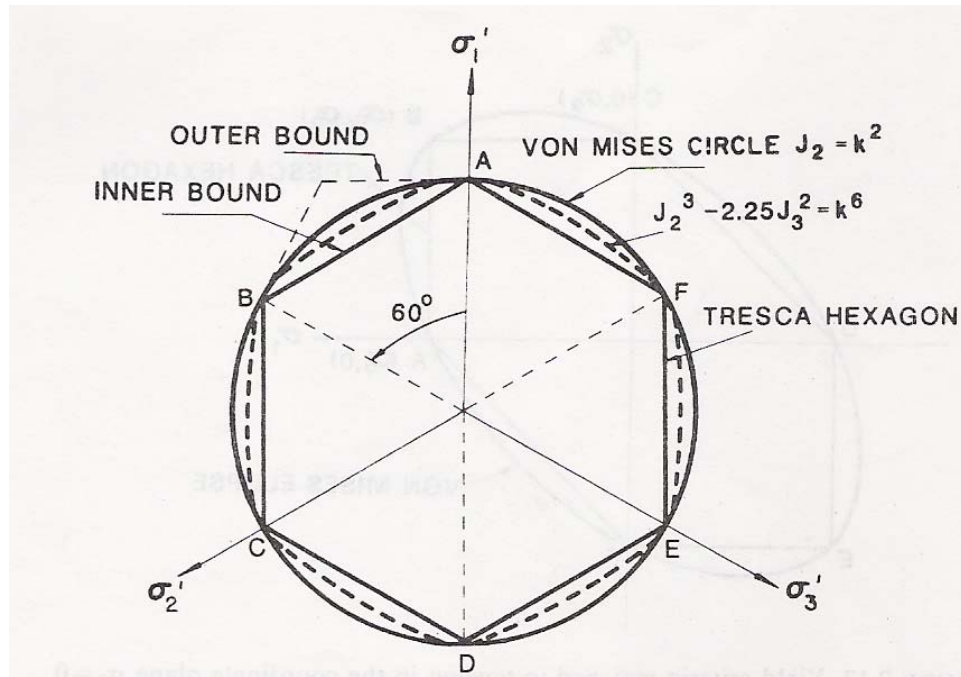


Figure 142: Maximum Shear Stress Deviatoric Plane (Chen 1995)

2.4.1.2 PRESSURE SENSITIVE MODEL

A pressure sensitive failure criterion introduces a second parameter, I_1 , into the material model. I_1 is the first invariant of the stress tensor. The first invariant of the stress tensor incorporates the dilational behavior of the material. Thus, a pressure sensitive model uses two parameters; J_{2D} , which incorporates the distortional behavior as described previously, and I_1 .

In the 1900's, Mohr developed Coulomb's 1773 era two dimensional stress state failure model into a three dimensional failure model. The Mohr-Coulomb failure criterion is pressure dependent, and is based upon maximum

shear stress. The Mohr-Coulomb model considers the limiting shear stress in a plane to be dependent on the normal stress in that plane. The model is shown in Figure 10. The parameters c and ϕ are cohesion and the angle of internal friction, respectively. For the case $\phi = 0^\circ$, the material is defined as frictionless, and the Mohr-Coulomb model is the same as the Tresca pressure independent maximum shear stress model.

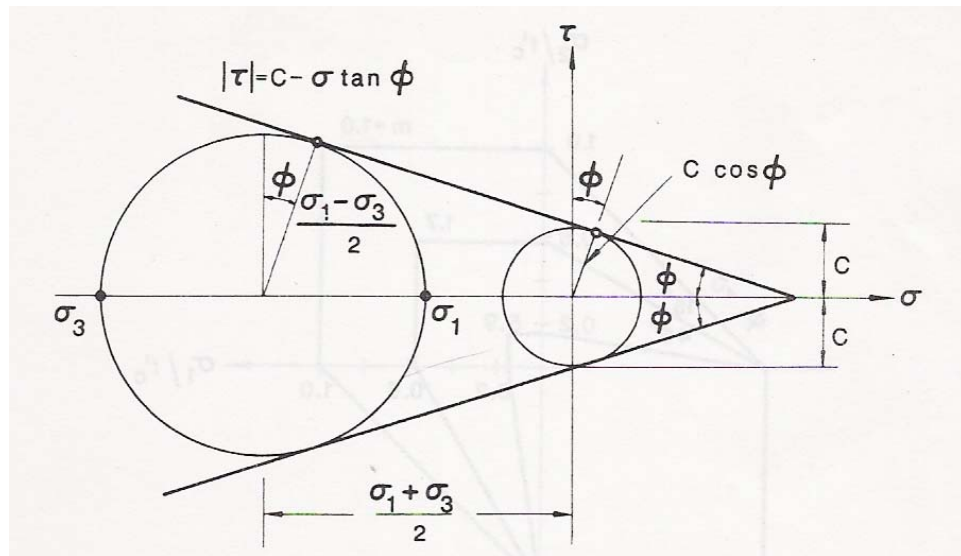


Figure 143: Mohr-Coulomb Model (Chen 1995)

The model is shown in 3D principal stress space in Figure 11. The left side of Figure 11 shows the Mohr-Coulomb model along the tensile and compressive meridians.

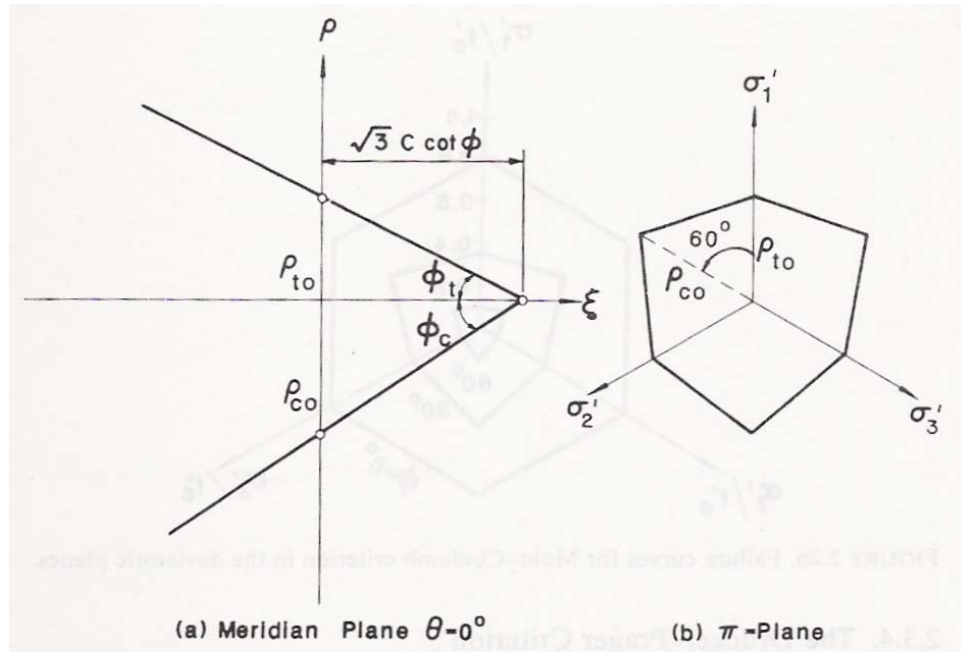


Figure 144: Mohr-Coulomb 3D Space (Chen 1995)

Figure 12 shows the Mohr-Coulomb model for the plane stress, 2D, stress state, where $\sigma_3 = 0$. Shown is the effect of varying the material parameter ϕ . Different tensile and compressive strengths are possible for the Mohr-Coulomb criteria, as opposed to the Tresca and von Mises models where the tensile and compressive strengths are the same. Thus, the Mohr-Coulomb model does not have symmetry in the tensile and compressive quadrants. The parameter m is the ratio of a material's compressive and tensile strengths. The Mohr-Coulomb model can thus be used for soils, rocks and concrete, which have little strength in tension. For concrete, which has a ratio of compressive to tensile strength, m , of about 10, ϕ would be 55° .

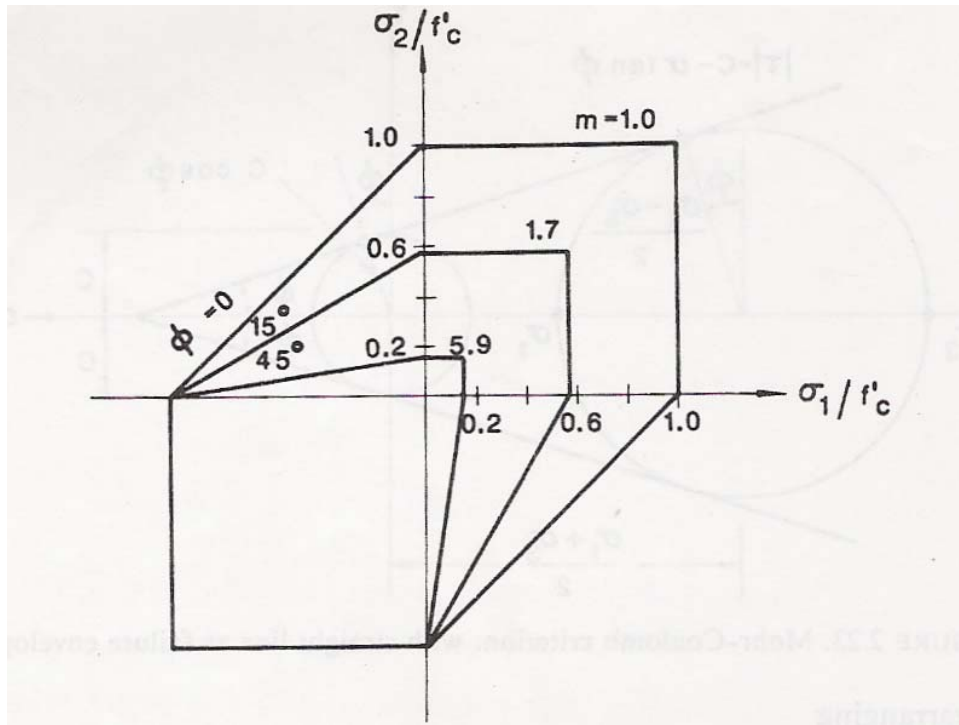


Figure 145: Mohr Coulomb Plane Stress (Chen 1995)

In 1952, Drucker and Prager formulated a two-parameter, pressure dependent model, from the earlier von Mises model, that based the yield criterion on the octahedral shear stress. Figure 13 shows the Drucker-Prager model in 3D principal stress space.

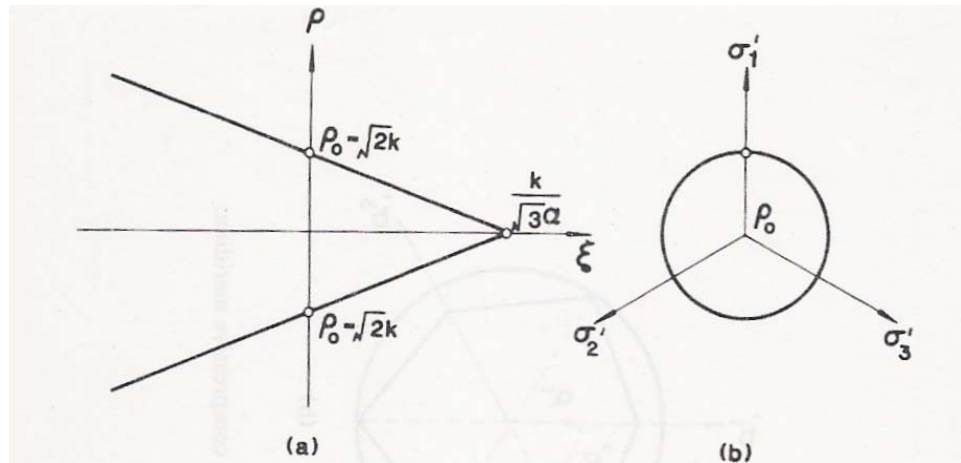


Figure 146: Drucker-Prager 3D Space (Chen 1995)

Figure 14 shows the Mohr-Coulomb and the Drucker-Prager models superimposed on each other. The Mohr-Coulomb is shown for a material with different tensile and compressive strengths. The Drucker-Prager model can be made to match the Mohr-Coulomb model only along one meridian, thus limiting its value for materials with differing tensile and compressive strengths. Here, the Drucker-Prager model is matched to the Mohr-Coulomb model along the compressive meridian.

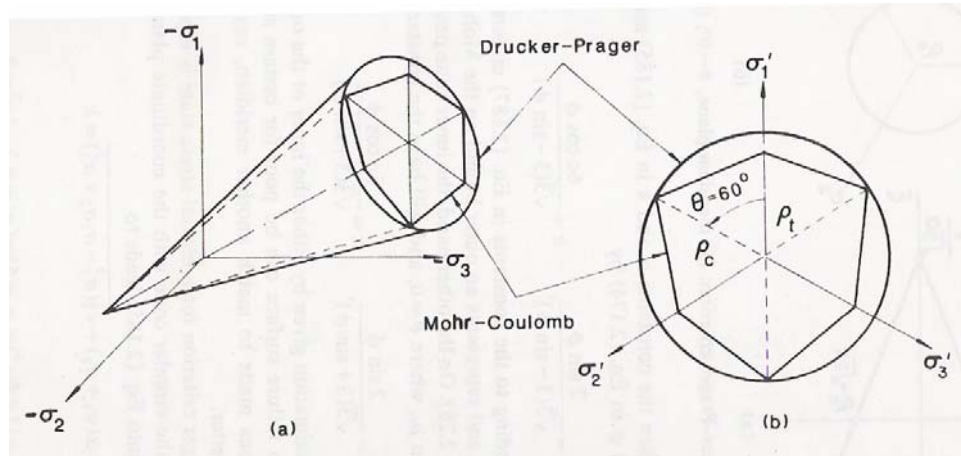


Figure 147: Mohr-Coulomb & Drucker-Prager (Chen 1995)

2.4.1.3 MAXIMUM TENSILE STRESS MODEL

Rankine's maximum tensile stress yield criterion, developed in 1876, is useful to model a brittle material in tension. The Rankine model is shown in Figure 15. This model is known today as the tension cutoff. It is useful to combine this tension cutoff criterion with the Tresca, von Mises, or Mohr-Coulomb criterion. An example is shown in Figure 16, where the Rankine tensile cutoff criterion is shown combined with both the Tresca and von Mises criterion. The Rankine tensile cutoff criterion can also be combined with the two parameter pressure dependent models of Mohr-Coulomb and Drucker-Prager.

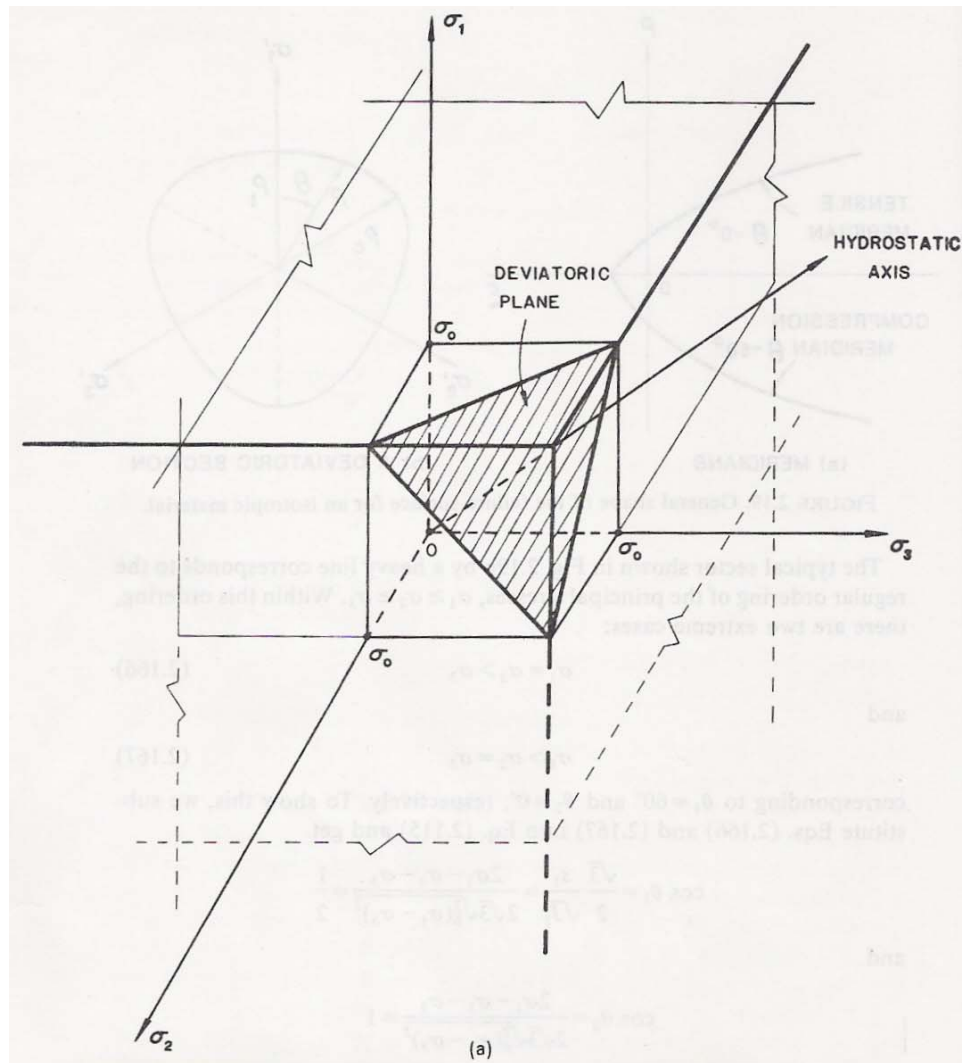


Figure 148: Rankine Maximum Principal Stress (Chen 1995)

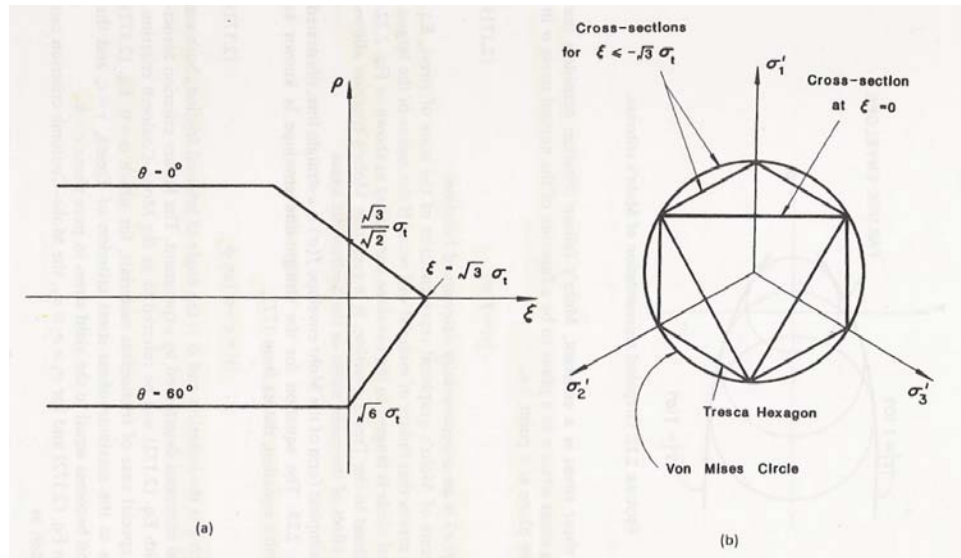


Figure 149: Tension Cut Off (Chen 1995)

2.4.2 FLOW RULE

For an elastic material, the deformations are fully recoverable upon unloading. The strains are the gradients of the stress potential function, i.e. the gradients of the complementary energy density function. Thus, the strains can be derived directly by differentiating the elastic stress potential function, or the complementary energy density function, with respect to the stresses. Similarly, the stresses are the gradients of the strain potential function, i.e. the gradients of the strain energy density function. A material with these properties is called a “hyperelastic” or a “Green elastic material”. A gradient of a potential function is normal to the potential function, thus the strains are oriented in a direction normal to the stress potential function.

Continued loading of an inelastic material at the yield condition will result in plastic strain, and the increment of energy used to deform the material is not fully recoverable. For a perfectly plastic material, none of the energy increment is recoverable. For a work hardening material, some of the energy increment is stored as elastic strain energy and is recoverable upon unloading, while the remaining part of the energy increment is used to plastically deform the material and is not recoverable.

The yield surface of a work hardening, inelastic, material expands as the material yields. Although a work hardening inelastic material exhibits a decreasing stiffness with increasing strain, the material can withstand an increase in stress. The strain increment at the yield condition has an elastic part, $d\epsilon_{ij}^e$, and a plastic part, $d\epsilon_{ij}^p$. An elastic, perfectly plastic, material can not withstand a stress increase, and the yield surface does not expand as the material yields inelastically, and the elastic strain increment is zero.

A flow rule must be formulated to relate the increment of plastic strain with the stress increment, when the material is loaded at the yield condition. The flow rule defines the magnitude and orientation of the components of the plastic strain increment. The plastic strain increment is a second order tensor, and has nine components in nine-dimensional strain space.

In the 1950's, Drucker developed the material stability postulate. The postulate states that positive work is done on a structure upon loading, and that the net work for a load increment is positive for a plastic deformation. Drucker developed the concepts of convexity, normality, linearity, continuity and uniqueness, which are significant for work hardening materials. Convexity requires that the initial and subsequent yield surfaces be convex. Normality requires that the plastic strain increment vector be normal to the yield surface. Linearity states that the plastic strain increment is linear in the stress increment. Continuity requires that there is no plastic strain increment for the neutral loading case, when the stress increment is tangential to the yield surface. Uniqueness requires that the increments of stress and strain be uniquely determined by the changes in external forces and displacements.

In 1928, von Mises proposed the concept of the plastic potential function as the logical extension of the elastic potential function used in elastic analysis. The plastic potential function, $g(\sigma_{ij})$, is a function of the stresses, σ_{ij} . Then, the plastic strain increment, $d\epsilon_{ij}^p$, can be written as a scalar multiple, $d\lambda$, of the gradient of the plastic potential function. A gradient of a potential function is normal to the potential function, thus the increments of the plastic strains are oriented in a direction normal to the plastic potential function.

$$(1) \quad d\epsilon_{ij}^p = d\lambda \partial g(\sigma_{ij}) / \partial (\sigma_{ij}) \quad \text{nonassociated flow rule} \quad (2.1)$$

An original theory on plasticity dates from the 1864 to 1872 papers of Tresca, with the concept of a maximum shear stress yield condition (Chen and Han, 1995). In 1870, St. Venant formulated the constitutive relations for a rigid, perfectly plastic, material in plane stress. St. Venant suggested the flow rule that the principal axes of the strain increment coincide with the principal axes of stress. The yield condition was formulated in three dimensions by Levy, later in 1870, and again independently in 1913, by von Mises.

2.4.2.1 ASSOCIATED FLOW RULE

The simplest flow rule is developed from the assumption that the plastic potential function, $g(\sigma_{ij})$, coincides with the yield function, $f(\sigma_{ij})$. Then the plastic flow develops along the normal to the yield surface, $\partial f(\sigma_{ij})/\partial(\sigma_{ij})$. The plastic flow is a scalar multiple of the gradient of the yield function. This is called an associated flow rule, because the plastic strain increment is associated with the yield function.

$$(2) \quad d\epsilon_{ij}^p = d\lambda \partial f(\sigma_{ij})/\partial(\sigma_{ij}) \quad \text{associated flow rule} \quad (2.2)$$

2.4.2.2 NONASSOCIATED FLOW RULE

A more general flow rule is developed from the assumption that the plastic potential function, $g(\sigma_{ij})$, does not coincide with the yield function, $f(\sigma_{ij})$. Then the plastic flow develops along the normal to the plastic potential function,

$\delta g(\sigma_{ij})/\delta(\sigma_{ij})$. This is called a nonassociated flow rule, because the plastic strain increment is not associated with the yield function.

2.4.3 WORK HARDENING

Many materials exhibit work hardening behavior, i.e., they can withstand an increase in stress after initial yielding. Figure 17 graphically depicts a work hardening material subjected to uniaxial loading, shown on the left, and biaxial loading, shown on the right. For the 2D and 3D loading conditions, a neutral loading is defined as a loading that does not result in additional plastic deformation. Plastic flow theory is used to relate the elastic and plastic strain increments to the stress increment at the yield condition. Three hardening rules are discussed, isotropic, kinematic, and mixed.

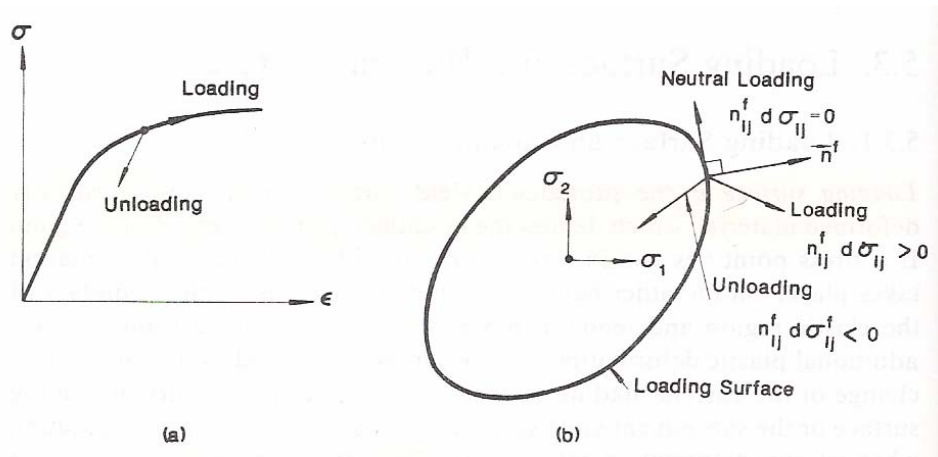


Figure 150: Loading (Chen 1995)

2.4.3.1 ISOTROPIC HARDENING

The isotropic hardening model predicts a uniform expansion of the yield surface as the material is loaded at the yield condition, as shown in Figure 18. The yield surface expands uniformly, without distortion, translation or rotation. Initial anisotropies in the material can be described by using nine dimensional stress space. The model is typically used for a monotonic loading condition, since work hardening of an initially isotropic material generally results in anisotropy, referred to as the “Bauschinger effect”. The isotropic hardening model is contrary to the “Bauschinger effect”, shown in Figure 19. The “Bauschinger effect” predicts a decrease in resistance to a plastic deformation after the material has been subjected to a plastic deformation in the opposite direction. Inaccuracies will result when this model is used for complex load paths with frequent stress reversals.

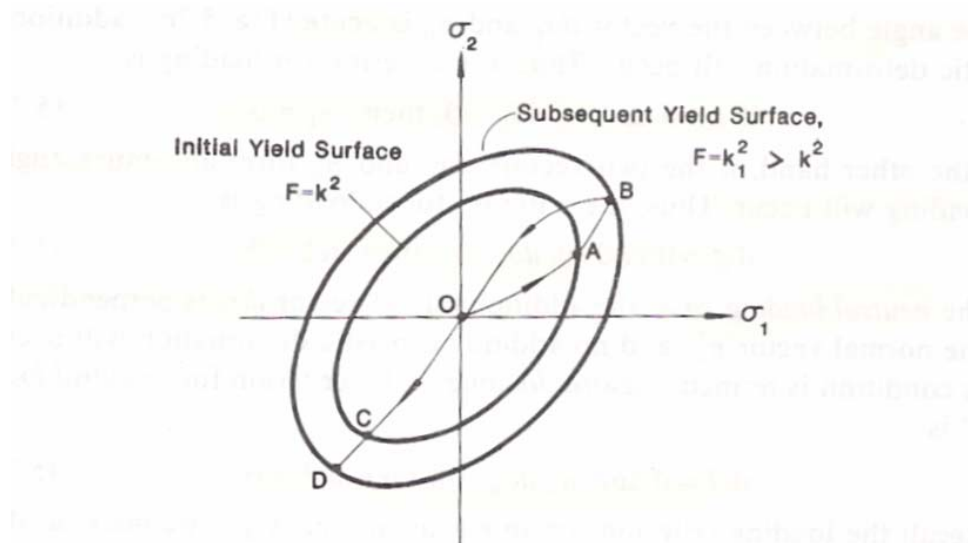


Figure 151: Isotropic Hardening (Chen 1995)

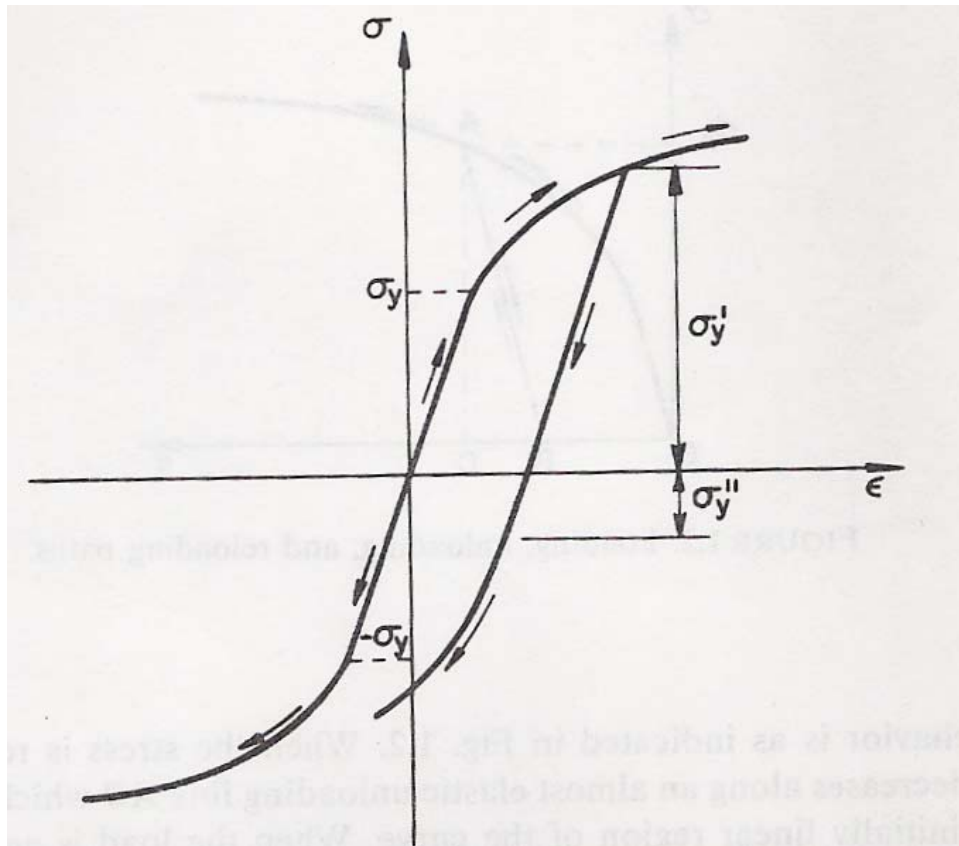


Figure 152: Bauschinger Effect (Chen 1995)

2.4.3.2 KINEMATIC HARDENING

The kinematic hardening model predicts a translation of the yield surface as the material is loaded at the yield condition, as shown in Figure 20. The yield surface translates without distortion or rotation. For an exact reversal of loading, the model predicts the initial failure surface to return to the initial position. Thus, the model predicts the material behavior observed in the “Bauschinger effect”.

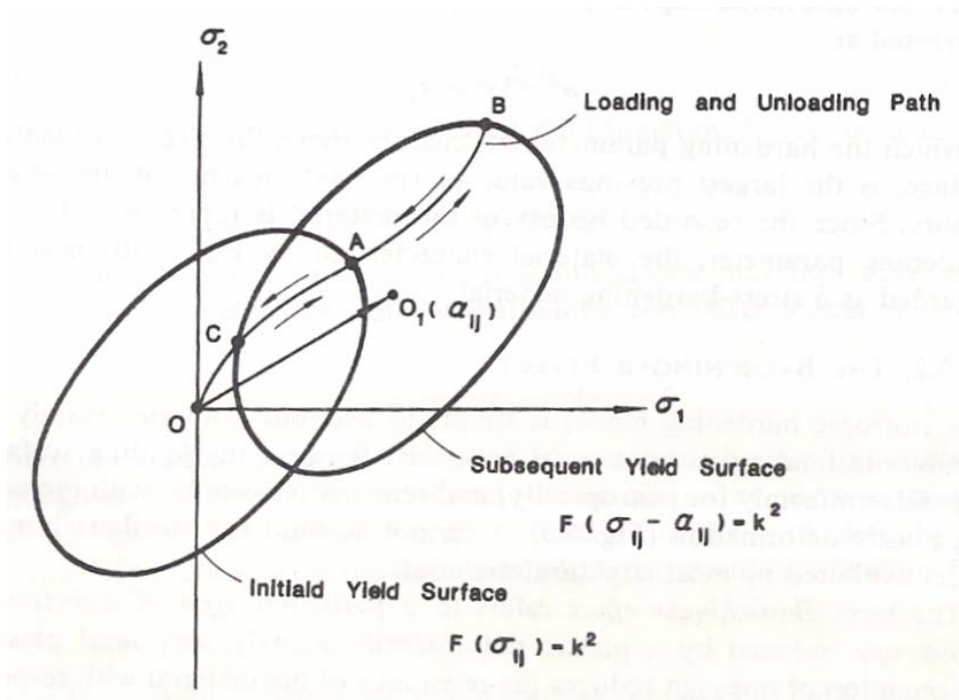


Figure 153: Kinematic Hardening (Chen 1995)

2.4.3.3 MIXED HARDENING

The mixed hardening model predicts both a translation and a uniform expansion of the yield surface, as the material is loaded at the yield condition, as shown in Figure 21. The yield surface does not distort, but retains its original shape. The yield surface translates, but does not rotate. Two hardening parameters are used to control the “Bauschinger effect”, and adjust the extent of the translation and expansion.

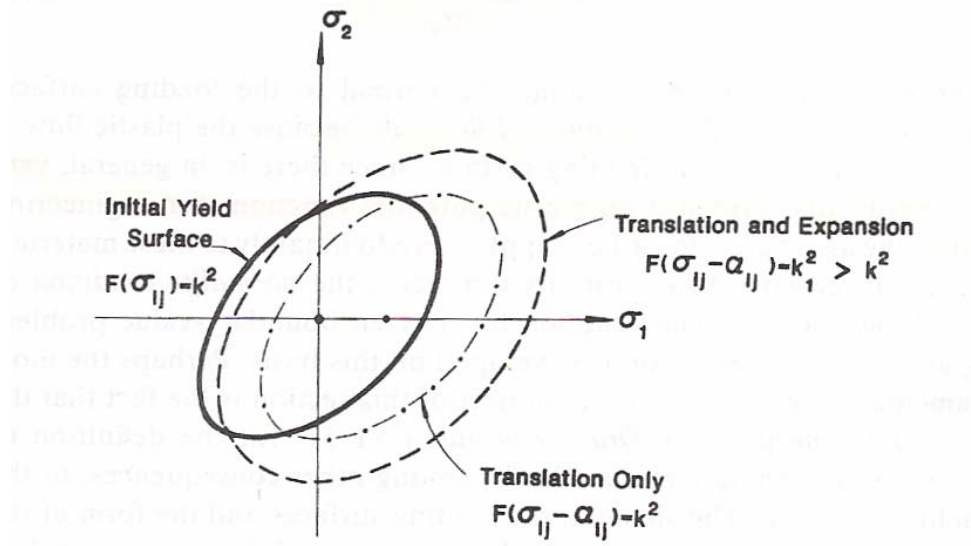


Figure 154: Mixed Hardening (Chen 1995)

2.4.4 STRAIN SOFTENING

Increased loading into the work hardening region can lead to strain softening in some materials. As shown in Figure 22, in the strain softening region, the material exhibits a reduction in its ability to resist the next load increment. The stress in the material decreases with the strain increment, as the material deforms plastically in combination with the occurrence of damage.

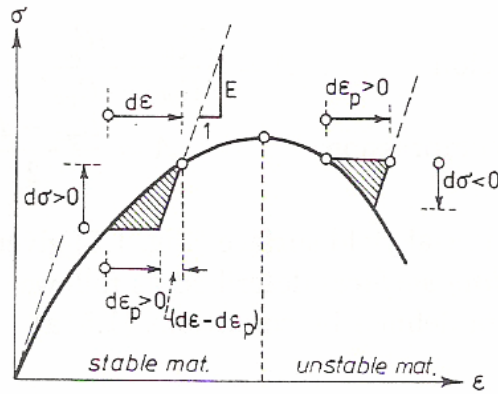


Figure 155: Hardening and Softening (Bittnar 1996)

Structural changes can occur in the material as the loading condition enters the material's strain softening region. The internal, elastic strain energy of the material degrades with the damage that occurs in the loading increment. Damage in concrete can consist of a change in volume as the material fractures and crushes. The combination of the theory of plasticity with damage, or fracturing, theory allows the formulation of stress-strain relations in the strain softening region (Han and Chen, 1986).

2.4.5 CONCRETE

Concrete behavior is highly dependent upon the loading condition. Sources of nonlinearity include magnitude of loading, cyclic loading, rate of loading, temperature, and time dependent effects such as volumetric changes from creep and shrinkage. Cyclic loading will degrade the stiffness of reinforced concrete structures as the concrete progressively cracks, the reinforcement yields,

and the bond of reinforcing steel to concrete is affected. Time dependent effects will produce additional deformation, and equilibrium will require the redistribution of stresses.

When confined, concrete will exhibit ductility under a compressive loading. The biaxial failure surface for concrete is shown in Figure 23. Concrete resists compressive loading well, but has a tensile strength of only about one-tenth its compressive strength. Inadequately reinforced concrete will exhibit an undesirable brittle tensile failure behavior. The tension response of unreinforced concrete is linear elastic, followed by brittle failure. Tensile loading results in cracking normal to the maximum principal stress direction (Jirasek and Bazant, 2002). Concrete can also fail in a shear mode.

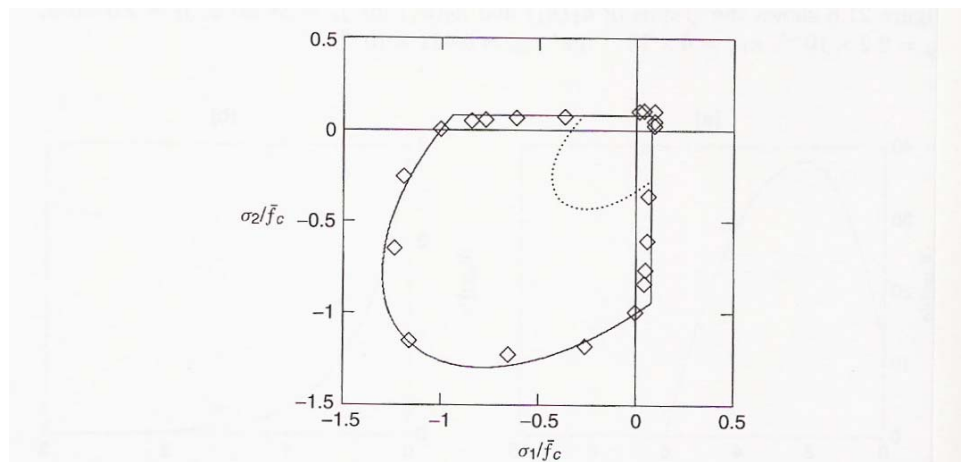


Figure 156: Concrete Biaxial Failure Surface (Jirasek 2002)

Concrete is a pressure sensitive, highly nonlinear material, and its behavior is much different in compression than in tension or pure shear. In compression, concrete can be approximated as linear elastic for only a small portion of its loading range. As shown in the left side of Figure 24, concrete has a relatively wide inelastic range, where concrete hardens after initial yield. Concrete hardening is then followed by softening, as damage in the material occurs. Concrete does not exhibit a plastic yield plateau, except in the case of large hydrostatic pressure. Instead, concrete exhibits localized effects, and softens after the peak stress as the material strains inelastically. The right side of Figure 24 shows a tension softening model for concrete.

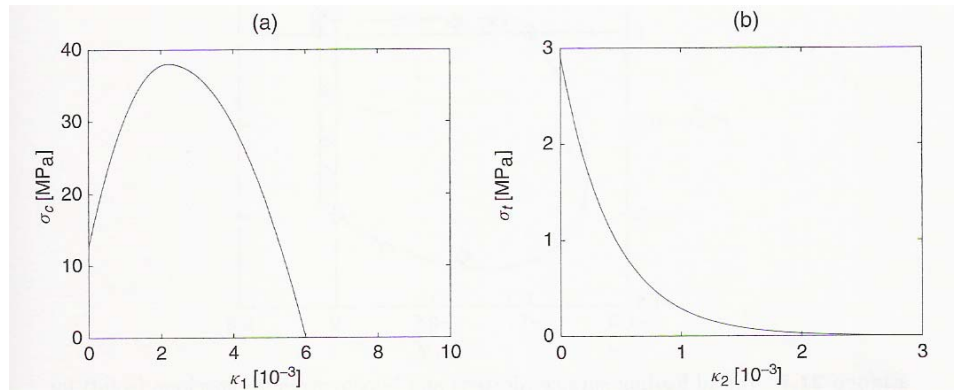


Figure 157: Concrete Uniaxial Hardening & Softening (Jirasek 2002)

Concrete is a pressure sensitive material, with a significant difference in compressive and tensile strengths. The early maximum shear stress theory failure models of Tresca and von Mises are pressure independent models. These models were modified in the Mohr-Coulomb and Drucker-Prager models, to include the

effect of hydrostatic pressure. Biaxial failure surfaces of these models are shown in Figure 25. Figure 26 shows these models in 3D stress space. The Drucker-Prager model provides a continuous, smooth failure surface, advantageous in numerical modeling, but does not accurately model a material such as concrete, a material with different properties in the tensile and compressive regions. A tension cutoff, such as the Rankine model, can be superimposed onto these models.

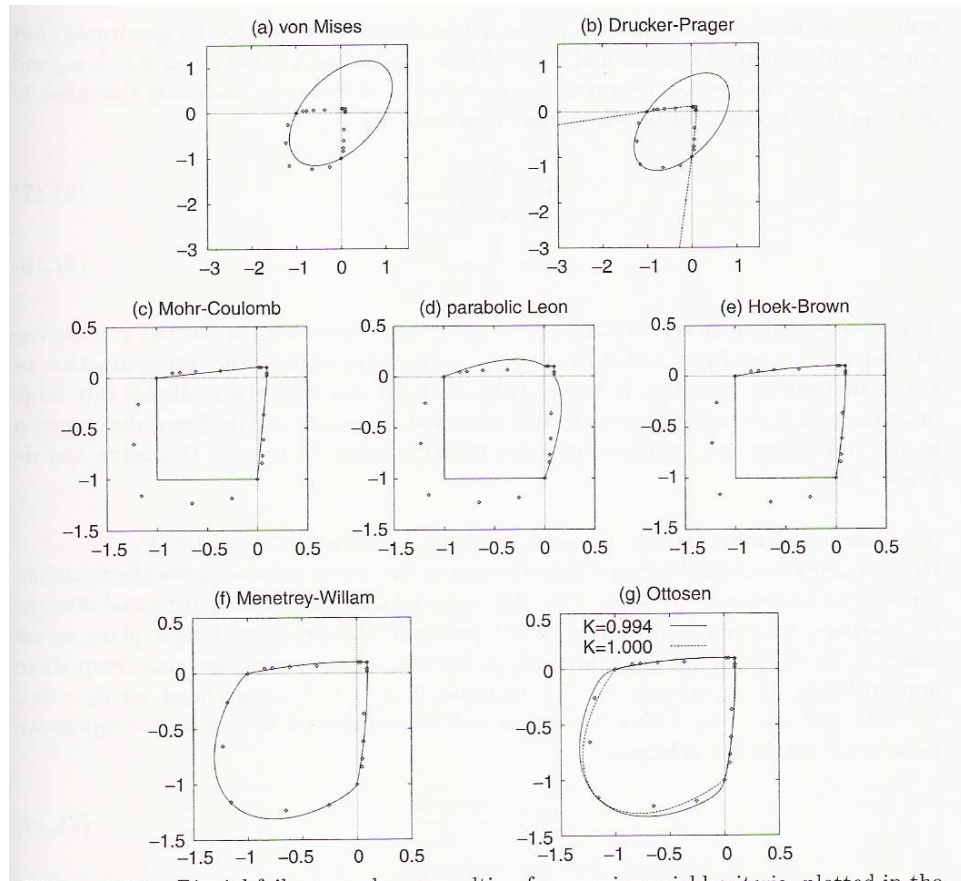


Figure 158: Concrete Biaxial Failure Surface (Jirasek 2002)

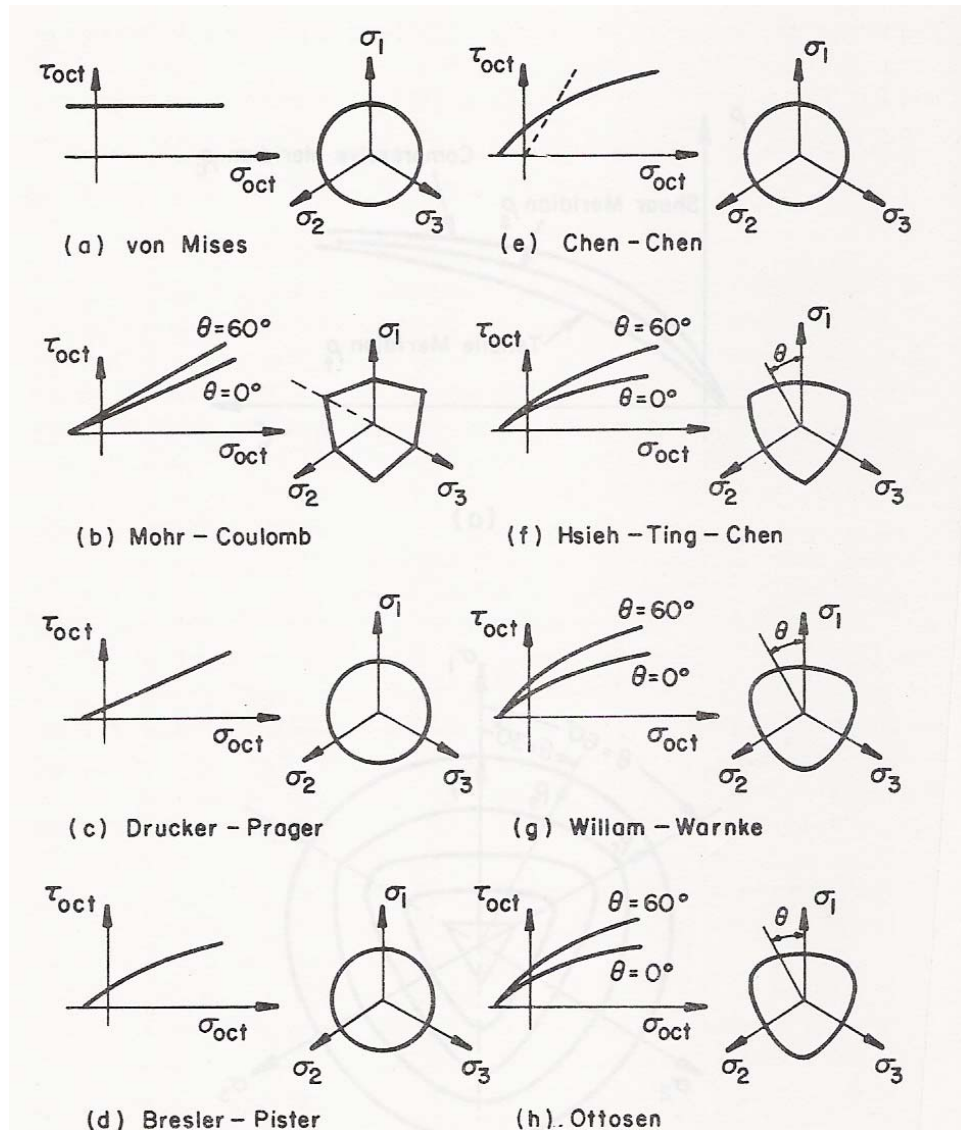


Figure 159: Concrete Models in 3D Space (Chen 1995)

Figure 27 shows a concrete's failure surface in principal stress space. The left side depicts the effect of increased hydrostatic pressure, and the successively larger failure surfaces are deviatoric sections farther out along the hydrostatic axis. The right side shows the expansion of the yield surface due to the effect of work hardening.

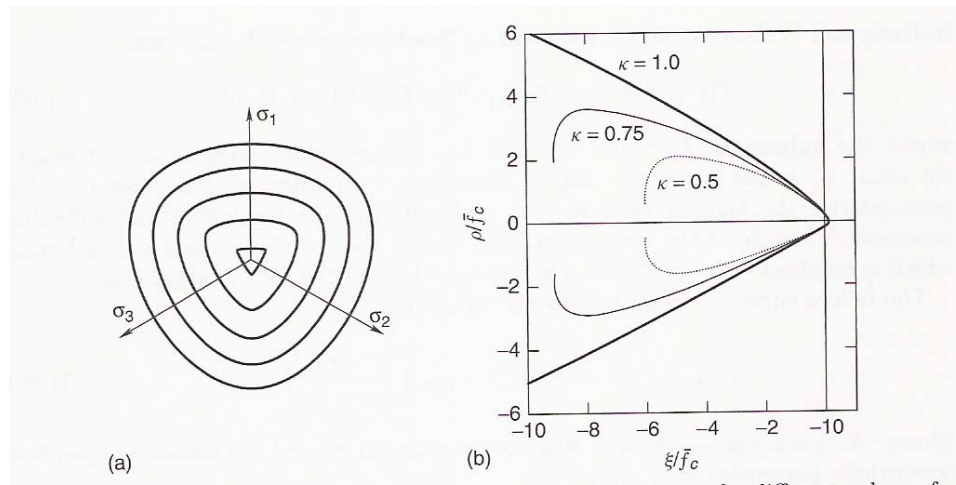


Figure 160: Concrete Yield Surface (Jirasek 2002)

In more complex models, a nonassociated flow rule with a variable dilatancy factor is used to better predict the behavior of concrete, since concrete exhibits inelastic volumetric contraction and dilation (Chen and Han, 1995). Concrete subjected to a compressive loading, exhibits inelastic volume contraction at the beginning of yielding, and volume dilation at about 75 to 90% of ultimate strength. The shape of the initial yield surface is much different than the shape of subsequent yield surfaces, and the yield surfaces are not isotropic. Therefore, nonuniform hardening rules are used which are not isotropic. Combinations of plasticity and damage theories can be used to model concrete in the softening range (Han and Chen, 1986). Experimentalists have further discovered that volumetric dilation and octahedral shear strength are influenced by concrete strength, (Chin, 2001).

2.4.6 MILD STEEL AND PRESTRESSING STRAND

Steel is a pressure independent material. Therefore, the von Mises model can be used to model the mild steel used as reinforcing steel and the tempered, high strength steel used as prestressing steel. The stress strain curve for mild steel is shown in Figure 28, and the prestressing steel in Figure 29.

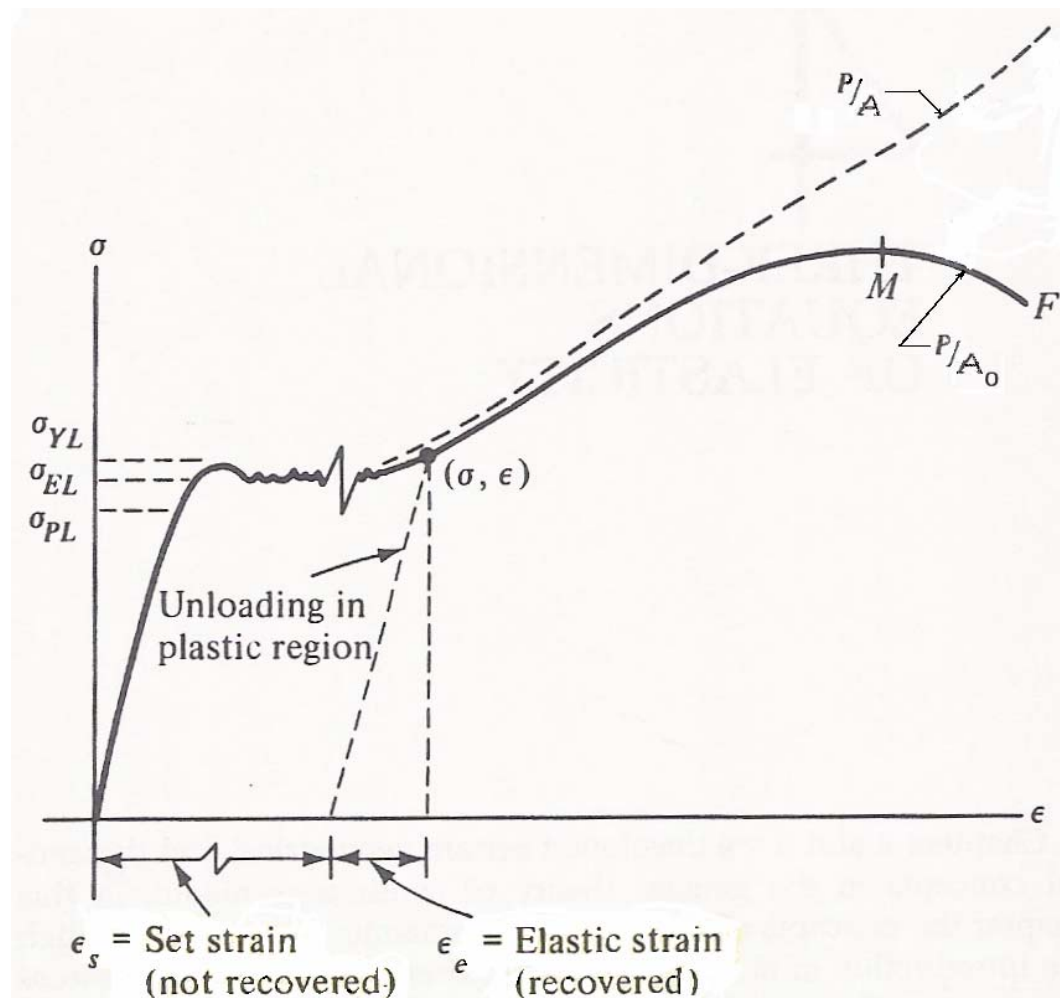


Figure 161: Mild Steel Material Model (Boresi 1987)

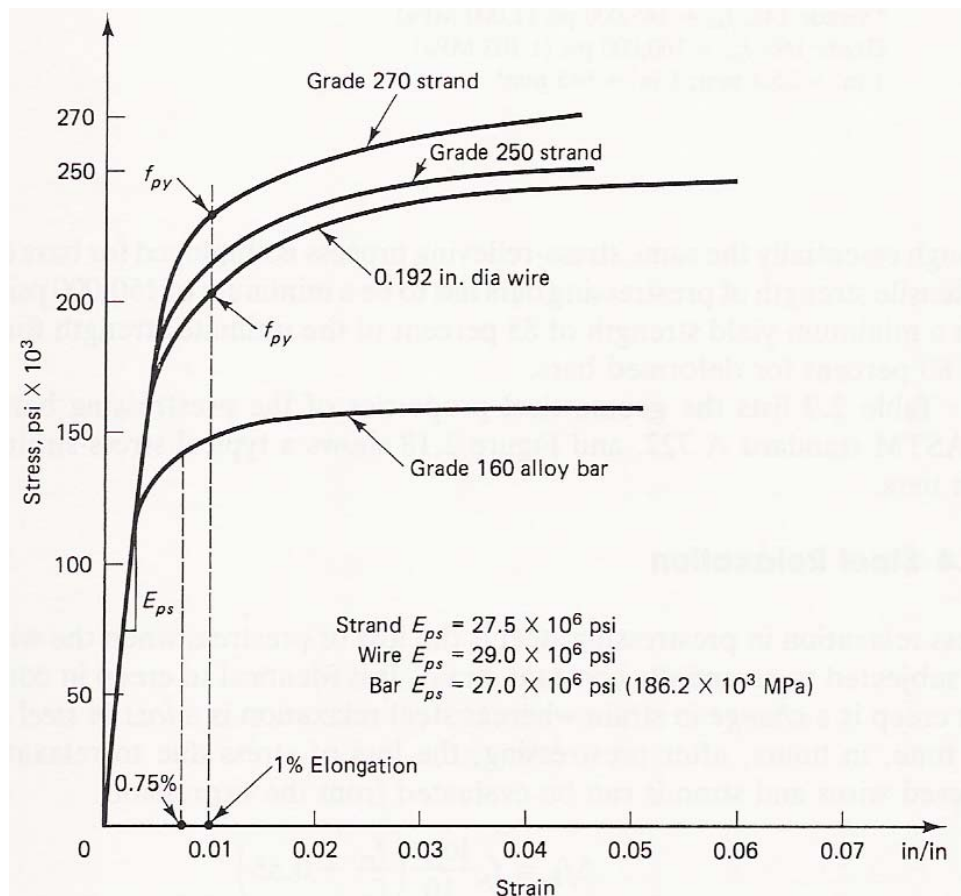


Figure 162: Prestressing Steel Model (Nawy 1996)

2.4.7 CRACK MODEL

Most present analyses use the concept of a “smeared” crack distributed either over the entire element, or at integration points within an element. The normal to the plane of the crack is oriented in the direction of the principle tensile strain. The modeling of discrete cracks is typically not performed due to the

complications encountered in circumstances such as stress reversals from dynamic or cyclic loading conditions.

2.4.8 BOND MODEL

The bond model of reinforcing steel to concrete is typically simplified as either a perfect bond model, or a linear bond stress model.

2.5 NUMERICAL ANALYSIS

The following is a summary of the static, linear, finite element stiffness method. The method is derived by equating internal virtual work to external virtual work. The underscored variables are vectors, and the brackets indicate a matrix.

Before the structure can be discretized, and the structure's nodal equilibrium equations solved for the unknown displacements, the following relations must be developed for each type of structural element that will be used in the structural model.

$$(3) \quad \underline{v} = [H] \underline{u} \quad \text{the element displacement interpolation relation} \quad (2.3)$$

$$(4) \quad \underline{\epsilon} = [B] \underline{u} \quad \text{the element strain-displacement relation} \quad (2.4)$$

$$(5) \quad \underline{\sigma} = [D] \underline{\epsilon} \quad \text{the element stress-strain relation} \quad (2.5)$$

$$(6) \quad [k] = \int [B]^T [D] [B] dv \quad \text{element stiffness matrix} \quad (2.6)$$

$$(7) \quad \underline{f} = [k] \underline{u} \quad \text{element nodal equilibrium relation} \quad (2.7)$$

where,

\underline{e} = element strain vector

\underline{f} = element nodal force vector

\underline{u} = element nodal point displacement vector

$[k]$ = element stiffness matrix

\underline{v} = element internal displacement vector

$[B]$ = element strain-displacement matrix

$[D]$ = element stress-strain (constitutive) matrix

$[H]$ = element displacement interpolation function

The structural global nodal equilibrium equations, Eq. (2.8), are solved to determine the unknown nodal displacements. The element strains and stresses are computed from the solution for the unknown nodal displacements. Before the global equilibrium equations can be solved, the structural global stiffness matrix is developed by assembling the stiffness of each element. Prior to the assembly, the individual element equations are transformed from local element coordinates to global structural coordinates. The stiffness matrix remains constant for all load conditions only in the case of a linear problem. Typically, nonlinearities in the problem require that the stiffness be recomputed at least as often as each load increment.

$$(8) \quad \underline{P} = [K] \underline{U} \quad \text{structural global nodal equilibrium relation} \quad (2.8)$$

where,

$[K]$ = structural stiffness matrix

\underline{P} = structural nodal force vector (knowns)

\underline{U} = structural nodal point displacement vector (unknowns)

2.5.1 CONSISTENT TANGENT STIFFNESS

Numerical analysis techniques are used to evaluate the integral in the element stiffness matrices. Newton-Raphson iterative solution is typically used to solve a structural mechanics equilibrium problem. Figure 30 shows the Euler (left of figure), Newton-Raphson (center in figure) and modified Newton-Raphson (right in figure) iterative solution schemes. Error accumulates at each increment of load for the Euler method. Equilibrium is satisfied at each load increment for the Newton-Raphson method, as shown in the center and right portions of Figure 30. Each successive trial solution for the equilibrium equations is based on the tangent stiffness matrix. The tangent stiffness matrix is computed using a variation in the stresses and strains, the variation is computed from the previous approximation to the current approximation. The basis of the modified Newton-Raphson method is to minimize computations, so the tangent stiffness matrix is not updated throughout the load increment.

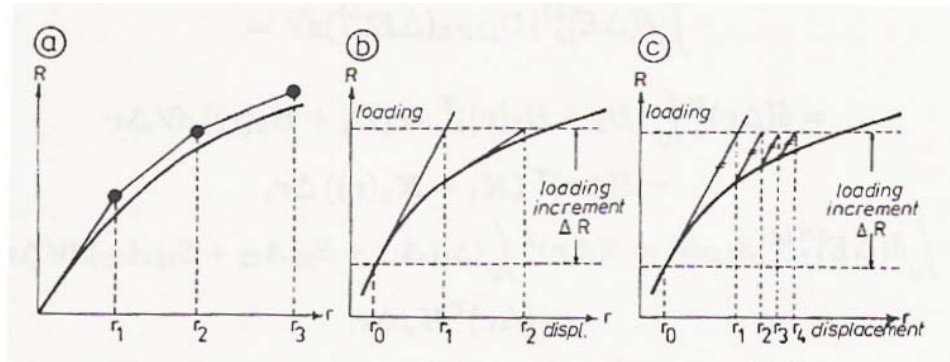


Figure 163: Solution Methods (Bittnar 1996)

The solution is iterated until convergence meets the required accuracy criteria. In nonlinear problems, the stiffness matrix can become singular, i.e. possessing non-unique solutions, resulting in convergence difficulties. For example, this can occur during a nonlinear buckling analysis where an equilibrium position is possible after an initial collapse.

A more rapid convergence rate can be obtained through the use of a “consistent tangent stiffness matrix”. The consistent tangent stiffness matrix is developed from derivatives of the stresses and strains. Since derivatives are used, the convergence rate is second order. The use of the tangent stiffness matrix provides only a first order convergence rate.

2.5.2 SOLUTION METHODS

2.5.2.1 h-METHOD

The h-method can be used for both linear and nonlinear types of analyses. Typically, the h-method requires a finer mesh than the p-method. In the h-method, the level of interpolation (e.g. linear, quadratic...) is the same in the elements. Achieving a more accurate solution generally requires refining the mesh (i.e. adding more elements). The h-method is more amenable to nonlinear analysis.

2.5.2.2 p-METHOD

The p-method can be used only for linear structural static analyses. The p-method can be used to solve a problem to a desired level of accuracy using a coarse mesh. The p-method increases the level of interpolation in the elements to achieve a required level of accuracy. Hence, the number of elements is held fixed but the interpolation may be increased to very high levels (e.g. 6, 8,... order polynomials). This method is not amenable to nonlinear analysis because it cannot handle large deformations, contact, and/or nonlinear material models well.

2.6 APPLICATIONS OF FINITE ELEMENT ANALYSES

The finite element method is a numerical technique used on a wide range of engineering problems including stress analysis, heat transfer, fluid flow and electromagnetism. Several types of structural analyses can be performed; static analysis, modal and spectrum analyses, harmonic and transient dynamic analyses, buckling analysis, and explicit dynamic analysis (ANSYS, Inc., 2002).

2.6.1 STATIC ANALYSIS

A finite element analysis determines displacements, strains, stresses, and forces in a structural system. A static analysis does not consider time varying loads, such as inertia and damping effects, but rather the structure's response reflects a steady, time independent, loading condition. The loading effects due to steady state inertia forces, such as from gravitation or rotational velocity, can be approximated as equivalent static loads. Temperature effects, and initial strains due to prestress, can also be considered by using initial strains and stresses.

Nonlinearities can originate from various sources; from geometry such as large deformations, from material such as nonlinear elasticity and hyperelasticity and plasticity, from volume changes due to creep and shrinkage, from boundary or loading conditions, and from contact elements.

2.6.2 MODAL ANALYSIS

A modal analysis determines the free vibration characteristics of a structural system; i.e. the structure's natural frequencies and mode shapes. The structural system is typically assumed to be performing within its linear range, when determining its natural frequencies and mode shapes. Damping effects on the structure can be considered when determining its free vibration characteristics. The effects of prestress and temperature on the structure's free vibration characteristics can also be considered.

2.6.3 HARMONIC RESPONSE ANALYSIS

A harmonic, or sustained cyclic, response analysis determines the effect upon a structure due to a sustained cyclic load. This type of analysis is used to determine the effects of resonance and fatigue on a structure due to a forced vibration. The structure is subjected to harmonic loads, i.e. sinusoidal varying loads with respect to time, and the steady state response of the structure is determined. The structure's response is determined for varying frequencies of the forced vibrations, and the structure's response is plotted versus the forcing frequency. Thus the structure's peak response is determined for the range of frequencies studied. The response values are typically deflections, but other responses such as peak reactions, strains or stresses could be studied. The response is determined for the steady state condition, and the initial, transient effects of the forced vibration are not determined by this analysis. The structural system is typically assumed to be performing within its linear range, when determining its steady state response. The effects of prestress on the structure's forced vibration characteristics can be considered, provided the effects of the prestress dominates the harmonic stresses.

2.6.4 TRANSIENT DYNAMIC ANALYSIS

When inertia or damping effects are important, i.e. they significantly influence the structure's time varying displacements, strains, stresses, and forces, a transient dynamic analysis is performed. The time history of the forced vibration is used to determine the dynamic response of the structure. All types of

nonlinearities can be considered in a transient dynamic analysis. The forced vibration time history is divided into successive time points, called integration time steps, and all displacements, strains and stresses are determined for each time step.

2.6.5 SPECTRUM ANALYSIS

A spectrum analysis determines a structure's response to a known spectrum. Stresses and displacements in the structure are determined from an analysis using the structure's modal analysis results, and a response spectrum. The response spectrum used, which is a graph of some spectral value versus frequency, can capture the effect of the random or time dependent load history being studied. When used, the spectrum analysis would capture the magnitude and frequency of a transient dynamic analysis that uses a time history of the loading condition.

2.6.6 BUCKLING ANALYSIS

A buckling analysis is used to determine critical loads when a structure becomes unstable, and the structure's buckled mode shapes. A buckling analysis can be either linear or nonlinear. A linear analysis predicts the theoretical buckling strength of an ideal, linear, elastic structure. The results of a linear buckling analysis will overestimate the strength of a structure. A linear analysis ignores nonlinearities in material behavior, and imperfections in geometry such as initial straightness of axially loaded members.

In a nonlinear buckling analysis, the structure's response beyond the buckling load can be monitored, provided the nature of the structure is such that the structure buckles into a stable condition. The effect of nonlinearities can be considered, such as plastic material behavior, initial member straightness, gaps in the structure, and large deformations. A nonlinear buckling analysis is a static analysis. In a nonlinear buckling analysis, as the structure is loaded near the buckling load, the solution begins to diverge. Therefore, for accurate results, the load increments must be small near buckling.

2.6.7 EXPLICIT DYNAMIC ANALYSES

The difference between an explicit dynamic analysis and an implicit dynamic analysis is in the method of time integration (Bittnar and Sejnoha, 1996). In an explicit dynamic analysis, the known values of the acceleration, velocity and displacement vectors are used in the equation of motion to predict the next time step. In an implicit dynamic analysis, the equation of motion is used to predict the next time step based on an average constant acceleration across the time increment. A central difference time integration method is typically used in an explicit dynamic analysis, and Newmark's "average acceleration" method is typically used in an implicit dynamic analysis.

An explicit dynamic analysis considers the inertial effects of mass and damping. The mass is typically assumed to be “lumped” at the nodes, so the mass matrix can be easily inverted. An implicit dynamic analysis is typically used for linear problems, problems with very long time durations, and problems that do not include contact. For implicit dynamic analysis, the inertia effects of mass and damping are usually not included, and the stiffness matrix is usually assumed constant, since inversion of the stiffness matrix is required. Alternatively, an explicit dynamic analysis is typically used in a nonlinear problem, to consider the effects of nonlinearities in materials and geometry. Contact problems are particularly amenable to solution using explicit methods because no tangent stiffness matrix is required in explicit dynamics. Typically, a data table is used to describe nonlinear material properties.